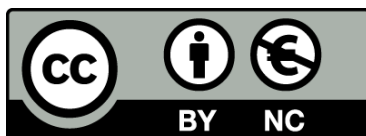




UNIVERSITAT<sub>DE</sub>  
BARCELONA

## Selective CO<sub>2</sub> capture using MOF/Graphene Oxide Materials

Elizabeth Martínez Medina



Aquesta tesi doctoral està subjecta a la llicència **Reconeixement- NoComercial 4.0. Espanya de Creative Commons**.

Esta tesis doctoral está sujeta a la licencia **Reconocimiento - NoComercial 4.0. España de Creative Commons**.

This doctoral thesis is licensed under the **Creative Commons Attribution-NonCommercial 4.0. Spain License**.



UNIVERSITAT DE  
BARCELONA

Doctoral Program in Engineering and Applied Science

---

Selective CO<sub>2</sub> capture using  
MOF/Graphene Oxide materials

---

Author: **Elizabeth Martinez Medina**

Supervisors:

**Dr.-Ing. Elena Xuriguera Martín**

**Dr. Monica Martínez López**

Academic tutor:

**Mercè Segarra Rubí**

Departament de Ciència de Materials i Química Física, Facultat de Química

2025





# UNIVERSITAT DE BARCELONA

Programa de Doctorat en Enginyeria i Ciències Aplicades

---

## Captura selectiva de CO<sub>2</sub> a través de materials MOF/Òxid de Grafè

---

Autora: **Elizabeth Martinez Medina**

Supervisores:

**Dr.-Ing. Elena Xuriguera Martín**

**Dr. Monica Martínez López**

Tutora:

**Mercè Segarra Rubí**

Departament de Ciència de Materials i Química Física, Facultat de Química



*Je suis prest*



---

# Summary

In recent years, climate change has become a central concern in the scientific community, primarily caused by greenhouse gas emissions; carbon dioxide (CO<sub>2</sub>) being one of the most significant contributors. Among the proposed strategies to mitigate its impact, porous materials have emerged as a potential solution to capture these harmful gases that present a risk to both society and the environment. Among these, Metal Organic Frameworks (MOFs) stand out due to their exceptional properties, such as thermal stability, large specific surface area, high porosity and tunable functionality, all of which are crucial for efficient gas sorption.

There is notable variability in measuring CO<sub>2</sub> capture using MOFs in the literature, which are mostly performed at low temperatures and/or high pressures, where most porous materials perform better. These conditions are not usual in emission sources like industrial chimneys or vehicle exhausts and, to overcome this, this study explores enhancing CO<sub>2</sub> adsorption performance and properties of MOF materials, specifically at 25°C and up to 1.3 atmospheres.

The present thesis explores the development, characterization, and performance of HKUST-1 and their hybrid combination with graphene-based materials, specifically graphene oxide (GO) and reduced graphene oxide (rGO), for CO<sub>2</sub> capture. The research aims to address urgent environmental concerns through the design of efficient adsorbents capable of capturing CO<sub>2</sub>.

Firstly, this work focuses on the synthesis of HKUST-1/GO hybrid materials by adding GO at several concentrations, ranging from 0.15% up to 9% w/w of GO. Using Mixed-Solvent Methods (MSM), commonly used in the synthesis of MOFs, the study identifies the optimal content of GO that enhances CO<sub>2</sub> adsorption performance at 25°C and up to 1.3 atmospheres. Additionally, a novel methodology, named here as Reverse Quantification (RQ); has been developed to quantify the experimental GO content in the hybrids, addressing inconsistencies often found in literature. As a

## Summary

result, it is determined that the theoretical amount of GO used during synthesis is not entirely incorporated into the HKUST-1 samples. A deviation from the ideality is observed across 0 to 9% GO range, generally resulting in lower experimental GO content than theoretically added. Since RQ is employed in all syntheses of this study, it proves, through different trends, the deviation from the ideal behavior in all cases. In this instance, the sample containing 0.25% w/w of experimental GO obtained via MSM exhibits the highest CO<sub>2</sub> adsorption performance, with a specific value of  $5.33 \pm 0.16$  mmol CO<sub>2</sub>/g at 1.3 atm, achieving up to 80% greater CO<sub>2</sub> uptake compared to pristine HKUST-1.

Additionally, the major focus of the research is to optimize the method of synthesis, developing a more environmentally friendly synthesis method. HKUST-1 materials are commonly synthesized by MSM using harmful and ecotoxic solvents, such as dimethylformamide, at high temperatures (85°C). Consequently, mechano-chemical synthesis through the liquid-assisted grinding (LAG) method using ball milling (BM) is explored. The results confirm that this method offers a more sustainable alternative while maintaining material performance. Two synthesis scales are investigated: small-scale (sBM) and medium-scale (bBM), with GO concentrations between 0.15–2.5% w/w, based on prior results obtained by MSM. sBM samples achieved CO<sub>2</sub> adsorption up to  $4.93 \pm 0.28$  mmol/g at 0.48–0.55% of experimental GO content, comparable to MSM results. In contrast, bBM samples reached  $3.77 \pm 0.07$  mmol/g at 0.25–0.30% w/w of experimental GO, though with less correlation between GO content and performance. Overall, mechano-chemical synthesis using ball milling proves effective, potentially scalable, and environmentally friendly.

Another important aspect is the cyclability of the synthesized material, since HKUST-1/GO hybrid material presents a notable regeneration capability over multiple adsorption-desorption cycles. Hence, the incorporation of reduced graphene oxide (rGO) into the HKUST-1 synthesis is investigated. As rGO offers

---

potential for CO<sub>2</sub> desorption via electrical heating, the main goal is to synthesize hybrid HKUST-1/rGO and HKUST-1 with mixtures of the graphenic materials (GM): rGO and GO, HKUST-1/GM; and check their CO<sub>2</sub> adsorption properties. As a result, HK-rGO samples showed slightly lower CO<sub>2</sub> adsorption than GO-based ones, and a maximum of 5.10 mmol/g is achieved at 0.80% w/w of experimental rGO. In contrast, HK-GM samples (rGO/GO mixtures) expose a better performance, reaching 6.00 mmol CO<sub>2</sub>/g with the best result at 0.60% GM (1:3 ratio of rGO/GO mixtures, respectively). These findings suggest that combining rGO and GO can enhance the adsorption of pure GO-based materials, making them a promising candidate for cyclable adsorption processes, with CO<sub>2</sub> desorption via electrical heating.

Finally, this thesis also explores the interaction between water (humidity) and CO<sub>2</sub> during adsorption processes when using HKUST-1/GO samples, both for samples obtained via mechano-chemical methods and MSM. Further analysis explores the competition of H<sub>2</sub>O with CO<sub>2</sub> during adsorption processes under post-combustion conditions, using streams of 15 % CO<sub>2</sub> and 50% RH. Specifically, this part of the research focuses on the behavior of H<sub>2</sub>O and CO<sub>2</sub> adsorption processes by using different characterization techniques, such as Infrared Spectroscopy (IR), Dynamic Vapor Sorption (DVS), Breakthrough Analysis (BTA) and Solid-State <sup>13</sup>C Nuclear Magnetic Resonance (<sup>13</sup>C NMR). A competition is observed between H<sub>2</sub>O and CO<sub>2</sub> for the material's adsorption sites, with H<sub>2</sub>O molecules exhibiting a higher affinity. The results suggest that H<sub>2</sub>O adsorption is produced mainly in carboxylate and aromatic functional groups, while CO<sub>2</sub> molecules only show preference for aromatic functional groups. The experiments also confirm that CO<sub>2</sub> has higher adsorption kinetics than H<sub>2</sub>O, aligned with RMN and IR experiments. It is also determined that the incorporation of GO increases the number of favorable adsorption sites for CO<sub>2</sub>, such as aromatic carbon, and partially blocks H<sub>2</sub>O adsorption near copper nuclei, reducing the sample degradation. As a result, HKUST-1/GO that exhibits higher CO<sub>2</sub> uptake also indicates enhanced cycling behavior than pure HKUST-1. On the contrary, CO<sub>2</sub>

## *Summary*

adsorption under humid conditions is significantly reduced, highlighting that HKUST-1/GO materials are most effective in dry environments.

Additionally, the interaction with water is studied using colorimetric sensors, as the color of HKUST-1/GO changes from light to dark blue upon drying, indicating structural changes confirmed by X-ray diffraction, linked to water content. CO<sub>2</sub> exposure also induces color changes that correlate with CO<sub>2</sub> adsorption behavior. These initial results highlight the similarity between CO<sub>2</sub> adsorption and colorimetry in HK-GO samples, with HKUST-1 showing color changes upon interaction with CO<sub>2</sub>, enabling detection of adsorbed CO<sub>2</sub> under dry conditions.

Overall, this work contributes to the field of sustainable materials for gas capture by combining advanced synthesis techniques, aligned with the principles of green chemistry, with emerging hybrid systems. The findings support the potential of HKUST-1-graphenic materials as effective and versatile CO<sub>2</sub> adsorbents.

## ***Keywords***

Metal Organic Frameworks, graphene Oxide, CO<sub>2</sub> capture, adsorption, green chemistry

---

# Resum

En els darrers anys, el canvi climàtic s'ha convertit en una preocupació central de la comunitat científica, causat principalment per les emissions de gasos d'efecte hivernacle; on el diòxid de carboni ( $\text{CO}_2$ ) destaca per ser un dels majors contribuents. Entre les estratègies proposades per mitigar-ne l'impacte, els materials porosos han sorgit com una potencial solució per capturar aquests gasos nocius, els quals presenten un risc tant per a la societat com per al medi ambient. Entre aquests, els *Metal Organic Frameworks* (MOF) destaquen per les seves propietats excepcionals, com l'estabilitat tèrmica, la gran superfície específica, l'elevada porositat i la seva funcionalitat, totes elles crucials per a processos eficients d'adsorció de gasos.

D'altra banda, la bibliografia exhibeix una notable diversitat en les condicions de mesura de l'adsorció de  $\text{CO}_2$  mitjançant MOF, que generalment es realitzen a baixa temperatura i/o altes pressions (on la majoria dels materials porosos funcionen millor). Aquestes condicions no són habituals en les fonts d'emissió més comunes, com ara les xemeneies industrials o els gasos d'escapament de vehicles. Per aquest motiu, aquest estudi es centra en millorar el rendiment d'adsorció de  $\text{CO}_2$  i analitzar les propietats dels materials MOF, concretament a  $25^\circ\text{C}$  i fins a 1,3 atmosferes.

La present tesi explora el desenvolupament, caracterització i l'eficiència d'adsorció de  $\text{CO}_2$  del HKUST-1 i la seva combinació amb materials basats en grafè, específicament òxid de grafè (GO) i òxid de grafè reduït (rGO). Aquesta investigació pretén donar resposta a les preocupacions ambientals urgents mitjançant la fabricació de materials adsorbents capaços de capturar  $\text{CO}_2$ .

En primer lloc, aquest treball es centra en la síntesi de materials híbrids HKUST-1/GO mitjançant la introducció de diferents concentracions de GO, que van des del 0,15% fins al 9% w/w de GO. Aquest estudi identifica el contingut òptim de GO que millora el rendiment d'adsorció de  $\text{CO}_2$  a  $25^\circ\text{C}$  i fins a 1.3 atmosferes de pressió. D'aquesta manera, el material es sintetitza inicialment fent servir un mètode de síntesis que

utilitza barreges de dissolvents, *Mixed-Solvent Method* (MSM), i que s'utilitza habitualment per a la obtenció de HKUST-1. A més, una nova metodologia, anomenada en aquest treball com a *Reverse Quantification* (RQ) es desenvolupa per quantificar el contingut experimental de GO en els híbrids, abordant les inconsistències que sovint es troben a la literatura amb respecte la quantitat òptima de GO que millora les propietats adsorbents del MOF. Com a resultat, es determina que la quantitat teòrica de GO utilitzada durant la síntesi no s'acaba d'incorporar completament a les mostres de HKUST-1/GO. S'observa una desviació de la idealitat en un rang de 0 a 9% de GO, que generalment resulta en un contingut experimental de GO inferior al que s'afegeix teòricament. La RQ s'utilitza en totes les síntesis de la present tesi i demostra, a través de diferents tendències, que aquesta desviació del comportament ideal es troba present en tots els casos. En el cas de les mostres sintetitzades fent servir el mètode MSM, la mostra que presenta més capacitat de captura de CO<sub>2</sub> conté un 0,25% w/w de GO experimental, i aconseguix fins a un 80% més d'adsorció de CO<sub>2</sub> en comparació amb el HKUST-1 pur, amb un valor de  $5,33 \pm 0,16$  mmol CO<sub>2</sub>/g a 1.3 atm.

D'altra banda, l'optimització del mètode de síntesi esdevé un dels principals reptes d'aquesta tesi, amb l'objectiu de desenvolupar procediments més respectuosos amb el medi ambient. Els materials HKUST-1 es sintetitzen habitualment amb dissolvents nocius i eco-tòxics, com la dimetilformamida (DMF), fent servir altes temperatures als processos d'obtenció (85°C). En conseqüència, s'explora la síntesi mecanoquímica mitjançant el mètode de molturació amb molí de boles facilitada en medi líquid (*liquid-assisted grinding*, LAG). Els resultats confirmen que aquest mètode ofereix una alternativa més sostenible alhora que manté les propietats adsorbents del material. A través d'aquest mètode de síntesi s'investiguen dues escales de producció: petita escala (sBM) i a escala mitjana (bBM), amb concentracions de GO entre el 0,15 i el 2,5% w/w. En aquest cas, els rangs de concentracions de GO utilitzats en sBM i bBM es basen en els resultats obtinguts per les mostres sintetitzades fent servir el mètode inicial MSM. D'aquesta manera, els resultats de

---

les mostres obtingudes amb sBM van aconseguir una adsorció de CO<sub>2</sub> de fins a 4,93 ± 0,28 mmol CO<sub>2</sub>/g amb un contingut experimental de GO en el rang de 0,48-0,55% w/w GO, comparable als resultats de les mostres de MSM. En canvi, les mostres de bBM van assolir 3,77 ± 0,07 mmol CO<sub>2</sub>/g en les mostres amb un contingut experimental de GO comprès entre 0,25-0,30% w/w. Tot i això, es va observar una menor correlació entre el contingut de GO i l'eficiència de captura de CO<sub>2</sub>. Com a resultat, la síntesi mecano-química mitjançant el molí de boles resulta eficaç, potencialment escalable i és respectuosa amb el medi ambient.

Un altre aspecte important és la ciclabilitat del material, i en aquest cas el material híbrid HKUST-1/GO presenta una notable capacitat de regeneració durant múltiples cicles d'adsorció-desorció. A més, s'investiga la incorporació d'òxid de grafè reduït (rGO) a la síntesi HKUST-1. Com que rGO ofereix una potencial desorció de CO<sub>2</sub> mitjançant calefacció elèctrica, l'objectiu és sintetitzar HKUST-1/rGO i HKUST-1 híbrids amb barreges dels materials basats en grafè de rGO i GO (GM), HKUST-1/GM; per comprovar les seves propietats d'adsorció de CO<sub>2</sub> amb les noves formulacions. Com a resultat, les mostres HK-rGO mostren una adsorció de CO<sub>2</sub> lleugerament menor que les basades en GO, amb un màxim de 5,10 mmol CO<sub>2</sub>/g amb un contingut experimental de 0,80% w/w de rGO. En canvi, les mostres HK-GM (mescles de rGO/GO) exposen una capacitat de captura de CO<sub>2</sub> superior, arribant fins a 6,00 mmol CO<sub>2</sub>/g amb el millor resultat obtingut per la mostra que conté una proporció experimental de GM del 0,60% w/w (proporció 1:3 de mescles rGO/GO, respectivament). Aquests resultats suggereixen que la combinació de rGO i GO pot millorar l'adsorció de materials HKUST-1 combinats amb en GO, convertint-los en un candidat prometedor per a processos d'adsorció ciclables, amb desorció de CO<sub>2</sub> potencialment facilitada mitjançant l'escalfament elèctric.

Finalment, aquesta tesi també explora la interacció entre l'aigua (humitat) i el CO<sub>2</sub> durant els processos d'adsorció quan s'utilitzen mostres de materials HKUST-1/GO, obtingudes tant pel mètode mecano-químic com per el mètode que fa servir

dissolvents. En aquest sentit, es porten a terme una sèrie d'experiments que exploren la competència de l'H<sub>2</sub>O amb el CO<sub>2</sub> durant els processos d'adsorció en condicions de postcombustió, utilitzant específicament concentracions d'un 15% de CO<sub>2</sub> i un 50% d'humitat relativa (RH). Concretament, aquesta part de la investigació se centra en el comportament dels processos d'adsorció d'H<sub>2</sub>O i CO<sub>2</sub> mitjançant l'ús de diferents tècniques de caracterització, com ara l'espectroscòpia d'infrarojos (IR), l'adsorció dinàmica de vapor (DVS), *breakthrough analysis* (BTA) i la ressonància magnètica nuclear <sup>13</sup>C d'estat sòlid (RMN <sup>13</sup>C). S'observa una competència entre H<sub>2</sub>O i CO<sub>2</sub> pels llocs d'adsorció del material, amb les molècules d'H<sub>2</sub>O que presenten una afinitat més alta. Els resultats suggereixen que l'adsorció d'H<sub>2</sub>O es produeix principalment en grups funcionals carboxilats i aromàtics, mentre que les molècules de CO<sub>2</sub> només mostren una preferència pels grups funcionals aromàtics. Els experiments també confirmen que el CO<sub>2</sub> presenta una cinètica d'adsorció més alta que l'H<sub>2</sub>O, d'acord amb els experiments de RMN <sup>13</sup>C i IR. També es va determinar que la incorporació de GO augmenta el nombre de llocs d'adsorció favorables per al CO<sub>2</sub>, com l'anell aromàtic, i bloqueja parcialment l'adsorció d'H<sub>2</sub>O prop dels nuclis de core, reduint així la degradació de la mostra. Com a resultat d'aquesta part experimental, les mostres òptimes de HKUST-1/GO que tenen la major capacitat de captació de CO<sub>2</sub>, també tenen un millor comportament de ciclabilitat adsorció-desorció respecte el HKUST-1 pur. Per contra, l'adsorció de CO<sub>2</sub> en condicions humides es veu significativament reduïda, fet que posa de manifest que els materials HKUST-1/GO són més efectius en ambients secs.

A més, la interacció amb l'aigua s'estudia mitjançant sensors colorimètrics, ja que el color tan del HKUST-1 com del HKUST-1/GO canvia de blau clar a blau fosc durant el procés d'activació (assecat del material). Això indica canvis estructurals relacionats amb el contingut d'aigua adsorbit, confirmats per difracció de raigs X. D'altra banda, els resultats indiquen que l'exposició al CO<sub>2</sub> també induïx canvis de color que es correlacionen amb el comportament d'adsorció del gas. Aquests resultats

---

preliminars posen de manifest una relació entre els canvis colorimètrics i l'adsorció de CO<sub>2</sub>, fet que permetria la detecció de CO<sub>2</sub> adsorbit en condicions seques.

En conjunt, aquest treball contribueix al camp dels materials sostenibles per a la captura de CO<sub>2</sub>, combinant tècniques de síntesi avançades, alineades amb la química verda, amb sistemes híbrids emergents. Les dades obtingudes corroboren el potencial dels compostos HKUST-1-materials basats en grafè com a adsorbents de CO<sub>2</sub> efectius i versàtils.

### ***Paraules clau***

*Metal Organic Frameworks, òxid de grafè, captura de CO<sub>2</sub>, adsorció, química verda*



---

# Resumen

En los últimos años, el cambio climático se ha convertido en una preocupación central para la comunidad científica, debido al aumento de las emisiones de gases de efecto invernadero, entre los cuales el dióxido de carbono ( $\text{CO}_2$ ) destaca por ser uno de los mayores contribuyentes. Entre las estrategias propuestas para mitigar el impacto, los materiales porosos han surgido como una potencial solución para capturar estos gases nocivos, cuya presencia presenta un riesgo tanto para la sociedad como para el medio ambiente. Entre ellos, los *Metal Organic Frameworks* (MOFs) destacan por sus propiedades excepcionales, como su alta estabilidad térmica, gran superficie específica, elevada porosidad i versátil funcionalidad, todas ellas cruciales para procesos eficientes de adsorción de gases.

Por otro lado, la bibliografía indica una notable diversidad en las condiciones de medición de la adsorción de  $\text{CO}_2$  mediante MOF, que suelen realizarse a baja temperatura i/o altas presiones (dónde la mayoría de los materiales porosos funcionan mejor). Sin embargo, estas condiciones no son habituales en las fuentes de emisión más comunes, como las chimeneas industriales o los gases de escape en coches. Por este motivo, este estudio se centra en mejorar el rendimiento de la adsorción de  $\text{CO}_2$  y analizar las propiedades de los materiales MOF, concretamente a  $25^\circ\text{C}$  y hasta 1,3 atmosferas.

La presente tesis explora el desarrollo, caracterización y eficiencia de adsorción de  $\text{CO}_2$  del HKUST-1 y su combinación con materiales basados en grafeno, específicamente óxido de grafeno (GO) y óxido de grafeno reducido (rGO). Esta investigación tiene como objetivo responder a las preocupaciones ambientales urgentes mediante la fabricación de materiales adsorbentes capaces de capturar  $\text{CO}_2$ .

En primer lugar, este trabajo se centra en la síntesis de materiales híbridos HKUST-1/GO mediante la introducción de diferentes concentraciones de GO, que

van desde el 0,15% hasta el 9% w/w de GO. El material se sintetiza inicialmente utilizando un método de síntesis que utiliza mezclas de disolventes, *Mixed-Solvent Method* (MSM), y que se utiliza habitualmente para la obtención de HKUST-1. Adicionalmente, se desarrolla una nueva metodología, nombrada en este estudio como Reverse Quantification (RQ), con el objetivo de cuantificar el contenido experimental de GO en los híbridos, abordando las inconsistencias que usualmente se encuentran en la literatura con respecto a la cantidad óptima de GO que mejora las propiedades adsorbentes del MOF.

Como resultado, se determina que la cantidad teórica de GO utilizada durante la síntesis no acaba de incorporarse completamente a las muestras de HKUST-1/GO. Se observa una desviación respecto al comportamiento ideal en el rango estudiado de 0 a 9% de GO, con contenidos experimentales de GO más inferiores a los valores teóricos. El procedimiento RQ se aplica en todas las síntesis de esta investigación y demuestra a través de diferentes tendencias que esta desviación del comportamiento ideal se observa en todos los casos. En las muestras sintetizadas mediante el método MSM, la muestra que presenta una mayor capacidad de captura de CO<sub>2</sub> contiene un 0,25% w/w de GO experimental, alcanzando un 80% más de adsorción de CO<sub>2</sub> en comparación con el HKUST-1 puro, con un valor de  $5,33 \pm 0,16$  mmol CO<sub>2</sub>.

Por otra parte, la optimización del método de síntesis se convierte en uno de los principales retos de esta tesis, con el objetivo de desarrollar procedimientos más respetuosos con el medio ambiente. Los materiales HKUST-1 se sintetizan habitualmente con disolventes nocivos y eco-tóxicos, como la dimetilformamida (DMF), utilizando altas temperaturas en los procesos de obtención (85°C). En consecuencia, se explora la síntesis mecano-química mediante el método de molturación con molino de bolas facilitada en medio líquido (*liquid-assisted grinding*, LAG). Los resultados confirman que este método ofrece una alternativa más sostenible al tiempo que mantiene las propiedades adsorbentes del material.

---

A través de este método de síntesis se investigan dos escalas de producción: a pequeña escala (sBM) y a escala media (bBM), con concentraciones de GO entre el 0,15 y el 2,5% w/w. En este caso, los rangos de concentraciones de GO utilizados en sBM y bBM se basan en los resultados obtenidos por las muestras sintetizadas utilizando el método inicial MSM. De esta forma, los resultados de las muestras obtenidas con sBM alcanzaron una adsorción de CO<sub>2</sub> de hasta  $4,93 \pm 0,28$  mmol CO<sub>2</sub>/g con un contenido experimental de GO en el rango de 0,48-0,55% w/w GO, comparable a los resultados de las muestras de MSM. En cambio, las muestras de bBM alcanzaron  $3,77 \pm 0,07$  mmol CO<sub>2</sub>/g con un contenido experimental de GO comprendido entre 0,25-0,30% w/w. Sin embargo, se observó una menor correlación entre el contenido de GO y la eficiencia de captura de CO<sub>2</sub>.

Otro aspecto importante es la ciclabilidad del material, en cuyo caso el material híbrido HKUST-1/GO presenta una notable capacidad de regeneración durante múltiples ciclos de adsorción-desorción. Además, se investiga la incorporación de óxido de grafeno reducido (rGO) en la síntesis HKUST-1. Dado que rGO ofrece una potencial desorción de CO<sub>2</sub> mediante calefacción eléctrica, el objetivo es sintetizar HKUST-1/rGO y HKUST-1 híbridos con mezclas de los materiales basados en grafeno de rGO y GO (GM), HKUST-1/GM; para comprobar sus propiedades de adsorción de CO<sub>2</sub> con nuevas formulaciones. Como resultado, las muestras HK-rGO muestran una adsorción de CO<sub>2</sub> ligeramente menor que las basadas en GO, con un máximo de 5,10 mmol CO<sub>2</sub>/g con un contenido experimental de 0,80% w/w de rGO. En cambio, las muestras HK-GM (mezclas de rGO/GO) exponen una capacidad de captura de CO<sub>2</sub> superior, llegando hasta 6,00 mmol CO<sub>2</sub>/g con el mejor resultado obtenido por la muestra que contiene una proporción experimental de GM del 0,60% w/w (proporción 1:3 de mezclas rGO/GO, respectivamente). Estos resultados sugieren que la combinación de rGO y GO puede mejorar la absorción de los materiales HKUST-1 combinados con GO, convirtiéndolos en un candidato prometedor para procesos de adsorción ciclables, con desorción de CO<sub>2</sub> potencialmente facilitada mediante el calentamiento eléctrico.

Por último, esta tesis también analiza la interacción entre el agua (humedad) y el CO<sub>2</sub> durante los procesos de adsorción cuando se utilizan muestras de materiales HKUST-1/GO, obtenidas tanto por el método mecano-químico como por el método que utiliza disolventes. En este sentido, se llevan a cabo una serie de experimentos que exploran la competencia del H<sub>2</sub>O con el CO<sub>2</sub> durante los procesos de adsorción en condiciones de postcombustión, utilizando específicamente concentraciones de un 15% de CO<sub>2</sub> y un 50% de humedad relativa (RH). Esta parte de la investigación se centra en el comportamiento de los procesos de adsorción de H<sub>2</sub>O y CO<sub>2</sub> mediante el uso de diferentes técnicas de caracterización, tales como la espectroscopia de infrarrojos (IR), la adsorción dinámica de vapor (DVS), *breakthrough analysis* (BTA) y la resonancia magnética nuclear (RMN <sup>13</sup>C). Se observa una competencia entre el H<sub>2</sub>O y el CO<sub>2</sub> por los sitios de adsorción del material, donde las moléculas de H<sub>2</sub>O presentan una mayor afinidad. Los resultados sugieren que la adsorción del H<sub>2</sub>O se produce principalmente en grupos funcionales carboxilato y aromático, mientras que las moléculas de CO<sub>2</sub> solo muestran preferencia por los grupos funcionales aromáticos. Los experimentos también confirman que el CO<sub>2</sub> presenta una cinética de adsorción más alta que el H<sub>2</sub>O, en consonancia con los experimentos de RMN <sup>13</sup>C e IR. También se determinó que la incorporación de GO aumenta el número de sitios de adsorción favorables para el CO<sub>2</sub>, como el anillo aromático, y bloquea parcialmente la adsorción de H<sub>2</sub>O cerca de los núcleos de cobre, reduciendo así la degradación de la muestra. Como resultado de esta parte experimental, las muestras óptimas de HKUST-1/GO que tienen la mayor capacidad de captación de CO<sub>2</sub>, también tienen un mejor comportamiento de ciclabilidad adsorción-desorción respecto al HKUST-1 puro. Por el contrario, la adsorción de CO<sub>2</sub> en condiciones húmedas (en presencia de moléculas de H<sub>2</sub>O) se ve significativamente reducida, hecho que pone de manifiesto que los materiales HKUST-1/GO son más efectivos en ambientes secos.

Además, la interacción con el agua se estudia mediante sensores colorimétricos, puesto que el color tanto del HKUST-1 como del HKUST-1/GO cambia de azul claro a

---

azul oscuro durante el proceso de activación (secado del material). Esto indica cambios estructurales relacionados con el contenido de agua adsorbido, confirmados por difracción de rayos X. Por otra parte, los resultados indican que la exposición al CO<sub>2</sub> también induce cambios de color que se correlacionan con el comportamiento de adsorción del gas. Estos resultados preliminares ponen de manifiesto una relación entre los cambios colorimétricos y la adsorción de CO<sub>2</sub>, lo que permitiría la detección de CO<sub>2</sub> adsorbido en condiciones secas.

En su conjunto, este trabajo contribuye al campo de los materiales sostenibles para la captura de CO<sub>2</sub>, combinando técnicas de síntesis avanzadas, alineadas con los principios de la química verde, con sistemas híbridos emergentes. Los datos obtenidos corroboran el potencial de los compuestos HKUST-1- materiales basados en grafeno como adsorbentes de CO<sub>2</sub> efectivos y versátiles.

### ***Palabras clave***

*Metal Organic Frameworks*, óxido de grafeno, captura de CO<sub>2</sub>, adsorción, química verde



---

# Agradecimientos

Cuando empecé esta tesis académica era una persona completamente diferente. La vida da muchas vueltas, y una vez Sergio Huete me dijo: ya verás todo lo que vas a vivir durante los años de tu tesis...Y la verdad es que tenía razón. En estos 5 años mi vida no ha sido solo mi tesis. Ha sido un camino en el que me han acompañado muchísimas personas, me he despedido de otras tantas, y he aprendido más que nunca en mi vida, tanto a nivel personal como profesional. Por eso, me gustaría dejar constancia en estas páginas, parte de esas personas que me han acompañado y han sido importantes para mí durante el transcurso de esta tesis.

En primer lugar, quiero agradecerles a mis directoras de tesis Elena y Mónica, por todo lo que han hecho por mí. Me han enseñado muchas cosas a lo largo de esta tesis y para mí siempre van a ser un modelo a seguir y unos grandes referentes. Estoy muy agradecida de haber tenido la oportunidad de realizar esta tesis bajo su dirección y siempre lo voy a recordar con mucho cariño. También quiero agradecer a mi tutora de tesis, Mercè, que siempre ha estado ayudándonos y también ha sido un pilar fundamental en este trabajo.

Por otro lado, quiero agradecer a todo el grupo DIOPMA. Desde el primer momento que empecé este trabajo me he sentido muy acogida en el grupo y siempre me han ayudado en todo lo que he necesitado. Inés, Joan, Camila, Esther, Chema, Jessica, Alejandro y a todos mis compañeros del grupo y laboratorio. En especial, agradecer a Quim, Adrià, Camilo, Carla, Anna, Pol, Adela, Marta, Javi y, sobre todo, a Padi. Muchas gracias a todos vosotros por haberme acompañado en este camino. Estoy muy agradecida de haber formado parte de DIOPMA y siento que cada uno de vosotros ha sido siempre indispensable.

También quiero hacer una especial mención a Maria de Jaén. Quiero dedicarle esta tesis en gran parte a ella, con la que no solo he compartido una investigación científica, congresos y cafés en la universidad, sino que también he compartido

muchas cosas de mi vida personal con ella y estoy muy agradecida de haber podido conocerla en estos años de tesis. Ella ha sido un pilar fundamental en la evolución de este proyecto y una gran amiga.

En especial, también quiero agradecerles a mis amigos más cercanos haberme acompañado durante este camino. Anna, Laura, Irene y Marina, muchas gracias por ser mis mejores amigas y estar siempre a mi lado en todos mis proyectos.

Alba y Arturo, a vosotros no solo os dedico parte de esta tesis, sino que también os quiero dar las gracias por haber sido mis mejores amigos desde el instituto y haberme apoyado siempre. Ya formáis parte de mi familia y también estoy muy orgullosa de vosotros y de vuestros logros.

Por último, quiero agradecer a mi familia todo el apoyo y cariño que he recibido durante estos años que he realizado este trabajo.

Muchas gracias, mamá y papá, gracias por confiar en mí. Gracias por llevarme en coche siempre que lo necesité, por todos los *tuppers*, bocadillos, y por escucharme cada vez que hablaba de mi investigación (aunque muchas veces no entendierais de lo que hablaba). Gracias por quererme tanto, por estar a mi lado siempre que lo he necesitado y, sobre todo, por haberme enseñado los valores que tengo. He llegado tan lejos gracias a vosotros y siempre estaré agradecida por ello.

Y a mi hermana, Elena. Muchas gracias por ser mi hermana, por estar siempre a mi lado y por quererme tanto como te quiero yo a ti. Te dedico esta tesis y te agradezco todo lo que has hecho por mí. Aunque nos peleemos eres y serás siempre mi persona favorita y más importante en mi vida. Pero por favor, deja de robarme ropa que tengo casi 30 años y tú casi 25.

También quiero hacer una especial mención a mi tío Javi. Él siempre ha sido mi mayor ejemplo a seguir con respecto a todos los objetivos en la vida (el mío y el de toda la familia). Desde que fui pequeña, siempre te he admirado y espero que estés tan

---

orgullosa de mí como lo está toda nuestra familia de ti y de lo lejos que has llegado en tu carrera, personal y profesional.

Y por último...pero no menos importante, quiero agradecerme por creer en mí. Quiero agradecerme por hacer este trabajo tan duro. Quiero darme las gracias por haber sido todo el tiempo yo. Quiero darme las gracias a mí misma por haber aprendido tanto, por haber tenido tanta paciencia, por haber superado tantos momentos difíciles durante estos años y por no haberme rendido nunca.

*Y también gracias yaya Cele, por formar parte de mí y por estar siempre a mi lado. Espero que estés orgullosa de tu nieta favorita desde allí donde estés.*



---

## Table of contents

---

<b>Summary</b> .....	<b>i</b>
Keywords.....	iv
<b>Resum</b> .....	<b>v</b>
Paraules clau.....	ix
<b>Resumen</b> .....	<b>xi</b>
Palabras clave.....	xv
<b>Agradecimientos</b> .....	<b>xvii</b>
<b>Table of contents</b> .....	<b>xxi</b>
<b>1 Chapter I: Introduction</b> .....	<b>- 1 -</b>
<b>Summary of the chapter</b> .....	<b>- 1 -</b>
1.1 Introduction.....	- 3 -
1.1.1 Industrial process of CO <sub>2</sub> capture.....	- 5 -
1.1.2 CO <sub>2</sub> capture from direct atmospheric air.....	- 7 -
1.2 CO <sub>2</sub> capture and adsorption key performance indicators.....	- 10 -
1.3 Metal organic frameworks.....	- 18 -
1.3.1 Synthesis of MOFs using Mixed solvent method.....	- 23 -
1.3.2 Synthesis of MOFs using microwave synthesis.....	- 26 -
1.3.3 Synthesis of MOFs using sonochemical synthesis.....	- 28 -
1.3.4 Synthesis of MOFs using electrochemical synthesis.....	- 29 -
1.3.5 Synthesis of MOFs using mechanochemical synthesis.....	- 31 -
1.4 Metal organic frameworks and CO <sub>2</sub> adsorption performance.....	- 36 -
1.5 MOF combined with graphenic materials.....	- 41 -
1.5.1 MOF combined with graphene oxide.....	- 41 -
1.5.2 MOFs combined with reduced graphene oxide.....	- 46 -

1.5.3	MOF combined with graphene nanoplatelets.....	- 47 -
1.5.4	MOFs combined with carbon nanotubes .....	- 48 -
1.5.5	MOF combined with fullerenes .....	- 49 -
1.6	Final discussion and research perspective.....	- 59 -
<b>2</b>	<b>Chapter II: Motivations and Objectives .....</b>	<b>- 65 -</b>
2.1	Motivation.....	- 67 -
2.2	Objectives .....	- 69 -
<b>3</b>	<b>Chapter III: Synthesis and characterization of HKUST-1/GO composites obtained by Mixed Solvent Method (MSM) .....</b>	<b>- 71 -</b>
	<b>Summary of the chapter.....</b>	<b>- 71 -</b>
3.1	Mixed solvent method synthesis .....	- 73 -
3.2	Materials characterization and performance for samples obtained via MSM.....	- 77 -
3.2.1	Elemental analysis .....	- 78 -
3.2.2	X-ray-diffraction, infrared spectroscopy and Raman spectroscopy-	79 -
3.2.3	Thermogravimetry analysis .....	- 84 -
3.2.4	Scanning electron microscopy.....	- 89 -
3.2.5	Particle size measurements.....	- 93 -
3.2.6	Gas sorption measurements and surface properties.....	- 94 -
3.2.7	Reverse quantification.....	- 104 -
3.3	Conclusions .....	- 110 -
<b>4</b>	<b>Chapter IV: Synthesis and Characterization of HKUST-1/GO Materials via Ball Milling Methods .....</b>	<b>- 111 -</b>
	<b>Summary of the chapter.....</b>	<b>- 111 -</b>
4.1	Mechano-chemical synthesis.....	- 113 -
4.2	Materials characterization and performance for samples obtained via small ball milling.....	- 121 -

4.2.1	Reverse quantification.....	- 122 -
4.2.2	Gas sorption measurements and surface properties.....	- 124 -
4.2.3	Particle size measurements.....	- 134 -
4.2.4	X-ray diffraction and infrared spectroscopy.....	- 136 -
4.2.5	Thermogravimetry analysis.....	- 143 -
4.2.6	Scanning electron microscopy.....	- 146 -
4.3	Statistical analysis (small ball milling).....	- 149 -
4.4	Materials characterization and performance for samples obtained via bBM.....	- 151 -
4.4.1	Reverse quantification.....	- 152 -
4.4.2	Gas sorption measurements properties and surface properties .	- 153 -
4.4.3	Particle size measurements.....	- 158 -
4.4.4	X-ray diffraction and infrared spectroscopy.....	- 159 -
4.4.5	Scanning electron microscopy.....	- 161 -
4.5	Statistical analysis (big ball milling).....	- 163 -
4.6	Comparative evaluation of the synthetic methods: MSM, sBM and Bbm.....	- 166 -
4.7	Conclusions.....	- 173 -

## **5 Chapter V: Synthesis of HKUST-1/Graphenic Materials via Ball Milling..... - 177 -**

### **Summary of the chapter..... - 177 -**

5.1	Mechano-chemical synthesis with graphenic materials.....	- 179 -
5.2	Materials characterization and performance.....	- 182 -
5.2.1	Reverse quantification.....	- 183 -
5.2.2	Gas sorption measurements.....	- 185 -
5.2.3	Particle size measurements.....	- 189 -
5.2.4	X-ray diffraction and infrared spectroscopy.....	- 191 -
5.2.5	Thermogravimetric analysis.....	- 194 -

5.2.6	Scanning electron microscopy.....	- 197 -
5.3	Comparative evaluation of the synthetic methods for HKUST-1/Graphenic materials.....	199
5.4	Conclusions .....	- 205 -
<b>6</b>	<b>Chapter VI: The influence of H<sub>2</sub>O molecules on HK-GO materials.....</b>	<b>- 207 -</b>
	<b>Summary of the chapter.....</b>	<b>- 207 -</b>
6.1	The influence of H <sub>2</sub> O in the color of HKUST-1 .....	- 209 -
6.2	Colorimetry .....	- 213 -
6.2.1	Color change of HKUST-1.....	- 215 -
6.2.2	Color change of HKUST-1/GO .....	- 218 -
6.2.3	Simultaneous CO <sub>2</sub> and H <sub>2</sub> O signal response .....	- 220 -
6.3	Infrared spectroscopy: Influence of H <sub>2</sub> O and CO <sub>2</sub> adsorption .....	- 222 -
6.3.1	Experimental approach to analyze vibrational changes in HK-GO materials under CO <sub>2</sub> and H <sub>2</sub> O adsorption .....	- 224 -
6.4	Mapping adsorption of H <sub>2</sub> O and CO <sub>2</sub> via solid-state <sup>13</sup> C NMR .....	- 235 -
6.5	Co-adsorption of CO <sub>2</sub> and H <sub>2</sub> O.....	- 244 -
6.5.1	Dynamic vapor sorption .....	- 245 -
6.5.2	Breakthrough analysis .....	- 256 -
6.6	Conclusions .....	- 262 -
<b>7</b>	<b>Chapter VII: Conclusions.....</b>	<b>- 265 -</b>
	<b>References.....</b>	<b>- 273 -</b>
	<b>Appendix.....</b>	<b>- 291 -</b>

# Glossary

---

## A

**ATR-FTIR:** Attenuated Total Reflectance - Fourier Transform Infrared Spectroscopy

---



## B

**bBM:** Big Ball Milling

**BET:** Brunauer–Emmett–Teller

**BM:** Ball Milling

**BTA:** Breakthrough Analysis

**BTC / H<sub>3</sub>BTC:** 1,3,5-benzenetricarboxylic acid (trimesic acid)

---



## C

**CCS:** Carbon Capture and Sequestration

**CH<sub>3</sub>Cl:** Chloroform

**CNT:** Carbon Nanotube

**CO<sub>2</sub>:** Carbon Dioxide

**CA:** Citric Acid

**Cu(NO<sub>3</sub>)<sub>2</sub>·2.5H<sub>2</sub>O:** Copper(II) nitrate hemipentahydrate

---



## D

**DEEA:** Diethylethanolamine

**DEF:** N,N-Diethylformamide

**DI water:** Deionized Water

**DIOPMA:** Centro de diseño y optimización de procesos y materiales

**DMF:** Dimethylformamide



**DVS:** Dynamic Vapor Sorption

---

## E

**EA:** Elemental Analysis

**EtOH:** Ethanol

---



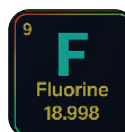
## F

**FUM:** Fumaric acid

**FDCA:** 2,5-furandi-carboxylic acid

**FTIR:** Fourier Transform Infrared Spectroscopy

---



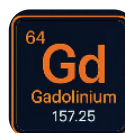
## G

**GCB:** Global Carbon Budget

**GM:** Graphenic Material (rGO/GO mixtures)

**GO:** Graphene Oxide

---



## H

**H<sub>3</sub>BTC:** Trimesic acid

**H<sub>3</sub>BDC:** Terephthalic acid

**H<sub>3</sub>BTB:** 1,3,5-tris(4-carboxyphenyl) benzene

**H<sub>3</sub>ETTB:** 4,4',4''-benzene-1,2,3-triyl tris(ethylene-2,1-diyl) tribenzoate

**H<sub>3</sub>BPB:** 1,3,5-Tris(4'-carboxy[1,1'-biphenyl]-4-yl) benzene

**H<sub>4</sub>DHTP:** 4,4'-Dihydroxy-[1,1'-biphenyl]-3,3',5,5'-tetracarboxylic acid

**HK:** Short for HKUST-1

**HK-GM:** HKUST-1 combined with GM (rGO/GO mixtures)

**HK-GO:** HKUST-1 combined with GO



**HK-rGO:** HKUST-1 combined with rGO

**HK-X:** Nomenclature for HKUST-1 materials, being X the proportion of GO.

**HK-XGM:** Variant of HK combined with GM

**HK-XGO:** Variant of HK combined with GO

**HKUST:** Hong Kong University of Science and Technology MOF

---

## I

**IAST:** Ideal Adsorbed Solution Theory

**ILAG:** Ion and Liquid Assisted Grinding

**INA:** Isonicotinic Acid

**IR:** Infrared Spectroscopy

**IRMOF:** Isorecticular Metal–Organic Framework

---



## L

**LAG:** Liquid Assisted Grinding

---



## M

**MAX30105:** Optical module with LED and photodiode

**MEA:** Monoethanolamine

**MIL:** Matériaux de l'Institut Lavoisier

**MIND:** Micro-nanotechnology research group

**MOF:** Metal–Organic Framework

**MOF-GO:** MOF hybrid with Graphene Oxide

**MSM:** Mixed Solvent Method

**MeIM:** 2-Methylimidazole



**MeOH:** Methanol

---

## N

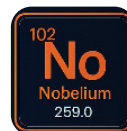
**NH<sub>2</sub>-BDC:** 2-Amino-1,4-benzenedicarboxylic acid

**NMP:** N-Methyl-2-pyrrolidone

**NG:** Neat Grinding

**N<sub>2</sub>:** Nitrogen

---



## O

**OMS:** Open Metal Sites

---



## P

**PLA:** Polylactic Acid

**PPy:** Polypyrrole

---



## R

**RH:** Relative Humidity

**RQ:** Reverse Quantification

**rGO:** Reduced Graphene Oxide

---



## S

**SA:** Synthetic Air

**SSA:** Specific Surface Area

**sBM:** Small Ball Milling

---



## T

**TBAB:** Tetrabutylammonium bromide

**TEA:** Triethylamine

---



---

## U

**UiO-66:** University of Oslo MOF (with Zr and BDC)



---

## X

**XPS:** X-ray Photoelectron Spectroscopy

**XRD:** X-ray Diffraction



---

## Z

**ZIF:** Zeolitic Imidazolate Framework

**Zn(BDC):** Zinc terephthalate MOF





---

## Chapter I: Introduction

---

### *Summary of the chapter*

*The following chapter introduces the context and scope of this thesis, providing some data related to greenhouse gas emissions, with specific focus on the contribution of CO<sub>2</sub>. The main key performance indicators (KPI) commonly used to assess gas capture performance are explained, including gas adsorption, porosity, cyclability, selectivity and scalability.*

*After describing the current situation and criteria for selecting effective CO<sub>2</sub> sorbent material, Metal Organic Frameworks (MOFs) are presented as a potential solution. Various synthetic methods are discussed, along with examples of CO<sub>2</sub> capture results reported in the literature.*

*Additionally, the combination of MOFs with graphenic materials is explored by reviewing recent studies. This includes MOFs combined with graphene oxide (MOF/GO), reduced graphene oxide (MOF/rGO), combinations using GO/rGO (MOF/Polym/GO/rGO), nanoplatelets of graphene (MOF/GNP), carbon nanotubes (MOF/CNTs) and fullerenes (MOF/C<sub>60</sub>). Notable examples of functional materials from these combinations are highlighted, and the corresponding CO<sub>2</sub> adsorption performance of these structures is discussed, summarizing all the collected data in a comparative table.*

*Finally, the introduction of this thesis presents a brief discussion of the key considerations outlined above. Based on the data analyzed, MOF-GO are identified as the promising candidates for achieving significant CO<sub>2</sub> capture, particularly the combination of HKUST-1/GO. The potential advantages and challenges of fabricating this hybrid material are also discussed.*



## 1.1 Introduction

Currently, the fight against climate change is a challenge. Pollutants, specifically CO<sub>2</sub>, remain in the atmosphere at high concentrations and trigger processes such as the greenhouse effect. It is forecasted that if the magnitude of CO<sub>2</sub> emitted persists throughout the years, large-scale damaging effects will arise including melting ice caps,<sup>1</sup> rising sea levels,<sup>2</sup> ozone layer depletion,<sup>3</sup> ocean acidification<sup>4</sup> and desertification.<sup>5</sup> Moreover, global warming has been rising at a rate of approximately 0.2 °C per decade since 1970, resulting in a total increase of about 1 °C. This acceleration is expected to continue over the coming years, and predictions show that reaching the 1.5 °C threshold could be surpassed between 2030 and 2050.<sup>6</sup> Conversely, under normal conditions, CO<sub>2</sub> is retained through natural processes, such as absorption in aqueous media (oceans and rivers) and photosynthesis. In aqueous environments, CO<sub>2</sub> reacts with water to form carbonic acid, which is incorporated into animal tissues and rocks and eventually remains on the seabed as sediments. Meanwhile, during photosynthesis, CO<sub>2</sub> is transformed into carbohydrates and oxygen, playing a crucial role in the carbon cycle. On the other hand, CO<sub>2</sub> emissions are also produced by vegetal and animal breathing and volcanic eruptions, as well as by anthropogenic activities such as industry, transport and mining. However, when the biogeochemical cycle becomes unstable, unbalanced emissions are produced and CO<sub>2</sub> accumulates in large quantities increasing the greenhouse effect.<sup>7</sup>

Some data revealed that the concentration of CO<sub>2</sub> in the atmosphere is approximately 419.3 ppm.<sup>8</sup> Figure 1.1 show the evolution of CO<sub>2</sub> emissions from 1990 to 2024 and as can be seen, during 2020 there was a lower impact of emissions due to the COVID-19 pandemic. Even though China's emissions strongly declined during February and emissions decayed in the rest of the world, April was the month with the lowest CO<sub>2</sub> production. Though, this value is extremely high compared with concentration in 1750, when the estimated quantity of atmospheric CO<sub>2</sub> was

approximately 277 ppm. Atmospheric CO<sub>2</sub> concentration has increased around 50 % since then and, according to the literature, the contribution of fossil fuel combustion through constant anthropogenic activity are the cause of this remarkable intensification of contaminants (e.g. transport, heating and cooling, industry, fossil industry own use, and natural gas flaring).<sup>3,9</sup> Specifically, the massive abundance of CO<sub>2</sub> in the atmosphere can no longer be balanced by natural cycles leading to serious environmental problems in the not-so-distant future.<sup>10</sup>

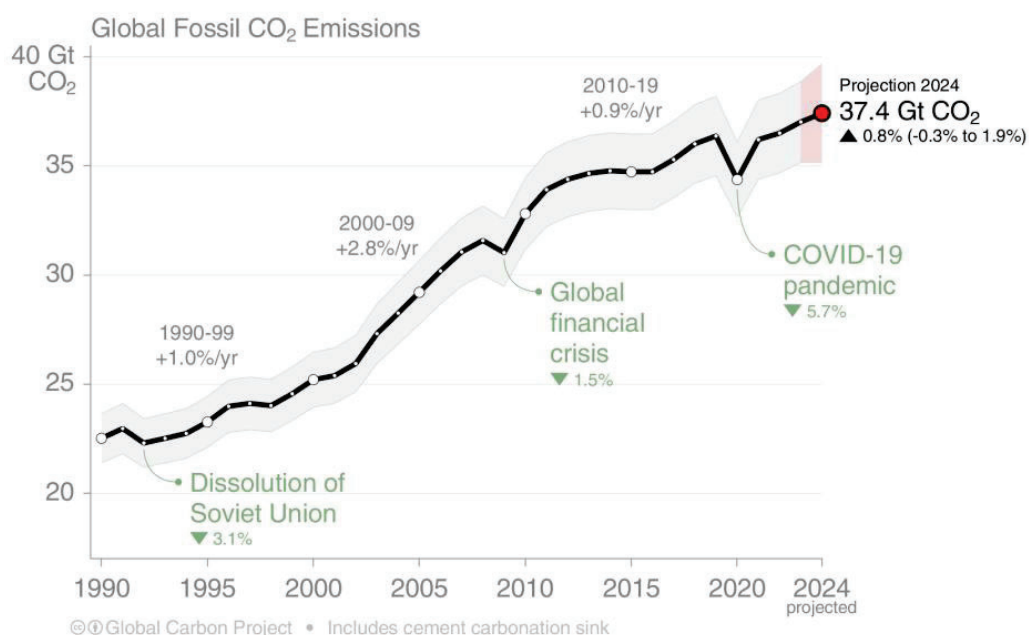


Figure 1.1. Global fossil CO<sub>2</sub> emissions. Used with permission of the Global Carbon Project under the Creative Commons Attribution 4.0 International license.

Statistics and estimations vary every time, but around two-thirds of the accumulated atmospheric CO<sub>2</sub> is attributable to Europe and the USA. However, new economies are emerging and are growing rapidly. Therefore, they need new energy supplies, and the cheapest option is often coal.<sup>11-13</sup> Considering the information displayed by *the Global Carbon Budget*,<sup>10</sup> during 2023, the world's CO<sub>2</sub> leading emitter and the most contaminated country was China, with 11.47 GtCO<sub>2</sub> per year. Being the most densely populated country in the world, the country emitted the largest increase in CO<sub>2</sub> emissions from fossil sources such as oil, natural gas, and coal. USA ranks second with 4.81 GtCO<sub>2</sub> per year, the EU follows with 2.59 GtCO<sub>2</sub> per year, and India have

---

produced 2.96 GtCO<sub>2</sub> per year. World's global data show emissions of 37.4 GtCO<sub>2</sub> per year (including emissions from bunkers). Contemplating the statistics referring to the year 2024, global CO<sub>2</sub> emissions increased to 41.6 GtCO<sub>2</sub>.<sup>14</sup>

The use of renewable energy resources such as solar or wind energy is an option to remedy CO<sub>2</sub> production. However, radical change and the transition to renewable energy is complex, since global energy systems are heavily reliant on non-renewable sources, among other factors. The main source of global energy consumption remains fossil fuels, accounting for approximately 81.5% of the total in 2023. In comparison, renewable energy sources, such as hydroelectricity, nuclear energy, geothermal, biomass, solar and wind, account for a smaller percentage of the global energy demand. However, by 2024, renewable energy significantly grew, with notable increases in solar and wind energy, which represented 32% of global electricity generation.<sup>15-17</sup> Despite this progress, the use of fossil fuels will continue to be used for the next few decades, and a new development method of novel materials that can mitigate CO<sub>2</sub> effects through direct carbon capture and sequestration (CCS) or conversion into valuable chemicals and fuels is required.<sup>18,19</sup>

### **1.1.1 Industrial process of CO<sub>2</sub> capture**

Generally, the most common methodology in the industrial field is the capture of CO<sub>2</sub> using functional amines.<sup>20-25</sup> This strategy appeared in 1930 when aqueous purification mechanisms based on alkanolamines were established.<sup>26</sup> CO<sub>2</sub> is absorbed from a fuel gas near ambient temperature and through an aqueous solution of functional amines with low vapor pressure. The system consists of a solution containing functional amines that undergo nucleophilic attack on the CO<sub>2</sub> carbon molecule, giving carbamate or bicarbonate as a product. This procedure is usually implemented in coal-fired power plants because other technologies have slower reaction kinetics and do not capture CO<sub>2</sub> efficiently within the required time.<sup>27</sup> Min Xiao et al. investigated carbon dioxide capture using mono- and di- amines in aqueous solution, and the results showed that diethylethanolamine

(DEEA) performed higher CO<sub>2</sub> loading than monoethanolamine (MEA).<sup>28</sup> Although amine filters are highly selective in CO<sub>2</sub> capture and perform well at low partial pressures, they have several limitations. Among them, large-scale implementation is the main disadvantage because large amounts of corrosive material are produced, such as formic acid and other degradation products. On the other hand, the calorific capacity of the amine increases, subsequently increasing the global temperature of the reactor, producing high adsorption enthalpies, and increasing the total energy cost. In addition, amines are often instable at high temperatures and present low yield.<sup>29</sup>

Certain industrial processes involve the development and implementation of CO<sub>2</sub> capture technologies to reduce CO<sub>2</sub> emissions from fossil-fuel combustion plants. These are post-combustion, pre-combustion, and oxyfuelling (Figure 1.2).

The first involves the 4–8% capture of CO<sub>2</sub> by volume for natural gas-fired power plants and 12-15% for coal-fired power plants. Usually, the bases of the capture work through solvents and subsequent solvent regeneration.<sup>30</sup>

On the other hand, pre-combustion is commonly used in a coal or natural gas-based plant, where CO<sub>2</sub> is captured processing the primary fuel with steam and air/oxygen. This method captures a high-pressure gas mixture that contains between 15-40% CO<sub>2</sub>.<sup>31</sup> The synthesis gas reacts with steam to form H<sub>2</sub> and CO<sub>2</sub>, and the CO<sub>2</sub> produced by the reaction is then removed by physical adsorption (such as the Rectisol, Selexol, or Purisol process)<sup>32–34</sup> or chemical absorption (generally amine-based solvents).

Finally, oxyfueling captures CO<sub>2</sub> in a power plant involving the combustion of fossil fuel with pure oxygen using recycled flue gas. Producing flue gas with high concentration of CO<sub>2</sub> and water vapor, the CO<sub>2</sub> is removed using dehydration and low temperature purification process.<sup>35,36</sup>

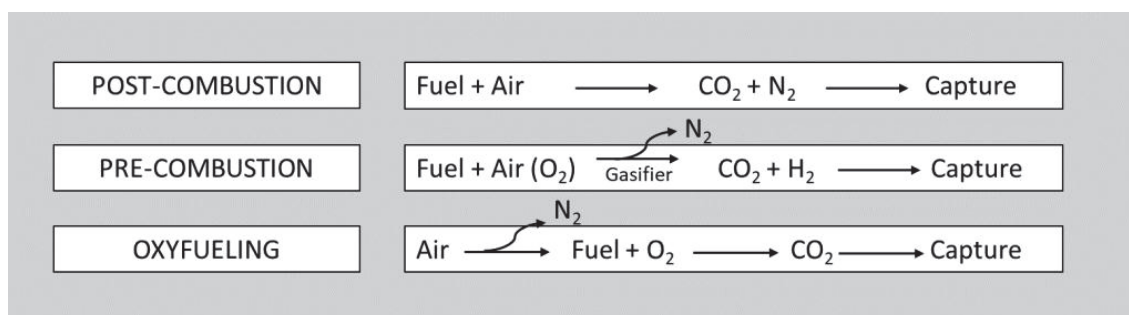


Figure 1.2. Industrial carbon capture technologies and the chemical reaction employed to capture CO<sub>2</sub>.

### 1.1.2 CO<sub>2</sub> capture from direct atmospheric air

Although the capture of CO<sub>2</sub> directly from the air is a difficult task due to the low concentration rates, there exists a huge variety of projects that focus their strategies on capturing and converting CO<sub>2</sub> directly from the atmosphere.<sup>37–39</sup> The methods developed to capture CO<sub>2</sub> can be based on adsorption or absorption processes, which can occur through chemical reactions (chemisorption) or physical interactions (physisorption) (Figure 1.3). Some examples of chemisorption mechanisms include the use of absorbents, such as alkanolamines or amino acids. In contrast, physisorption processes involve the use of solid materials, such as metal organic frameworks (MOFs), zeolites or silica. Additionally, more complex capture systems, like Rectisol, Selexol or Purisol processes, rely on physical absorption using liquid solvents.

More specifically, adsorption involves the adhesion of atoms, ions, or molecules of the adsorbed substance to the surface of the material (absorbent). This process differs from absorption, where the adsorbed fluid (absorbate) is dissolved by a liquid or the absorbent. Furthermore, absorption involves the whole volume of the material, involving stronger molecular interactions, whereas adsorption is a surface phenomenon and usually precedes absorption.<sup>40</sup> Absorption-based mechanisms often prove to be inefficient in both production and energy usage. Alternatively, adsorption is considered a more efficient method to capture CO<sub>2</sub> directly from the

atmosphere, since it is a less laborious and simpler mechanism that requires less energy, has higher kinetics and is often reversible.

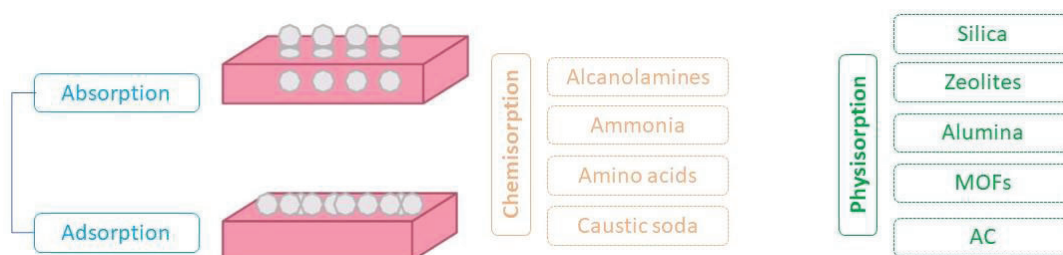


Figure 1.3. Flow diagram of CO<sub>2</sub> capture by adsorption and absorption and examples of materials commonly utilized in capture processes.

Among the leading technologies related to Direct Air Capture (DAC) using the adsorption process, *Climeworks* stands out. The mechanism they use consists of a series of CO<sub>2</sub> collectors employed in selective capture, followed by a two-step process. First, air is added to the collector using an industrial fan. The surface of a highly selective material captures CO<sub>2</sub> inside the collectors when it is completely impregnated. Then, the collector closes, and the temperature increases from 80 to 100 °C, releasing CO<sub>2</sub> at a purity greater than 99%. Each collector can capture around 50 tons of CO<sub>2</sub> per year, and the material used is a combination of cellulose and 3-aminopropylmethyldiethoxysilane (APDES).<sup>41</sup> Alternatively, the company *Skytree* captures CO<sub>2</sub> directly from the air using their own commercial adsorbent material named ERSA, a polymer functionalized with a primary amine.<sup>42</sup> Other example is *Infinitree LCC*, that captures CO<sub>2</sub> molecules using a resin combined with zeolites, active alumina, active magnesia and iron oxide. CO<sub>2</sub> is adsorbed on the surface of the composite, and a chemical reaction occurs between specific anions and the captured CO<sub>2</sub> producing carbonate.<sup>43</sup>

Industrial adsorption mechanisms are in current development and although there is a long way ahead, the design of new porous solid adsorbents is promising. In general, adsorbent materials have a set of properties that make them stand out, such as high stability, high adsorption capacity, high selectivity, low cost, and scalability. Flanked

by these characteristics, solid materials are one of the most potential candidates to alleviate CO<sub>2</sub> emissions, being zeolites, activated carbon or MOFs, some examples. Specifically, there are many hopes concentrated on the development of MOFs as novel porous crystalline materials for CO<sub>2</sub> capture.<sup>38</sup>

## 1.2 CO<sub>2</sub> capture and adsorption key performance indicators

To examine and analyze emerging technologies, it is crucial to consider key factors. There are diverse methods for CO<sub>2</sub> capture, but they differ in their Technology Readiness Levels (TRLs), indicating contrasting levels of system maturity and real-world applicability.<sup>44</sup> Consequently, a comprehensive assessment of different Key Performance Indicators (KPIs) is essential. Below, is described a series of common parameters that play key roles in the field of CO<sub>2</sub> capture using solid materials, such as the gas adsorption units, porosity, cyclability or selectivity.

### Gas adsorption

*Gas adsorption* units usually appear in mmol CO<sub>2</sub>/g of adsorbent. The use of mmol CO<sub>2</sub>/g and cm<sup>3</sup>/g STP units is frequently used in research studies where the amount of gas stored in the composite predominates with respect to the permeability or permeance. Generally, these units are used when the objective of the synthesized material is to capture as much gas as possible through the pores of the composite and to quantify it with respect to the total adsorbent mass.

According to the most used techniques for CO<sub>2</sub> adsorption quantification, BET isotherms of CO<sub>2</sub> stand out. This technique is based on the determination of the gas dosed into the sample tube from the difference in pressures in the manifold before and after the dose is carried. The quantity of gas adsorbed by the sample is determined through the quantity of gas persisting in the free space of the sample tube once equilibrium is achieved from the quantity of gas originally introduced. This technique presents a remarkable versatility in measurements and the results are typically presented in units of mmol/g. Additionally, BET isotherms are commonly used to measure specific surface area and porosity of the material.<sup>45,46</sup>

In the scope of CO<sub>2</sub> adsorption, lower temperatures are frequently highlighted for their effectiveness in gas adsorption. This is attributed to the superior stages of surface adsorption on the samples compared to higher temperatures, where the

kinetics of adsorbed molecules are heightened, leading to a decrease in the adsorption process. As can be seen in the Figure 1.4, the CO<sub>2</sub> isotherms of a core-shell ZIF-8@ZIF-67 materials are presented as an example of CO<sub>2</sub> sorption performance (this material is a hybrid structure in which the MOF ZIF-8 is coated by a layer of ZIF-67). The obtained isotherms show the maximum quantity of CO<sub>2</sub> that the sample can absorb according to the increase of pressure applied to the system.

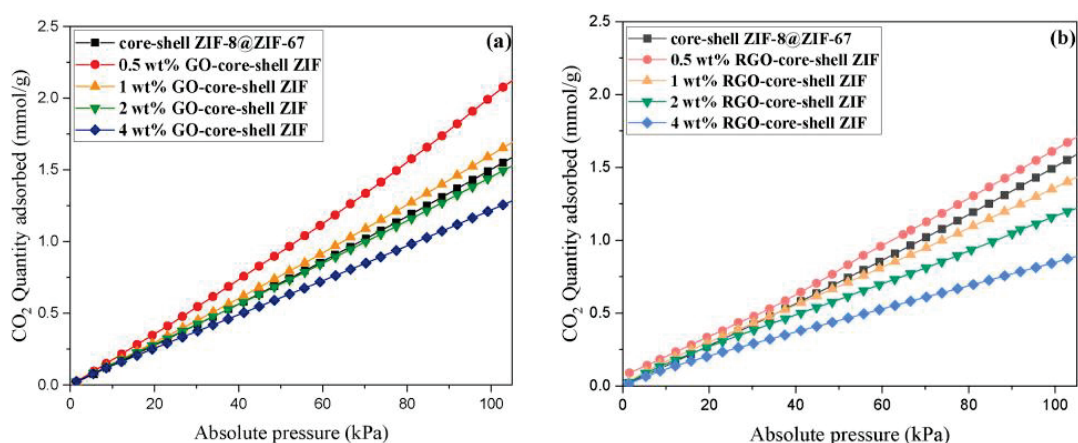


Figure 1.4. Adsorption CO<sub>2</sub> isotherms of core-shell ZIF-8@ZIF-67 combined with (a) GO and with (b) rGO, performed at 273 K. Reprinted from ref.<sup>47</sup>

In the figure, the samples tested show a maximum of 2.15 mmol CO<sub>2</sub>/g at around 100 kPa of absolute pressure in the case of 0.5 GO based nanocomposites, and 1.73 mmol CO<sub>2</sub>/g in the case of 0.5 rGO based nanocomposites. The results from XPS and FTIR measurements showed some differences between GO and rGO based samples, in which the presence of oxygen-containing functional groups was acting like anchoring sites for the CO<sub>2</sub> molecules. Hence, in the case of GO based samples, these interactions are higher and probably led to an increased CO<sub>2</sub> adsorption capacity than rGO based samples. Additionally, this study also performed N<sub>2</sub> isotherms under identical conditions at 273K, reproducing almost the same ranking of adsorbent samples but adsorbing lower quantity of gas molecules, suggesting an increased selectivity for CO<sub>2</sub> compared to N<sub>2</sub> (Figure 1.5).<sup>47</sup>

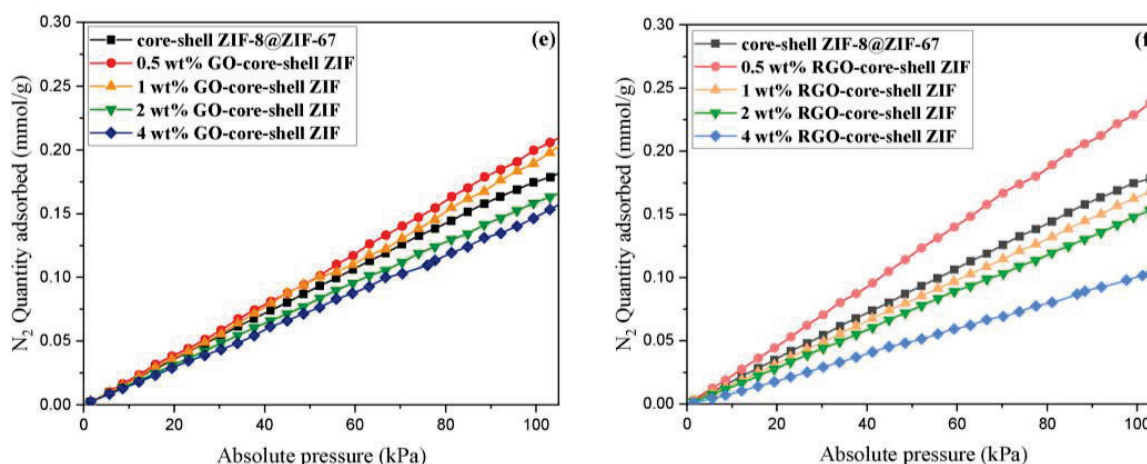


Figure 1.5. Adsorption  $N_2$  isotherms of core-shell ZIF-8@ZIF-67 combined with (a) GO and with (b) Rgo, performed at 273 K. Reprinted from ref.<sup>47</sup>

Although BET adsorption isotherms are a precise way to quantify the amount of  $CO_2$  retained in the adsorbent material, there are other alternatives, such as gravimetric analysis. Thermogravimetry, for example, not only provides information on the structural composition but also determines the amount of  $CO_2$  molecules absorbed by the difference in weight once  $CO_2$  is absorbed. He et al. examined  $CO_2$  adsorption/desorption through TGA curves, where the samples were weighted and filled using a ceramic crucible before the activation step with nitrogen flow gas. As a result, using thermogravimetric experiments, the group concluded that PEI-GO solid adsorbents presented a good adsorption capacity.<sup>48</sup>

### **Surface properties**

The *porosity* of a material is another key parameter in the  $CO_2$  capture field since, in general, as higher is the porosity better is the  $CO_2$  adsorption performance. This is because when a material possesses high porosity inside the structure, it presents enhanced availability of potential adsorption sites for  $CO_2$  molecules. Consequently, porosity significantly impacts a material's capacity to adsorb gases, which holds crucial importance in various applications such as air purification, gas separation, and catalysis.<sup>49</sup>

Moreover, greater porosity in a solid material generally corresponds to a larger *specific surface area*, facilitating enhanced gas adsorption. The specific surface area is the relationship between the surface and total mass of the material. This parameter provides information on the adsorption capacity and can also be an indicator of reactions that take place on surfaces or provide some data about heterogeneous catalysis processes.<sup>50</sup> According to MOF composites specific surface area values usually are significantly higher compared with other porous materials.

### **Cyclability**

*Cyclability* is one of the most pursued considerations in terms of gas capture. The possibility of finding new composites that are capable of regeneration to save reagents and generate less waste and cost is always desired in any industrial process. Generally, porous materials can desorb CO<sub>2</sub> molecules and are exposed to a new adsorption cycle. The regeneration capacity is usually studied by carrying out adsorption-desorption cycles of the gas capture procedure.

Zhang et al. described in their publication an example of cyclability test performance, where several adsorption-desorption cycles of flexible MOF nanofilms were carried out using thermogravimetric analysis. They performed up to 100 thermogravimetric experiments using cycles of CO<sub>2</sub> adsorption-desorption at 298 K and at a 378 K for 40 min in every cycle. As a result, after 100 CO<sub>2</sub> adsorption-desorption cycles, the material retained 95% of the initial CO<sub>2</sub> capacity, concluding that the growth of crystals and activation times were crucial steps to improve CO<sub>2</sub> capacity.<sup>51</sup>

### **Selectivity**

*Selectivity* plays a crucial role because it determines the adsorbed molecular proportion of a specific gas with respect to other molecules found in the analyzed gas mixture. Various methods exist for calculating this parameter. Some equations for determining selectivity, compiled from literature, are summarized in Table 1.1.

Table 1.1. Summary of theories and equations employed to calculate selectivity for gas mixture adsorption.

Method	Equation	Theory	Ref.
1.	$S = \frac{x_1/x_2}{y_1/y_2}$	Ideal Adsorption Theory (IAST)	45
2.	$q = q_A + q_B = \frac{q_{sat,A} b_A p^{c_A}}{1 + b_A p} + \frac{q_{sat,B} b_B p^{c_B}}{1 + b_B p}$	Dual-site Langmuir-Freundlich (DSLIF)	47
3.	$q = \frac{q_{sat} b p}{1 + b p}$	Single-site Langmuir Model	52
4.	$S = \frac{n_{CO_2}}{n_{N_2}}$	Simplest method reported	53
5.	$S = \frac{n_{CO_2}}{n_{N_2}} \cdot \frac{P_{N_2}}{P_{CO_2}}$	Simplest method reported	53
6.	$\ln(n_i \times p^{-1}) = A_0 + A_1 \times n_i + A_2 \times n_i^2 + A_3 \times n_i^3$	Henry's Law	53
7.	$K_H = e^{A_0}$	Henry's Law	53

In the first case (Method 1),  $x$  corresponds to the adsorption capacity value,  $y$  to the gas pressure, and 1 and 2 correspond to gas components 1 and 2, respectively. The most common ratio of  $CO_2 / N_2$  for industrial gas mixtures is 85:15. This equation is based on the Ideal Adsorption Theory (IAST), which is the most common way to deduce selectivity in gas mixtures within an adsorbent. The calculation uses pure-component adsorption isotherms at a certain temperature, and the result shows a prediction of the mixture adsorption equilibrium.<sup>45,54</sup>

In the case of the equation extracted from Method 2, the dual-site Langmuir-Freundlich (DSLIF) model is used to fit a single-component isotherm, where  $p$  is the bulk gas pressure at equilibrium (kPa),  $q_A$  and  $q_B$  are the saturation capacities (mmol/g) of  $A$  and  $B$  components,  $b_A$  and  $b_B$  are the coefficient affinities (1/kPa) of  $A$  and  $B$ , and  $c_A$  and  $c_B$  are the deviations from an ideal homogeneous surface.<sup>47</sup> Even though most systems that describe the adsorption of gases in solid adsorbents can

be defined with the single-site Langmuir model of equation, a simpler approach to approximate the adsorption capacity is often used. Following the IAST, the selectivity can also be calculated using Method 3.<sup>52</sup> Here,  $p$  is the pressure of the gas at equilibrium with an adsorbed phase,  $q$  is the quantity of gas adsorbed per mass of adsorbent,  $q_s$  is the maximum capacity of the adsorbent, and  $b$  is the affinity coefficient.

Other approaches applied to calculate selectivity are the method published by Barbara Szcześniak et al.<sup>53</sup> The selectivity was calculated using different approaches. First, they opted to use only the relation between the mols of CO<sub>2</sub> and the mols of N<sub>2</sub> adsorbed (Method 4). In this case,  $n_{CO_2}$  and  $n_{N_2}$  are the amounts of CO<sub>2</sub> and N<sub>2</sub> adsorbed by the sample at 1 bar. Furthermore, they calculated the selectivity using Method 5 since mixture gas contained certain volumes of CO<sub>2</sub>/N<sub>2</sub> gas. They made another approximation of the selectivity, but with a gas mixture of 85:15 N<sub>2</sub>/CO<sub>2</sub> proportion of gases, simulating industrial flue gases, where  $p_{N_2}$  and  $p_{CO_2}$  are incorporated as the corresponding partial pressures of N<sub>2</sub> and CO<sub>2</sub>, respectively. On the other hand, they performed another selectivity calculation using Henry's law (Method 6). Here,  $p$  is the pressure (bar);  $n_i$  is the quantity of gas adsorbed; and  $A_1$ ,  $A_2$ , and  $A_3$  are the virial coefficients. Thus,  $A_0$  is related to Henry's constant. The group investigated the fabrication of HKUST-1 together with other composites and compared the results obtained evaluating the different selectivity values using these methods. As a result, although the selectivity of the same samples was calculated using different approaches, the tendency follows a trend: HKUST-1 containing 10% GO had the highest CO<sub>2</sub>/N<sub>2</sub> selectivity compared to the other composites studied by them. Hence, they concluded that microporous carbonaceous materials like aPAni and aPAni/GO can compete with highly microporous MOFs in terms of CO<sub>2</sub> capture properties, since both materials present optimal adsorption properties.<sup>53</sup>

However, analyzing in detail the characteristics of Henry's law, it is considered that Method 6 probably is not feasible to compare gas mixture selectivity in solid adsorbents because it is commonly used in systems where the gas is dissolved in a liquid.<sup>55</sup>

### **Scalability**

On the other hand, *scalability* is the capacity of producing bigger volumes of material without altering their properties. It is usually simpler with solid materials rather than liquid processes, as solids are more stable, easier to transport and involve process that typically reduce costs. However, producing bigger quantities while maintaining the properties of the materials is often a complex task, since a balance between costs, energy and production must be considered.

Although scalability of CO<sub>2</sub> adsorbent materials is a controversial field due to the wide variety of implications, some studies report methods of synthesis potentially scalable. As an example, Mei Wang et al. investigated about the preparation of nitrogen-enriched carbon microspheres for efficient CO<sub>2</sub> capture using the carbonization of melamine-resorcinol-formaldehyde (MRF) microspheres. The method they reported utilized a synthesis with high potential scalability due to the low cost and flexible parameters, allowing the control of the particle size and surface textural properties by adjusting the molar ratio of melamine to resorcinol.<sup>56</sup>

### **Shaping**

*Shaping* implies the conformation of materials that initially present low mechanical strength properties. Consequently, shaping powder material, such as materials derived from MOFs or zeolites, implies the modification of the final conformation to allow the use of the material in a specific system. Pelletization, 3D printing, and polymeric coatings are some of the most studied options.<sup>57-59</sup>

The study reported by Daniel W. Lee et al. analyzed the properties of pellets using shaped UiO-66 with alginates. They determined that alginates with a high content of

guluronic acid blocks (G-block) achieve obtaining higher mechanical strength compared to low contents. The study concludes that the alginate with 40:60 mannuronic-to-guluronic acid ratio and a molecular weight of 240-300 kDa was the best option to pelletize UiO-66 MOF.<sup>57</sup> However, most studies focus on finding the best adsorbent material, while determining the most suitable shaping method for integrating solid adsorbents into real industrial systems remains a major challenge.

### 1.3 Metal organic frameworks

Traditionally, zeolites and activated carbons were the main solid adsorbents applied to CO<sub>2</sub> capture. Nonetheless, MOFs have recently considered improved materials to progress the CO<sub>2</sub> adsorption efficiency.<sup>38</sup> Analyzing the results obtained by *Web of Science Database*, clearly these crystalline materials have acquired more scientific interest over the past years. The register shows the first publications about MOFs located in 2007 (being *metal organic framework* cited in the title and *carbon dioxide capture* mentioned as a topic). Since then, the publications have been increasing until they reach their peak in 2018, with 182 publications (Figure 1.6, left). Going further, analyzing the type of document that has been published most over the years, articles have reached 1.870 publications since then (2007-2025). Reviews are positioned in second place with only 274 publications followed by meeting (66), dissertation thesis (54), early abstract (52) and others (180) (Figure 1.6, right).

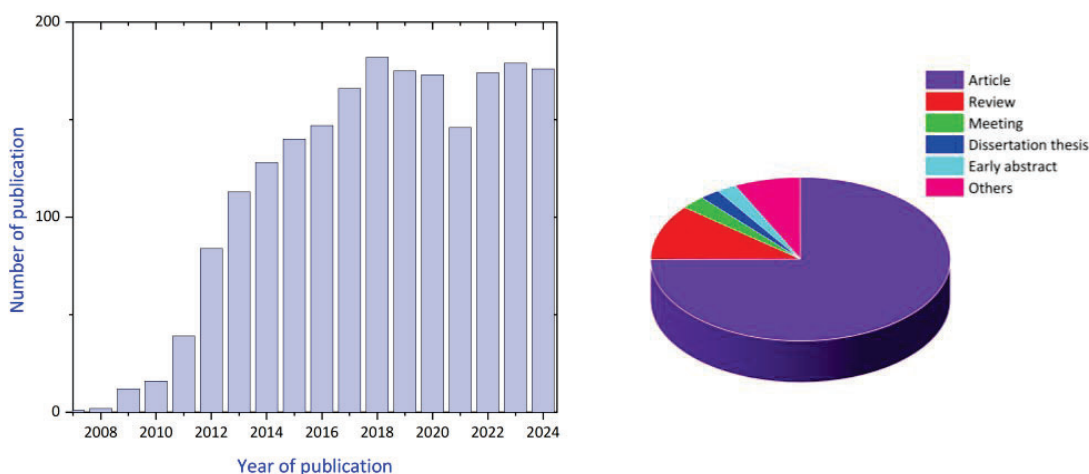


Figure 1.6. Number of publications of MOF composites in recent years (left) and representation of the extent according to document types (right). Data from ISI Web of Science until 2025.04.20.

Metal–organic frameworks (MOFs) are porous materials constructed by metal ions or metal ion clusters linked together through organic ligands. Compared with other adsorbent materials, MOFs exhibit some remarkable characteristics and are currently among the most promising porous crystalline materials for CO<sub>2</sub> capture at

the moment.<sup>60</sup> These materials were synthesized for the first time in 1959 with a wide range of properties, including permanent porosity, large volume of pores, large specific surface area and high thermal stability. Their applications extend to gas storage and separation, sensing, catalysis, and easy chemical tuneability, among others.<sup>61</sup> Moreover, MOFs are typically synthesized using metal salts and ligands with hydrothermal or solvothermal methods, which can be quite simple synthetic routes.<sup>62</sup>

Comprehending molecular and intermolecular interactions within the three-dimensional arrangement is crucial to understand MOFs behavior. The primary principles are the molecular interactions and the coordination bonds between metal ions and the organic ligands, such as other weak interactions like hydrogen bonds or  $\pi$ - $\pi$  interactions. Also, the large number of coordination geometries that metal ions adopted, the flexibility of the ligands or the reaction solvent are important parameters that could influence the final properties of the MOF. MOFs can adopt different coordination geometries through the metal nodes, which is essential to mold the network topology and dimensionality of the final material. The ligand used in the synthesis is usually linked by oxygen or nitrogen bonds working as a bridge between the ligand and the metal ion (Figure 1.7). Likewise, metals with a great variety of coordination numbers, geometries and oxidation states can provide a great diversity of three-dimensional structures (Figure 1.8).<sup>38,40,60,62-64</sup>

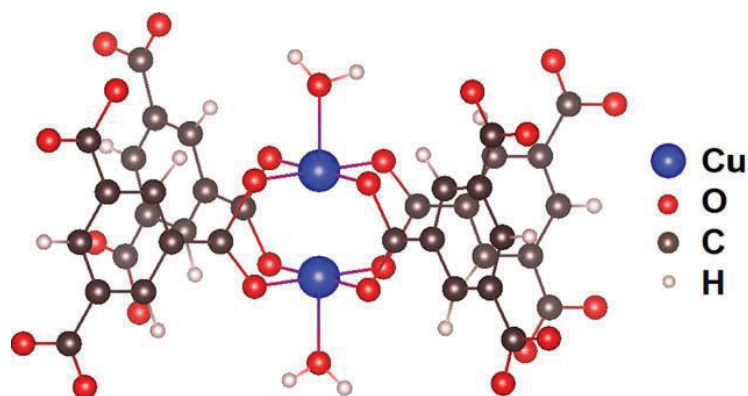


Figure 1.7. HKUST-1 MOF structure, formed by bonding two  $\text{Cu}^{2+}$  ions with four benzene 1,3,5-tricarboxylate linker ligands. Reprinted from ref.<sup>65</sup>

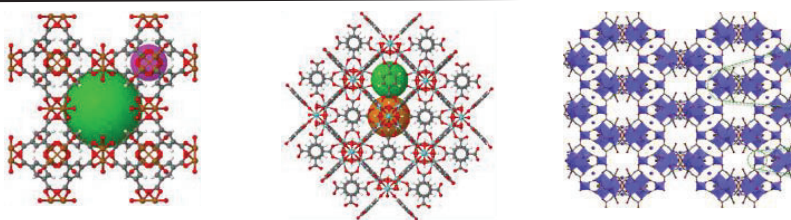


Figure 1.8. HKUST-1, UiO-66 and MIL-160 (Al) respectively. Reprinted from ref.<sup>65-67</sup>

On the other hand, MOFs are characterized mainly by powder X-ray diffraction (PXRD) usually to analyze the crystalline and phase purity of the MOF. In general, diffraction patterns are used to provide crucial information about the fingerprints of MOF. When a MOF structure is synthesized, the XRD spectrum obtained must necessarily be compared with its respective standard or simulated spectrum to ensure the correct formation of the material, as shown in Figure 1.9. Simulated powder patterns are usually calculated based on the hypothesis that crystallites are randomly oriented and sometimes some differences in peak intensities could be observed between simulated and experimental patterns due to impurities or trapped solvents in the crystalline framework.<sup>46</sup>

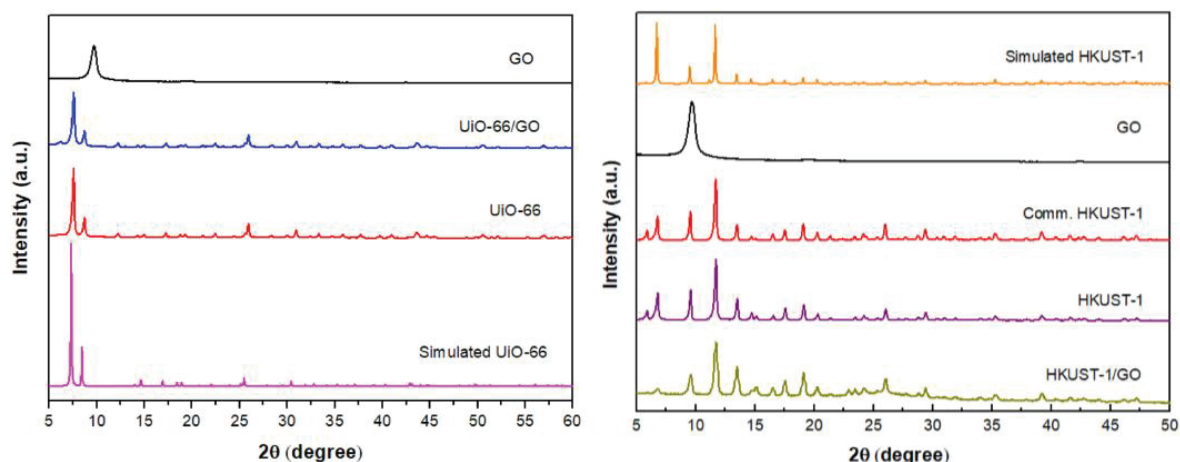


Figure 1.9. PDRX spectra obtained from GO, UiO-66, UiO-66/GO and simulated UiO-66 (left) and simulated HKUST-1, GO, commercial HKUST-1 and HKUST-1/GO (right) composites. Reprint from ref.<sup>65</sup>

Thus, morphology also assumes an important function. The most widely used technique for analyzing crystal shapes is scanning electron microscopy (SEM). Using SEM is possible to observe the different geometric shapes that MOF structures adopt. Geometry can be modified depending on the concentration of the reagents used in the synthesis, the reaction and activation temperature, or the solvents used. An illustrative example is the formation of MOF crystallites using two different synthetic routes. SEM images published by Shang et al. were obtained from the result of two different synthetic routes of HKUST-1. They determined that the synthesis of HKUST-1 using DMF solvent provided octahedral crystals, and synthesis without DMF solvent presented a rod-like crystal, which differs completely from the typical morphology (Figure 1.10).<sup>45</sup>

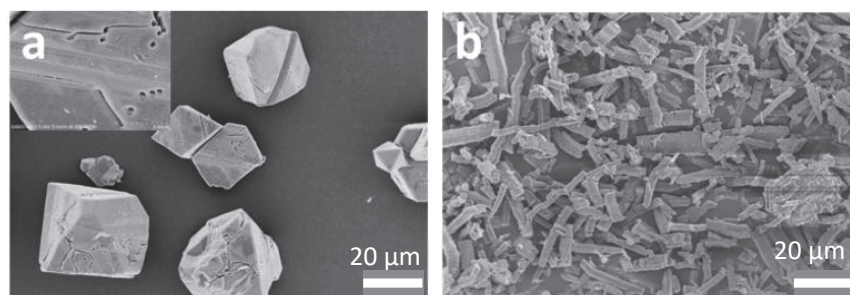


Figure 1.10. SEM images of (a) HKUST-1 and (b) Reference material of HKUST-1 -without DMF. Reprinted from ref.<sup>45</sup>

Currently, there is a wide variety of MOFs available, featuring diverse metallic centers and organic ligands, ranging from zirconium MOFs like UiO-66 to copper-based MOFs such as HKUST-1. The precursor to modern MOFs is a crystalline compound known as Langmuir-Blodgett made of stearate cadmium, first synthesized in 1959. Although its composition and properties differ somewhat from contemporary MOFs, it exhibits similar structural and crystalline properties. Kinoshita, Matsubara, Higuchi, and Saito reported the synthesis of bis(adiponitrile) copper(I) nitrate,  $[\text{Cu}(\text{NC}-\text{CH}_2-\text{CH}_2-\text{CH}_2-\text{CH}_2-\text{CN})_2]\text{NO}_3$ , through a straightforward reaction where reactants were mixed in hexanitrile at 60 °C, resulting in a dark precipitate. Upon filtration and cooling of the solution, yellowish crystals emerged and were studied using the Fourier method, a method that determines the crystal structure of the obtained materials. This determination paved the way for numerous similar compounds, many of which have evolved into the MOFs used today.<sup>61</sup>

Over the years, the studies related to MOFs have increased. Following the initial published synthesis, researchers have reproduced the method several times while altering various parameters such as temperature, reactants, and reaction time. Based on this, different techniques have been employed to grow MOF crystals. Among the most notable techniques are mixed-solvent synthesis, where a specific temperature and solvents are utilized to facilitate the reaction; microwave synthesis, which utilizes electromagnetic fields (often in the presence of solvents) to drive the chemical reaction; electrochemical synthesis, which produces MOFs through electrochemistry; sonochemical synthesis, where sonication enhances molecular movement and raises the solvent temperature; and mechanochemical synthesis, which utilizes mechanical processes such as grinding to fabricate MOFs (Figure 1.11).

In the following sections, these methods will be explained in detail, along with brief descriptions of some MOFs fabricated using these techniques.

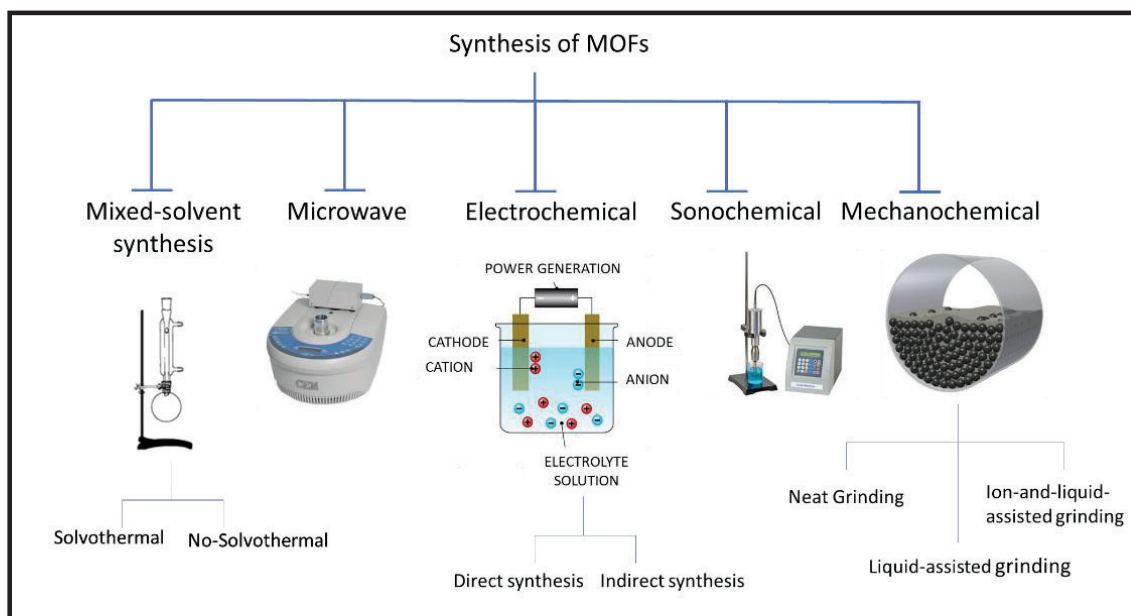


Figure 1.11. Diagram of the current techniques employed for the synthesis of MOFs.

### 1.3.1 Synthesis of MOFs using Mixed solvent method

This synthetic procedure is classified as a conventional synthesis because the reaction takes place using agitation and electric heating. This method involves dissolving the organic ligand and the metallic salt in a solvent and exposing them to heat treatment. Temperature is influential in this context, as the crystallization of MOFs depends on both the thermodynamics associated with the reaction and the kinetics. These parameters can be established at temperatures equal to or below the boiling point of the solvent used, and typically, the pressure is maintained in atmospheric conditions.

On the other hand, the growth time of crystals and the choice of solvent are also important factors. The concentration and solubility of the precursors can be influenced by temperature variation. Although this synthesis methodology is commonly used, the reproducibility of the crystals is complex due to the other

external factors involved in the reaction, such as proportion of solvents, polarity, the reaction time or the temperature.

MOFs can also be synthesized using solvothermal reactions, wherein the chemical reaction takes place in a closed pressure container, commonly referred to as an autoclave, at temperatures reaching the boiling point of the solvent employed during the synthesis. When water is the solvent employed, this method of synthesis is known as hydrothermal synthesis rather than solvothermal synthesis.

The mixed solvent method synthesis of MOFs is typically easy and enables the production of significant quantities of the desired product (a few grams) based on the initial stoichiometric ratios of reagents. However, the duration of the process and the variability of parameters, such as pH, generated pressure, or controlled temperature, can present challenges.

Some examples of MOFs synthesized using this method include IRMOF-1, first fabricated in 1999 and published by Omar M et al. in the journal *Nature*.<sup>68</sup> IRMOF-1, also known as MOF-5, has the formula  $Zn_4(O)O_{12}C_6$ . The researchers observed that dissolving triethylamine ( $N(CH_2CH_3)_3$ ) in a solution of zinc nitrate (II) ( $Zn(NO_3)_2$ ) and terephthalic acid ( $H_2BDC$ ) in DMF and chlorobenzene ( $C_6H_5Cl$ ) led to the deprotonation of the organic ligand, which then reacted with  $Zn^{2+}$  ions provided by the inorganic salt. Subsequently, the addition of hydrogen peroxide to the mixture resulted in the formation of  $O^{2-}$  anions, serving as the center of the secondary unit of the framework. The researchers then analyzed the cubic crystals and found that the MOF-5 contained DMF and  $C_6H_5Cl$  molecules inside the pores, as confirmed by elemental analyses and other characterization techniques.<sup>69</sup> This simple methodology allowed for the synthesis of similar MOFs with different diprotic carboxylate ligands, resulting in cubic networks with  $Zn^{2+}$  as the metallic center but differing in pore size and functionality.

On the contrary, considering more recent examples of MOFs, the synthesis of UiO-66 emerged, a zirconium MOF synthesized for the first time at the University of Oslo in 2008.<sup>70</sup> In this synthesis method, zirconium tetrachloride ( $ZrCl_4$ ) and the organic ligand,  $H_2BDC$ , are dissolved in DMF at room temperature. Subsequently, the mixture is transferred to an autoclave for solvothermal synthesis, where the reaction takes place for 24 hours in an oven at 120 °C. After cooling, the UiO-66 crystals are obtained by filtration.

Other examples, such as HKUST-1, despite being discovered in 1999, remain one of the most extensively studied structures due to its characteristics and properties. The synthesis typically follows the standard steps of a non-solvothermal synthesis, involving the dissolution of the metallic copper salt ( $Cu(NO_3)_2$ ) with the organic ligand ( $H_3BTC$ , benzen-1,3,5-tricarboxylic acid) in DMF, followed by a 24-hour reaction at 80 °C.<sup>45</sup> However, solvothermal synthesis is employed on several occasions when stricter control of crystal growth is required. An example is the research published by Ediati et al., where the reactants are dissolved beforehand in a mixture of EtOH and DMF for 30 minutes, and then transferred to an autoclave to react in the oven at 100 °C for 10 hours. The HKUST-1 crystals were obtained once the solution is allowed to cool for two days.<sup>71</sup>

The following table shows the examples mentioned above and some of the important parameters of the synthetic procedure (Table 1.2).

Table 1.2. Key parameters of mixed solvent method.

MOF	Organic linker	Inorganic salt	Solvent	Time	Reaction	Ref.
IRMOF-1	H <sub>2</sub> BDC	Zn(NO <sub>3</sub> ) <sub>2</sub>	C <sub>6</sub> H <sub>15</sub> N/ DMF/ C <sub>6</sub> H <sub>5</sub> Cl	-	Non-solvothermal	68
IRMOF-2	o-Br-BDC	Zn(NO <sub>3</sub> ) <sub>2</sub>	C <sub>6</sub> H <sub>15</sub> N/ DMF/ C <sub>6</sub> H <sub>5</sub> Cl	-	Non-solvothermal	69
UiO-66	H <sub>2</sub> BDC	ZrCl <sub>4</sub>	DMF	24 h	Solvothermal	70
HKUST-1	H <sub>3</sub> BTC	Cu <sub>2</sub> (NO <sub>3</sub> ) <sub>3</sub>	DMF	24 h	Non-solvothermal	45
HKUST-1	H <sub>3</sub> BTC	Cu <sub>2</sub> (NO <sub>3</sub> ) <sub>3</sub>	1:1 EtOH/DMF	10 h	solvothermal	71

### 1.3.2 Synthesis of MOFs using microwave synthesis

Alternatively, microwave synthesis is widely employed to rush reaction times in nanoporous materials under hydrothermal conditions. Electromagnetic radiation enables rapid heating, leading to a significant reduction in crystallization time. This technique not only reduces reaction times but also offers other potential advantages, including precise control over phase selectivity, achieving a narrow particle size distribution, and easy manipulation of the fabricated crystal's morphology. Commercial microwave equipment features adjustable power output and is equipped with fiber optic temperature and pressure controllers, ensuring high precision in material synthesis.

The methodology employed consists of introducing a mixture of substrates in a Teflon container, which is then sealed and placed in the microwave unit. Subsequently, the mixture is heated to a predetermined temperature and time. The rapid heating of the liquid phase is a result of the oscillating electric field generated by the microwave, coupled with the dipolar permanent moment of the molecules involved in the reaction synthesis, inducing molecular rotations. This leads to collisions between molecules, increasing the kinetic energy and temperature of the reaction medium. Consequently, this synthesis method is characterized not only by

the enhanced production rate of the final product but also by obtaining a crystalline phase with higher purity and approximately nanoscale crystal size.<sup>72</sup>

The first MOFs synthesized using microwave synthesis were reported in 2005. S.H. Jhung et al. reported the synthesis of Cr-MOF-100, also known as MIL-100, for the first time. This compound was synthesized in just 4 hours at 220 °C, yielding 44%. Additionally, the synthesis of MOF-5 was also achieved using microwave radiation. Over time, it became evident that by controlling the power level and the substrate concentration, the synthesis process of MOFs could be further accelerated. The researchers observed that MOFs synthesized within only 1 hour exhibited similar physicochemical properties compared to those synthesized using the standard microwave synthesis procedure, which differs from temperature, time and power level for example.<sup>73</sup>

A more recent example of a MOF obtained using the microwave method is Zr-based MIL-140, featuring  $Zr(\mu_3-O)_3O_4$ . This compound has demonstrated superior mechanical and chemical stability compared to the well-known Zr-based MOF, UiO-66.<sup>74</sup> MIL-101 (Cr) and MIL-100(Fe), as well as the HKUST-1 and the MIL-53(Fe) are other examples of potential synthesis of MOF materials using microwave radiation. In fact, it is a method widely used in laboratories today.<sup>75-78</sup>

While microwave synthesis proves to be an effective method, the current major drawback remains the limitation in production scale and the restricted selection of solvents compatible with microwave irradiation. Below is a table presenting some of the discussed MOFs of this section along with the parameters utilized in their respective syntheses (Table 1.3).

Table 1.3. Examples of synthesized MOF using microwave and key parameters.

MOF	Organic linker	Inorganic salt	Solvent	Conditions	Ref.
MOF-5	H <sub>2</sub> BDC	Zn(NO <sub>3</sub> ) <sub>2</sub> ·4H <sub>2</sub> O	NMP	800 W, 105 °C, 30 min	79
MIL-101 (Cr)	H <sub>2</sub> BDC	Cr(NO <sub>3</sub> ) <sub>3</sub> ·9H <sub>2</sub> O	1:280 HF/H <sub>2</sub> O	600 W, 210 °C, 40 min	75
MIL-100 (Fe)	H <sub>2</sub> BTC	Fe powder	1:400 HF/H <sub>2</sub> O	600 W, 200°C, 30 min,	76
HKUST-1	H <sub>2</sub> BTC	Cu(NO <sub>3</sub> ) <sub>2</sub> ·3H <sub>2</sub> O	EtOH	300W, 140 °C, 60 min	77
MIL-53 (Fe)	H <sub>2</sub> BDC	FeCl <sub>3</sub> ·6H <sub>2</sub> O	DMF	300 W, 150 °C, 10 min	78

### 1.3.3 Synthesis of MOFs using sonochemical synthesis

This synthetic method has been widely used in the field of organic synthesis and the preparation of nanomaterials.<sup>80</sup> In the case of MOFs, ultrasonic vibrations accelerate the homogeneous nucleation of MOF crystals, achieving a considerable reduction in particle size compared to mixed-solvent method. The procedure consists of exposing the substrate solution to ultrasound treatment using a sonicator at a certain amplitude and power. The formation and collapse of solution bubbles after sonication produce elevated temperatures and pressures, resulting in extremely rapid heating and cooling processes that produce fine crystals.

In this type of synthesis, besides controlling the amplitude and selected power, the choice of solvent is a determining factor. Highly volatile solvents typically do not result in efficient MOF production. This is due to their high vapor pressure, which reduces the energy released during the collapse of bubbles formed, thereby reducing the previously achieved high temperatures and pressures.<sup>81</sup>

The earliest publications on sonochemical reaction methods date back to 2008. Qiu and colleagues reported the synthesis of Zn<sub>3</sub>(C<sub>9</sub>O<sub>6</sub>H<sub>3</sub>)<sub>2</sub>·12H<sub>2</sub>O, also known as MOF-1. The procedure involves dissolving zinc acetate dihydrate (Zn(C<sub>2</sub>H<sub>3</sub>O<sub>2</sub>)<sub>2</sub>·2H<sub>2</sub>O) with

H<sub>3</sub>BTC in 20% ethanol in water (v/v) under ultrasonic irradiation at ambient temperature and pressure for varying reaction times.<sup>82</sup> Other synthesized MOFs recently fabricated using sonochemistry are MOF-5, HKUST-1, Mg-MOF-74 or ZIF-8.<sup>83–86</sup> The parameters of synthesis are shown in Table 1.4.

*Table 1.4. Examples of obtained MOFs using sonochemical synthesis and the key parameters employed.*

MOF	Organic linker	Inorganic salt	Solvent (v/v)	Time	Cond.	Ref.
MOF-1	H <sub>3</sub> BTC	Zn(CH <sub>3</sub> COO) <sub>2</sub> · 2H <sub>2</sub> O	1:4 EtOH/H <sub>2</sub> O	5 min	-	82
MOF-5	H <sub>2</sub> BDC	Zn(NO <sub>3</sub> ) <sub>2</sub> · 6H <sub>2</sub> O	NMP	30 min	50% power level	83
HKUST-1	H <sub>3</sub> BTC	Cu(CO <sub>2</sub> CH <sub>3</sub> ) <sub>2</sub> · 2H <sub>2</sub> O	1:2:3 EtOH/H <sub>2</sub> O/DMF	5 min	60W 40KHz	84
Mg-MOF-74	H <sub>4</sub> DHTP	Mg(NO <sub>3</sub> ) <sub>2</sub> · 6H <sub>2</sub> O	TEA	60 min	500W at 20 kHz	85
ZIF-8	HMelm	Zn(NO <sub>3</sub> ) <sub>2</sub> · 6H <sub>2</sub> O	300:1 DMF/TEA	60 min	500W at 20 kHz	86

In summary, most publications utilize this synthesis report that enables the rapid production of MOFs with high yields. Compared to other synthesis methods, this approach is often regarded as more efficient in terms of performance and cost-effectiveness. Some experiments reported that it is feasible to produce higher quantities while maintaining high crystallinity and comparable specific surface areas (around 7 g).<sup>87</sup>

### 1.3.4 Synthesis of MOFs using electrochemical synthesis

The electrochemical synthesis of MOFs can be achieved through two methods: direct synthesis and indirect synthesis. The first is the more common and widely used approach, wherein metallic ions in anodic solution serve as the metal source instead of metallic salts. In this method, an electrode is immersed in a solution containing a

supporting electrolyte and the organic linker. When the current is applied, the electrode is oxidized and, consequently, the metallic ions are reduced and deposited in the surface of the other electrode, which reacts with the organic linker forming the MOF in the electrode surface. To prevent metallic deposition on the cathode, protic solvents are utilized, generating  $H_2$  molecules.<sup>72,88</sup>

This procedure was published in 2005 by Mueller and his colleagues from BASF, who described the synthesis of HKUST-1 using electrochemical reactions (Figure 1.12). In this case, copper plates were employed as the anode in an electrolytic cell where the linker  $H_3BTC$  had been previously dissolved in methanol, with a copper cathode present. In this system, a voltage of 12-19 V was applied for 150 minutes, with a current of 1.3A, resulting in the formation of the corresponding HKUST-1 crystals.<sup>89</sup>

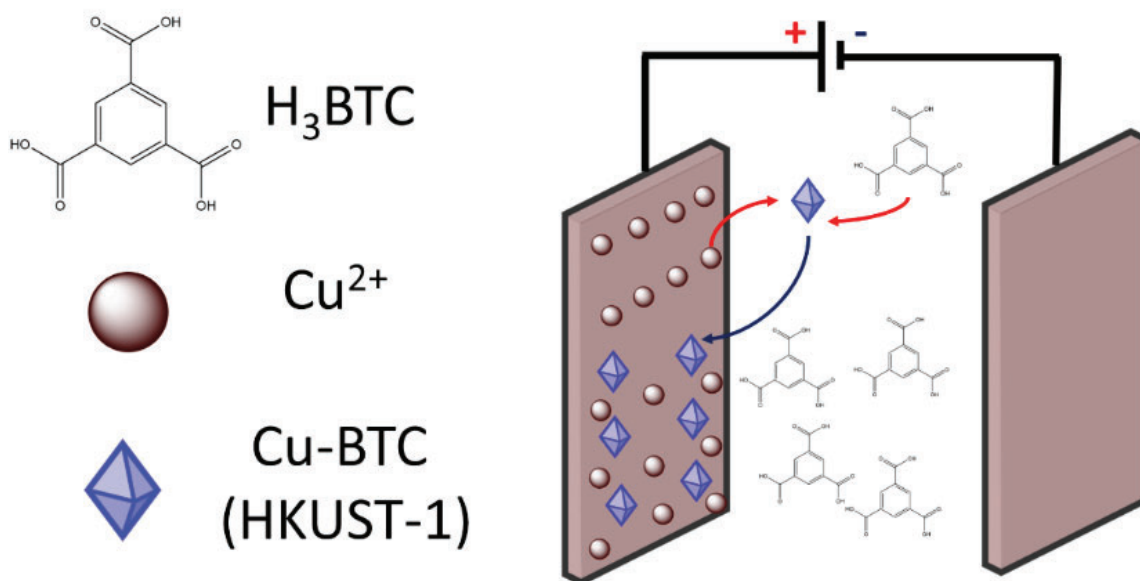


Figure 1.12. Scheme of electrochemical synthesis of HKUST-1 using anodic dissolution. Adapted from ref.<sup>88</sup>

Moreover, MOFs can also be indirectly synthesized through other methods, such as galvanic displacement, electrophoretic deposition, or self-templated synthesis. These methods involve the use of electrochemical reactions at some stage of the procedure to synthesize the MOF. Thus, electrochemistry is not the main synthesis route but rather plays a role in specific steps of the process. In general, there is

currently a broad field enabling the synthesis of MOFs via electrochemistry.<sup>88</sup> The following table displays some of the characteristics and parameters that have been applied in synthesizing MOFs through electrochemical reactions (Table 1.5).

*Table 1.5. Examples of MOFs obtained using electrochemical synthesis through anodic dissolution methodology and the key parameters employed.*

MOF	Organic linker	Substrate	Solvent	Conductive salt	Cond.	Ref.
HKUST-1	H <sub>3</sub> BTC	Cu plate	MeOH	-	150 min 12-19V, 1.3A	88
ZIF-8	MeIM	Zn plate	DMF or MeOH or EtOH or H <sub>2</sub> O	KCl	50 mA	90
Al-MIL-100	H <sub>3</sub> BTC	Al plate	75:25 EtOH/H <sub>2</sub> O	-	60 °C	90
IRMOF-3	NH <sub>2</sub> -H <sub>2</sub> BDC	Zn plate	DMF/EtOH	TBAB	5 V 180 min	91
MIL-53 (Al)	H <sub>2</sub> BDC	Al plate	90:10 H <sub>2</sub> O/DMF	NaCl	10-100 mA	92
MOF-5	H <sub>2</sub> BDC	Zn plate	DMF	Zn(NO <sub>3</sub> ) <sub>2</sub> · 6H <sub>2</sub> O	0.025 A/cm <sup>2</sup>	93

### 1.3.5 Synthesis of MOFs using mechanochemical synthesis

Mechanochemistry is a method that employs mechanical energy to induce and facilitate chemical reactions through the physical impact of the reagents. This procedure is emerging as a promising synthesis routes, offering a versatile approach for synthesizing a wide range of advanced materials such as alloys, nanoparticles, and zeolites. Although this technique has been used in chemistry for a long time, it is now becoming more popular in organic chemistry, inorganic chemistry, and polymer production. Particularly noteworthy is its application in the synthesis of Metal-Organic Frameworks (MOFs), which has garnered significant attention due to

its ability to conduct reactions at room temperature, eliminate the need for solvents, and achieve relatively short reaction times.

This innovative approach was first documented in a groundbreaking publication by A. Pichon et al. in 2006, detailing the synthesis of  $[\text{Cu}(\text{INA})_2]$ . In this study, a ball mill was employed to grind together copper acetate monohydrate,  $\text{Cu}(\text{O}_2\text{CCH}_3)_2 \cdot \text{H}_2\text{O}$ , and isonicotinic acid,  $\text{NC}_5\text{H}_4\text{-4-CO}_2\text{H}$  (INAH). The experimental setup involved a 20 mL steel vessel containing a steel ball bearing and approximately 0.5 g of reactants. The milling process was conducted at an oscillation rate of 25 Hz, which was maintained for a duration of 10 minutes.<sup>94</sup>

In general, mechanochemical synthesis methods can be categorized into three groups: neat grinding (NG), liquid-assisted grinding (LAG), and ion-and-liquid assisted grinding (ILAG). Some characteristics of each one are explained below.

### **Neat grinding (NG)**

This method involves conducting the reaction without the use of any solvent. It relies on obtaining chemical products by manually or automatically grinding the reagents under free-solvent conditions, simply by grinding them together in their solid form. The force applied during the grinding process breaks the intermolecular bonds and, in some cases, intramolecular bonds of the reagents, inducing the formation of a new compound. This facilitates the formation of new chemical bonds between the metal centers and the organic ligands, particularly in the context of synthesizing Metal-Organic Frameworks (MOFs).

To accelerate the formation of MOFs, hydrated reagents can be used as reactants with low melting points. This approach enhances the efficiency of the reaction by promoting the rapid formation of the desired MOF structure.

The pioneering work utilizing the technique of dry grinding for synthesizing MOFs was conducted by A. Pichon et al., who reported the first synthesis of MOFs using

this method. However, more recent studies have emerged, such as the work published by Zhang et al., which describes the synthesis of the ultra-microporous MOF ZU-66-Ni through neat grinding. In their procedure, a mixture of  $\text{Ni}(\text{NO}_3)_2$ ,  $(\text{NH}_4)_2\text{GeF}_4$ , and pyrazine (in a 1:1:3 molar ratio) is subjected to ball milling for approximately 10 minutes.<sup>95</sup> Additionally, other examples comprehend the creation of ZIF-8, a highly studied zeolitic imidazole framework. Taheri et al. utilized ball milling to grind the reactants, yielding ZIF-8, cobalt-containing ZIF-8 and ZIF-67 materials. During the synthesis process, they ground metal acetate (zinc and/or cobalt) and 2-methylimidazole for 2 hours, obtaining the respective MOFs.<sup>96</sup>

### **Liquid assisted grinding (LAG)**

In the liquid-assisted grinding (LAG) method, a small amount of liquid solvent is introduced into the reaction to enhance the mobility of the reactants. This addition of liquid facilitates the reaction by providing a medium for the reactants to move and interact more freely, thereby accelerating the reaction at the molecular level. The inclusion of liquid solvents in mechanochemical processes often leads to shorter reaction times due to the increased mobility of the reactants.

Several examples of MOFs synthesized using the LAG method have been reported. For instance, Fabián et al. described the synthesis of MOF-2 and MOF-3 ( $\text{Zn}(\text{BDC})\text{H}_2\text{O}$  and  $\text{Zn}_2(\text{NO}_3)(\text{BTC})$ , respectively). They utilized 4,4'-dipyridyl(bipy) or trans-1,2-bis(4-pyridyl)-ethylene (bpe) and fumaric acid (FUM) as ligands, along with zinc oxide as a metal source. During the synthesis process, small amounts of solvents such as DMF, MeOH, EtOH, and i-PrOH were added, and the reaction was completed after 20 minutes at room temperature.<sup>97</sup>

Additionally, Lewinski et al. reported the synthesis of the MOF IRMOF using the LAG method. They employed terephthalic acid together with zinc oxo-carboxylate, and in the presence of DMF, the reactants underwent collision generated by grinding, resulting in the formation of MOF-5.<sup>98</sup>

These examples demonstrate the versatility and effectiveness of the LAG method in synthesizing various MOFs, offering a convenient approach for their production with shortened reaction times and improved efficiency.

### **Ion-and-liquid assisted grinding (ILAG)**

The ion-and-liquid assisted grinding (ILAG) method involves mechanochemical reactions where catalytic quantities of both liquid and ionic salt additives are incorporated into the reactant mixture. The aim is to enhance the dissolution process of solid reactants, promote reaction homogeneity, and increase reactivity. This synthesis method is particularly beneficial for reactions involving metal oxides as precursors, where complete transformation into the desired product may not be achievable using neat grinding (NG) or liquid-assisted grinding (LAG) methods alone.

A crucial aspect of the ILAG process is the selection of the additive, as it can significantly impact the selectivity and purity of the resulting MOFs. In 2010, Friščić et al. published a work based on the synthesis of MOF-2 (Zn(BDC)), demonstrating for the first time the efficacy of incorporating catalytic amounts of certain salts to enhance LAG reactions. Based on these results, the synthesis methodology was further extended to produce Zeolitic Imidazolate Frameworks (ZIFs) based on imidazole (HIm), 2-methylimidazole (HMeIm), and 2-ethylimidazole (HEtIm).<sup>97</sup>

By employing this technique, ZIFs can be synthesized using liquid reaction media such as DMF, EtOH, and N,N-diethylformamide (DEF), along with additive salts such as ammonium nitrate ( $\text{NH}_4\text{NO}_3$ ), ammonium sulfate ( $\text{NH}_4)_2\text{SO}_4$ ), and ammonium methane sulfonate ( $\text{NH}_4\text{CH}_3\text{SO}_3$ ). These additive salts play a crucial role in improving the coordination between ZnO and the organic ligands utilized in the synthesis process, thereby facilitating the formation of high-quality MOF structures with enhanced performance characteristics.<sup>99</sup>

These examples highlight the versatility and efficacy of mechanochemical synthesis for producing various MOF structures, offering a promising avenue for the

development of advanced porous materials. The following table shows a summary of the different MOFs mentioned above (Table 1.6).

*Table 1.6. Examples of MOFs synthesized using mechanochemical synthesis and the key parameters employed.*

MOF	Organic linker	Inorganic salt	Solvent	Method	Cond.	Ref.
[Cu(INA) <sub>2</sub> ]	INAH	Cu(O <sub>2</sub> CCH <sub>3</sub> )·H <sub>2</sub> O	-	NG	25Hz, 10min	94
ZU-66-Ni	(NH <sub>4</sub> ) <sub>2</sub> GeF <sub>4</sub>	Ni(NO <sub>3</sub> ) <sub>2</sub>	-	NG	10 min	95
ZIF-8	Hmlm	Zn(CH <sub>3</sub> COO) <sub>2</sub>	-	NG	120 min	96
Zn(BDC)H <sub>2</sub> O	FUM	ZnO	DMF, MeOH,EtOH or i-PrOH	LAG	20 min	97
Zn <sub>2</sub> (NO <sub>3</sub> )(BTC)	FUM	ZnO	DMF, MeOH,EtOH or i-PrOH	LAG	20 min	97
IRMOF	H <sub>2</sub> BDC	Zn(CH <sub>3</sub> COO) <sub>2</sub>	DMF	LAG	30 min	98
Zn(BDC)	FUM	ZnO	EtOH	ILAG	30 min	97

## 1.4 Metal organic frameworks and CO<sub>2</sub> adsorption performance

CO<sub>2</sub> capture is achieved using MOFs through explicit sites resulting in enhanced host-guest interactions. In this context, MOFs materials are characterized by exhibiting these explicit sites, commonly named open metal sites (OMS); which arise from metal ions that are not fully coordinated when vacant Lewis's acid sites on the metal ions or cluster nodes are generated. The presence of OMS increases when coordinated solvents are removed from MOF structures when the sample is exposed to high temperatures, specifically during the dryness of the sample in the activation step.<sup>100</sup>

Among the prominent MOFs capable of adsorbing higher amounts of CO<sub>2</sub>, one of the most protuberant materials is HKUST-1, a copper-based MOF formed with H<sub>3</sub>BTC as a ligand. Recent studies describe the performance and synthesis of HKUST-1, such as the research published by Shang et al. They reported the synthesis and optimization of HKUST-1 and proposed an alternative way to synthesize HKUST-1 compared with the common technique using mixed solvents. Based on the results, the novel HKUST-1 showed higher specific surface area and total pore volume compared with the reference HKUST-1, along with an enhancement of the CO<sub>2</sub> adsorption properties (8.02 mmol/g at 273 K and 1 bar) surpassing that of HKUST-1 obtained through a standard synthesis approach.<sup>45</sup> Additionally, Nika Vrtovec et al. published some results about the improvement of the CO<sub>2</sub> capture capacity synthesizing HKUST-1 doped with ethylene diamine and through post synthesis incorporation. In this case, the results showed that the functionalization reduces the specific surface area and the CO<sub>2</sub> sorption capacity.<sup>101</sup>

UiO-66 is another recurrent synthesized MOF in the field of CO<sub>2</sub> adsorption. This MOF is composed of zirconium ions as the metallic component and terephthalate ligand (BDC) as the organic structure. Jeewan Pokhrel et al. published the synthesis and characterization of UiO-66, and their results showed that the value of CO<sub>2</sub>

adsorption capacity was 1.50 mmol/g at 1 bar and 298 K, with a selectivity of CO<sub>2</sub>/N<sub>2</sub> of 12.91. The same publication showed some data on combinations with graphene oxide (GO), which will be analyzed in the next section.<sup>46</sup> On the other hand, cobalt-based MOFs were synthesized and evaluated as a novel CO<sub>2</sub> adsorbent by the group of Pei-Pei Cui. Different MOFs were synthesized using two auxiliary ligands: 3,5-bis(pyridine-4-yl)benzoic acid (Bipy-BDC) and 1,4-benzenedicarboxylic acid (H<sub>2</sub>BDC).

Changing the substituent groups of the second one, a set of samples were evaluated to determine their CO<sub>2</sub> adsorption capacity. The results suggested that all the samples exhibit good CO<sub>2</sub> capture capability and selectivity, being the maximum values of adsorption for each sample (1-6): 4.09, 6.12, 4.32, 12.72 and 5.29 mmol CO<sub>2</sub>/g.<sup>102</sup> M. P. Silva et al. investigated the adsorption of CO<sub>2</sub> through Al-MOF MIL-160, a metal organic framework based on inorganic aluminum helical chains connected by 2,5-furandicarboxylate groups. In this case, the material synthesized achieved to adsorb 6.21 mmol/g at 283 K.<sup>103</sup> Otherwise, Sanjit Gaikwad et al. published the synthesis and characterization of a novel metal-organic framework (UTSA-16 (Zn)). They replaced cobalt in the synthesis with zinc using microwave irradiation and consequently improving the results of CO<sub>2</sub> adsorption. This material could achieve a CO<sub>2</sub> adsorption capacity of 4.71 mmol/g at 298 k and at 1 bar, with a remarkably CO<sub>2</sub>/N<sub>2</sub> selectivity of 118.<sup>104</sup>

Overall, MOFs have been widely used for CO<sub>2</sub> capture and their use is taking more interest over the years since there exist a huge variety of MOF materials with attractive properties for CO<sub>2</sub> capture.

As a summary, some parameters of the information provided in this section concerning MOF structures and CO<sub>2</sub> adsorption performance is collected in the Table 1.7.

Table 1.7. Summary of synthesis and CO<sub>2</sub> adsorption data from different metal organic.

MOF	Metallic salt	Organic Ligand	Conditions (K, bar)	CO <sub>2</sub> adsorption (mmol/g)	CO <sub>2</sub> /N <sub>2</sub> selectivity	Ref.
HKUST-1	Cu(NO <sub>3</sub> ) <sub>2</sub>	H <sub>3</sub> BTC	273, 1	8.02	29	45
UiO-66	ZrCl <sub>4</sub>	H <sub>3</sub> BDC	298, 1	1.5	12.91	46
MIL-160 (Al)	Al(OH)(CH <sub>3</sub> COO) <sub>2</sub>	FDCA	298, 1	6.21	---	103
UTSA (Zn)	Zn(O <sub>2</sub> CCH <sub>3</sub> ) <sub>2</sub> (H <sub>2</sub> O) <sub>2</sub>	CA	298, 1	4.71	118	104

Although MOFs have a large set of useful properties for capturing gases, it is possible to improve these materials by adding specific functional groups to enhance the adsorption performance. Using high-affinity functionalities is the current strategy and amine-functionalization is the top of the common tuning for selective CO<sub>2</sub> adsorption under flue gas conditions.<sup>20,105,106</sup> The adsorption process is quite simple: amine groups attract CO<sub>2</sub> molecules to the surface of the MOF material, and they react producing zwitterionic carbamate or carbamic acid.<sup>46</sup> The most frequent strategy is to perform the functionalization during the synthesis of the MOF itself using previous amino precursors.<sup>46,107</sup> Then, the amino ligand reacts with the metal salt creating an amino three-dimensional structure. An example is the synthesis of UiO-66-NH<sub>2</sub>, where UiO-66-NH<sub>2</sub> is synthesized replacing H<sub>2</sub>BDC ligand of UiO-66 with the corresponding molar amount of 2-amino-terephthalic acid (H<sub>2</sub>BDC-NH<sub>2</sub>). As a result, the functionalized MOF exhibited higher CO<sub>2</sub> capacity of adsorption than UiO-66 and the highest CO<sub>2</sub>/N<sub>2</sub> selectivity observed among all the MOF structures tested by the Jeewan Pokhrel and colleagues, concluding that amine functional groups in the organic linkers successfully enhance the CO<sub>2</sub> affinity.<sup>46</sup> Contrastingly, a higher affinity resulting from the bonds formed between CO<sub>2</sub> molecules and the functionalized amines implies a more complicated recyclability process. This is because it becomes more challenging to break the newly formed nitrogen bonds

with CO<sub>2</sub> molecules, thus preventing alterations to the MOF's pristine state once the sample is regenerated.

Other approaches of amine-functionalization are the synthesis published by Dong Kyu Roh et al. They reported a facile procedure to obtain MOF nanoparticles with a controllable external structure and an internal pore structure using NH<sub>2</sub>-MIL-125 (Ti), a titanium-based MOF. In this case, the synthesis route was also the same: the addition of metallic salt and aminated organic linkers together obtaining as a result an enhanced MOF structure with improved CO<sub>2</sub> adsorption and selectivity.<sup>105</sup>

Additionally, the use of thiol groups in the functionalization of MOFs provide interesting characteristics to the structure such as increasing the local reactivity by the lone pair of electrons of sulfur atom or increasing interaction with oxygen atoms and the induced polarizability.<sup>108</sup> Although the use of thiol groups is not common on MOF functionalization, the group formed by Hongliang Huang et al. reported some molecular simulations about CO<sub>2</sub> adsorption performance of three isostructural MOFs synthesized with different functional groups: -2NO<sub>2</sub>, -2NH<sub>2</sub> and -2SO<sub>3</sub>H. They analyzed and compared the performance for CO<sub>2</sub> adsorption of each sample using grand canonical Monte Carlo (GCMC) simulations. Then, the results obtained from the adsorption performance and selectivity demonstrated that the samples with the highest adsorption parameters were Zr-NDC-2SO<sub>3</sub>H and Zr-NDC-2NH<sub>2</sub>. Otherwise, the Zr-NDC-2SO<sub>3</sub>H sample was not as stable because of the large polarity of the -SO<sub>3</sub>H group, which reduces the stability of Zr-O coordination bonds from the tridimensional composite.<sup>109</sup>

The possibility of tuning MOF structures through functional groups opens a wide path to improving the adsorption capacity. But the path is even broader if the MOF itself is combined with another material that can also improve the adsorption capacity, such as carbonaceous materials (specially graphenic material). In these

cases, the most successful procedure is to carry out the synthesis directly by adding the carbonaceous material together with the precursors.<sup>46</sup>

The following sections provide a more detailed analysis of the combination of MOFs with other materials that, according to the literature, enhance CO<sub>2</sub> adsorption performance.

## 1.5 MOF combined with graphenic materials

The combination of graphenic materials with MOFs represents the most noteworthy material to date. Porosity, good conductivity, high stability, easy surface functionalization and low cost are excellent properties of them.<sup>110,111</sup> Among the huge variety of carbonaceous materials, allotropic graphene structures are current materials combined with MOFs.

MOFs can capture CO<sub>2</sub> due to their exceptionally high surface area and pore volume, as well as their surface tunability and dispersive forces. However, the addition of graphenic materials contributes to improving porosity and dispersive forces due to the high atomic density and a large number of surface functional groups.<sup>45</sup> Graphenic materials and MOFs combinations are quite interesting due to the possible combinations of the allotropes (Figure 1.13), such as carbon nanotubes,<sup>110</sup> single-layer graphene,<sup>112</sup> reduced graphene oxide<sup>113</sup> or graphene oxide.<sup>114</sup>

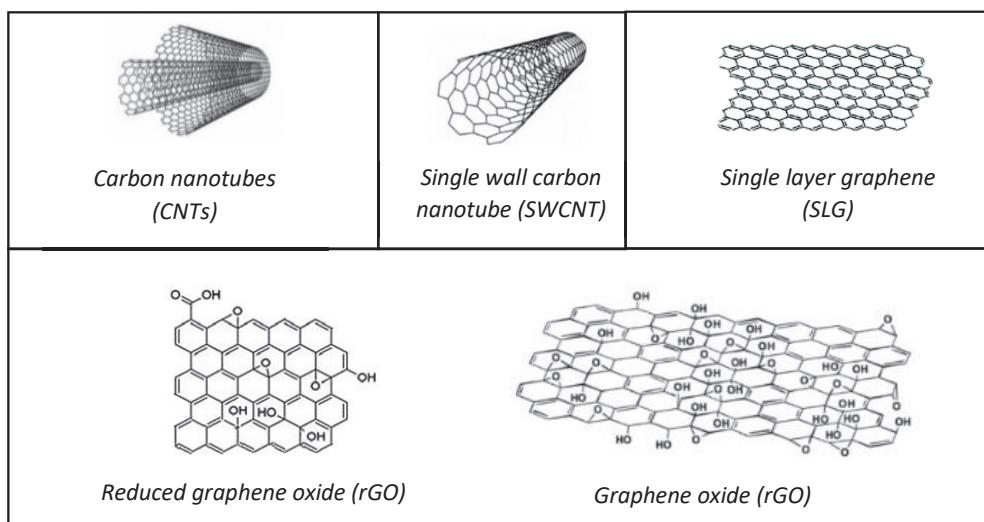


Figure 1.13. Allotropic structures of graphene: CNTs, SWCNT, SGL, Rgo and GO. Reprinted from ref. 110,113,115

### 1.5.1 MOF combined with graphene oxide

MOF/GO materials can capture CO<sub>2</sub> because of the dispersive environment obtained owing to the synergy of both combined molecules capable of enhancing the

physisorption mechanism of capture. Jeewan Pokhrel et al., as mentioned in the previous sections,<sup>46</sup> described the synthesis and characterization of copper and zirconium metal organic frameworks and compared the original MOFs with the MOF/GO composites. The incorporation of graphene oxide layers to MOF structures was analyzed by SEM images and, as a result, GO flakes adopt the agglomerates of graphene sheets surrounding MOF crystallites. As can be seen in the images of Figure 1.14 although no GO layers are observed due to the low concentration of GO, lower degree of aggregation can be observed comparing the pristine UiO-66 composite with the UiO-66/GO composite. The authors of this publication concluded that GO layers interact with MOFs through dispersive forces and specific interactions by their functional carboxyl and hydroxyl surface groups.

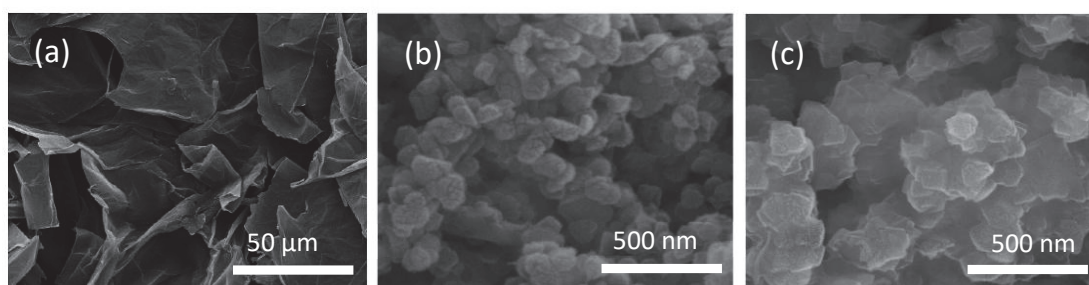


Figure 1.14. SEM images of (a) GO, (b) UiO-66, and (c) UiO-66/GO. Adapted from ref.<sup>46</sup>

Regarding the CO<sub>2</sub> adsorption performance of the samples, the results were diverse: UiO-66 adsorbed 1.50 mmol CO<sub>2</sub>/g while the composite with 10% of GO adsorbed 1.05 mmol CO<sub>2</sub>/g at 1 bar and 25 °C. On the other hand, HKUST-1/GO composite, containing 50% of GO, showed a capacity of adsorption of 0.98 mmol CO<sub>2</sub>/g while HKUST-1 displayed an adsorption of 1.59 mmol CO<sub>2</sub>/g. Then, both MOF/GO materials suggested the same behavior observed before achieving lower CO<sub>2</sub> adsorption capacity at the same pressure and temperature conditions. In contrast, the N<sub>2</sub>/CO<sub>2</sub> selectivity values were higher than the original MOF's values in both cases, being 7 times more CO<sub>2</sub> selective for HKUST-1/GO and 4 times more selective for UiO-66/GO compared with their pristine MOF, respectively. Otherwise, they concluded that

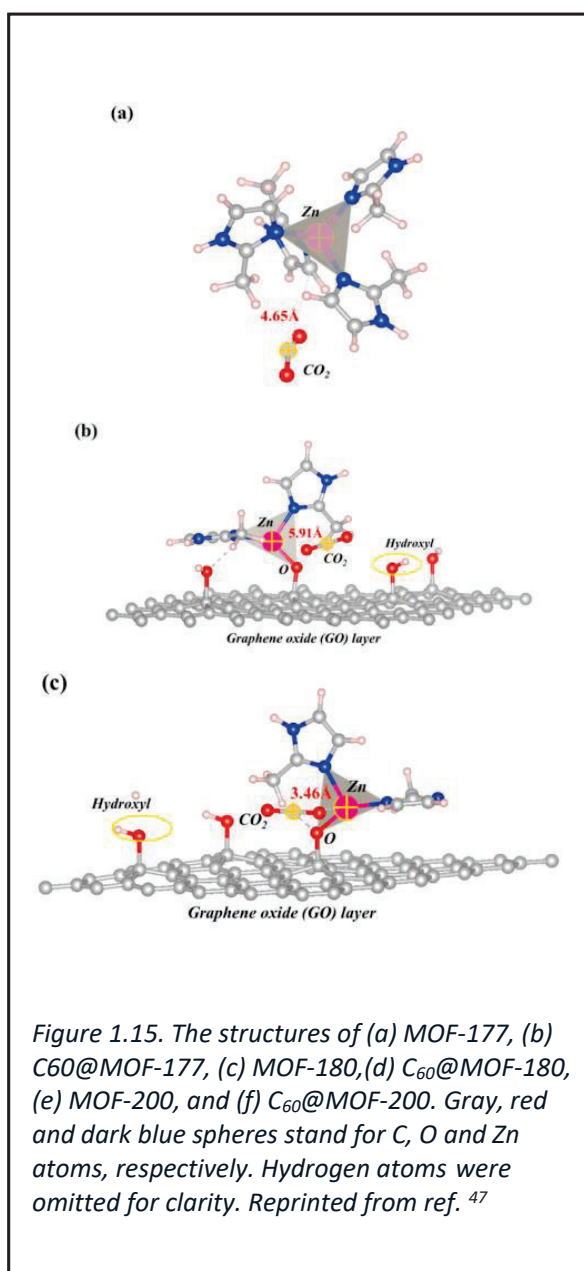
MOF/GO composites with relatively low GO concentrations are preferential since a balance is required between adsorption and selectivity.<sup>46</sup>

Hybrid compounds formed by MOFs and graphene oxide are crystalline structures that generally present high porosity and specific morphology depending on the precursors used in the synthesis. The research of Yunxia Zhao et al. investigated the porosity and specific surface area on MOF materials combined with GO and the effect on the CO<sub>2</sub> adsorption properties. Based on the results of this research, they determined that MOFs with similar pore size to CO<sub>2</sub> molecules lead to superior performance of gas adsorption. Then, high CO<sub>2</sub> adsorption capacity is related to high surface area and pore volume, and similar pore size to CO<sub>2</sub> and extra reactive sites in the composites provide better adsorption performances. Specific surface area from MOF-5-O (290 m<sup>2</sup>/g) was improved by adding GO (325 m<sup>2</sup>/g) and consequently, CO<sub>2</sub> adsorption performance was also enhanced. On the other hand, MOF-5-H displayed lower specific surface area values when combining with GO and aminated GO (AGO), and lower CO<sub>2</sub> performance as well.<sup>116</sup>

Other studies that relate MOFs and GO materials for improving the CO<sub>2</sub> adsorption performance expose the results of chromium MOFs performance. Xin Zhou et al. analyzed the samples using different graphene oxide percentages and concluded that the 1% doped composite provided significantly improved surface area and pore volume, while the composites with 10% of GO had remarkably higher CO<sub>2</sub> adsorption, reaching 10.81 mmol CO<sub>2</sub>/g corresponding to the fitted LF model calculated.<sup>117</sup> Otherwise, Armin Taheri et al. synthesized and characterized MOF-101 (Cr), a chromium-based MOF, and composite MOF-101 (Cr)/GO to investigate the separation of methanethiol (MeSH) from CO<sub>2</sub> and CH<sub>4</sub>. According to the results obtained, the researchers concluded that GO incorporation to the MOF(Cr) generates composites with increased BET specific surface areas, except for samples with GO additions greater than 10%. The composite with 5% GO was the optimal

MOF/GO combination resulting in 12% increase of CO<sub>2</sub> adsorption capacity (20 mmol CO<sub>2</sub>/g) in comparison with the MOF-101(Cr) (17.6 mmol CO<sub>2</sub>/g) when CO<sub>2</sub> adsorption isotherms are performed at 298 K and until 40 bars of pressure. Additionally, 5% of GO composites could regenerate repeatedly after MeSH adsorption.<sup>118</sup>

The zeolitic imidazole frameworks, called ZIFs; are other example of MOF structures. These tridimensional structures are like zeolites since they offer comparable characteristics, such as thermal and chemical stability or high surface area and crystallinity. Niu Liu and co-workers published the results of the ZIF-8@ZIF-67 nanocomposites supported by the GO core-shell. In this case, the CO<sub>2</sub> adsorption capacity decreased as the GO amount increased. The highest adsorption value was 2.15 mmol/g at 273 K and 1 bar provided by the composite with 0.5%. In addition, the group investigated the mechanism of CO<sub>2</sub> capture of the nanocomposite to understand the interaction between CO<sub>2</sub>-active sites using molecular simulations. Three optimized structures of CO<sub>2</sub> adsorption mechanisms were examined: Zn–N<sub>4</sub> model, Zn–N<sub>3</sub>–O model and Zn–N<sub>2</sub>–O model, and the data showed that the OMS in the structure allowed the access of CO<sub>2</sub> molecules, being oxygen atoms of CO<sub>2</sub> molecules attracted to the adsorption sites. In



---

addition, the unsaturated Zn-N<sub>2</sub>-O metal sites in GO-supported nanocomposites presented higher binding energy than Zn-N<sub>4</sub> metal sites in the original core-shell ZIF-8@ZIF-67 (Figure 1.15).<sup>47</sup>

Furthermore, Sami Ullah's et al. prepared metal organic frameworks using zinc nitrate hexahydrate (Zn(NO<sub>3</sub>)<sub>2</sub>·6H<sub>2</sub>O) and 1,3,5-tris(4-carboxy[1,2-biphenyl]-4-yl)-benzene) (H<sub>3</sub>BBC) through post-synthesis functionalization. They combined the MOF with GO and compared the uptake capacity of CO<sub>2</sub> at different temperatures, resulting in a 15% increased adsorption capacity than the original MOF. In this publication the authors attribute the enhancement of CO<sub>2</sub> adsorption properties due to the specific surface area loss after post-synthetic functionalization, decreasing from 3624 m<sup>2</sup>/g (MOF-200) to 3359 m<sup>2</sup>/g (MOF-200/GO),<sup>119</sup> which often differs from the findings obtained from other publications that relate higher CO<sub>2</sub> adsorption performance for samples with higher specific surface area.<sup>45,120</sup>

Samples of HKUST-1 and HKUST-1/GO are other examples investigated by Alfonso Policichio et al. In the study, they concluded that the samples exhibited increased CO<sub>2</sub> adsorption with decreasing temperature. Additionally, the synthesis of HKUST-1 with 10% GO resulted in a 33% enhancement in adsorption capacity at 298 K, and a 43% enhancement at 277 K when compared to the pristine HKUST-1 at the same temperature and measured in the pressure range 0.0–1.5 MPa.<sup>121</sup> The case study published by Shang et al. was similar, as they compared the different HKUST-1/GO adsorption capacities at various percentages of GO. As a result, the optimal CO<sub>2</sub> adsorption value was observed in the HKUST-1/GO1 sample, achieving an 11% higher adsorption compared to pure HKUST-1, measured at 273 K and up to pressures of 0.1 MPa. The remaining composites studied (HKUST-GO 0.5, 3, and 5% of GO) demonstrated similar adsorption values to pure HKUST-1, without any improvement in the CO<sub>2</sub> adsorption performance. Furthermore, although HKUST-1/GO1 exhibited the highest CO<sub>2</sub> uptake, its isosteric heat of CO<sub>2</sub> adsorption

was lower than that of HKUST-1, indicating that less energy is required for regeneration.<sup>45</sup> The group of Feng Xu studied the preparation of the same MOF structures using hydrothermal synthesis and compared the values of adsorption obtained from the samples. They concluded that lower concentrations of GO achieve an optimization of adsorption in the final material, resulting in HKUST-1/GO2 exposing an increase of 32% of CO<sub>2</sub> adsorption in comparison with the parent HKUST-1. These results suggest stronger interactions between CO<sub>2</sub> molecules and the composites, probably attributed to the slightly higher isosteric heat obtained from the process of adsorption compared to the pristine HKUST-1. Moreover, they also studied the selectivity and determined that, at 1 bar, the CO<sub>2</sub>/N<sub>2</sub> selectivity was 186 for HKUST-GO2 and 103 for HKUST-1, showing again the optimization attained.<sup>122</sup>

### **1.5.2 MOFs combined with reduced graphene oxide**

Considering hybrid materials with reduced graphene oxide (rGO), the incorporation of rGO to ZIF nanocomposites was investigated by Niu Liu et al. Their strategy consisted of adding different concentrations of rGO and GO to the ZIF-8@ZIF-67 composites. Subsequently, they evaluated the differences between the physicochemical properties obtained by each hybrid material. Then, comparing the results obtained, the adsorption capacity of rGO-supported composites was lower than that of GO-supported composites even though both displayed similar textural properties (specific surface area, pore volume and pore size distribution). However, comparing the CO<sub>2</sub> retention capacity of the novel core-shell ZIF-8@ZIF-67 with the rGO-ZIF-8@ZIF-67, the last presented better CO<sub>2</sub> uptake. In conclusion, the authors determined that the presence of oxygen-functional groups in the surface of rGO layers acts like anchoring sites for the CO<sub>2</sub> molecules, such as in the case of GO.<sup>47</sup>

### 1.5.3 MOF combined with graphene nanoplatelets

The versatility of graphenic materials is one of the strengths of these materials, providing a wide range of allotropic structures with similar features. Graphene nanoplatelets are another example of graphene-based material and some studies also report the combination of this structure with MOFs materials for enhancing the sorption properties.

Sina Pourebrahimi et al. investigated the synthesis and characterization of MIL-53(Al)/GNP. The aluminum MOF structure combined with graphene nanoplatelets (GNP) showed an enhancement of CO<sub>2</sub> adsorption, revealing that the adsorption capacity of the composites with 2.5 and 5 wt% was 35 % higher than the original MOF. Particularly, MIL-53(Al)/GNP at 2.5 wt% composite reached 12 mmol CO<sub>2</sub>/g and MIL-53 (Al)/GNP reached 12.95 mmol CO<sub>2</sub>/g, both measured at 298 K and 40 bars. As a result, the group determined that the improvement of CO<sub>2</sub> adsorption was due to the modification of the surface dispersive forces along with the increase of the specific surface area and the total micropore volumes.<sup>120</sup>

Another case study of CO<sub>2</sub> adsorption using MOFs and graphenic materials is the publication of M. Alfe et al. In this case, the studied MOFs were combined with graphene-like layers (GL), which are not exactly the same as GNP, but they have some similarities. While GL is a material made of layers with similar properties of graphene but with some irregularities and defects, GNP, instead, is formed by small particles and sheets of graphene, often presented as monolayer or multi-layer. Thus, they studied three MOFs (HKUST-1, Al-MIL96 and Fe-MIL100) and the basis of their work was comparing the results of CO<sub>2</sub> and CH<sub>4</sub> adsorption using these MOFs and their hybrids combined with GL. As a result, the combination with GL using low concentrations (5%) negatively impacted on the CO<sub>2</sub> adsorption performance of HKUST-1 and had little effect on Fe-MIL100's at high pressure (up to 1.5 MPa). However, a different behavior was observed in Al-MIL96 and Al-MIL100/GL at low

pressure, where the enhancement was noted at 0.2 MPa. In this case, except for Al-MIL96/GL hybrids, MOF/GL hybrids didn't notably improve CO<sub>2</sub> and CH<sub>4</sub> adsorption capacities compared to pristine MOFs, especially at high pressures.<sup>121</sup>

#### 1.5.4 MOFs combined with carbon nanotubes

Xiang Z. et al. published experimental and theoretical results about hybrid MOF structures and explored the improvement of these materials obtained using two synthetic routes: incorporation of CNTs into HKUST-1; and MOF doping with Li<sup>+</sup> ions. The results indicated an improvement of the CO<sub>2</sub> adsorption performance, reaching 13.52 mmol CO<sub>2</sub>/g with CNT@[Cu<sub>3</sub>(BTC)<sub>2</sub>] and 15 mmol CO<sub>2</sub>/g with Li@CNT@[Cu<sub>3</sub>(BTC)<sub>2</sub>]. However, the authors exposed that an excess of lithium ions in the structure could cause the deformation of the framework, concluding that low concentrations are the optimal ranges, being the finest Li/Cu ratio of 0.001 mol mol<sup>-1</sup>.<sup>123</sup>

Contrastingly, Ata-ur-Rehman group published the synthesis of MOF-5 particles in well-dispersed carboxy derived multiwalled carbon nanotubes (MWCNTs) using solvothermal method. In this case, MOF-5@MWCNTs nanocomposites showed an enhancement in both stability and BET surface area and the results also revealed that nanocomposites presented better stability against atmospheric moisture, attributable to the carbonaceous material added and H-bonding interactions between ZnO<sub>4</sub> (MOF subunit) and H-atoms (CNTs).<sup>124</sup>

Additionally, the group formed by Jonathan Cortés-Suarez et al. investigated SWCNT@HKUST-1 composite using Raman studies. They studied the interaction of CO<sub>2</sub> with the samples and the results revealed that the 5 wt% SWCNT@HKUST-1 exhibited better CO<sub>2</sub> adsorption. As indicated in Figure 1.16 (a) and (b), Raman spectroscopy analysis of HKUST-1 and 5% SWCNT@HKUST-1 before and after CO<sub>2</sub> adsorption shows that the characteristic Cu-Cu vibration is shifted with the adsorption of CO<sub>2</sub>. Moreover, Cu-Cu-CO<sub>2</sub> (OMS) vibration is also observed, and they

corroborated that even though samples were fully activated, the samples continued covering adsorbed water molecules due to their high hygroscopicity.<sup>125</sup>

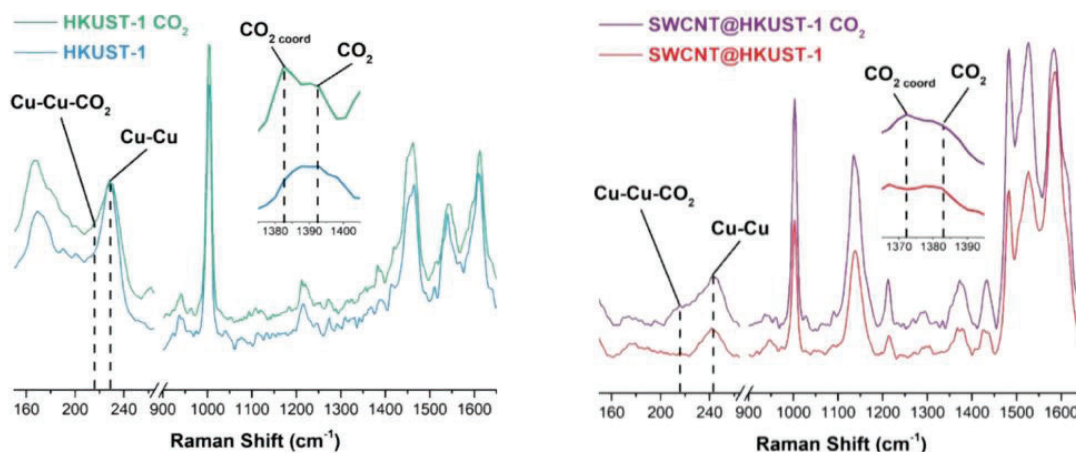


Figure 1.16. Raman spectra for (a) HKUST-1 and (b) 5 wt % SWCNT@HKUST-1, before and after CO<sub>2</sub> adsorption. Reprinted from ref. <sup>125</sup>

### 1.5.5 MOF combined with fullerenes

Other interesting approaches are the fabrication of MOFs combined with fullerenes. Fullerenes, also called C<sub>60</sub>; have been widely studied as possible candidates for CO<sub>2</sub> capture due to the possibility of functionalizing their surface producing active sites in the cage structure.<sup>126</sup> Genjian Xu et al. published some molecular simulation data about the CO<sub>2</sub> adsorption and adsorptive separation of three samples of MOFs impregnated with C<sub>60</sub>: C<sub>60</sub>@MOF-177, C<sub>60</sub>@MOF-180, and C<sub>60</sub>@MOF-200. The group investigated the separation of CO<sub>2</sub> from CO<sub>2</sub>/CH<sub>4</sub>, CO<sub>2</sub>/CO and CO<sub>2</sub>/H<sub>2</sub> mixtures by grand canonical Monte Carlo simulations and they concluded that C<sub>60</sub> impregnation considerably enhances the separation of CO<sub>2</sub> from the gas mixtures. They also calculated the saturation of CO<sub>2</sub> in MOF-n and C<sub>60</sub>@MOF-n (n=177, 180 and 200). As a result, CO<sub>2</sub> uptake was significantly improved in all cases after C<sub>60</sub> impregnation since at lower pressures compared to original MOFs. The authors attributed this improvement to the increased adsorption heat of CO<sub>2</sub>, the expanded surface area and mainly to the reduction in free volume.<sup>127</sup>

The next pages present a summary table of the hybrid materials discussed above with some key parameters (Table 1.8).

Table 1.8. Summary of gas-phase adsorption and storage parameters of the adsorbent materials reported.

Composite	Metallic salt	Organic ligand	GM	Conditions (K/bar)	BET (m <sup>2</sup> /g)	Total Pore volume (cm <sup>3</sup> /g)	N <sub>2</sub> /CO <sub>2</sub> Selectivity	CO <sub>2</sub> Adsorption (mmol/g)	Ref.
HKUST-1	Cu(NO <sub>3</sub> )·3H <sub>2</sub> O	H <sub>3</sub> BTC	-	298/1	434	0.29	1.96	1.59	46
HKUST-1	Cu(NO <sub>3</sub> )·3H <sub>2</sub> O	H <sub>3</sub> BTC	-	273, 1	1580	0.636	26	8.02	45
HKUST-1/GO50	Cu(NO <sub>3</sub> )·3H <sub>2</sub> O	H <sub>3</sub> BTC	GO	298, 1	369	0.4	13.74	0.98	46
HKUST-1/GO1	Cu(NO <sub>3</sub> )·3H <sub>2</sub> O	H <sub>3</sub> BTC	GO	273, 1	1772	0.718	39.2	8.9	45
HKUST-1	Cu(NO <sub>3</sub> )·3H <sub>2</sub> O	H <sub>3</sub> BTC	-	298, 1	1760	0.83	20	5.33	53
HKUST-1	Cu(NO <sub>3</sub> )·3H <sub>2</sub> O	H <sub>3</sub> BTC	-	298, 14.7	2632	1.11	-	12.8	121
HKUST-1	Cu(NO <sub>3</sub> )·3H <sub>2</sub> O	H <sub>3</sub> BTC	-	298, 18	1587	0.73	-	6.70	123
HKUST-1	Cu(NO <sub>3</sub> )·3H <sub>2</sub> O	H <sub>3</sub> BTC	-	298, 1	892	0.428	-	2.32	123

Composite	Metallic salt	Organic ligand	GM	Conditions (K/bar)	BET (m <sup>2</sup> /g)	Total Pore volume (cm <sup>3</sup> /g)	N <sub>2</sub> /CO <sub>2</sub> Selectivity	CO <sub>2</sub> Adsorption (mmol/g)	Ref.
HKUST-1	Cu(NO <sub>3</sub> )·3H <sub>2</sub> O	H <sub>3</sub> BTC	-	298, 15.3	892	0.428	-	7.09	123
HKUST-1/GO0.5	Cu(NO <sub>3</sub> )·3H <sub>2</sub> O	H <sub>3</sub> BTC	GO	273, 10	1675	0.689	~26	8.34	45
HKUST-1/GO1	Cu(NO <sub>3</sub> )·3H <sub>2</sub> O	H <sub>3</sub> BTC	GO	273, 10	1772	0.718	~27	8.95	45
HKUST-1/GO3	Cu(NO <sub>3</sub> )·3H <sub>2</sub> O	H <sub>3</sub> BTC	GO	273, 10	1668	0.700	~26	8.31	45
HKUST-1/GO5	Cu(NO <sub>3</sub> )·3H <sub>2</sub> O	H <sub>3</sub> BTC	GO	273, 10	1637	0.670	~27	8.33	45
HKUST-1/GO10	Cu(NO <sub>3</sub> )·3H <sub>2</sub> O	H <sub>3</sub> BTC	GO	295, 1	1010	0.491	-	3.09	128
HKUST-1/GO10	Cu(NO <sub>3</sub> )·3H <sub>2</sub> O	H <sub>3</sub> BTC	GO	273, 1	1010	0.491	-	5.52	128
HKUST-1	Cu(NO <sub>3</sub> )·3H <sub>2</sub> O	H <sub>3</sub> BTC	GO	273, 1	892	0.428	-	3.86	129
HKUST-1/GO2	Cu(NO <sub>3</sub> )·3H <sub>2</sub> O	H <sub>3</sub> BTC	GO	298, 1	1820	0.88	18.7	5.12	129

Composite	Metallic salt	Organic ligand	GM	Conditions (K/bar)	BET (m <sup>2</sup> /g)	Total Pore volume (cm <sup>3</sup> /g)	N <sub>2</sub> /CO <sub>2</sub> Selectivity	CO <sub>2</sub> Adsorption (mmol/g)	Ref.
HKUST-1/GO5	Cu(NO <sub>3</sub> )·3H <sub>2</sub> O	H <sub>3</sub> BTC	GO	298,1	1520	0.78	19	4.79	53
HKUST-1	Cu(NO <sub>3</sub> )·3H <sub>2</sub> O	H <sub>3</sub> BTC	GO	298,1	1380	0.73	14.53	3.55	130
HKUST-1/GO10	Cu(NO <sub>3</sub> )·3H <sub>2</sub> O	H <sub>3</sub> BTC	GO	298,1	1323	0.77	14.33	5.14	130
HKUST-1/GO1	Cu(NO <sub>3</sub> )·3H <sub>2</sub> O	H <sub>3</sub> BTC	GO	298,1	1006	0.617	13.97	4.07	130
HKUST-1	Cu(NO <sub>3</sub> )·3H <sub>2</sub> O	H <sub>3</sub> BTC	GO	273,1	1380	0.73	14.53	7.32	130
HKUST-1/GO10	Cu(NO <sub>3</sub> )·3H <sub>2</sub> O	H <sub>3</sub> BTC	GO	273,1	1323	0.77	14.33	9.50	130
HKUST-1/GO1	Cu(NO <sub>3</sub> )·3H <sub>2</sub> O	H <sub>3</sub> BTC	GO	273,1	1006	0.617	13.97	7.62	130
HKUST-1	Cu(NO <sub>3</sub> )·3H <sub>2</sub> O	H <sub>3</sub> BTC	GO	273,1	1193	0.57	103	6.85	122
HKUST-1/GO2	Cu(NO <sub>3</sub> )·3H <sub>2</sub> O	H <sub>3</sub> BTC	GO	273,1	1554	0.711	186	9.02	122

Composite	Metallic salt	Organic ligand	GM	Conditions (K/bar)	BET (m <sup>2</sup> /g)	Total Pore volume (cm <sup>3</sup> /g)	N <sub>2</sub> /CO <sub>2</sub> Selectivity	CO <sub>2</sub> Adsorption (mmol/g)	Ref.
Al-MIL96	Al(NO <sub>3</sub> ) <sub>3</sub> ·9H <sub>2</sub> O	H <sub>3</sub> BTC	-	298, 14.7	51	0.05	-	4.13	121
Fe-MIL100	Fe(NO <sub>3</sub> ) <sub>3</sub> ·9H <sub>2</sub> O	H <sub>3</sub> BTC	-	298, 14.7	1105	0.74	-	18.18	121
UiO-66	ZrCl <sub>4</sub>	H <sub>2</sub> BDC		298, 1	1110	0.78	12.91	1.50	46
UiO-66/GO	ZrCl <sub>4</sub>	H <sub>2</sub> BDC	GO	298, 1	1016	1.47	53.3	1.05	46
MIL-53(Cr)	Cr(NO <sub>3</sub> ) <sub>3</sub> ·9H <sub>2</sub> O	H <sub>2</sub> BDC	-	298, ≤5	1197	0.47	-	4.81	117
MIL-53(Cr)/GO10	Cr(NO <sub>3</sub> ) <sub>3</sub> ·9H <sub>2</sub> O	H <sub>3</sub> BTC	GO	298, ≤5	1182	0.56	-	10.81	117
ZIF-8@ZIF-67	Zn(NO <sub>3</sub> ) <sub>2</sub> ·6H <sub>2</sub> O Co(NO <sub>3</sub> ) <sub>2</sub> ·6H <sub>2</sub> O	2-MeIM	-	273, 1	1490	0.93	8.43	1.61	47
ZIF-8@ZIF-67/GO0.5	Zn(NO <sub>3</sub> ) <sub>2</sub> ·6H <sub>2</sub> O Co(NO <sub>3</sub> ) <sub>2</sub> ·6H <sub>2</sub> O	2-MeIM	GO	273, 1	1378	1.27	14.91	2.15	47
MOF-200	Zn(NO <sub>3</sub> ) <sub>2</sub> ·6H <sub>2</sub> O	H <sub>3</sub> BBC	-	298, 1	3624	2.87	-	1.17	119

Composite	Metallic salt	Organic ligand	GM	Conditions (K/bar)	BET (m <sup>2</sup> /g)	Total Pore volume (cm <sup>3</sup> /g)	N <sub>2</sub> /CO <sub>2</sub> Selectivity	CO <sub>2</sub> Adsorption (mmol/g)	Ref.
MOF-200/GO	Zn(NO <sub>3</sub> ) <sub>2</sub> ·6H <sub>2</sub> O	H <sub>3</sub> BBC	GO	298, 1	3359	2.65	-	1.34	119
MIL-101 (Cr)	Cr(NO <sub>3</sub> ) <sub>3</sub>	H <sub>2</sub> BDC	-	298, 40	2486	1.12	-	28.65	118
MIL-101 (Cr)/GO5	Cr(NO <sub>3</sub> ) <sub>3</sub>	H <sub>2</sub> BDC	GO	298, 40	2872	1.34	-	32.19	118
MIL-53(Al)	Al(NO <sub>3</sub> ) <sub>3</sub> ·9H <sub>2</sub> O	H <sub>2</sub> BDC	-	298, 40	1132	0.52	-	9.61	123
MIL-53(Al)/GNP	Al(NO <sub>3</sub> ) <sub>3</sub> ·9H <sub>2</sub> O	H <sub>2</sub> BDC	GNP	298, 40	1196	0.56	-	11.75	120
MIL-53(Al)/GNP	Al(NO <sub>3</sub> ) <sub>3</sub> ·9H <sub>2</sub> O	H <sub>2</sub> BDC	GNP	298, 40	1281	0.63	-	12.95	120
Al-MIL96/GL	Al(NO <sub>3</sub> ) <sub>3</sub> ·9H <sub>2</sub> O	H <sub>2</sub> BDC	GL	298, 14.7	47	0.04	-	3.40	121
Fe-MIL100/GL	Fe(NO <sub>3</sub> ) <sub>3</sub> ·9H <sub>2</sub> O	H <sub>3</sub> BTC	GL	298, 14.7	959	0.59	-	8.63	121
CNT@[Cu <sub>3</sub> (btc) <sub>2</sub> ]	Cu(NO <sub>3</sub> ) <sub>2</sub> ·3H <sub>2</sub> O	H <sub>3</sub> BTC	CNTs	298, 18	1458	0.87	-	13.52	123

Composite	Metallic salt	Organic ligand	GM	Conditions (K/bar)	BET (m <sup>2</sup> /g)	Total Pore volume (cm <sup>3</sup> /g)	N <sub>2</sub> /CO <sub>2</sub> Selectivity	CO <sub>2</sub> Adsorption (mmol/g)	Ref.
Li@CNT@[Cu <sub>3</sub> (btc) <sub>2</sub> ]	Cu(NO <sub>3</sub> ) <sub>2</sub> ·3H <sub>2</sub> O	H <sub>3</sub> BTC	CNTs	298, 18	857	0.69	-	15	123
NH <sub>2</sub> -MIL-125(Ti)	Ti(OCH(CH <sub>3</sub> ) <sub>2</sub> ) <sub>4</sub>	NH <sub>2</sub> -BDC	-	298, 1	1490	1.15	-	0.39	131
ZIF-8@ZIF-67	Zn(NO <sub>3</sub> ) <sub>2</sub> ·6H <sub>2</sub> O Co(NO <sub>3</sub> ) <sub>2</sub> ·6H <sub>2</sub> O	2-MeIM	-	273, 1	1490	0.93	-	1.61	47
rGO-ZIF-8@ZIF-67	Zn(NO <sub>3</sub> ) <sub>2</sub> ·6H <sub>2</sub> O Co(NO <sub>3</sub> ) <sub>2</sub> ·6H <sub>2</sub> O	2-MeIM	rGO (0.5%)	273, 1	1490	1.60	-	1.73	47
rGO-ZIF-8@ZIF-67	Zn(NO <sub>3</sub> ) <sub>2</sub> ·6H <sub>2</sub> O Co(NO <sub>3</sub> ) <sub>2</sub> ·6H <sub>2</sub> O	2-MeIM	rGO (1%)	273, 1	1459	1.38	-	1.45	47
rGO-ZIF-8@ZIF-67	Zn(NO <sub>3</sub> ) <sub>2</sub> ·6H <sub>2</sub> O Co(NO <sub>3</sub> ) <sub>2</sub> ·6H <sub>2</sub> O	2-MeIM	rGO (2%)	273, 1	619	0.35	-	1.23	47
MOF-177	Zn(NO <sub>3</sub> ) <sub>2</sub> ·6H <sub>2</sub> O	H <sub>3</sub> BTB	-	298, 30	0.17 <sup>#</sup>	0.86 <sup>\$</sup>	-	31.76	127

Composite	Metallic salt	Organic ligand	GM	Conditions (K/bar)	BET (m <sup>2</sup> /g)	Total Pore volume (cm <sup>3</sup> /g)	N <sub>2</sub> /CO <sub>2</sub> Selectivity	CO <sub>2</sub> Adsorption (mmol/g)	Ref.
C <sub>60</sub> @MOF-177	Zn(NO <sub>3</sub> ) <sub>2</sub> ·6H <sub>2</sub> O	H <sub>3</sub> BTB	Fullerene	298, 20	0.26 <sup>#</sup>	0.44 <sup>§</sup>	-	7.75	127
MOF-180	Zn(NO <sub>3</sub> ) <sub>2</sub> ·6H <sub>2</sub> O	H <sub>3</sub> ETTB	-	298, 50	0.11 <sup>#</sup>	0.93 <sup>§</sup>	-	46.03	127
C <sub>60</sub> @MOF-180	Zn(NO <sub>3</sub> ) <sub>2</sub> ·6H <sub>2</sub> O	H <sub>3</sub> ETTB	Fullerene	298, 20	0.22 <sup>#</sup>	0.48 <sup>§</sup>	-	10.57	127
MOF-200	Zn(NO <sub>3</sub> ) <sub>2</sub> ·6H <sub>2</sub> O	H <sub>3</sub> BPB	-	298, 50	0.09 <sup>#</sup>	0.79 <sup>§</sup>	-	58.15	127
C <sub>60</sub> @MOF-200	Zn(NO <sub>3</sub> ) <sub>2</sub> ·6H <sub>2</sub> O	H <sub>3</sub> BPB	Fullerene	298, 20	0.19 <sup>#</sup>	0.53 <sup>§</sup>	-	14.34	127
IRMOF-10	Zn(NO <sub>3</sub> ) <sub>2</sub> ·6H <sub>2</sub> O	H <sub>2</sub> BDC	-	298, 1	0.12 <sup>#</sup>	0.86 <sup>§</sup>	-	2	127

#= Surface area in Å<sup>2</sup>/Å<sup>3</sup> ; §= free volume in cm<sup>3</sup>/cm<sup>3</sup>; GM : graphenic material



## 1.6 Final discussion and research perspective

In summary, the continuous challenge lies in the development of solid materials with improved properties for capturing relevant quantities of CO<sub>2</sub>. However, sometimes it is a complex task to find materials that meet all the criteria to be considered as an effective solid CO<sub>2</sub> adsorbent. Therefore, it may be convenient to prioritize high selectivity values, even if this implies a decrease in the material's adsorption capacity or vice versa, depending on the expected application of the material. Likewise, pressure and temperature conditions are determinants in CO<sub>2</sub> adsorption measurements. In this regard, there are MOF structures, such as MIL-101(Cr); which can achieve significant CO<sub>2</sub> adsorption values at high pressures, whereas others, such as HKUST-1 and MIL-160 (Al); can achieve optimal performance at 1 atm. Additionally, some other examples such as UiO-66 exhibit low capture capacity but stand out for their high CO<sub>2</sub> selectivity. Consequently, there is a wide range of considerations to be contemplated when it is desired to capture CO<sub>2</sub> using MOFs materials. Identifying the most suitable MOF is closely linked to the conditions under which the material will perform as an adsorbent along with characteristics of the emission source.

Additionally, a general observation from this analysis is that high values of CO<sub>2</sub> adsorption are often related to high values of specific surface area, which are consistent with the literature since exposing CO<sub>2</sub> molecules to a higher material surface increases the number of available adsorption sites, improving as a result the gas-solid interactions. Otherwise, other characteristics such as selectivity, scalability and shaping of MOFs materials must be considered. Hence, striking a balance among adsorption conditions, KPI parameters and CO<sub>2</sub> adsorption capacity is a relevant concern.

Considering the combination of MOFs with graphene allotropes, a general trend emerges highlighting the synergy established between both components. Although

the conditions of CO<sub>2</sub> performance and the graphenic material vary, these combinations tend to improve the overall properties of the resulting materials, leading to an enhancement in stability and CO<sub>2</sub> performance. From this perspective, among the diversity of hybrid materials discussed in the previous sections of this chapter, the combination of GO with MOFs stands out considering practical conditions (298 K and 1 atm). Some publications describe that using a small amount of GO during the synthesis of HKUST-1 provides a better CO<sub>2</sub> adsorption capacity, as in the case of HKUST-1 with a proportion of 1%, which outperforms 50% compared to the pristine HKUST-1. Otherwise, not all MOFs combined with graphene can develop enhanced properties. Figure 1.17 compiles some data from Table 1.8 categorized based on graphene combination, temperature, and pressure conditions.

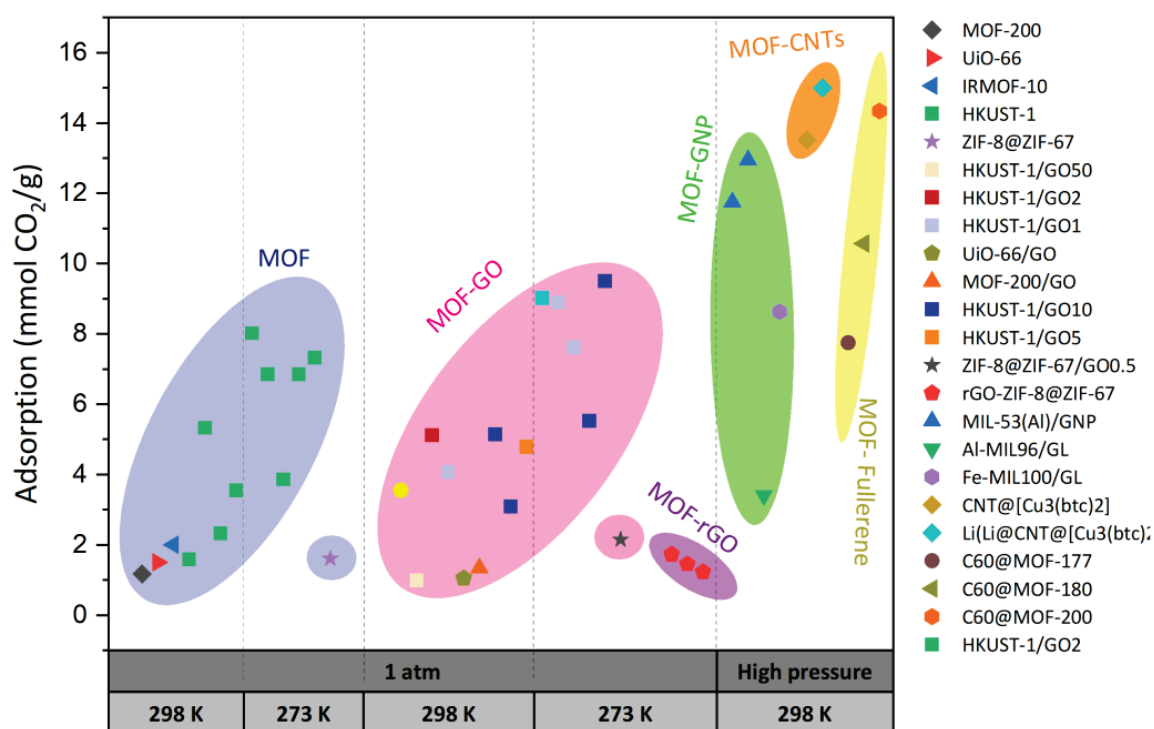


Figure 1.17. CO<sub>2</sub> adsorption capacity of different MOFs at different temperatures and pressures. Colored bubbles indicate groups of different combinations of MOF with graphenic materials.

On the one hand, the data indicates that HKUST-1 and HKUST-1/GO materials present the highest CO<sub>2</sub> adsorption performance compared to other MOFs tested at

similar conditions (indicated as a squares symbol in the graph). Hence, HKUST-1 predominates as one of the most adsorbent options in all cases of this analysis.

Moreover, the synthesis employed plays a key role in CO<sub>2</sub> adsorption performance, since aspects such as control of temperature and pressures during the formation of the MOFs crystals can alter the textural properties of the samples, which are directly related to the adsorption capacity. As an example, the sample of HKUST-1 stands out from the rest, reaching an adsorption of 5.33 mmol CO<sub>2</sub>/g at 298 K and 1 atm. In this case, the authors of these published results utilized a sonochemical method of synthesis facilitated with ZnO slurry,<sup>53</sup> which is not the most common strategy found in the literature to obtain HKUST-1.

In contrast, when MOFs are combined with GO, data collection indicates the potential to optimize CO<sub>2</sub> capture, yielding values of up to 5 mmol of CO<sub>2</sub>/g in many cases at 298K and 1 atm. And, as can be seen, there is a special increase in the CO<sub>2</sub> adsorption behavior when samples are measured at 273 K, where hybrid MOF-GO materials, such as HKUST-1/GO10, can achieve adsorptions of up to 9.5 mmol CO<sub>2</sub>/g. However, the results display some uncertainty regarding the precise optimal GO concentration required in the synthesis. As a result, some incongruencies regarding the optimal GO content arise since publications describe similar CO<sub>2</sub> uptakes for different GO contents, as in the case of 2%, 1% and 10% w/w GO depicted in the Figure 1.17 (green, light and darker blue symbol; respectively).

Considering the results of MOFs/rGO materials described in the literature, in this case, the CO<sub>2</sub> performance exhibits considerably lower values compared to the rest of samples. The collected data represented in the graph indicates that even testing the CO<sub>2</sub> adsorption isotherms at 273K, the adsorption performance is below 2 mmol CO<sub>2</sub>/g.

On the other hand, other graphene allotrope combinations, such as MIL-53(Al)/GNP, also demonstrate higher CO<sub>2</sub> capture performance, reaching up to 12.95 mmol CO<sub>2</sub>/g at 298 K and 40 atm of pressure. Similarly, CNT@[Cu<sub>3</sub>(BTC)<sub>2</sub>] exhibits CO<sub>2</sub> adsorption of 13.52 mmol CO<sub>2</sub>/g, under conditions of 298 K and 18 atm of pressure. In general, the combinations of MOFs with CNTs, GNP, or fullerene, typically tested their CO<sub>2</sub> adsorption performance under extreme pressure conditions. Consequently, extrapolating these findings into industrial or atmospheric air setups remains a challenging task.

In conclusion, although the data doesn't align standard considerations for all the CO<sub>2</sub> adsorption performances, such as synthesis methods utilized; the most attractive option for developing adsorbent materials is the MOF HKUST-1, specially synthesized with GO. Based on the results depicted in Figure 1.17, these combinations revealed the optimal performance of CO<sub>2</sub> adsorption at practical conditions of testing (1 atm and 298 K).

In this context, HKUST-1/GO materials exhibit remarkable CO<sub>2</sub> adsorption capacities compared to the rest of the materials due to favorable characteristics and properties. Some of these characteristics include high thermal and chemical stability, which allow these materials to operate without losing their performance at different temperatures and atmospheric conditions. Moreover, several studies also reported high selectivity's values achieved in the adsorption processes considering N<sub>2</sub> molecules along with high cyclability performance, which indicates that these materials present a high potential to regenerate and perform adsorption-desorption cycles several times.

Conversely, one of the primary challenges observed is the use of organic solvents in the most common synthesis method utilized (mixed-solvent method), such as DMF, and their associated environmental impact. Ecotoxic organic solvents continue to be a significant concern in the chemical industry and the obtention of HKUST-1

materials using a greener chemistry method is not as deeply investigated as mixed solvent method. Hence, these aspects along with the difficulty of obtaining good selectivity, adsorption performance and potential scalable samples, as well as considering other parameters and specifications, remain a daunting task.

Additionally, the interaction of ambient moisture is a problem due to the competition between H<sub>2</sub>O and CO<sub>2</sub> molecules, producing as a result a decrease in efficiency of CO<sub>2</sub> capture in most cases. As humidity is present in a major part of the CO<sub>2</sub> emission sources, studying this interaction more deeply is necessary since in most published results regarding HKUST-1/GO materials this aspect is not considered.

Table 1.9 summarizes the advantages and disadvantages of these combinations, specifically MOF/GO materials.

*Table 1.9. Advantages and disadvantages of MOF/Graphene Oxide materials.*

<b>HKUST-1/GO materials</b>	
<b>Advantages</b>	<b>Disadvantages</b>
High stability	The use of organic solvents in the synthesis
High selectivity's	Achieve ideal KPIs in a single material
High adsorption capacity	Interaction with moisture
Cyclability	Scalability

Overall, finding materials that maintain their CO<sub>2</sub> capture properties at 25°C, and atmospheric pressure is already challenging, and when other complexities are added, the task of discovering an ideal CO<sub>2</sub> capture material becomes even more complex.



---

## **Chapter II: Motivations and Objectives**

---



---

## 2.1 Motivation

Climate change, caused by continuous CO<sub>2</sub> emissions, is one of the most challenging problems to solve. Although regulations on CO<sub>2</sub> emissions are established in the European Union, such as the progressive increase in the percentage of low-emission vehicles, these measures are still insufficient. Consequently, additional solutions are urgently needed to address the current levels of CO<sub>2</sub> in the atmosphere.<sup>7</sup>

The key motivation of this thesis focuses on developing a material capable of capturing significant quantities of CO<sub>2</sub> and reducing the CO<sub>2</sub> present in the atmosphere, using eco-friendly methods of synthesis. Given this, the present work has been developed within the DIOPMA group in the Department of Materials Science and Physical Chemistry of the Faculty of Chemistry of the Universitat de Barcelona, in collaboration with the Greenova Foundation, as it is an industrial doctorate.

To achieve this, the material needs certain key properties and characteristics, such as high porosity, high specific surface area and tunable functionality, along with high thermal stability and regeneration capacity to increase its service life.

In this context, Metal Organic Frameworks (MOFs) are highly versatile solids that can operate under diverse conditions of temperature and pressure. Among the wide range of MOF's materials, the well-known HKUST-1, after the first synthesis of this material at the Hong Kong University of Science and Technology, demonstrates highly versatile and optimal properties for CO<sub>2</sub> capture compared to other MOFs.<sup>132</sup>

There is a significant variability in CO<sub>2</sub> capture measurements with MOFs, as most studies are conducted at low temperatures and/or high pressures. These conditions are not usual in emission sources like industrial chimneys or vehicle exhausts and highlight the need for research in more practical environments to improve the relevance and effectiveness of CO<sub>2</sub> capture materials.

This research is driven by the need to improve aspects related to sustainability in the synthesis of MOF materials, since the commonly used methods involve the use of eco-toxic solvents like dimethylformamide. Therefore, finding a more sustainable alternative is essential to reduce the ecological footprint of the synthesis process. Closely related to this aspect, with the increasing demand for effective CO<sub>2</sub> capture materials, enhancing the regeneration capability of the material is crucial to make CO<sub>2</sub> capture more cost-effective and sustainable.

Finally, one of the main limitations of porous materials for gas capture is the competition with water vapor during the adsorption process. Water molecules often hinder the adsorption of CO<sub>2</sub> and is present in nearly all environments. This highlights the need to explore how H<sub>2</sub>O molecules influence the CO<sub>2</sub> adsorbent performance of synthesized HKUST-1/GO materials.

---

## 2.2 Objectives

The key goal of this thesis is to synthesize HKUST-1/GO materials and find the optimal combination of HKUST-1 and GO to capture as much CO<sub>2</sub> as possible, aligning with the principles of green chemistry.

As a secondary main objective, the optimization of the synthesis process with an emphasis on sustainable methods is addressed, specifically using mechano-chemical processes through liquid-assisted ball milling. The central goal is to determine the feasibility of this alternative synthetic approach, along with its viability and potential for scalability.

These main objectives generate various secondary targets, such as enhancing the regeneration capacity of HKUST-1 materials for performing adsorption-desorption processes. This approach aims to improve the material's performance through the incorporation of reduced graphene oxide (rGO) into the synthesis of the MOF, taking advantage of rGO's electrical and thermal conductivity, as well as its structural resemblance to GO.

Since water is present in the majority of CO<sub>2</sub> emission sources, another objective is to understand the behavior of the HKUST-1 samples and how the incorporation of GO affects these materials under realistic conditions, such as post-combustion environments with 15% CO<sub>2</sub> and 50% relative humidity (RH). Specifically, this objective includes evaluating the competence between H<sub>2</sub>O and CO<sub>2</sub> molecules in conditions of simultaneous co-adsorption processes for both HKUST-1/GO and pristine HKUST-1 materials, as well as determining whether the incorporation of GO enhances the material's regeneration under these specific conditions.

Another objective related to these aspects is to understand the adsorption kinetics of H<sub>2</sub>O and CO<sub>2</sub> molecules, as well as determine how the incorporation of GO affects the CO<sub>2</sub> adsorption performance and the selectivity during simultaneous adsorption of both molecules.

An additional target is to determine what are the potential adsorption sites of the HKUST-1/GO materials to understand the synergy established between HKUST-1 and GO molecules, as well as the enhanced stability that this combination presents.

Also, under humid conditions it is well-known that HKUST-1 materials change its color. For this reason, another objective is to determine the relationship between the change of color and the adsorption of H<sub>2</sub>O and CO<sub>2</sub> molecules under the exposure of various conditions at different concentrations of RH and CO<sub>2</sub>.

In summary, this research aims to contribute to the development of effective and sustainable solutions to address the issue of CO<sub>2</sub> emissions by synthesizing porous materials, HKUST-1/GO, capable of efficiently capturing these molecules, by utilizing a method of synthesis which is potentially scalable and environmentally friendly.

---

## Chapter III: Synthesis and characterization of HKUST-1/GO composites obtained by Mixed Solvent Method (MSM)

---

### *Summary of the chapter*

*In the following chapter, the procedure and results from synthesizing a series of HKUST-1/GO materials with varying w/w % ratios of HKUST-1 combined with graphene oxide (GO) are exposed. The synthesis followed a mixed solvent method, wherein the reactants are mixed and dissolved in specific solvents within a flask, at a high temperature (373 K) and for a specific reaction time.*

*A comprehensive study has been conducted on the obtained samples, yielding significant information about the material's structure and properties through various characterization techniques. The analysis examines the influence of GO on the resulting samples by exploring the properties and characteristics arising from this combination.*

*Followed by the determination of the principal structural features of the samples, this study proceeds with characterizing the CO<sub>2</sub> adsorption properties, aiming to prove whether the inclusion of GO improves CO<sub>2</sub> capture. Hence, the synergistic relationship between GO and HKUST-1 is analyzed to determine which is the optimal proportion of each component for obtaining maximum CO<sub>2</sub> adsorption.*

*Remarkably, all CO<sub>2</sub> adsorption measurements are conducted at room temperature (298 K) and up to a maximum pressure of 1.13 atm to replicate current atmospheric conditions as closely as possible, whereas in many publications, these measurements are commonly performed at lower temperatures (around 273 K). The results indicate a discernible enhancement in CO<sub>2</sub> capture in certain samples, specifically within a GO concentration range of 0.25-0.75 w/w % of the theoretical GO added during*

synthesis. Furthermore,  $N_2$  adsorption measurements yield insights into specific surface area, facilitating the establishment of a relationship between  $CO_2$  adsorption and the exposed surface area.

A detailed experimental procedure is presented, describing the quantification of GO in the synthesized samples and named here as Reverse Quantification. This aspect holds particular importance, as the main literature often describes the features and emergent properties of the resulting material without focusing on precisely determining the actual remaining percentage of GO within the final sample structure, precluding that theoretical remains with a 100% performance. Consequently, after an extensive literature review, discrepancies in reported values among various articles may arise due to variations in the quantities of GO used, potentially leading to descriptions of  $CO_2$  capture processes with probably different GO proportions under the same nomenclature. Therefore, the subsequent chapter aims to detail the methodology employed in this study, which discerns the actual (experimental) concentration of GO incorporated within the synthesized HKUST-1 samples. The results indicate that enhanced  $CO_2$  adsorption properties are achieved at experimental GO concentrations of 0.25 w/w %, compared to pristine HKUST-1.

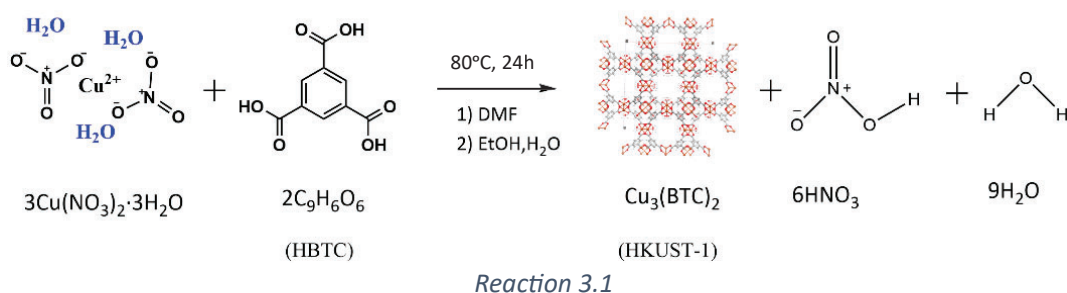
Finally, the methodology for obtaining  $CO_2/N_2$  selectivity data is illustrated. The process utilized to obtain selectivity values is described using the calculations of the ideal adsorbed solution theory (IAST). The outcomes align with those of  $CO_2$  adsorption and specific surface area, with the most selective samples exhibiting higher selectivity at increased working pressures, synthesized within the theoretical 0.25-0.75 w/w % GO concentration range.

### 3.1 Mixed solvent method synthesis

#### HKUST-1

For the synthesis of HKUST-1 (also called  $\text{Cu}_3(\text{BTC})_2$ ), Mixed Solvent Method (MSM) was employed.<sup>46</sup> Thus, the procedure followed the next steps. First, 0.6 g of copper (II) nitrate 2.5-hydrate ( $\text{Cu}(\text{NO}_3)_2 \cdot 2.5\text{H}_2\text{O}$ ) and 0.3 g of ligand 1,3,5-benzene tricarboxylic acid ( $\text{H}_3\text{BTC}$ ) were solved in 15 mL of dimethylformamide (DMF) vigorously stirring and sonicating for 5 min. Then, 5 mL of EtOH were added to this solution and further stirred and sonicated again for 5 min. 15 mL of De-ionised (DI) water was added to the mother solution, and sonicated for 5 min. The whole solution was immediately transferred to a 50 mL balloon and stirred for 24 h at 80 °C under reflux. After filtering and washing the product with  $\text{CH}_3\text{Cl}$  (3 times with 40 mL), the product was dried under vacuum at 170 °C overnight.

The reaction that took place is the following (Reaction 3.1):



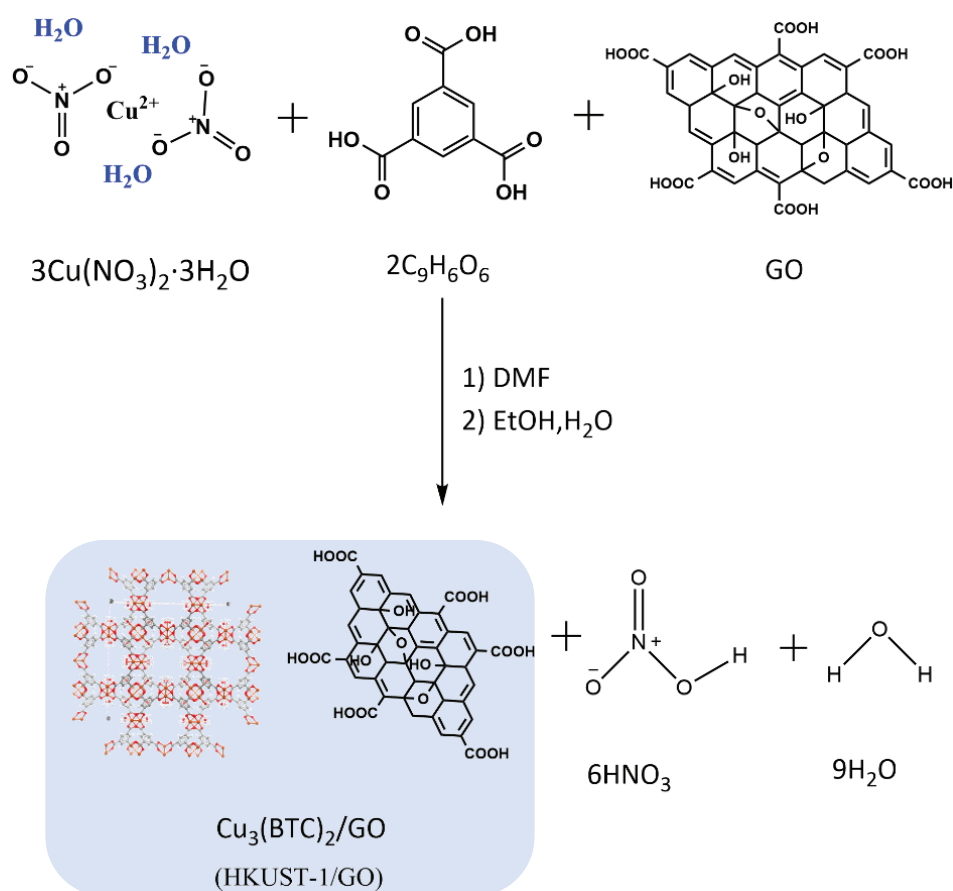
#### HKUST-1/GO

The samples of HKUST-1 combined with Graphene Oxide (GO) followed the same procedure described above, but instead of adding only DI water, DI water with a dispersion of GO was added. Samples were obtained by adding different amounts of GO ranging between 0.15 and 9% of GO. From this point forward, the MOF HKUST-1 will be referred to as HK, and samples containing GO will be labelled as HK-X, with X representing the amount of GO used in the synthesis, as indicated in the nomenclature of Table 3.1.

Table 3.1. Nomenclature of HKUST-1/GO synthesis.

Nomenclature	Theoretical % GO	Nomenclature	Theoretical % GO
HK	0	HK-1	1.0
HK-0.15	0.15	HK-2.5	2.5
HK-0.25	0.25	HK-5	5.0
HK-0.5	0.50	HK-9	9.0
HK-0.75	0.75		

In this case, the reaction that takes place is the following (Reaction 3.2):



Reaction 3.2

In this context, the main difference between both syntheses lies in the addition of GO. While in the synthesis of pure HKUST-1, a few milliliters of DI water are added, in this synthesis the water is added with a GO suspension, along with DMF and EtOH. This stage is necessary because adding the GO agglomerated powder in the reactant mixture doesn't promote the incorporation of GO in the HKUST-1 structure and may

conduct two separated phases. A forced de-agglomeration of the GO powder is carried out through sonication, followed by the immediate addition of this suspension to the synthesis reaction along with the rest of the solvents, following the same steps as in the synthesis of HKUST-1. In this study, samples of HKUST-1/GO were conducted with different proportions of GO, obtaining a final product with a yield of approximately 90%, with around 0.5 g/sample.

The illustrative steps of the procedure are shown in the figures (Figure 3.1 (a-h)). The reaction takes place using a round-bottom flask where the reactants are mixed and a cooling column is employed (Figure 3.1 (a), (b), (e) and (f)). Then, the sample is vacuum filtered using a Büchner flask (Figure 3.1 (c), (g)) and subsequently dried in a vacuum oven (activation step). A blue turquoise bright color is obtained from the HK sample (Figure 3.1 (d)). However, when adding GO the samples become darker according to the percentage of theoretical GO (Figure 3.1 (h)).

Additionally, another aspect to take into account is the color changing of the final material, where it drastically changes color from light blue turquoise to dark blue once the activation process is completed using vacuum and a temperature of 170°C overnight (Figure 3.2 (a) and (b)). This phenomenon occurs because when the samples are activated, they expel the remnants of solvents present within their pores (such as water, ethanol, or DMF). It is observed that this change is primarily due to water molecules, as the longer the activated samples remain in contact with the atmosphere, the lighter their color becomes (Figure 3.2 (c)). This fact is primarily due to the relative humidity of the environment, where despite expelling solvent molecules after the activation process, the sample is capable of inherently adsorbing water molecules present in the atmosphere.

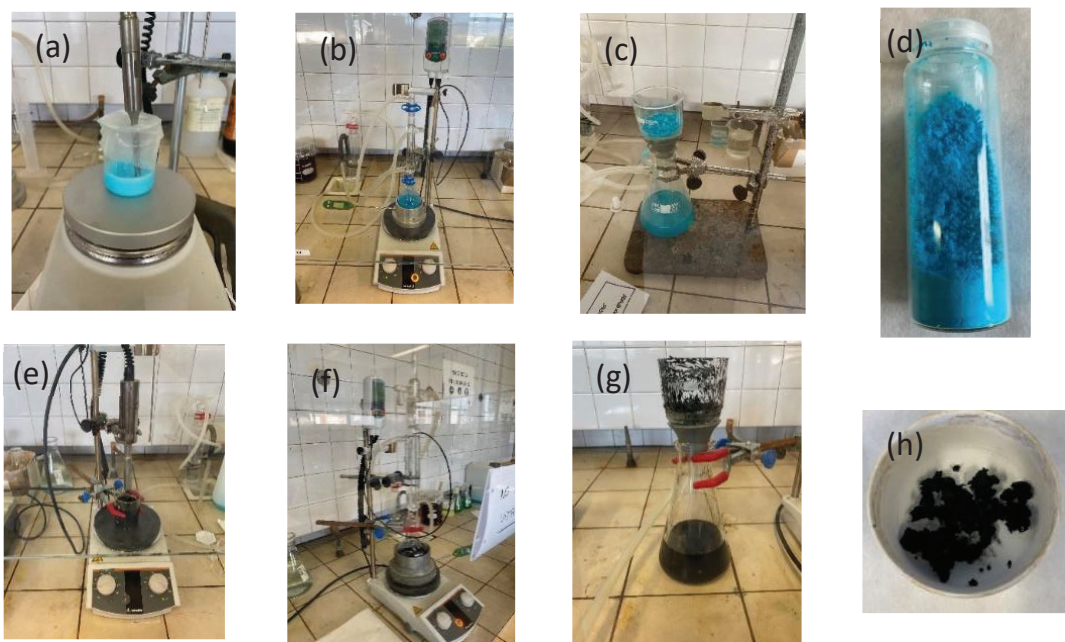


Figure 3.1. Experimental procedure of MSM synthesis for (a-d) HK and (e-h) HK-GO samples.

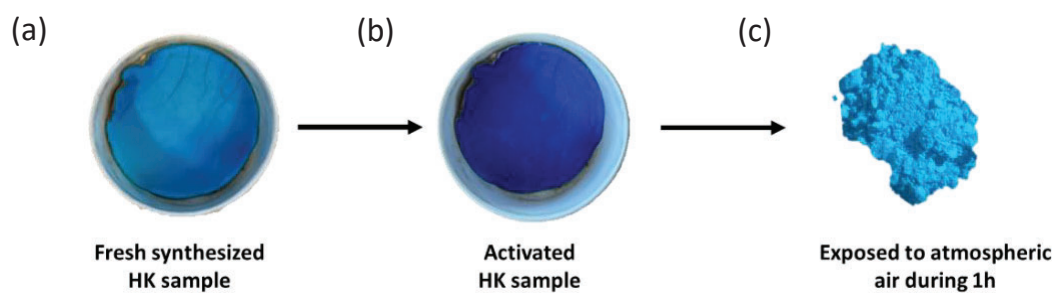


Figure 3.2. Changing color of HK samples in different state of activation.

### **3.2 Materials characterization and performance for samples obtained via MSM**

The following sections provide the results of the characterization of HK-GO samples synthesized with different percentages of GO, specifically between 0.15 and 9% GO. The samples were characterized to determine the correct formation of the HK and to analyze the incorporation of GO.

Additionally, a special focus is on the CO<sub>2</sub> adsorption performance of the samples, along with surface properties and the calculation of the selectivity of all the samples.

Finally, a new experimental procedure for determining the experimental GO is developed during this research and presented in *Section 3.2.7*. This procedure is named in this study as Reverse Quantification (RQ).

### 3.2.1 Elemental analysis

Elemental Analysis (EA) was employed to assess the chemical formula of HK material composition, and the analysis was carried out using NCHS Analyzer EA-1108 Fisons Instruments equipment.

The results indicate that the sample contained nitrogen atoms, obtaining the formula  $\text{Cu}_3(\text{C}_3\text{H}_3\text{O}_2)_9\text{N}_3$  (Table 3.2a). This chemical formula differs from the citation of the bibliography, which indicates  $\text{Cu}_3(\text{C}_9\text{H}_3\text{O}_6)_2 \cdot (\text{H}_2\text{O})_6$ .<sup>133</sup> However, according to the references and the synthetic procedure described, HK usually contains traces of the solvents used in the synthesis and, in this case, DMF is added to the reaction providing nitrogen atoms to the structure. Consequently, if nitrogen atoms are negligible, the molecular formula is approximated to  $\text{Cu}_3(\text{C}_9\text{H}_3\text{O}_7)_2 \cdot 2\text{H}_2\text{O}$  (Table 3.2b), which is very close to what is usually observed in the publications that describe HK using solvothermal and mixed solvent methods.<sup>134,135</sup>

Table 3.2. Elemental Analysis of HK sample.

<b>Mass sample</b>	0.01 g	Extracting DMF molecules	
%N	4.8		
%C	36.7	%C	24.4
%H	3.6	%H	1.2
%O	33.9	%O	28.5
<b>a) Estimated formula</b>		<b>b) Estimated formula</b>	
$\text{Cu}_3(\text{C}_3\text{H}_3\text{O}_2)_9\text{N}_3$		$\text{Cu}_3(\text{C}_9\text{H}_3\text{O}_7)_2 \cdot 2\text{H}_2\text{O}$	

EA was exclusively conducted on HK samples, excluding HK-GO due to interference from the presence of GO, which invalidates the precise determination of the chemical formula. HK is a three-dimensional molecule rich in carbon, oxygen, and hydrogen bonds, in addition to copper atoms. In contrast, GO also comprises carbon, hydrogen,

and oxygen atoms. The primary distinction lies in the copper content, which is challenging to correlate precisely with a specific organic percentage. Furthermore, the composition of the organic and inorganic components can vary depending on the sample. Consequently, this analysis enabled the verification of the structural integrity of the as-synthesized HK sample.

### 3.2.2 X-ray-diffraction, infrared spectroscopy and Raman spectroscopy

Once the obtention of HK and HK-GO materials is achieved, X-Ray diffraction is performed in all the samples to ensure the correct formation of the crystalline structure. The interpretation of all the XRD diffractograms followed the similitudes with the pattern. Specifically, HKUST-1 material has not any standard reference since the structural determination of the material is not found in the literature. Hence, all the synthesized samples present a XRD diffractogram that coincides with the pattern obtained from the publication of Yakovenko et al., which follows the pattern indicated in Figure 3.3.

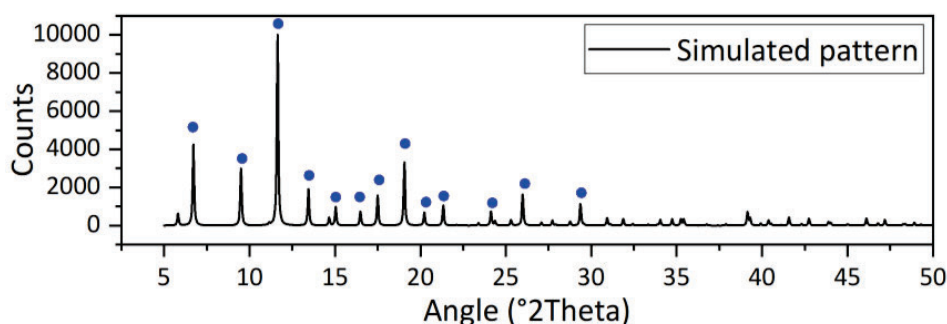


Figure 3.3. Simulated XRD pattern of HKUST-1.

The results showed that all the samples have almost the same peak displacements according to the simulated HK pattern<sup>136</sup> (Figure 3.4). The resulting intense sharp peaks located at 6.7, 9.5, 11.6, 13.4, 14.7, 15, 16.5, 17.5, 19, 26 and 29.4° are consistent with the pattern displacement peaks and suggest that the HK crystalline structure is retained. Thus, based on the XRD diffractograms, the addition of GO doesn't significantly alter the crystalline structure of HK. A secondary peak is

observed at  $5.8^\circ$ , for samples with GO content less than 0.75 displaying variability across different samples. It is suspected that moisture could influence the crystalline structure, leading to alterations in the intensity of specific peaks, including the one mentioned. Nevertheless, additional research focused on this effect is analyzed to confirm this hypothesis in the following sections (See Chapter IV, Section 4.2.3).

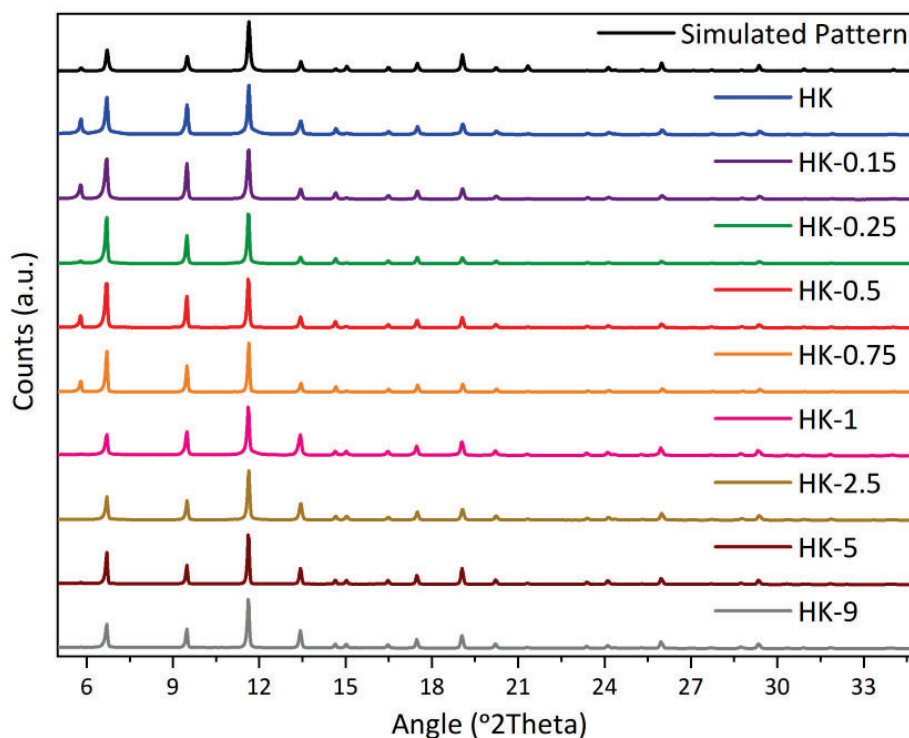


Figure 3.4. XRD diffractograms of HK simulated pattern and the synthesized HK-GO samples, from 0 to 9 w/w % of GO added following the nomenclature of Table 3.1.

On the other hand, Attenuated Total Reflectance Fourier Transform Infrared Spectroscopy (ATR-FTIR) was carried out to determine the chemical bonds and functional groups of samples. The equipment used for all the measurements was PerkinElmer FT IR Spectrometer Spectrum Two and the obtained spectra was compared with some vibrational bands described in the literature of HKUST-1 materials concerning -OH, -COOH, -C=O, -CH  $sp^2$  and -CH  $sp^3$  benzene ring vibration bands.

Figure 3.5 shows three different spectra: the IR spectra of the pristine HK, the spectrum of the corresponding GO and, as an example, the spectrum of one synthesized sample combined with GO, in this case HK-5.

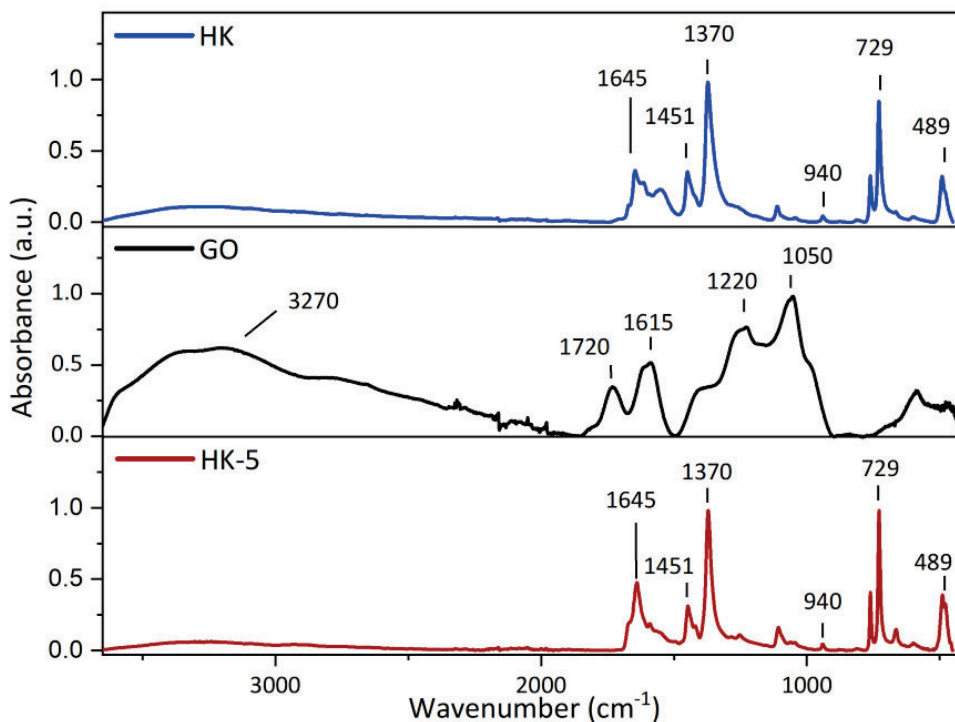


Figure 3.5. Infrared spectra of HK, GO and HK-5 samples; respectively.

In close agreement with the literature, the spectra of HK and HK-5 show vibration bands between 489 and 940  $\text{cm}^{-1}$ , assigned to the vibrations out-of-plane attributed to the BTC benzene ring. Bands at 1370-1450  $\text{cm}^{-1}$  are attributed to the symmetric stretching vibrations of carboxylate, even as bands in the range of 1585-1645  $\text{cm}^{-1}$  are due to the asymmetric stretching vibration of carboxylate.<sup>45,46</sup> As can be seen, HK and HK-5 spectra remain almost the same with similar peak displacements. On the other hand, GO spectrum shows bands at 1050 and 1220  $\text{cm}^{-1}$  attributed to C-O and C-OH bonds. The band at 1615  $\text{cm}^{-1}$  is related to C=C bond vibrations and at 1720  $\text{cm}^{-1}$  is related to carboxylate and ketone groups. Also, it is possible to distinguish a broad band situated at 3270  $\text{cm}^{-1}$  attributed to the -OH groups.<sup>137</sup> GO bands are not entirely detected on the HK-GO spectra, probably due to the low concentrations

contained in the sample. Although HK-GO samples contain GO in different proportions, the spectra obtained of all the samples are almost the same as the pristine HK.

As a summary, the following table shows the most relevant peaks observed in the IR spectra related to HK, HK-GO and GO samples, indicating the corresponding position of the spectra and the assignment of each band (Table 3.3).

Table 3.3. Peak assignments of HK, HK-GO and GO samples.

Sample	Peak	Assignment
HK and HK-GO	1585-1645 $\text{cm}^{-1}$	Asymmetric stretching ( $-\text{COO}^-$ )
	1370-1450 $\text{cm}^{-1}$	Symmetric stretching ( $-\text{COO}^-$ )
	489 - 940 $\text{cm}^{-1}$	Out-of plane (benzene ring)
GO	3200-3600 $\text{cm}^{-1}$	Hydroxyl groups ( $-\text{OH}$ )
	1700-1750 $\text{cm}^{-1}$ and 1580-1620 $\text{cm}^{-1}$	Carboxylic groups ( $-\text{COOH}$ )
	1050-1250 $\text{cm}^{-1}$	Epoxy groups ( $-\text{O}-$ )
	580 $\text{cm}^{-1}$	Epoxy groups ( $\text{C}-\text{O}$ )

Raman Spectroscopy was also performed, using a dispersive spectrometer Jobin-Yvon LabRam HR 800, coupled to an optical microscope Olympus BXFM. In this case, the measurements were conducted to determine the crystallinity of the synthesized HK-GO materials through molecular vibrations, rotations and low energy modes.

The analysis performed reveals a high level of crystallinity since the peaks observed are intense and defined, as indicated in Figure 3.6. Regarding pristine HK, distinct peaks are observed such as the Cu (II) core vibrations, detected in the region between 500 and 77  $\text{cm}^{-1}$ , the peaks at 825 and 743 attributed to O-C-O bonds: the carboxylic group vibrations at 1466 and 1110  $\text{cm}^{-1}$  and the benzene ring modes at 1615 and 1550  $\text{cm}^{-1}$ .

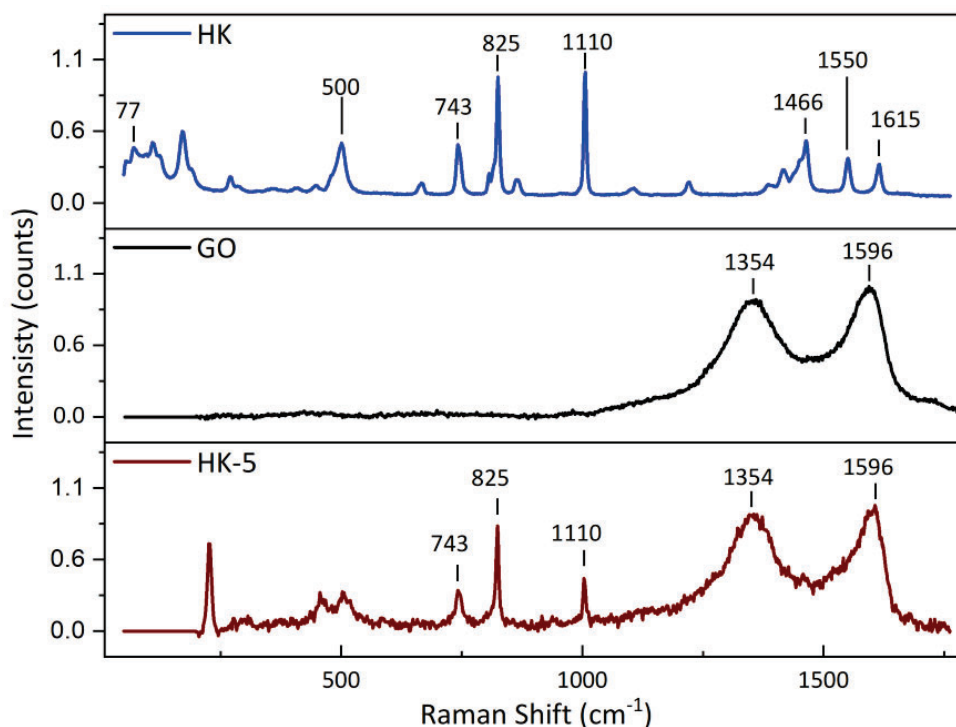


Figure 3.6. Raman spectra of HK, GO and HK-5 samples; respectively.

Concerning GO sample, the Raman spectrum suggests two broad bands at 1354 and 1596  $\text{cm}^{-1}$  with similar intensity values. The first one is assigned to the defects and the lattice distortion, and large amounts of  $\text{sp}^3$ -like defects caused by the oxidation process. The latter is attributed to the out-of-plane breathing mode of  $\text{sp}^2$  hybridized C-C bonds.

When analyzing the Raman spectrum of HK-GO samples, in contrast to IR spectra, the presence of GO is more evident even with the incorporation of small amount. As an example, the Raman spectrum of HK-5 is depicted at the bottom of the Figure 3.6. Similar peak shifts are observed compared with the pristine HK but showing the broad signal between 1400 and 1600  $\text{cm}^{-1}$ , indicating the presence of the GO vibration modes. Between 77-500  $\text{cm}^{-1}$  HK-5 presents some peak variations, as in the case of the peak at 77  $\text{cm}^{-1}$ , when compared with pristine HK, suggesting differences related to the Cu-core vibrations.<sup>125</sup>

### 3.2.3 Thermogravimetry analysis

Thermogravimetry measurements were conducted, in the first instance, to determine the thermal stability of the as-synthesized samples and determine the differences between HK and HK-GO samples. Moreover, experiments were also performed to assess whether it was feasible the possibility of quantifying experimental GO retained in the structures of HK-GO. The equipment utilized to perform the analyses was TA Instruments SDT-Q600 Simultaneous TGA/DSC and the experiments were conducted in nitrogen atmosphere at a flow rate of  $50 \text{ mL min}^{-1}$ , using around 5 mg of sample. To obtain the weight loss curves, the sample was heated from 25 to  $1000 \text{ }^\circ\text{C}$  with a ramping rate of  $10 \text{ K min}^{-1}$ .

The results of the thermogravimetries performed to HK samples and to HK-5 samples, as an example of HK-GO samples, are depicted in the diagram of the Figure 3.7. Although the other HK-GO samples are not represented, their thermal stability is similar to that of the example provided.

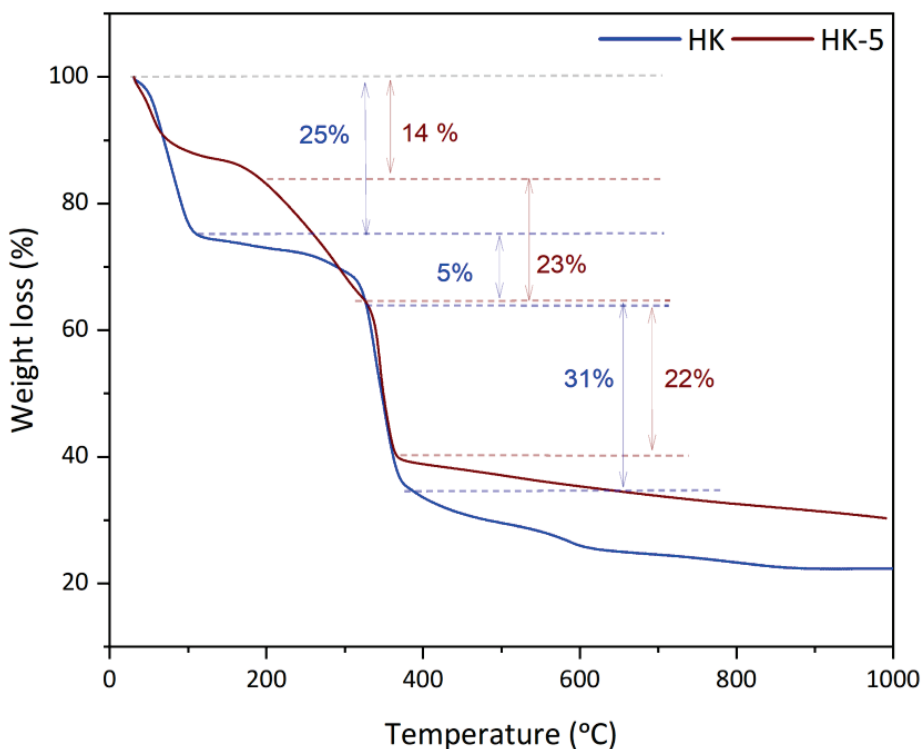
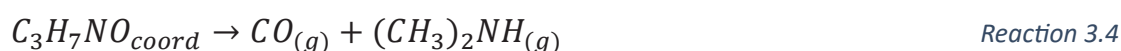


Figure 3.7. Thermogravimetric analysis of HK and HK-5 samples, measured in  $\text{N}_2$  atmosphere.

Therefore, the results indicate that the samples undergo thermal degradation in three steps:

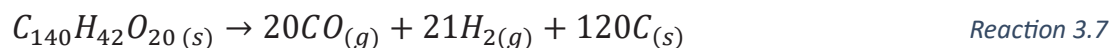
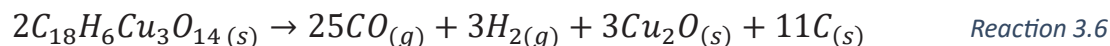
1. **Solvent removal:** The desorption of solvents trapped inside the pores, which occurs around 100°C and is represented by 25% weight loss for HK and 14% for HK-5. This process can be approximated by Reaction 3.3 (water evaporation) and Reaction 3.4 (DMF evaporation):



2. **Degradation of the functional groups:** The functional groups of the surface degraded and result in a weight loss of 5% for HK and 23% for HK-5 at around 200°C and until 300°C approximately. This process can be described by an estimated decomposition reaction, as indicated in Reaction 3.5, where  $R$  is the HK or HK-5 and  $-OH$  is the hydroxyl group, as an example. In this step, probably some traces of DMF solvent can be evaporated as well, as the boiling point of this solvent is 153°C.



3. **Decomposition of the carbon skeleton:** The final stage corresponds to the degradation of the carbon framework, which represents 31% for HK and 22% for HK-5 and occurs at around 300°C. This process results in solid  $Cu_2O$  molecules and residual C atoms. However, the mass loss does not stabilize completely and continues decreasing even at 1000°C, indicating ongoing degradation. The approximate reactions of HK and GO molecules decomposition are indicated in Reaction 3.6 (HK) and Reaction 3.7 (GO):



Considering the stoichiometric calculations and the percentage attributable to the removal of solvents in each sample, the final percentage of solid obtained in HK-GO samples is always higher than in the case of HK because of the presence of copper oxide and the remaining carbon atoms that persist at the end of the sample degradation. Although the weight of the samples analyzed is almost the same across all the thermal experiments, GO percentage tends to decompose in carbon atoms at high temperatures, which increases the proportion of solids at the end of the experiment.

Thus, the possibility of determining the quantity of GO incorporated into the samples is also investigated. However, although having good precision and resolution of the resulting diagram, the findings showed that there is not a stable weight composition at high temperatures since it is continuously losing weight. Moreover, when small quantities of GO are analyzed (like in the case of the HK samples in the range of 0.15-2.5) it is a challenge to assume that any difference in weight loss is attributed to GO. An additional challenge arises from the difficulty in obtaining identical MOFs with the same chemical structure across different samples, as both HK and GO contain organic components that degrade within a similar temperature range, leading to decomposition into carbon at high temperatures ( $C_{(s)}$ , indicated in Reaction 3.6 and Reaction 3.7).

Afterwards, a second thermogravimetric experiment was running out, but in this case using synthetic air (20%  $O_2$ , 80%  $N_2$ ) to ensure that the final weight remaining is only  $CuO(s)$  and to determine more precisely the experimental GO incorporated in the structure. The experiment was performed in all the samples, but as HK-GO samples

show similar thermal stability in all cases, Figure 3.8 indicates the thermogravimetry of HK and HK-5 as an example.

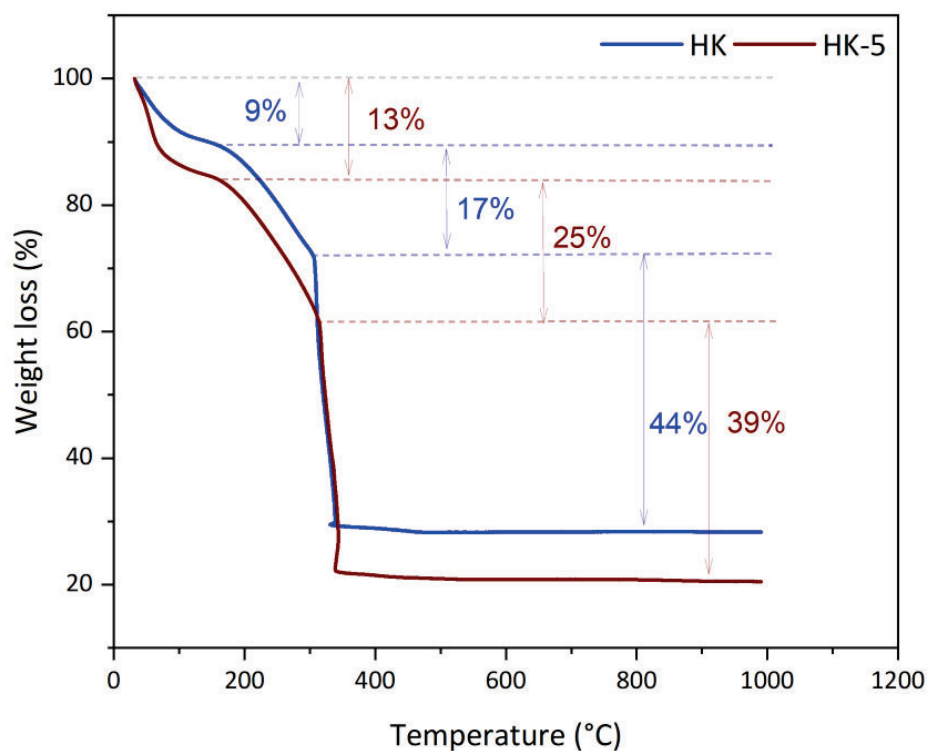
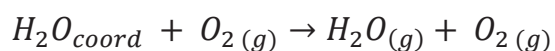


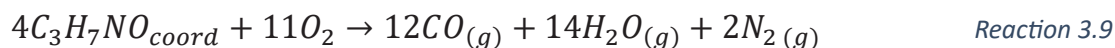
Figure 3.8. Thermogravimetric analysis of HK and HK-5 samples measured using air atmosphere.

As a result, the thermal stability of the samples is also illustrated in three steps, following the same pattern of evaporation of solvents and thermal degradation of the observed experiments using  $N_2$ . However, weight loss and the suspected reactions that occur during the thermogravimetric analysis are not the same:

1. **Solvent removal:** The initial weight loss attributed to the removal of the solvent is, in this case, approximately 9 % for HK and 13 % for HK-5 and occurs at around 100 °C. The approximate reactions are indicated in Reaction 3.8 (water evaporation) and Reaction 3.9 (DMF evaporation).



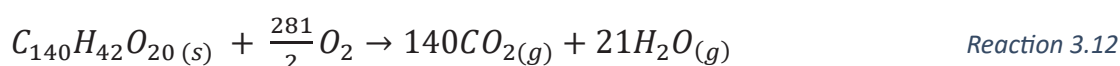
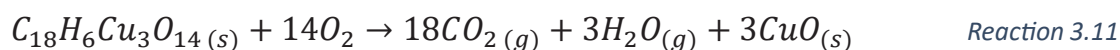
Reaction 3.8



2. **Degradation of the functional groups:** The subsequent weight loss, 17 % for HK and 25 % for HK-0.25, is linked to the residual DMF within the internal pores of the structure and the decomposition of surface functional groups (from 200 °C to 300 °C, approximately). In this case, the reactions that take place in the presence of oxygen are also slightly different than the decompositions observed with N<sub>2</sub> atmosphere. An example of hydroxyl degradation is Reaction 3.10 where -OH is oxidized to carboxylic acid. The state of these residual products could be an intermediate of solid.



3. **Decomposition of the carbon skeleton:** Beyond 300°C, a third weight loss is evident, attributed to the decomposition of the organic carbon skeleton of the compound, accounting for about 44 % in HK and 39 % in HK-5. No significant weight loss is observed at temperatures between 500 °C and 1000 °C, suggesting only the presence of CuO. In this case, an approximation of the reactions that occur during the decomposition of the carbon framework of HK and GO are illustrated in Reaction 3.11 (HK) and Reaction 3.12 (GO).



Therefore, knowing the initial weight of the sample, the weight of solvents in the structure, the weight of CuO remaining after the analysis and the reaction that occurs (Reaction 3.11), quantifying an approximate amount of GO incorporated in each

sample is studied. However, although stabilization of the weight loss is achieved in the third step of degradation, this methodology is not entirely accurate for similar reasons as in the case of thermogravimetry using N<sub>2</sub> atmosphere, since each sample contains different quantities of solvents retained in the structure and it's not entirely clear the point at which each solvent is released, specifically DMF which can be removed with the superficial functional groups of GO and HK. Nevertheless, the results of samples that contain higher contents of w/w % GO indicate higher differences in the final weight compared to pristine HK, as in the case of HK-9. Specifically, HK shows a higher remaining weight of the sample at the end of the experiment since there's more residual CuO. Compared to HK-9, there's a difference of approximately 8% which is very close to those 9 w/w % of GO. Consequently, the addition of GO implies that the weight loss of the sample during thermal degradation at high temperatures is higher for HK-9 than for pristine HK (since GO is completely degraded into CO<sub>2</sub> (g) and O<sub>2</sub> (g) molecules, as indicated in Reaction 3.12) .

In summary, while TGA analysis is useful for estimating the amount of GO retained in HK, further testing and analysis are required to accurately determine the actual quantity incorporated. This is due to challenges such as variations in solvent evaporation between samples and the difficulty of obtaining two identical HK frameworks with the same chemical composition, which hinder precise GO quantification and limit it to an approximation. Additionally, when the GO content is very low, the small differences observed may result from these factors rather than actual variations in GO incorporation.

### **3.2.4 Scanning electron microscopy**

Scanning Electron Microscopy (SEM) was performed to examine the morphologies and surface characteristics of the synthesized sample, using a JEOL JSM-7001F microscope. Although all the synthesized samples were analyzed, the following page displays as a representative example the SEM images of HK, HK-0.50, HK-0.75 and

HK-9, where it is possible to distinguish some features with respect to the particle size, degree of agglomeration and surface defects.

The outcomes are illustrated in Figure 3.9.

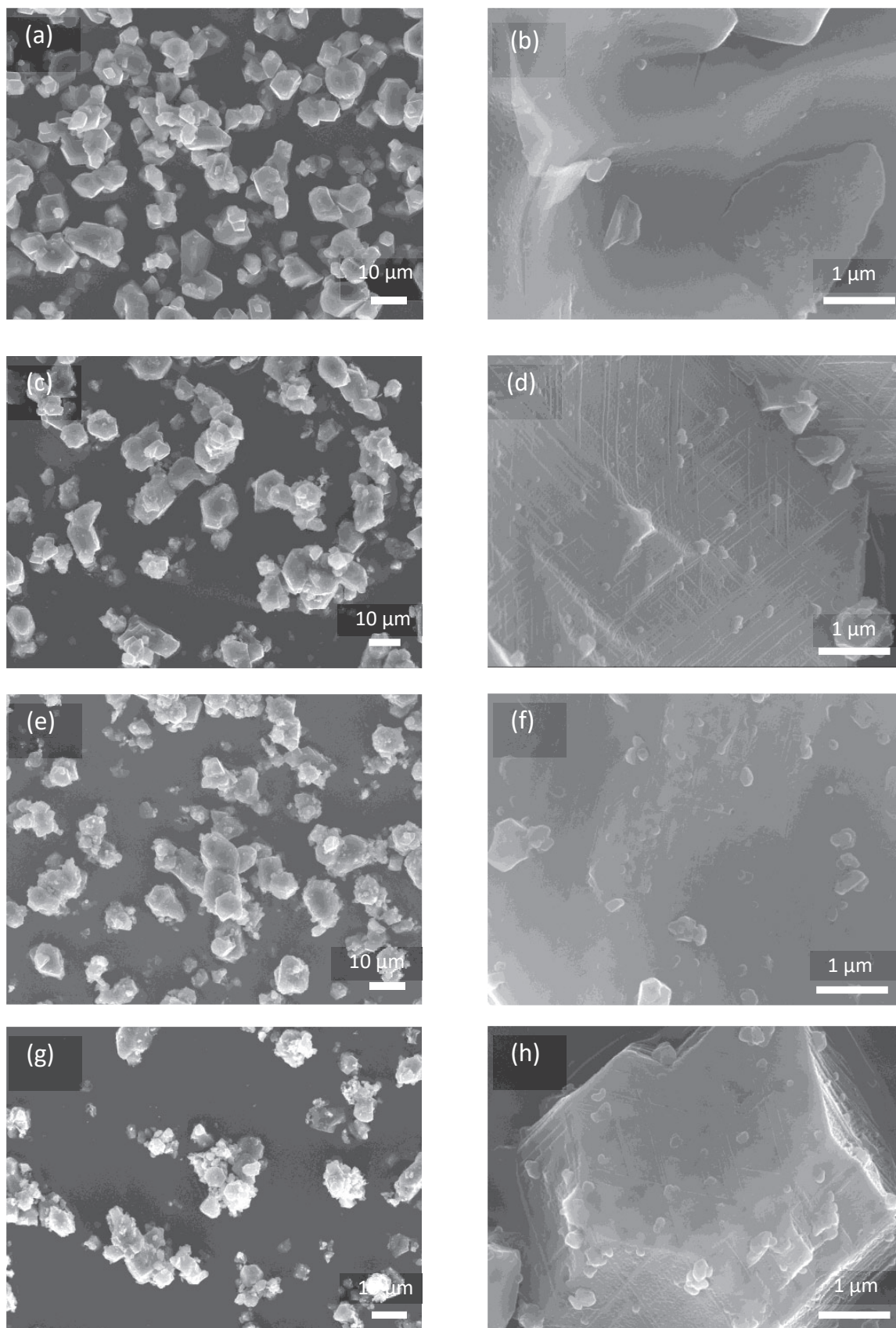


Figure 3.9. SEM images of (a-b) HK, (c-d) HK-0.75, (e-f) HK-0.5, (g-h) HK-9.

Regarding sample HK, the images indicate a crystal geometry close to octahedral, with flat and smooth MOF crystal faces and small formation of crystals (Figure 3.9 (a) and (b)). In the case of HK-GO samples (Figure 3.9 (c-h)), the morphology of the MOF crystal faces changes, leading to the emergence of some imperfections and an increase in surface irregularities. A line hatching appears and is repeated throughout the external crystal structure, forming a surface network of defects (Figure 3.9 (d), (f) and (h)). It is suspected that the defects observed on the surface of the crystals are the cause of the synergistic effect of GO on HK in terms of specific surface area and CO<sub>2</sub> adsorption. This pattern can be observed in all the synthesized HK-GO samples.

Another observation is that although crystals are dispersed similarly in all cases, samples which contain GO seem to be slightly more agglomerated than the pristine HK. This can be easily detected in the sample which contains a higher content of GO (HK-9, Figure 3.9(g) and (h)), which suggests that the addition of GO into the synthesis of HK samples produces a higher level of agglomerated particles.

Additionally, one of the main differences between the HK and the HK-GO samples is the formation of small MOF crystals, especially on the surface filled with this type of defect. Unlike the HK-GO samples, HK crystal only maintains its flat faces. Clearly, in the HK-GO samples, the growth of new MOF crystals is increased on the surface of the MOF faces with defects. Consequently, SEM images reveal that the combination of GO with HK structures facilitates the nucleation and growth of new HK crystals. GO multilayer stacking mechanism is described in the literature: as the concentration of GO increases, the GO layers contract and the space between them decreases.<sup>114</sup> Thus, this could support the explanation that the addition of GO is beneficial only in small concentrations since its incorporation helps the growth of new MOF crystals and the generation of new surface defects. However, large quantities of GO lead to an agglomeration that prevents potential adsorption gaps from becoming free.

### 3.2.5 Particle size measurements

In addition to assessing morphology and defects, particle size was measured using Dynamic Light Scattering (DLS) through Beckman Coulter LS 13 320 equipment. The measurements were performed to compare the different sizes obtained from all the samples.

All the samples showed almost the same result: the distribution of particle size delivered in the range of 0.4-1  $\mu\text{m}$ , with a maximum peak around 0.6  $\mu\text{m}$  with some aggrupation of nanometric crystals and consistent with the SEM images previously analyzed. The following picture shows the particle size distribution of all the samples measured by % of number (Figure 3.10).

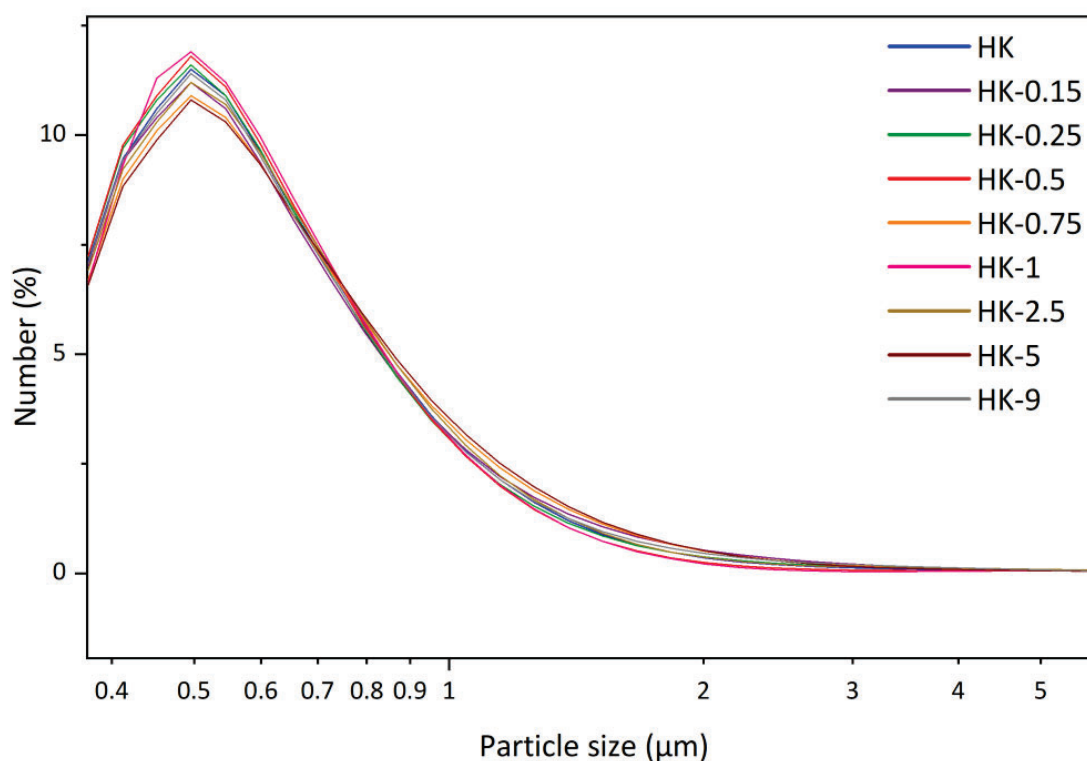


Figure 3.10. Particle size distribution by number for HK-GO samples.

Analyzing the statistical data, particle diameters comprising the bottom 10% of the entire sample ( $d_{10}$ ) are around 0.425  $\mu\text{m}$ , those constituting the bottom 50% ( $d_{50}$ ) are

around 0.6  $\mu\text{m}$ , and those constituting the bottom 90% ( $d_{90}$ ) are around 1  $\mu\text{m}$  (Table 3.4).

Table 3.4. Particle size distribution of HK-GO samples ( $d_{10}$ ,  $d_{50}$  and  $d_{90}$ ).

Sample	$d_{10}$	$d_{50}$	$d_{90}$	Sample	$d_{10}$	$d_{50}$	$d_{90}$
HK	423	586	1027	HK-1	424	593	1031
HK-0.15	426	605	1162	HK-2.5	425	596	1067
HK-0.25	424	594	1162	HK-5	424	598	1068
HK-0.50	422	581	1009	HK-9	424	598	1094
HK-0.75	425	604	1118				

### 3.2.6 Gas sorption measurements and surface properties

Many studies focus on measuring  $\text{CO}_2$  capture capacity under extreme conditions of pressure and/or temperature<sup>120,127</sup> which can be challenging to replicate in real systems operating at ambient temperature and pressure. In this work, the initial measurement conditions on all the samples were specifically chosen at 25 °C and up to 1000 mmHg aiming to closely replicate typical atmospheric conditions.

On the other hand, BET (Brunauer, Emmett and Teller) theory is commonly used to evaluate the gas adsorption data and generate a specific surface area. Here, it was performed to observe how the incorporation of GO into the HK samples affects the specific surface area and the  $\text{CO}_2$  adsorption properties.

#### **$\text{CO}_2$ adsorption isotherms**

$\text{CO}_2$  isotherms were performed to analyze the adsorptive behavior of all the samples and the equipment used to obtain the data was Micromeritics Tristar 3000. The  $\text{CO}_2$  adsorption isotherms of all the samples are depicted in Figure 3.11, along with the  $\text{CO}_2$  adsorption isotherm of GO.

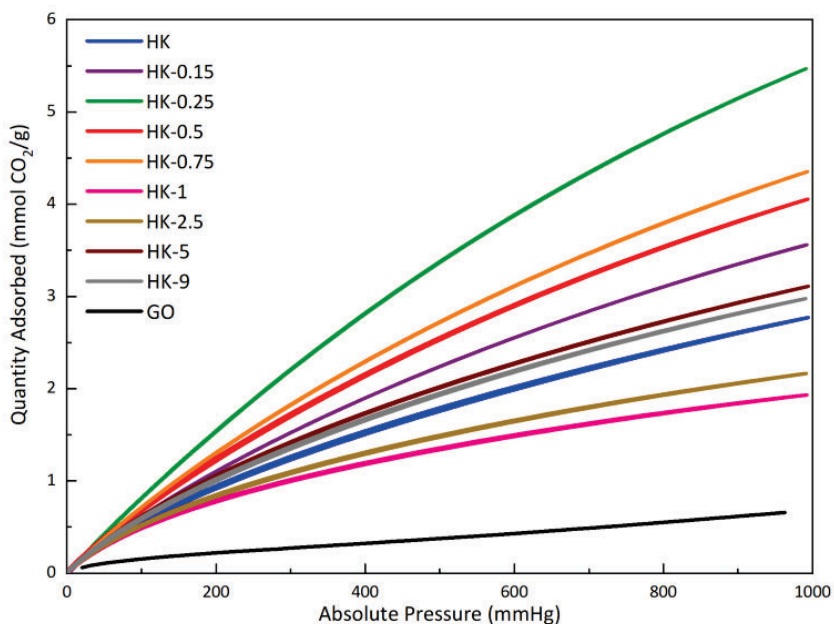


Figure 3.11.  $\text{CO}_2$  isotherms of HK-GO samples and GO sample, tested at 298 K and until 1000 mmHg.

Herein, the isotherms present that samples with less percentage of GO, specifically in the range 0.25-0.75 w/w %, are the samples which capture higher amounts of  $\text{CO}_2$ . When GO content is below and above this range, the results indicate that  $\text{CO}_2$  adsorption is lower. Moreover, it is noted that the  $\text{CO}_2$  adsorption performance of the pristine GO powder presents the lowest uptake values compared to the synthesized samples. Therefore, following the results obtained by different batches, the sample with a GO content of 0.25 w/w % is the one that captures the greatest amount of  $\text{CO}_2$  ( $5.33 \pm 0.16$  mmol  $\text{CO}_2/\text{g}$  sample), followed by 0.5 w/w % ( $4.42 \pm 0.44$  mmol  $\text{CO}_2/\text{g}$  sample) and 0.75 w/w % ( $4.17 \pm 0.24$  mmol  $\text{CO}_2/\text{g}$  sample) at 1000 mmHg and 25 °C. These values are the highest adsorption values found in literature tested in similar conditions.<sup>46,53</sup> Concerning the results, there is an adsorption increase of 80% for the HK-0.25 sample, 49% for HK-0.5 and 41% for HK-0.75 in comparison with the  $\text{CO}_2$  performance of the pristine HK. So, these results prove that due to the synergy of the two combined components, HK and GO, it is

possible to improve CO<sub>2</sub> adsorption, but only in a specific range of GO using small concentrations.

### **Selectivity**

In the case of CO<sub>2</sub> capture from atmospheric air, the composition of other gases present in the atmosphere is mainly N<sub>2</sub> (78%), O<sub>2</sub> (21%), Ar (0.93%), and CO<sub>2</sub> (0.04%).<sup>138</sup> For this reason, understanding the selectivity of the adsorption performance is crucial. However, this factor would be less critical if the capture were conducted in areas with higher CO<sub>2</sub> concentrations, such as industrial chimneys, for example.

Hence, the main competence in terms of CO<sub>2</sub> adsorption (considering Direct Air Capture from atmospheric air) is N<sub>2</sub> molecules. To assess which level of competition is between both molecules, selectivity calculations were carried out and N<sub>2</sub> adsorption isotherms were also measured using the same conditions as with CO<sub>2</sub> (25 °C and 1100 mmHg). Similarly, like CO<sub>2</sub> isotherms, the samples with more N<sub>2</sub> adsorption capacity were HK-0.25, HK-0.5 and HK-0.75 (Figure 3.12).

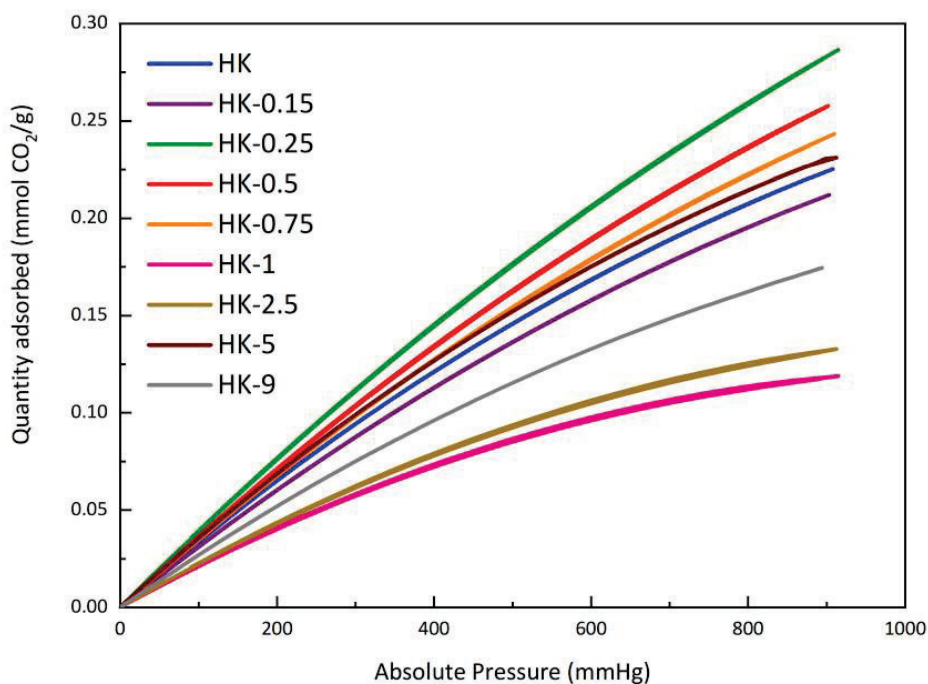


Figure 3.12.  $N_2$  isotherms of HK-GO samples, tested at 298 K and until 1000 mmHg.

Generally, selectivity is a parameter that can be calculated using different methods. In this study, the calculations used to obtain  $CO_2/N_2$  selectivity follow the IAST theory explained in *Chapter I, Section 1.2* as a Method 1. The experimental procedure to determine the selectivity is detailed below.

The first step is to input the experimental values obtained from the  $CO_2$  and  $N_2$  sorption isotherms into the linearized Langmuir equation (Equation 3.1), where  $\theta$  is the fractional surface coverage,  $P$  is the absolute pressure, and  $K$  is the ratio of the adsorption and desorption constants ( $K = K_a/K_d$ ).

$$\frac{1}{\theta} = K \frac{1}{P} + 1 \quad \text{Equation 3.1}$$

To develop this linearization, preliminary calculations derived from the initial Langmuir equation (Equation 3.2) are necessary. Langmuir theory describes that the  $\theta$  is directly proportional to the rate of desorption from the surface. Consequently, the adsorption and desorption rates are equivalent at equilibrium.<sup>139,140</sup>

$$K_a Y(1 - \theta) = K_d \theta \quad \text{Equation 3.2}$$

Where  $K_a$  is the rate constant for adsorption,  $K_d$  is the rate constant for desorption and  $Y$  is the number of gram molecules of gas striking each sq. cm. of surface per second. From this equation, the most common Langmuir adsorption equation (Equation 3.3) can be derived, followed by its linearization (Equation 3.4).

$$\theta = \frac{KP}{1 + KP} \quad \text{Equation 3.3} \quad \longrightarrow \quad \frac{1}{\theta} = K \frac{1}{P} + 1 \quad \text{Equation 3.4}$$

Once all the samples have been plotted according to the linearized Langmuir equation,  $K_{CO_2}$ ,  $K_{N_2}$  and the maximum quantity of adsorbed gas,  $n_{max}$ ; can be extracted using  $CO_2$  and  $N_2$  experimental isotherms. Through these parameters, the amount of gas adsorbed for  $CO_2$  and  $N_2$ , represented by  $n_{CO_2}$  and  $n_{N_2}$  are calculated using Equation 3.5 and Equation 3.6.

$$n_{CO_2} = \frac{PK_{CO_2}}{PK_{CO_2} + 1} \times n_{max} \quad \text{Equation 3.5}$$

$$n_{N_2} = \frac{PK_{N_2}}{PK_{N_2} + 1} \times n_{max} \quad \text{Equation 3.6}$$

Consequently, through IAST (Equation 3.7), it is possible to obtain an approximate calculation of the selectivity of a gas mixture from pure component isotherms. To replicate the atmospheric conditions, partial pressures are adjusted to the real partial pressures in air, which are related to the molar fraction of  $CO_2$  and  $N_2$  in air. For these calculations, it will be assumed 0.0004 and 0.9996 as a molar fraction of gas in air, respectively, and represented as  $X_{CO_2}$  and  $X_{N_2}$ .

$$S_{CO_2/N_2} = \frac{\frac{n_{CO_2}}{X_{CO_2}}}{\frac{n_{N_2}}{X_{N_2}}} \quad \text{Equation 3.7}$$

Figure 3.13 presents the selectivity obtained from all the samples using the Equation 3.7 calculations described above.

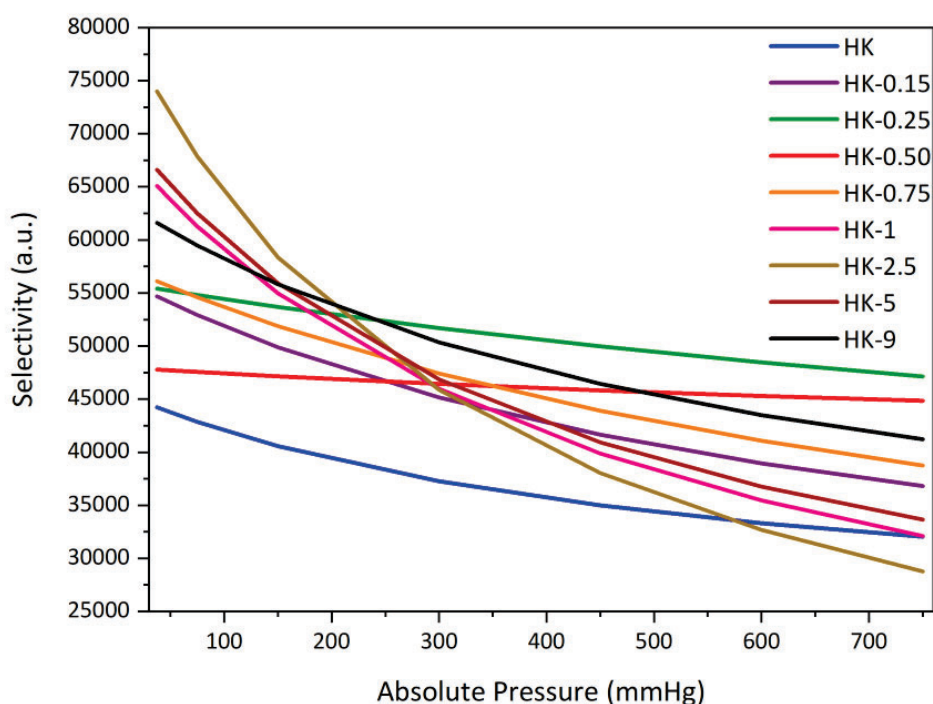


Figure 3.13. Representation of Selectivity's values according to the pressure.

HK-GO samples have significantly higher selectivity for CO<sub>2</sub> over N<sub>2</sub>, reaching values up to 75000 at low pressures. However, at higher pressures, selectivity decreases, reaching a maximum value of around 45000-50000 for the most selective samples. Specifically, HK-0.25 and HK-0.50 samples present higher selectivity at lower pressures, and these values decrease at higher pressures.

As observed, the sample exhibiting the highest CO<sub>2</sub>/N<sub>2</sub> selectivity value is HK-0.25, which correlates with having the highest adsorption capacity for CO<sub>2</sub> and the highest

specific surface area. Therefore, the results about selectivity have significant implications for the industrial sector: higher selectivity for CO<sub>2</sub> capture at lower pressures can reduce operational costs, enhance the efficiency of gas separation processes using low-pressure equipment, provide design flexibility, and improve viability in natural and biological applications, such as greenhouses. However, not all samples correspond to being the most efficient in terms of adsorption and selectivity. For instance, the sample containing 9 w/w % GO appears to be quite selective but not as efficient in CO<sub>2</sub> adsorption as the other samples (Figure 3.13, Table 3.5).

#### **Specific surface area and pore size distribution**

Specific surface area measurements were carried out to obtain information about porosity and the potential surface area to be occupied by the adsorbed CO<sub>2</sub> molecules. The equipment used in all the measurements was the same utilized for measuring CO<sub>2</sub> adsorption isotherms. Based on the data obtained, the samples with the larger specific surface area are HK-0.25, 0.5 and 0.75 with 1418, 1327 and 1084 m<sup>2</sup>/g, respectively, also coinciding with the highest CO<sub>2</sub> adsorption capacity samples measured. In contrast, higher amounts than 0.75 w/w % of GO and amounts less than 0.25 w/w % of GO show fewer specific surface area. Different batches of HK-GO samples were analyzed to compare the CO<sub>2</sub> with the results of the specific surface area obtained from BET N<sub>2</sub> isotherms (Figure 3.14).

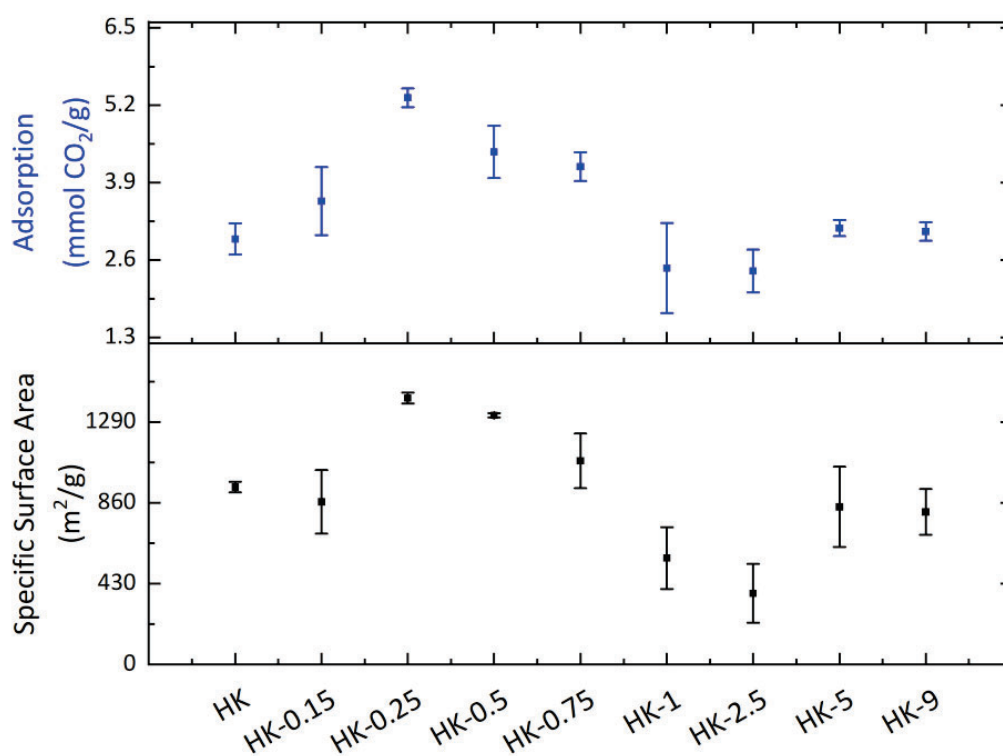


Figure 3.14. CO<sub>2</sub> maximum adsorption values, tested at 298 K and 1000 mmHg; and specific surface area values, tested at 77 K.

Concerning these values, it is determined that there exists a certain relationship between both parameters. Coinciding with some publications that describe similar capture processes,<sup>45,46</sup> the trend of CO<sub>2</sub> adsorption performance is related to the specific surface area. An exponential trend is noted, where the samples with higher BET surface area are the ones that have the highest CO<sub>2</sub> adsorption capacity (Figure 3.15), and particularly these optimal samples are in a w/w % GO range of between 0.25 and 0.75. Subsequently, it is observed that the incorporation of GO into HK structures influences both the specific surface area and CO<sub>2</sub> adsorption behavior. Table 3.5 indicates the results of each parameter obtained from different batches.

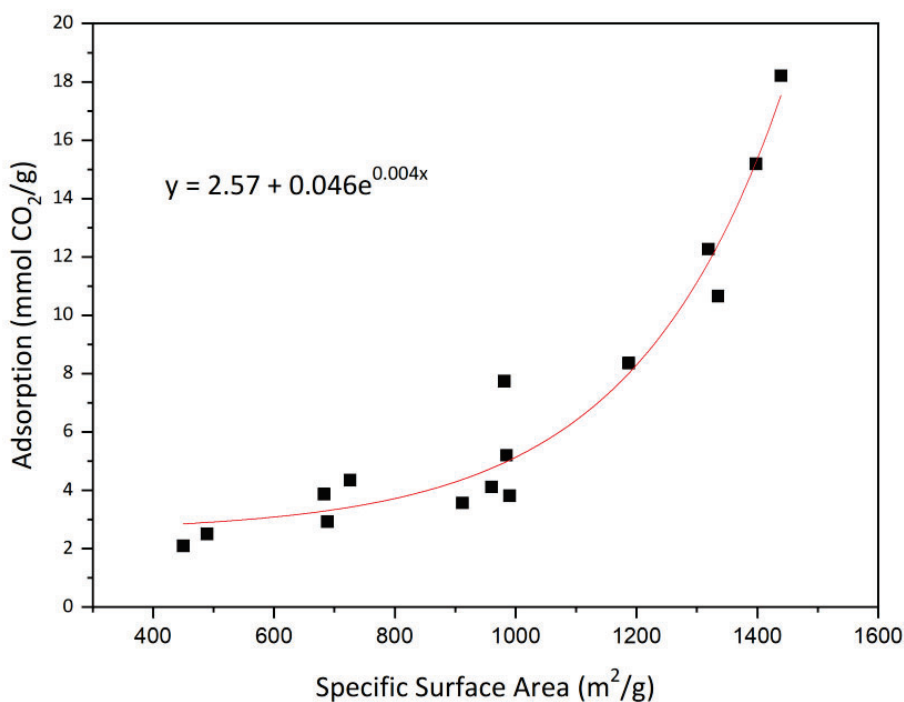


Figure 3.15. BET specific surface area and CO<sub>2</sub> adsorption relationship.

Table 3.5. Specific surface area, CO<sub>2</sub> adsorption and Experimental GO results.

Sample	BET surface area (m <sup>2</sup> /g)	CO <sub>2</sub> adsorption (mmol CO <sub>2</sub> /g)	Sample	BET surface area (m <sup>2</sup> /g)	CO <sub>2</sub> adsorption (mmol CO <sub>2</sub> /g)
HK	945 ± 28	2.96 ± 0.26	HK-1	567 ± 165	2.47 ± 0.76
HK-0.15	866 ± 169	3.56 ± 0.57	HK-2.5	379 ± 156	2.42 ± 0.36
HK-0.25	1418 ± 29	5.33 ± 0.16	HK-5	839 ± 214	3.13 ± 0.14
HK-0.5	1327 ± 11	4.42 ± 0.44	HK-9	812 ± 122	3.08 ± 0.16
HK-0.75	1084 ± 146	4.17 ± 0.24			

The porosity of all the samples was also measured along with the specific surface area measurements. This property of the samples was analyzed to characterize the nature of the pores in all the samples and to assess the effect of GO incorporation as some literature describes that the addition of GO to HKUST-1 materials produces an

increase in the size of the pores, thereby enhancing CO<sub>2</sub> adsorption performance.<sup>45,141</sup>

The results of some samples are presented in the Table 3.6.

*Table 3.6. Pore size distribution results of HK (MSM) samples.*

<b>Sample</b>	<b>V<sub>pore</sub> (cm<sup>3</sup>/g)</b>	<b>V<sub>mic</sub> (cm<sup>3</sup>/g)</b>	<b>V<sub>mic</sub>/V<sub>pore</sub> (%)</b>
<b>HK</b>	0.441	0.340	76.9
<b>HK-0.25</b>	0.623	0.480	76.5
<b>HK-0.50</b>	0.835	0.576	68.9
<b>HK-1</b>	0.716	0.235	32.8
<b>HK-2.5</b>	0.561	0.182	32.4
<b>HK-5</b>	0.674	0.238	35.1
<b>HK-9</b>	0.504	0.250	49.6

It is observed that the total pore volume tends to increase with higher concentrations of GO, indicating that the GO enhances the porosity of the samples. However, a slight decrease in pore volume is observed for the HK-2.5 and HK-5 samples, suggesting that excessive GO may block the pores, leading to a reduction in total porosity.

On the other hand, micropore volume shows a similar trend to the total pore volume, initially increasing with small amounts of GO and decreasing with higher contents of GO. This suggests that lower contents of GO may promote the formation of micropores, while higher concentrations of GO could hinder the development or accessibility of micropores. The relationship between the total pore volume and the volume of micropores decreases as GO increases, which reinforces that higher GO concentrations reduce the proportions of micropores in the samples.

In summary, GO affects notably the pore structure of the samples and the pore size distribution. With small amounts of GO, pore volume is improved, but when GO

increases, after HK-0.50 sample, these properties start to decrease. Additionally, with higher GO content, pore size volume increases.

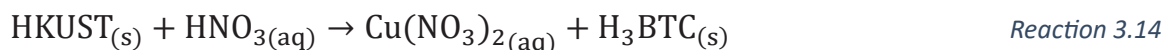
### 3.2.7 Reverse quantification

In the literature related to the synthesis of HK-GO, no data or methods have been found that indicate how to determine the actual amount of GO incorporated in the sample. In most cases, they assume that the amount initially added during the synthesis is the actual amount left in the final product, without any description of the homogeneity of the sample or the yield.<sup>45,46,53,142,143</sup> Consequently, determining the experimental amount of GO retained in the structures reveals differences between batches of the same sample and highlights some of the sources of systematic errors that may deviate from the observed trends.

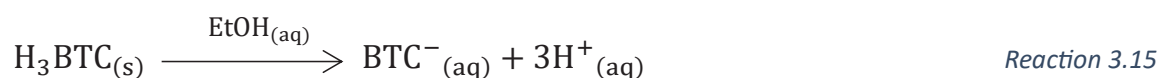
To determine accurately the actual amount of experimental GO incorporated in the synthesized samples, a new experimental methodology was developed, named here as Reverse Quantification (RQ). RQ can determine the actual content of GO retained in each sample following the next procedure. The HK-GO sample is dissolved using a solution of 1:1 HNO<sub>3</sub> : EtOH (Reaction 3.13).



When HKUST-1 reacts with HNO<sub>3</sub>, the mixture dissolves HKUST-1 and Cu<sup>2+</sup> cations react with the nitric acid to form Cu(NO<sub>3</sub>)<sub>2</sub>. Meanwhile, the organic ligand remains free in the solution (Reaction 3.14).



BTC ligands are dissolved due to the ethanol of the mixture (Reaction 3.15).



Hence, all the components are dissolved, except for the GO which remains solid in the solution. After the centrifugation process, GO is separated from the whole sample and weighed to determine the real quantity of GO in the analyzed sample. This simple method allows the quantification of the GO in the HK-GO samples through separation by solubility.

If experimental and theoretical GO are compared, it is possible to observe that the quantified values of GO obtained from RQ don't match with theoretical GO proportions used during the synthesis, which in all the cases are lower. As the theoretical concentration of GO increases, the experimental amount of GO retained in the structure exhibits more variability, particularly at higher concentrations (2.5-9 w/w %). This observation supports the idea that increasing concentrations of GO during synthesis difficult the correct dispersion into the sample (Figure 3.16).

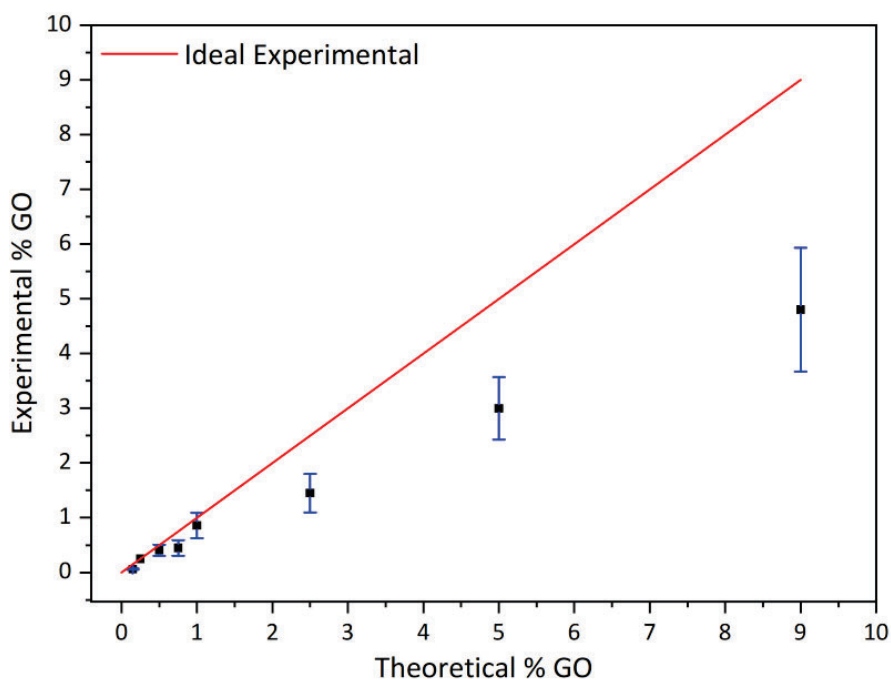


Figure 3.16. Experimental %GO vs. theoretical %GO of the synthesized samples (MSM). Red line represents the ideal value of 100% incorporation of GO in synthesis.

As the theoretical concentration of GO increases, the experimental amount of GO retained in the structure exhibits less reproducibility, particularly at higher concentrations compared to those at lower concentrations within the range of approximately 0.15-1 w/w %. Using this approach, the sample nomenclature would accurately reflect the respective proportions of experimental graphene oxide (GO) (Table 3.7).

Table 3.7. Theoretical GO and experimental GO data.

HK-GO nomenclature	Theoretical %GO <sup>#</sup>	Experimental %GO <sup>§</sup>
HK	0	0.00 ± 0.00
HK-0.15	0.15	0.06 ± 0.01
HK-0.25	0.25	0.25 ± 0.00
HK-0.50	0.50	0.40 ± 0.10
HK-0.75	0.75	0.45 ± 0.14
HK-1	1	0.86 ± 0.23
HK-2.5	2.5	1.45 ± 0.35
HK-5	5	3.00 ± 0.57
HK-9	9	4.80 ± 1.13

# is the percentage of GO added into the synthesis.

§ is the mean of 3 batches experimentally quantified of GO.

Based on the RQ results, a clear trend emerges when comparing the experimental GO from different batches with their corresponding maximum CO<sub>2</sub> adsorption values. Analyzing each sample individually, rather than grouping them by batch, further highlights this pattern. First, samples with GO content below or above the experimental 0.15-0.45 % w/w GO range show lower adsorption values compared with the adsorption of the pristine HK (2.96 ± 0.26 mmol CO<sub>2</sub>/g, Figure 3.17 (a)). Second, the samples with the highest adsorption capacity are synthesized with a theoretical 0.25 % w/w GO, being as well those that maintain this amount in the final sample as experimental 0.25 % w/w GO (Figure 3.17 (b)). Therefore, the enhancement of CO<sub>2</sub> adsorption properties is achieved when samples are synthesized using 0.15%, 0.25%, 0.5%, and 0.75% w/w of GO.

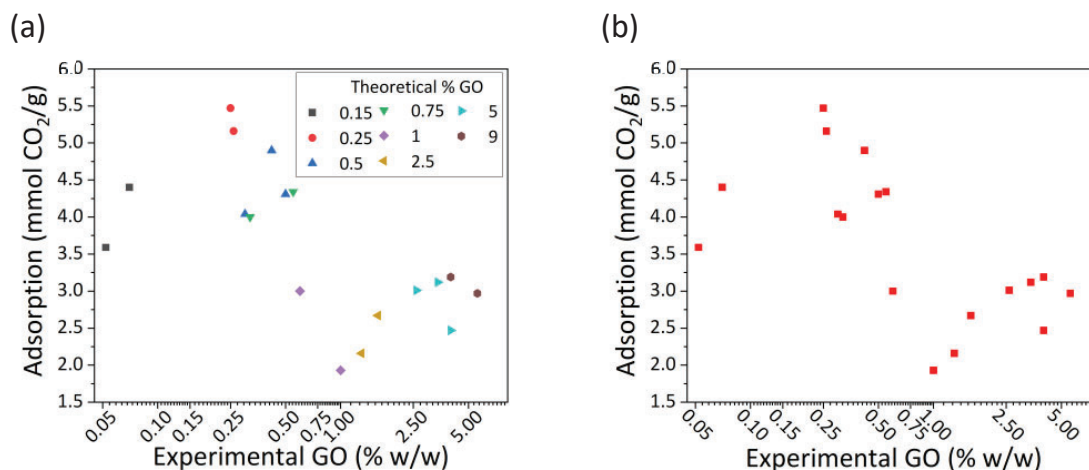


Figure 3.17. (a) Adsorption of CO<sub>2</sub> at 1000 mmHg vs. experimental % GO of the MSM samples indicating theoretical %GO, (b) Adsorption of CO<sub>2</sub> at 1000 mmHg vs. experimental % GO of the MSM samples without indicating theoretical %GO.

Given the obtained results, the samples located in the range of maximum adsorption acquired, 0.25, 0.40 and 0.45% of experimental GO, achieve an improvement of CO<sub>2</sub> adsorption of 80%, 49% and 41% respectively, compared to pristine HK. Once the quantity of GO is increased, apart from a decrease in adsorption capacity, the adsorption behavior seems to stabilize and remain around the 3 mmol CO<sub>2</sub>/g, which is very close, even lower in some cases, to the result when GO is not added during the synthesis.

Overall, the CO<sub>2</sub> adsorption performance data concerning the experimental GO values indicate that the trends remain consistent, even though the % of GO ranges differ. The following table shows the data collected from the specific surface area, the CO<sub>2</sub> adsorption isotherms and the corresponding percentage of experimental GO quantified using RQ (Table 3.8).

Table 3.8. Specific surface area, CO<sub>2</sub> adsorption maximum value obtained, and experimental GO results.

Sample	Specific Surface Area (m <sup>2</sup> /g)	CO <sub>2</sub> adsorption (mmol CO <sub>2</sub> /g)	Experimental GO (%)
HK	945	2.96 ± 0.26	0.00 ± 0.00
HK-0.15	866	3.56 ± 0.56	0.06 ± 0.01
HK-0.25	1418	5.33 ± 0.16	0.25 ± 0.00
HK-0.5	1327	4.42 ± 0.44	0.40 ± 0.10
HK-0.75	1084	4.41 ± 0.24	0.45 ± 0.14
HK-1	567	2.47 ± 0.76	0.86 ± 0.23
HK-2.5	379	2.41 ± 0.36	1.45 ± 0.35
HK-5	839	2.86 ± 0.35	3.00 ± 0.57
HK-9	812	3.08 ± 0.16	4.80 ± 1.13

### 3.3 Conclusions

HKUST-1 materials combined with different concentrations of graphene oxide (GO) have been successfully synthesized via mixed-solvent method (MSM). X-ray diffraction, infrared spectroscopy and thermogravimetry results confirm the correct formation of HKUST-1 and determine that the introduction of GO doesn't alter the crystalline structure of the pristine MOF.

Graphene oxide (GO) was successfully quantified using the Reverse Quantification (RQ) process presented in this research. In this case, RQ for the MSM method reveals that samples with lower amounts of GO are closer to ideal performance. This behavior is attributed to the fact that small amounts of GO disperse and adhere more easily to the final structure of the HKUST-1 compared to the addition of larger amounts of GO, which agglomerate and tend to separate from the HKUST-1.

An increase in the CO<sub>2</sub> adsorption performance is achieved, particularly with those samples synthesized using 0.25% w/w of experimental GO. Compared to the pristine HKUST-1, an improvement of 80% in CO<sub>2</sub> adsorption performance is achieved, reaching maximum values of  $5.33 \pm 0.16$  mmol CO<sub>2</sub>/g.

SEM images provide information about GO and the effect produced on the size and geometry of the MOF particles. GO promotes and increases the nucleation points for the formation of HK crystals as well as the creation of different structural and morphological defects.

Regarding selectivity, it is determined that the samples with the highest CO<sub>2</sub> adsorption capacity are also the most selective at high pressures (up to 760 mmHg).

---

## Chapter IV: Synthesis and Characterization of HKUST-1/GO Materials via Ball Milling Methods

---

### *Summary of the chapter*

*In the following chapter, a new synthesis method for HK-GO samples is proposed, focusing on green chemistry through mechano-chemical synthesis using ball milling (BM). Based on the results obtained in the previous chapter using Mixed Solvent Method (MSM), the samples were synthesized in a narrower range rather than up to 9% w/w GO, specifically within 0.15 to 2.5 w/w % of GO, as previous findings suggest that the enhancement in CO<sub>2</sub> capture falls between 0.25 and 0.75 w/w % of GO.*

*The results of this new method are presented in two sections. First, the characteristics and outcomes of samples obtained from a small-scale synthesis are discussed and referred to throughout the chapter as sBM (small ball milling). Second, a medium-scale upscaling is conducted by increasing the quantities of synthesized product up to 13 times more amount compared to sBM method. The results of this upscaling production are presented under the designation bBM (big ball milling).*

*Additionally, a detailed analysis of the CO<sub>2</sub> adsorption properties is described for samples synthesized using sBM and bBM, focusing on the relationship between CO<sub>2</sub> adsorption performance and the experimental GO of each sample (quantified using Reverse Quantification described in Chapter III). The features of all the samples are exposed, and the results are compared to MSM data, showing some statistical calculations between the methods. As a result, the ball milling methodology allows the production of samples with CO<sub>2</sub> capture efficiencies comparable to those obtained using MSM, while offering the significant advantage of eliminating the need for harmful and ecotoxic solvents, such as dimethylformamide (DMF), which are*

commonly used in solvent-based synthesis techniques. Specifically, the results indicate that samples produced using sBM reach the maximum adsorption performance of  $4.93 \pm 0.28$  mmol CO<sub>2</sub>/g for those samples which contain 0.48-0.55% w/w of experimental GO, reproducing a similar adsorption performance observed on the MSM samples, where the samples with higher CO<sub>2</sub> adsorption performance are those with 0.25% w/w of experimental GO.

On the other hand, samples produced using bBM present a maximum adsorption performance of  $3.77 \pm 0.07$  mmol CO<sub>2</sub>/g with those samples containing 0.25-0.30% w/w of experimental GO. Moreover, while sBM samples achieve CO<sub>2</sub> capture efficiencies comparable to MSM and the correlation between GO content and CO<sub>2</sub> adsorption is evident, in bBM samples it is not significant, suggesting the need for further optimization of this upscaling approach.

Thus, BM method not only aligns with Green Synthesis standards but also provides HK-GO materials with improved CO<sub>2</sub> adsorption performance.

## 4.1 Mechano-chemical synthesis

Mechano-chemical synthesis consists of producing a chemical transformation facilitated by mechanical forces without the utilization of additional heat to perform the chemical reactions. Some examples of advanced materials synthesized using this methodology include nanoparticles, zeolites, supramolecular complexes, etc.<sup>144–146</sup>

Particularly, MOFs can be synthesized by mechanical grinding, which can be realized manually through a mortar or utilizing ball milling instead.<sup>147</sup> As described in *Chapter I, Section 1.3.5*, mechanochemical strategies for synthesizing MOFs include neat grinding (NG), liquid assisted grinding (LAG) and ion-and-liquid assisted grinding (ILAG). In the case of LAG and ILAG, the wet medium inside the recipe, where the mill is produced, facilitates the chemical interaction between the reagents leading to the formation of a product.

Ball Milling (BM) is based on the reduction of the particle size of a solid sample through the impact and the friction exerted by the balls and the material introduced in the grinding jar. In recent years, the use of ball milling has gained significant attention due to its potential to be used as a synthesis method.<sup>142,148–150</sup>

When ball milling is utilized, it is necessary to consider some essential parameters. The grinding material, the diameter and the number of balls, the time of grinding, the quantity and the initial conditions of the sample introduced into the grinding jar, and the revolutions selected in the process are some examples.<sup>151</sup>

One of the main aspects is the material of the employed jar and the introduced balls, which need to be the same to avoid generating any kind of defect in the jar (such as cracks and deformations) or wear or fracture of the balls, which could lead to contamination of the sample obtained. Considering this, it is recommended that both the balls used, and the material of the jar were made of the same material. The optimal ball and jar material is chosen according to the input of energy needed in the process, related to the ground sample. In this sense, soft materials such as

pharmaceutical products or soil obtain optimum grinding through the utilization of low/medium density materials of grinding, like polytetrafluoroethylene (PTFE), agate or sintered aluminum oxide. On the other side, it is recommended to use grinding materials capable of generating higher energy inputs for harder samples like ores or alloys, employing tungsten carbide, steel, or zirconium oxide as grinding materials. Depending on the type of sample introduced into the system, the material employed may vary in hardness.<sup>152</sup>

Although BM is generally carried out dry, the procedure can be realized using wet conditions, which facilitate the mixing of the material and is usually performed when the objective of the grinding is to obtain ultra-fine particles in the final product or facilitating the dissolution of the reactants in a mechano-chemical synthesis.

Given the process described, standard procedures using BM equipment require a series of steps to ensure good operational practices. As a general guideline, it is recommended that grinding processes follow the 1/3 rule. This rule suggests that before starting the grinding, the amount of the sample introduced in the jar (either wet, along with the corresponding dispersant, or dry reactants) should be approximately 1/3 of the grinding jar's volume. Another 1/3 should be filled with grinding balls (with ball sizes  $\leq 3$  mm when the initial particle size of the reagents is  $< 1$  mm). Additionally, the remaining 1/3 of the volume should be left as free space. These steps are recommendations; failing to follow them may result in abrasion of the grinding jar and introduce impurities into the ground sample.<sup>152</sup>

In the following sections, the BM method is employed to produce samples of HK and HK-GO. Since *Chapter III* presented that the enhancement of CO<sub>2</sub> adsorption properties occurs in the range of 0.25-0.75 % w/w of theoretical GO, the sample set in this chapter is synthesized within a narrower range, from 0.15% to 2.5% w/w GO, instead of extending up to 9% as in the case of MSM method.

Initially, samples are produced in small quantities using Micro Mill PULVERISETTE 7 (Figure 4.1 (c) with 15 mL jar Figure 4.1 (a)). This synthesis method is referred to as small ball milling (sBM).

Additionally, a medium-scale upscale is explored using larger jars (of 500 mL) (Figure 4.1(b) and a PM 100 planetary ball mill from RETSCH, Figure 4.1 (d)). This method referred to as big ball milling (bBM), allows for an increase in sample production of up to 13 times compared to sBM.



Figure 4.1. Jar pots of (a) sBM and (b) bBM and (c) ball milling sBM and (d) ball milling of bBM equipment.

### **Small ball milling (sBM)**

Considering all the previously mentioned aspects, this section describes the process carried out to synthesize the samples using small ball milling (sBM) as an alternative to the mixed solvent method.

### **Solvent-free ball milling approach**

In the first instance, the preliminary experiments were carried out in solvent-free conditions (neat grinding synthesis). The synthesis of HKUST-1 using sBM was explored by mixing 0.59 g of copper (II) acetate,  $\text{Cu}(\text{CH}_3\text{COOH})_2$ , and 0.41 g of trimesic acid,  $\text{H}_3\text{BTC}$ , along with 10 zirconium oxide balls of 5 mm of diameter in 15 mL of zirconium oxide jar pots. The parameters for the selected setup consisted of four cycles at 600 RPM of 5 min in one direction, with a 2-minutes pause between each cycle, followed by four cycles in the opposite direction with the same parameters.<sup>153</sup>

XRD diffractogram, shown in Figure 4.2, displays the results of the HK synthesis using this procedure. The diffractogram reveals unreacted traces of the reactants, indicating that the reaction was not complete. This suggests that HKUST-1 can be obtained through solvent-free synthesis using ball milling, but the procedure needs further optimization.

However, the synthesis performed for obtaining HK-GO samples presented some difficulties regarding the correct formation of the sample. When the synthesis of HK-GO sample was performed, GO was not incorporated during the synthesis and remained completely separate from HK. The primary reason for this was that GO agglomerates and cannot be properly dispersed without a solvent. Consequently, GO is not well dispersed, and the synthesis of HK-GO samples results in HK without GO.

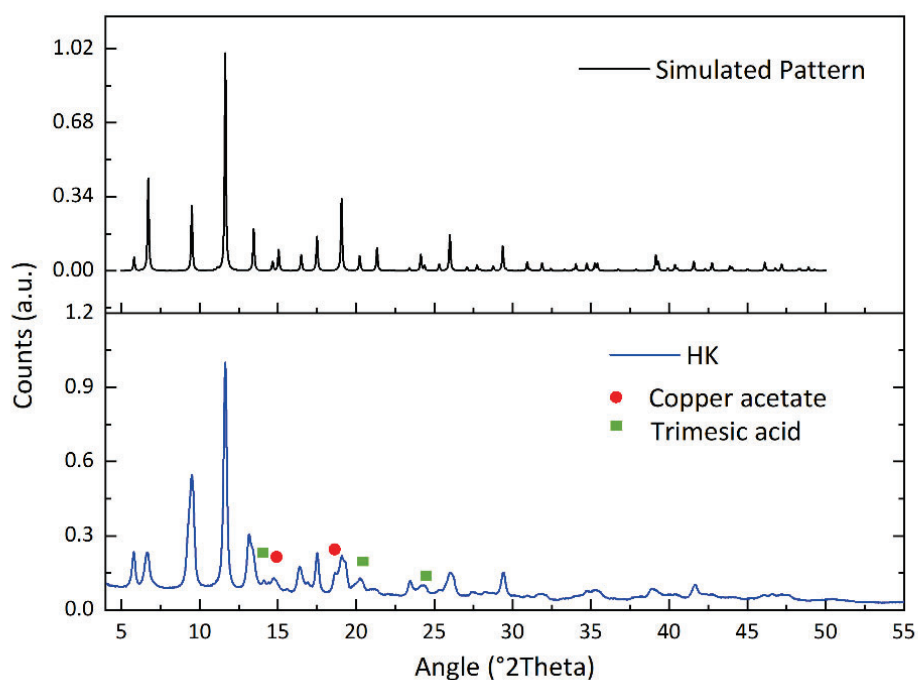


Figure 4.2. XRD diffractograms of the simulated pattern (top) and HK sample synthesized using solvent-free synthesis with sBM method (bottom).

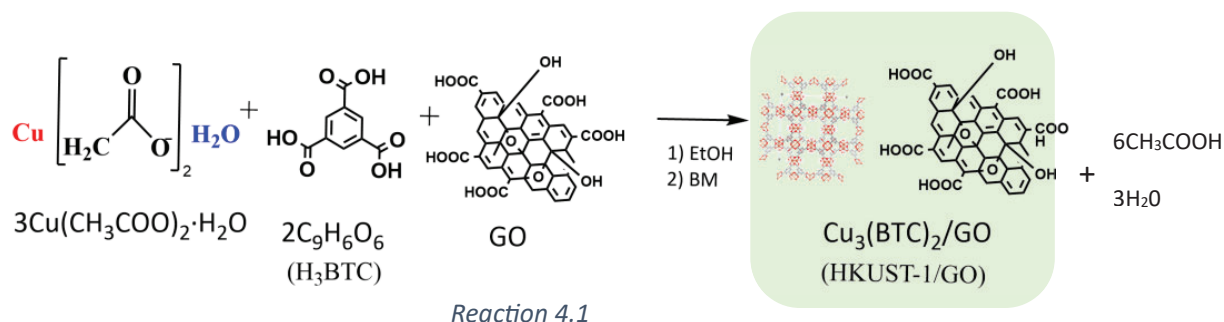
So, it was decided not to continue synthesizing samples using the solvent-free method, as it is not possible to synthesize HK-GO samples. Instead, the preparation of all samples, with and without GO, continued using liquid-assisted grinding.

#### Liquid-assisted ball milling approach

HK and HK-GO samples between 0.15 and 2.5% w/w GO were synthesized using a liquid-assisted grinding method with sBM, modifying the synthesis proposed by Timothy Steenhaut et al.<sup>153</sup>

The reactants (0.59 g of  $\text{Cu}(\text{CH}_3\text{COOH})_2$  and 0.41 g of  $\text{H}_3\text{BTC}$ ) were introduced into the jars with 10 zirconium balls. Here, the ball-to-power ratio (BPR), which indicates the relationship between the weight of balls in the grinding process and the weight of the grinding sample; was 13.12. Then, a dispersion of graphene oxide (GO) in 7.5 ml of ethanol was added to the mixture (for HK samples, ethanol was added without GO). This step of the experimental procedure facilitated the dispersion of the GO powder and the dissolution of the reactants.

The reaction which takes place is the indicated in Reaction 4.1.



The experimental procedure followed the same settings of cycles and revolutions used in solvent-free ball milling approach: four cycles at 600 RPM of 5 min in one direction, with a 2-minutes pause between each cycle, and then four cycles in the opposite direction with the same specifications.

After the milling process, the product obtained was a blue paste (Figure 4.3 (a)). Subsequently, it was washed with 200 mL solution of 1:1 H<sub>2</sub>O/EtOH, stirring vigorously the mixture before filtration (Figure 4.3 (b)). Then, the sample was dried (activation step) under vacuum at 170 °C overnight to completely dry the sample. This procedure results in a final product with a variable yield, typically ranging from 70% to 80%. This corresponds to a product quantity of 0.8-1.3 g per sample. In comparison, MSM samples achieve a higher yield, around 90%.

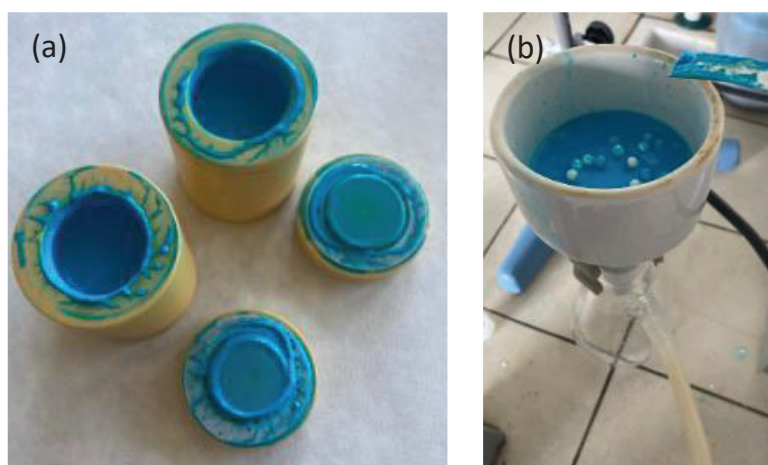


Figure 4.3. HK sample paste obtained from sBM method and (b) filtration of the paste.

**Big ball milling (bBM)**

This synthesis is based on the mechano-chemical reaction performed in sBM (Reaction 4.1), but with larger jars (500 mL, Figure 4.1 (b)), allowing for the production of a bigger batch, approximately 13 times more than using sBM method. The process of scaling up the sample quantities was determined to be at a medium-small scale, considering the cost of reactants, the availability of equipment, and the time required to produce a set of different sample batches. Subsequently, the technical steps of this novel synthesis and the principal outcomes obtained are exposed.

Regarding the scaling process used in the synthesis of these samples, the following parameters were considered:

- The ball to power ratio (BPR). BPR is maintained at 13.12, the same ratio used on the small scale.
- The diameter of grinding balls. This procedure uses the same diameter employed in the grinding balls as in the case of the previous small-scale synthesis, which was 5 mm.
- The scalability factor. The reagents used in this experiment were increased in mass by a factor of 20.

On the other hand, the preliminary experiments revealed that operating the grinding process at 600 RPM posed significant challenges due to equipment instability. Despite the correct balancing with the metallic bowl, the additional weight of the safety ring used in the closure (around 0.87 kg) introduced imbalance issues. Consequently, a series of tests were conducted using varying RPM settings, with 250 RPM being identified as the best option for stability.

Moreover, the direction of revolutions was another parameter to adjust. Instead of executing 4 cycles in one direction followed by another 4 cycles in the opposite direction with a 2-minute-pause between each cycle, optimal stability was achieved

by implementing 2 cycles of 30 minutes each using the reverse direction option (the only option available in the new scale equipment used), with a 10-minute pause between cycles. Moreover, the reactants were sonicated, along with the dispersed GO in ethanol, for 10 minutes before introducing them into the grinding bowls. Since XRD spectra showed the correct formation of HK-GO samples (presented in *Section 4.4.4*), it was determined that the most similar adjustment of scalable parameters was the one described above.

Specifically, 500 mL capacity  $\text{Al}_2\text{O}_3$  grinding jars were employed in bBM method. Following the procedure described in *the small ball milling (sBM)* section but changing some parameters according to the set-up and the specifications mentioned, 11.8 g of  $\text{Cu}(\text{CH}_3\text{COOH})_2$  and 8.2 g of  $\text{H}_3\text{BTC}$  were introduced into the jar, along with 154.81 g of  $\text{Al}_2\text{O}_3$  grinding balls measuring 5 mm in diameter, maintaining the BPR in 13.12 as in the synthesis using sBM method. Subsequently, 300 mL of EtOH containing the corresponding quantity of dispersed GO powder (previously sonicated for 10 minutes using a sonicator set at 50% power) was added to the mixture of reactants and sonicated again for 10 minutes before the grinding. The use of larger quantities along with the ethanol solvent, required the implementation of a safety closure mechanism to mitigate the risk of substance spills and potential pressure-related incidents. With these specifications, it was possible to obtain around 10-13 g of the final HK-GO samples, achieving an approximate yield of 70%. Compared to the samples obtained using sBM (yields of 70-80%) and MSM (yields of 90%) methods, this yield value was the lowest.

## **4.2 Materials characterization and performance for samples obtained via small ball milling**

In the previous chapter, it was concluded that determining the experimental GO content in the samples is essential for accurately assessing its impact on CO<sub>2</sub> adsorption performance. Therefore, in this chapter, the first point addressed in this section is the determination of the experimental GO content in sBM samples using Reverse Quantification.

Additionally, as proceeded in *Chapter III*, the samples were analyzed and characterized using a series of techniques validating the formation of HKUST-1, to corroborate the effects of GO on HK-GO samples and how it influences CO<sub>2</sub> adsorption performance. In this case, although particle size measurements were conducted using different equipment than those used for MSM samples, the techniques employed for analyzing sBM samples were the same as those used for MSM samples.

### 4.2.1 Reverse quantification

Reverse Quantification (RQ) was employed to determine the experimental percentage of GO in the sBM samples, following the same procedure used for the MSM samples. However, discrepancies were observed between the theoretical amount of GO used during synthesis and the experimental amount determined.

Figure 4.4 illustrates the relationship between experimental and theoretical GO, showing a relation that deviates from ideality, with some dispersion in the results.

Considering the experimental GO, four groups of synthesized samples were identified: one group with approximately 0.30% w/w GO, another with approximately 0.50% w/w GO, a third with around 0.75% w/w GO, and a fourth with about 1.5% w/w GO (indicated each group using a different color). Moreover, the findings indicate that samples HK-0.15, HK-0.25 and HK-0.50 show higher experimental content of GO than the theoretical GO content. For the rest of the samples experimental content is lower compared to the theoretical GO.

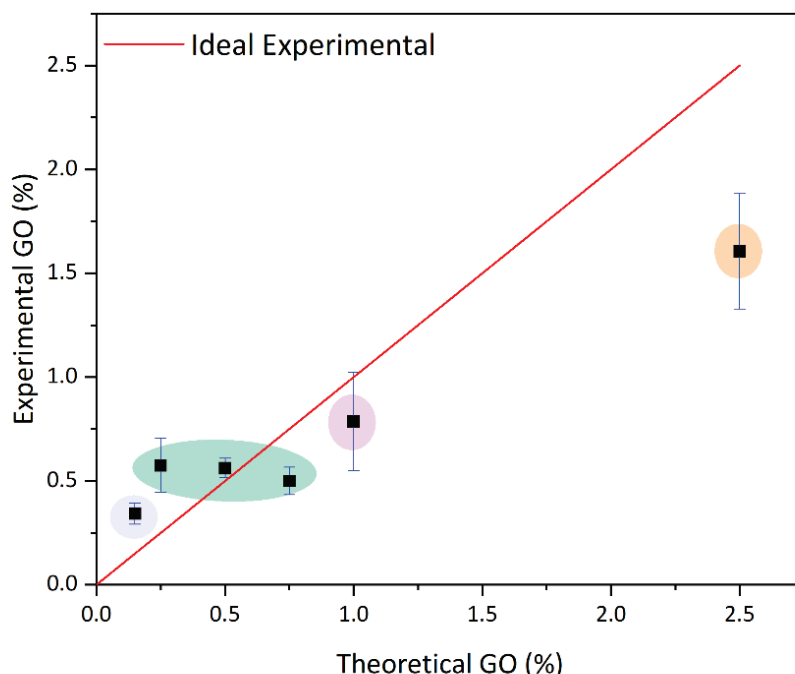


Figure 4.4. Experimental %GO vs. theoretical %GO of the synthesized samples (sBM). Red line represents the ideal value of 100% incorporation of GO in synthesis and shaded areas indicate group of samples with similar experimental GO values.

In the case of MSM samples, all the experimental GO content was lower than the theoretical GO content, which was expected as not all the GO utilized in the synthesis was incorporated in the structures. However, for the sBM samples, the experimental RQ reveals a different trend, which can be explained by the yield analysis of the synthesis (i.e. the percentage of product obtained relative to the theoretical maximum). The differences in the experimental GO content are likely related to the growth of the MOF within the GO layers. Specifically, the first three samples (with 0.15%, 0.25% and 0.50% w/w of theoretical GO) exhibited considerably lower yields compared to the rest of samples below the ideal linearity (with 0.75%, 1% and 2.5% w/w of theoretical GO). More precisely, samples with theoretical contents of 0.15-0.50% w/w GO presented yields of around 70%, while samples with theoretical contents of 0.75-2.5% w/w GO exhibited yields of approximately 80%.

All samples were synthesized using the same proportion of ligand and copper salt reactants, the only difference between them was the GO content. Since graphene oxide (GO) facilitates the formation and growth of HK on its surface, it is found that adding less than 0.50% w/w of theoretical GO (when using sBM) hinders the formation of HK molecules. As a result, the final amount of GO in the product is higher than expected. This occurs because not all reactants fully react, leading to a lower production of MOFs. Consequently, the final product ends up with a higher experimental %GO compared to the theoretical %GO initially added.

Additionally, some studies have reported that HKUST-1 is formed on GO surface using nucleation points from carboxylate and epoxy functional groups of the molecule.<sup>151</sup> Therefore, the results suggest that performing the synthesis using the ball milling method with less than 0.50% w/w of theoretical GO affects the final product yield, likely due to the specific positions that GO molecules adopt during the growth of HKUST-1 on the GO surface.

## 4.2.2 Gas sorption measurements and surface properties

The next section presents the results from Reverse Quantification (RQ), with the corresponding analysis of the CO<sub>2</sub> adsorption performance, selectivity calculations and specific surface area results of the samples. In this case, the nomenclature follows this format: *HK-Xe*. Here, HK refers to the MOF HKUST-1, while X represents the experimental GO content of the sample, emphasizing that it is experimental by using the letter 'e'.

### CO<sub>2</sub> adsorption isotherms

CO<sub>2</sub> adsorption isotherms were performed at 298 K using BET equipment to evaluate the CO<sub>2</sub> capacity adsorption of the synthesized samples up to 1000 mmHg and at 25°C, using the same conditions of measurement as the HK-GO (MSM) samples, presented in *Chapter III, Section 3.2.6*. The samples were treated in ethanol using sonication at an amplitude of 50% for 30 minutes to ensure complete deagglomeration. Afterwards, the samples were filtered and dried overnight before each adsorption measurement. Figure 4.5 (a) and (b) display the results of CO<sub>2</sub> adsorption isotherms from the samples synthesized using sBM and MSM, along with the CO<sub>2</sub> isotherm of GO powder.

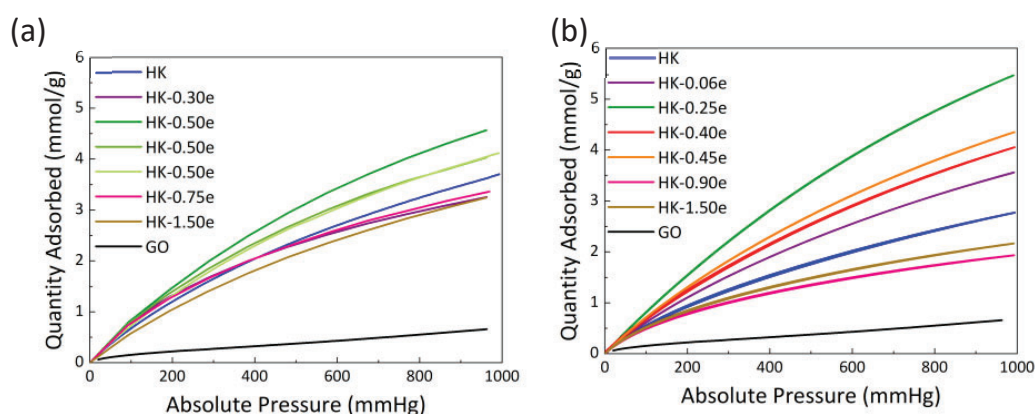


Figure 4.5. CO<sub>2</sub> adsorption isotherms of (a) HK-GO (sBM) samples and (b) HK-GO (MSM) samples, measured at 298 K and up to around 1000 mmHg.

As can be seen in the isotherms above, the CO<sub>2</sub> adsorption performance for GO is lower than all the HK-GO samples synthesized using MSM and sBM. On the other hand, sBM samples exhibit the most adsorbent performance for samples HK-0.50e (green lines). In contrast, HK-0.25e is the most CO<sub>2</sub> adsorbent sample for samples obtained via MSM method (also green line), followed by HK-0.40e and HK-0.45e (red line and orange line, respectively). On the other hand, the CO<sub>2</sub> adsorption of the remaining samples is higher for those obtained using sBM compared to the adsorption performance of those synthesized using MSM. Specifically, pristine HK (sBM) achieves capturing higher CO<sub>2</sub> molecules compared to HK (MSM) at high pressure values (1000 mmHg).

### **Selectivity**

As performed for MSM samples in *Chapter III, Section 3.2.6*; the selectivity of the samples was evaluated by conducting the corresponding N<sub>2</sub> adsorption isotherms, initially measured under the same conditions as CO<sub>2</sub> isotherms (at 25°C and up to 1000 mm Hg).

Using IAST calculations, a similarity was found between the results of MSM and sBM samples. The calculated selectivity for samples of both methods is depicted in Figure 4.6 (a) and (b).

The samples that exhibited higher CO<sub>2</sub>/N<sub>2</sub> selectivity at higher pressures were those with 0.50% w/w of experimental GO, followed by the pristine HK, HK-0.75e, HK-1.5e and HK-0.30e, respectively. Compared to the selectivity observed in MSM samples, although the most selective materials are similar, the remaining results differ in the slope of their selectivity curves. For instance, HK-1.50e (MSM) showed the highest selectivity at low pressures, but its performance sharply declined as pressure increased. In contrast, this behavior was not observed in the HK-1.50e (sBM) sample. On the other hand, at low pressures, the selectivity values of sBM samples are similar, around 60000, while at high pressures, the obtained values exhibit a high dispersion,

between 35000 and 55000. In the case of MSM samples, the selectivity values show a high dispersion at low and high pressures.

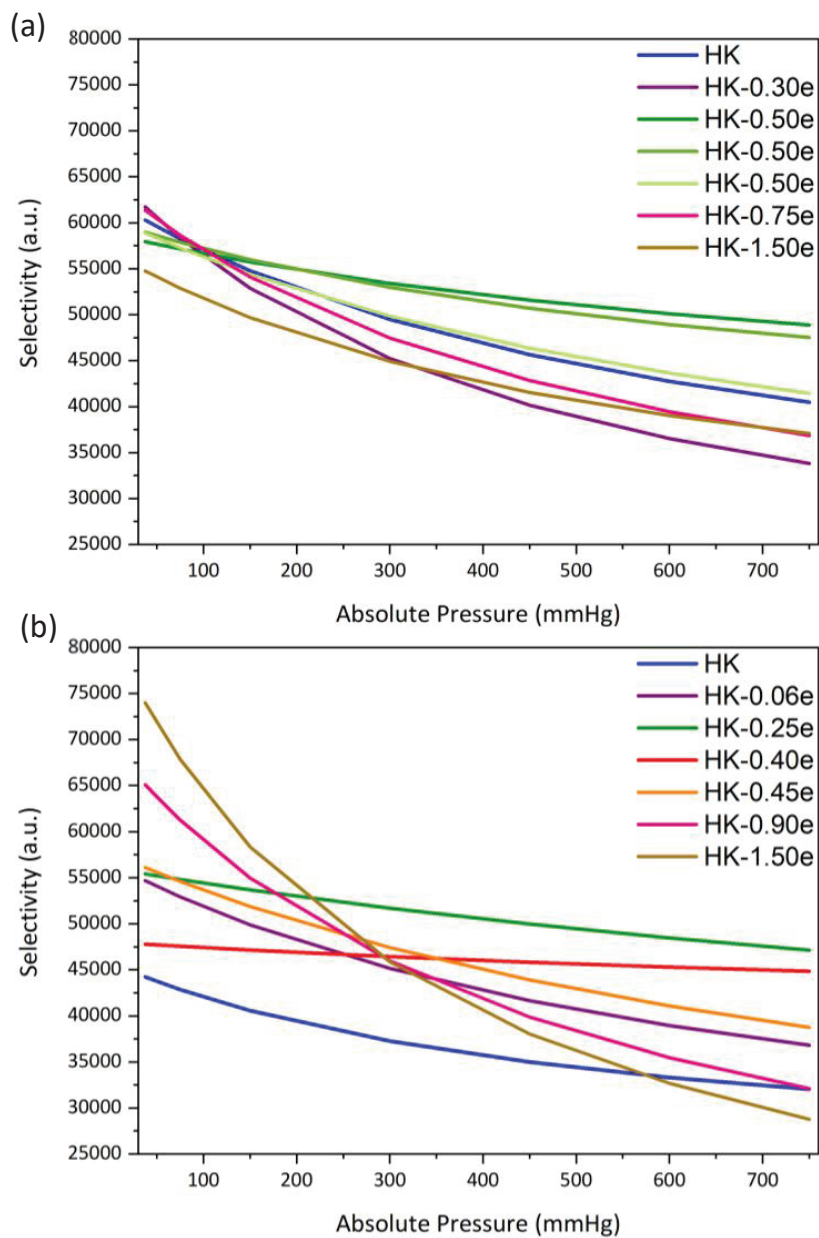


Figure 4.6. Selectivity values of (a) HK-GO (sBM) and (b) HK-GO (MSM) samples.

### **Specific surface area and pore size distribution**

A series of HK-GO samples from different batches were tested for CO<sub>2</sub> adsorption capacity and specific surface area, following the same procedure described in *Chapter III, Section 3.2.6*. This was carried out to assess their adsorption capacity and determine the most effective combination of HK and GO, while also considering reproducibility and the specific surface area trends (Figure 4.7).

In this case, adsorption values, at 1000 mmHg; of the samples with 0.50% w/w experimental GO (represented in 3 groups of samples in the graph) exhibit higher adsorption performance compared to the rest of samples. Contrastingly, the specific surface area of the samples displays some dispersion of the results.

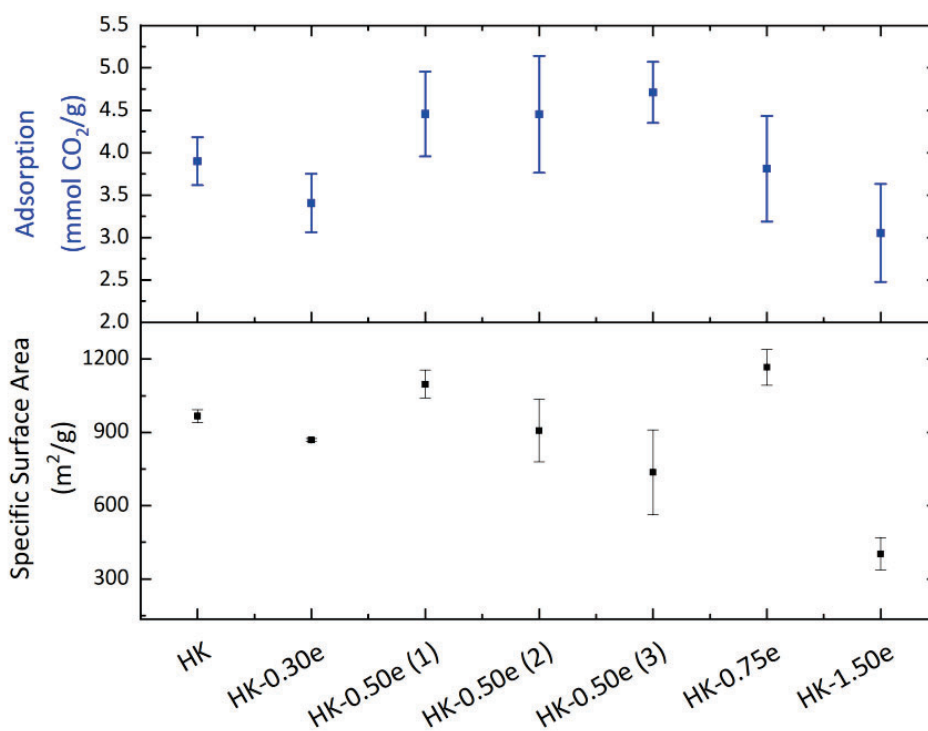


Figure 4.7. CO<sub>2</sub> maximum adsorption values obtained, tested at 298 K and 1000 mmHg and specific surface area, tested at 77 K.

The tendency indicates that achieving reproducible results is a complex task. This is due to the tendency of nanometric powder samples to agglomerate, making it challenging to reproduce results across different batches. Despite treating the sample before each sorption measurement using sonication, obtaining lower

variability of results was nearly impossible, which was a strong indication of low reproducibility. Similar challenges were encountered with specific surface area measurements, as some samples exhibit high values of standard deviation. On the other hand, another aspect to consider is the activation process of sBM samples, which led to various inconveniences, including water adsorption from the environment.

Like in the case of MSM samples, the porosity of sBM samples was measured to determine whether GO content affects the pore size distribution. Since measuring pore size distribution requires recording a complete adsorption-desorption isotherm over a wider range of relative pressures compared to specific surface area measurements, achieving equilibrium stabilization before data acquisition was particularly challenging for sBM samples due to their complex nature. As a result, complete deagglomeration was difficult to achieve, leading to significantly longer measurement times. However, representative results for selected samples are shown in Table 4.1, and key findings from these results can be discussed concerning the data.

*Table 4.1. Pore size distribution of sBM samples.*

<b>Sample</b>	<b><math>V_{\text{pore}}</math> (<math>\text{cm}^3/\text{g}</math>)</b>	<b><math>V_{\text{mic}}</math> (<math>\text{cm}^3/\text{g}</math>)</b>	<b><math>V_{\text{mic}}/V_{\text{pore}}</math> (%)</b>
HK	0.524	0.348	66.4
HK-0.30e	0.300	0.144	47.9
HK-0.50e	0.671	0.447	66.7
HK-0.50e	0.524	0.348	66.4
HK-1.5e	0.341	0.170	49.8

The samples exhibit some variation in total pore volume, ranging from 0.144 to 0.447  $\text{cm}^3/\text{g}$ . Additionally, the micropore volume data reveals that the highest values are found in the HK and HK-0.50e samples, which align with the relationship between micropore volume and total pore volume, indicating that these samples have a higher

micropore content compared to the others. In contrast, the HK-0.30e and HK-1.5e samples show lower values, suggesting that the effect of GO at these concentrations differs from that at 0.50% w/w, where a more significant impact on micropore volume is observed. In general, considering the ratio of micropore volume to total pore volume ( $V_{mic}/V_{pore}$ ), the samples predominantly exhibit microporosity.

### **CO<sub>2</sub> adsorption performance**

In this section, the correlation between the CO<sub>2</sub> adsorption performance and the experimental GO of all the samples is analyzed.

For sBM samples, the results indicate that higher concentrations of 0.50% w/w experimental GO do not lead to increased adsorption. This may be attributed to potential blockage of the open metal sites (OMS) within the MOFs' structure by higher concentrations of GO, or it could be that GO is optimally dispersed within the sample matrix at lower concentrations rather than at higher ones.

As a result, there is a 67% enhancement observed in the most adsorbent sBM samples compared to the pristine HK (sBM), which corresponds to the samples with 0.50% w/w of experimental GO (HK-0.50e) and reach  $4.93 \pm 0.28$  mmol CO<sub>2</sub>/g. Based on the results, it is noteworthy that the synergy between GO and HK is maintained, and the behavior is similar across both synthetic approaches.

The trends observed by analyzing the correlation between the experimental GO and the maximum amount of CO<sub>2</sub> adsorbed per sample is explained below.

Considering the results represented in Figure 4.8, the samples with the maximum CO<sub>2</sub> adsorption values indicate an experimental GO proportion of 0.48-0.55%. Above and below this range, CO<sub>2</sub> adsorption efficiency is not significantly optimized, except for those samples identified as a borderline samples (blue symbols).

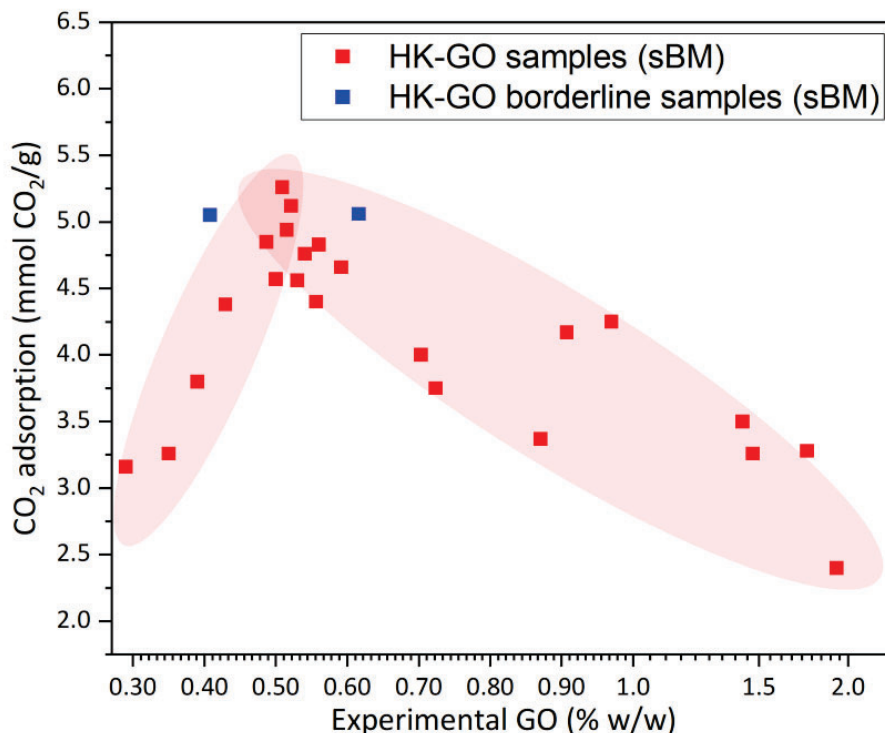


Figure 4.8. CO<sub>2</sub> adsorption values at 1000 mmHg vs. experimental %GO of HK-GO (sBM) samples. Red shadow highlights a proposed trend of the results.

On the other hand, borderline samples (blue symbols, Figure 4.8) represent those samples that although their experimental GO are close to the values of the most adsorbent samples of the trend, they are slightly deviated and not strictly within the optimal range. In this case, these samples present slightly lower particle sizes. Probably, this characteristic, analyzed in *Section 4.2.2* of this chapter, directly affects CO<sub>2</sub> adsorption performance. Overall, parameters such as the nature of each sample during adsorption and dissolution, particle size, degree of agglomeration and synthesis yield significantly impact the CO<sub>2</sub> performance of the samples.

On the other hand, the correlation between CO<sub>2</sub> adsorption and experimental GO from samples obtained via sBM and MSM is depicted in Figure 4.9. The results indicate a similar trend: initially, there is an increment of the adsorption values, followed by a peak within a specific range of experimental GO content (0.25% w/w

experimental GO for MSM samples and 0.48-0.55% w/w experimental GO for sBM samples), and a decrease in the adsorption when the GO exceeds that range (Figure 4.9 top and bottom).

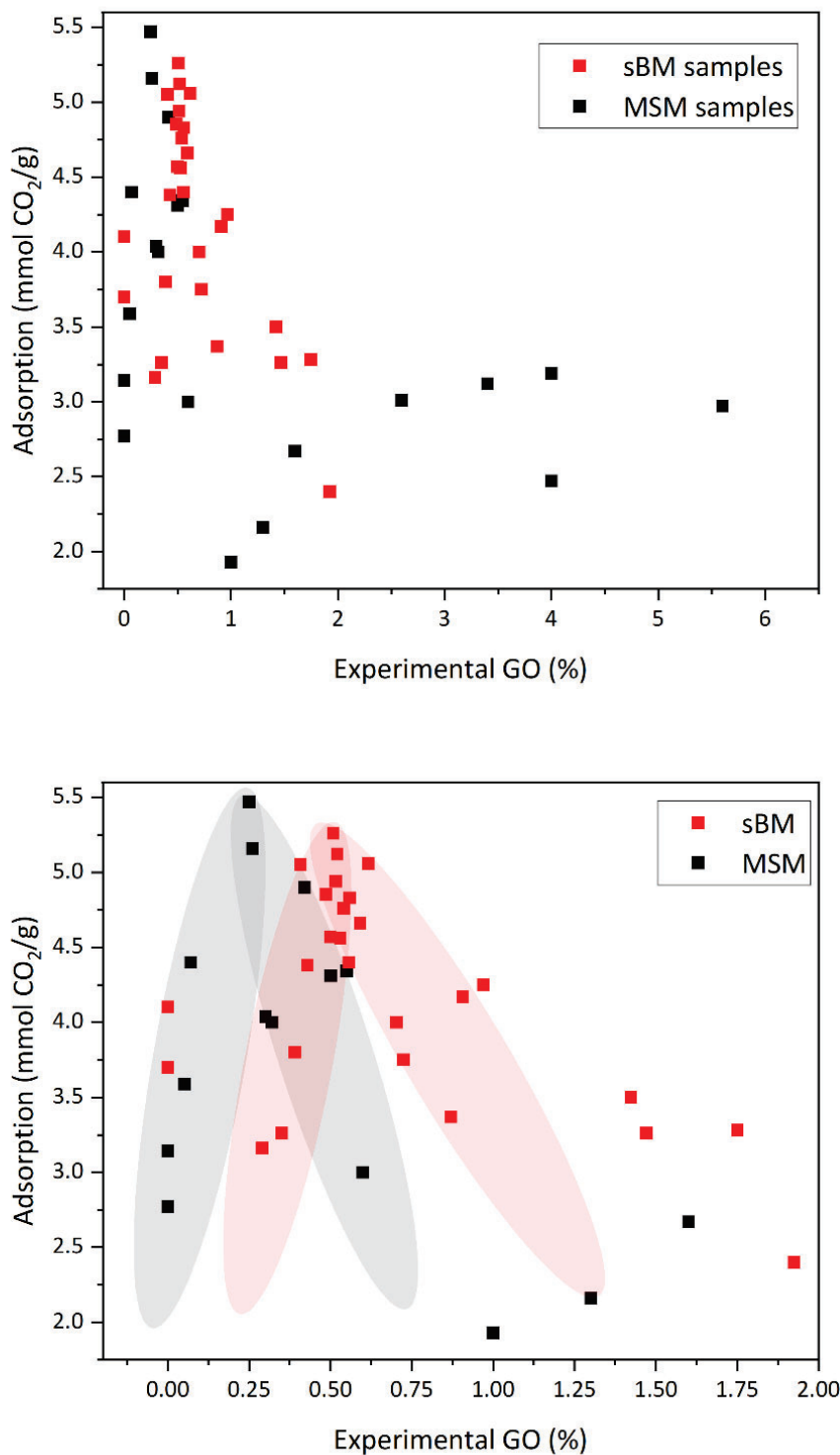


Figure 4.9. (top) CO<sub>2</sub> adsorption values at 1000 mmHg vs. experimental %GO of MSM and sBM HK-GO samples and (bottom) expanded section. Shaded areas highlight the proposed trends of the results.

The results suggest that enhancement of CO<sub>2</sub> capture performance can be achieved by controlling the experimental GO content of the material. Moreover, samples synthesized using different methods exhibit enhanced CO<sub>2</sub> adsorption properties with different experimental GO content.

### **Optimization of experimental procedures and recommendations**

The samples were dissolved at the end of the study for several reasons, including repeating adsorption measurements and using the samples for characterization through techniques such as XRD, IR, TGA, or colorimetry. On the other hand, in addition to the gap of time between adsorption and RQ, other factors could influence the results. These include reusing the sample for measuring other properties, experimental errors during the activation process, the degree of agglomeration during adsorption measurements and the obtained yield from the synthesis of some samples.

To enhance the procedure described above, a different approach would be necessary for obtaining more precise results and refining the tendencies. First, the samples should be dissolved and quantified within a shorter time frame between adsorption measurement and experimental GO determination via RQ. Secondly, the samples should be specifically synthesized for this purpose and not used for other characterization techniques to preserve their integrity.

Additionally, a parallel study would be essential to investigate the degradation of the samples and the effects of atmospheric humidity on their properties, which plays a crucial role in the whole determination of the characteristics and properties of this kind of material.

The following sections expose the results of the characterization techniques used to verify the proper formation of the samples obtained via sBM method. Although most techniques involved measurements of all the samples, the results are focused on those with the highest CO<sub>2</sub> adsorption performance.

### 4.2.3 Particle size measurements

Particle size measurements were carried out to determine the precise crystal size of each sample, and the equipment utilized to perform the measurements was Nanosizer ZS for sBM samples, which as in the case of MSM samples, Dynamic Light Scattering (DLS) is used. The measurements performed for MSM samples, in contrast, used Beckman Coulter LS 13 320 equipment, which also utilized DLS technique. Sonicating the samples before each measurement was necessary to prevent agglomeration and sedimentation to ensure accurate measurements. Therefore, the preparation of the sample before each measurement was sonicated for 10 minutes in ethanol in small quantities of sample. Although the particle size measurements were performed in all the batches of samples, Figure 4.10 shows the results of some selected samples as an example.

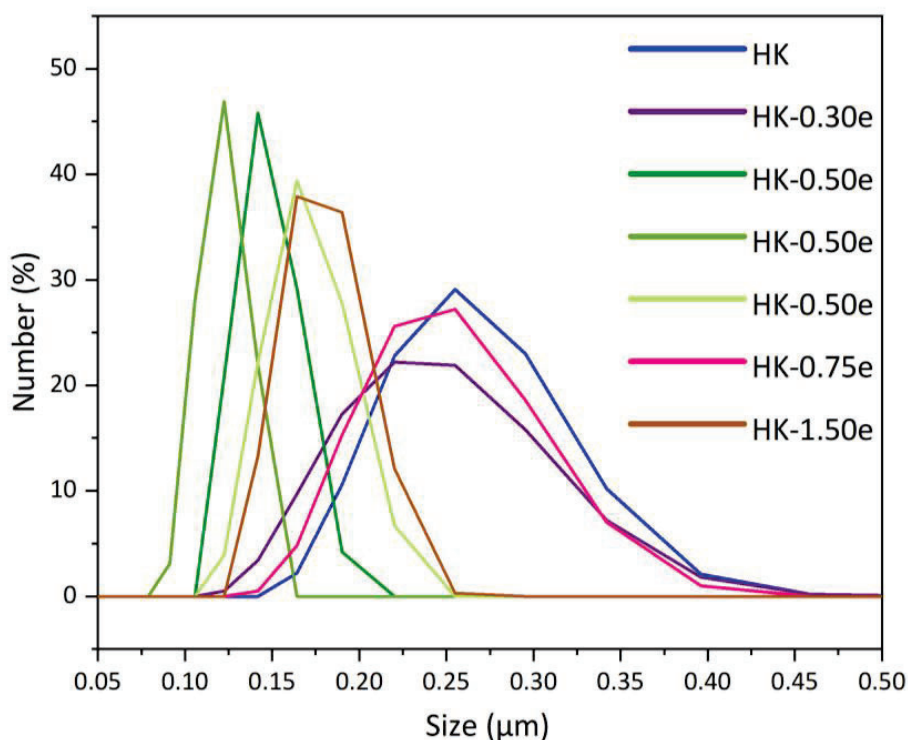


Figure 4.10. Particle size distribution by number for HK-GO (sBM) samples.

The results reveal that the particle sizes of HK-GO (sBM) samples range between 0.09 and 0.45  $\mu\text{m}$  in diameter. The smallest particle sizes were observed in samples

containing 0.50 w/w % of experimental GO, with a percentile  $d_{50}$  between 0.175 and 0.185  $\mu\text{m}$ . The particle sizes of the remaining samples exceeded these values, with the highest value obtained with a percentile  $d_{50}$  of 0.291  $\mu\text{m}$  for the pristine HK.

According to the results of  $\text{CO}_2$  adsorption performance, presented in the previous section of this chapter, those samples containing smaller particle size distribution displayed higher  $\text{CO}_2$  adsorption values. Specifically, HK-0.50e samples exhibited higher  $\text{CO}_2$  adsorption than the samples out of this range of experimental %GO, which precisely presents smaller particle sizes than the rest of samples. This is consistent with the literature, since particle size directly influences the specific surface area of the sample; the smaller the particle size, the greater the total surface area exposed to the adsorbed molecules. Additionally, the smaller the particle, the easier the diffusion of gases through the material, which also enhances the  $\text{CO}_2$  adsorption performance of the sample.<sup>154</sup>

Furthermore, when comparing the particle sizes of both synthetic approaches, it is manifested that samples synthesized using MSM indicate  $d_{50}$  particle sizes of approximately 0.600  $\mu\text{m}$ , with the highest values obtained of around 1.2  $\mu\text{m}$ . The highest particle size results may be attributed to agglomerates of HK-GO (MSM) samples. This value is almost three times the mean particle size obtained in sBM synthesis.

Comparing the results obtained from both experimental approaches, HK-GO (MSM) samples exhibit larger particle sizes and greater dispersion of results, as evidenced by the broader distribution curve obtained. In contrast, HK-GO (sBM) samples display smaller particle sizes, with results falling within a limited range, approximately between 0.175-0.291  $\mu\text{m}$  for the most adsorbent samples (Figure 4.11).

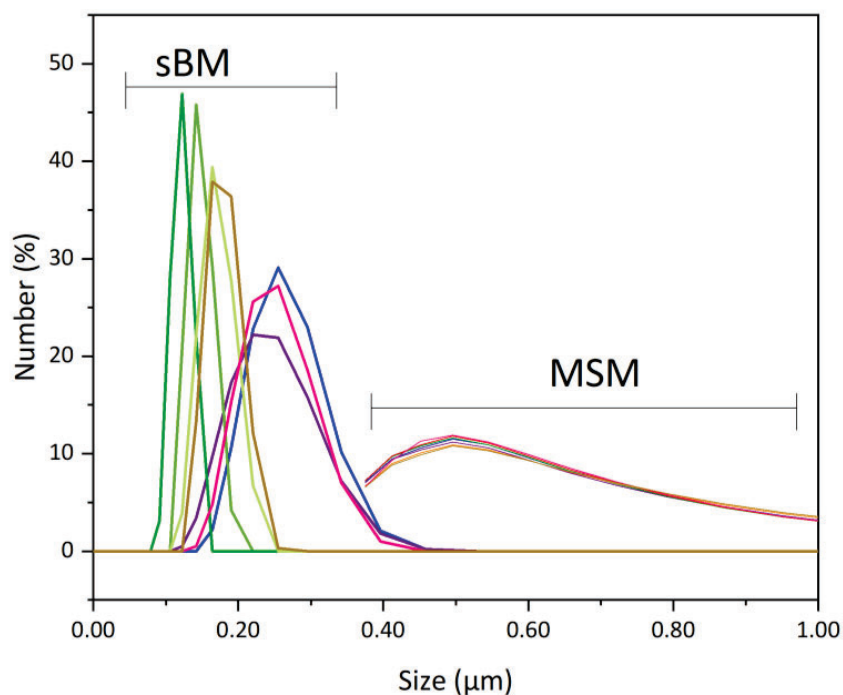


Figure 4.11. Particle size distribution by number for HK-GO samples from MSM and sBM.

#### 4.2.4 X-ray diffraction and infrared spectroscopy

All samples were analyzed using X Ray Diffraction to examine and assess the crystalline structure of the HK samples and determine whether it was altered by the incorporation of GO. Hence, the XRD diffractograms of sBM samples (HK-GO with 0-2.5% w/w GO) were analyzed and compared to the pristine HKUST-1 XRD simulated pattern. However, since the crystalline phase of all the samples remained similar without any alteration, only the XRD diffractogram of the HK and HK-0.50e samples are shown in Figure 4.12, along with the XRD diffractogram of the HK and HK-0.25e samples obtained using MSM, to facilitate comparison between the results from both methods.

The sBM samples present a similar XRD structure compared to the simulated pattern, differing in the intensity of some peaks such as in the case of  $\sim 5.9^\circ$ ,  $9.4^\circ$  or in  $19^\circ$ . Consequently, the results indicate that the incorporation of GO doesn't affect the crystalline structure of the samples when the synthesis is carried out using sBM.

Moreover, sBM samples show slightly greater width of peaks. This outcome suggests that the sBM method yields smaller crystals compared to those obtained through MSM synthesis, as depicted in Figure 4.11 of the previous section.

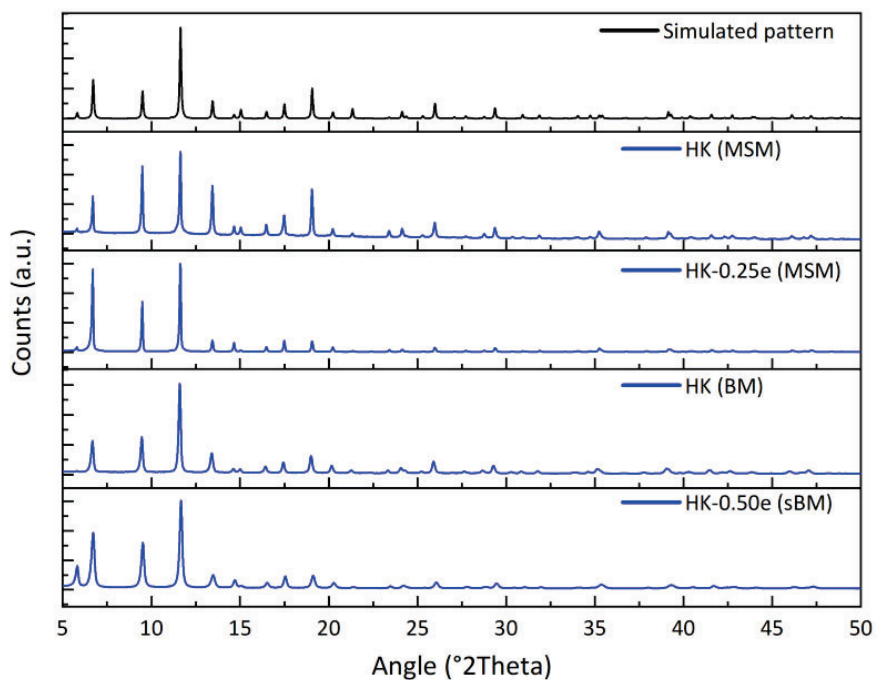


Figure 4.12. XRD simulated pattern of HKUST-1 and XRD diffractogram of HK and HK-GO samples synthesized using MSM and sBM.

### **Influence of Humidity on the XRD Spectra**

As it is suspected that the variations in the intensity of 5.6, 6.6, 9.4° or in 19 could be attributed to changes in the crystalline structure produced by the humidity of the environment (i.e., the conditions in which each sample is measured), a more thorough analysis of the variation of the intensities is performed. To investigate this, an experiment was conducted to detect changes in the XRD diffractogram during the activation process. The procedure involved obtaining diffractograms of HK (sBM) while simultaneously introducing a stream of synthetic air into the chamber and altering the sample temperature. In situ XRD diffractograms with temperature and synthetic air flow were collected successively every 30 minutes, starting at 25°C, then

continuing at 150 °C for three successive measurements, followed by decreasing again the temperature to 25°C (Figure 4.13).

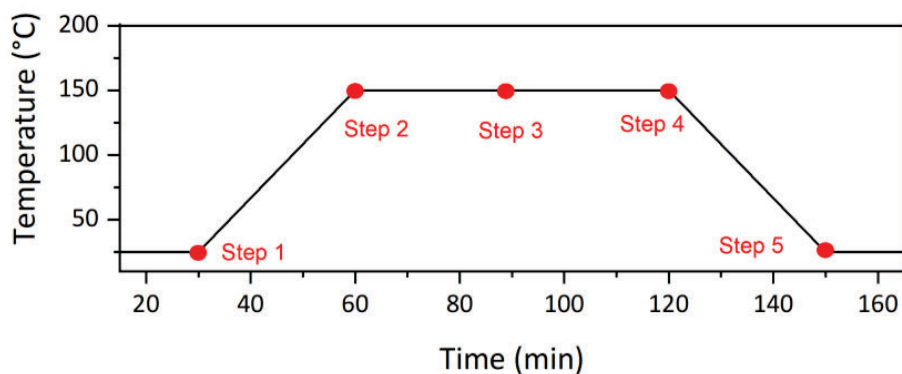


Figure 4.13. Steps of the experimental procedure carried out for determining changes in the XRD crystalline structure. Each step is the performance of a XRD diffractogram.

The results reveal several findings, showing differences in the intensity of some specific peaks at each step and the disappearance of some peaks (Figure 4.14).

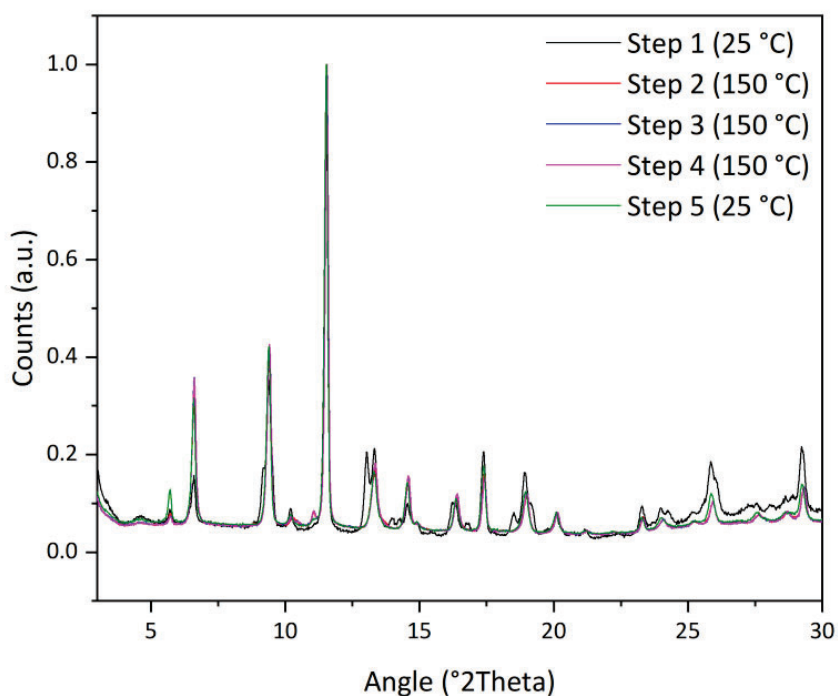


Figure 4.14. XRD pattern of HK sample at different levels of activation steps.

Firstly, the intensity of the peaks at  $5.6^\circ$  and  $6.6^\circ$  varied across the different levels of activation (Figure 4.15 (a)). Moreover, extra peaks observed in the diffractogram of step 1 disappear during the activation process, such as the double peak around  $13.1^\circ$  or the peaks around  $14^\circ$  and  $18.5^\circ$  (Figure 4.15 (b)).

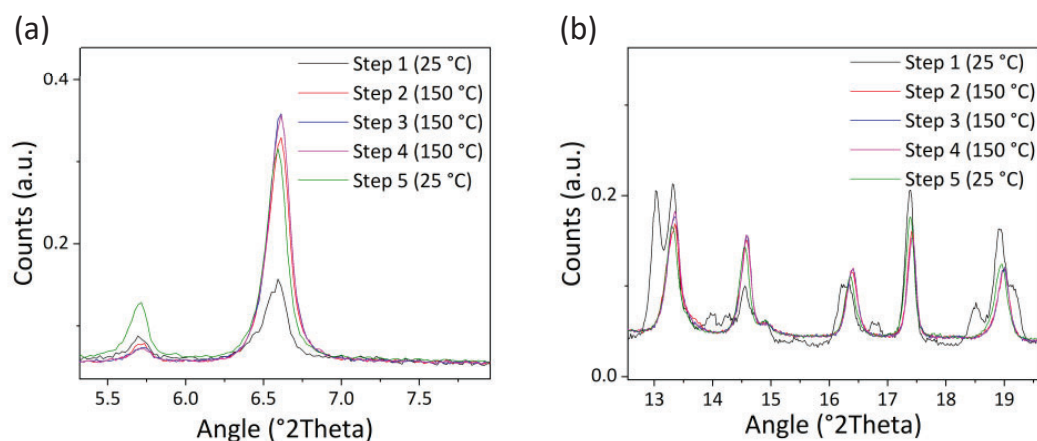


Figure 4.15. Expanded section of the XRD experiments performed on HK.

Once the sample reached  $25^\circ\text{C}$  in step 5, the intensity of the initial peaks situated at  $5.6^\circ$  and  $6.6^\circ$  varied again, indicating that although sample is completely activated, the decrease in temperature probably allowed some  $\text{H}_2\text{O}$  molecules from the environment to adsorb onto the surface (Figure 4.15 (a)). On the other hand, extra peaks detected on the diffractogram of step 1 are not observed in the diffractogram of step 5, which suggests that probably  $\text{H}_2\text{O}$  molecules are preferentially adsorbed in specific regions of the sample, affecting primarily in the initial peaks rather than other parts of the pattern (Figure 4.15 (b)).

These experiments demonstrated that the XRD diffractogram of the sample changes depending on the level of activation during the drying process, closely associated with the adsorption of water molecules from the environment, as previously suspected.

Considering these results, it was possible to verify the effect that water has on the crystalline structure of the samples. However, in *Chapter VI*,  $\text{H}_2\text{O}$  adsorption and the

corresponding competition with CO<sub>2</sub> molecules in the adsorption performance are analyzed in more detail using additional techniques and methods (Infrared Spectroscopy (IR), Dynamic Vapor Sorption (DVS), Breakthrough Analysis (BTA) and <sup>13</sup>C Nuclear Magnetic Resonance (<sup>13</sup>C-NMR)).

### **Effect of BM on Crystal Size**

The hypothesis of obtaining small crystals based on the observation of slightly broader peaks in the XRD diffractogram (as observed in the case of peaks at 9.5° and 11.6°, Figure 4.16) is consistent with reports in the literature. The BM process involves mechanical milling, wherein the reagents are forced to impact each other, thereby increasing both the kinetic and thermal energy within the reaction jar. The increase in energy can lead to an increase in pressure, both of which are fundamental factors influencing particle size in a chemical reaction. Apart from these parameters, which are controllable based on the revolutions and the employed time in the reaction, the size and quantity of balls used in the milling process are also considered. Utilizing smaller balls may yield finer milling and, consequently, a smaller particle size in the final product.<sup>155</sup>

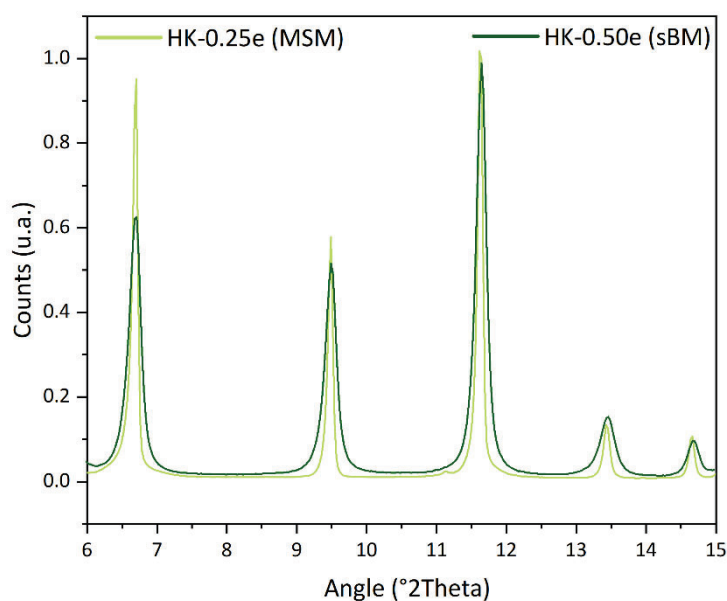


Figure 4.16. Expanded section of the overlapped XRD pattern of HK-0.50e (sBM) and HK-0.25e (MSM) samples.

To provide a more precise analysis of the peaks observed in the XRD diffractogram from both samples, an approximation of the crystal size is calculated using the *Debye-Scherrer* equation (Equation 4.1). This equation is utilized generally to obtain the crystal size of nanoparticles, where  $D$  is the crystal size in nanometers,  $K$  is the Scherrer constant (0.98),  $\lambda$  corresponds to the wavelength of the radiation used during the X-ray measurement, and  $\beta$  corresponds to the full width at half maximum (FWHM)<sup>156</sup>.

$$D = \frac{K\lambda}{\beta \cos\theta} \quad \text{Equation 4.1}$$

Based on the XRD diffractogram depicted in Figure 4.16, the calculations performed using equation 4.1 for both samples provide a result of 178 nm for the crystal size of HK-0.50e (sBM) and 1552 nm for the crystal size of HK-0.25e (MSM). Thus, the results align with the initial hypothesis, where samples obtained via sBM produce smaller crystal sizes than those samples obtained through MSM method.

### **Infrared Spectroscopy measurements**

Like MSM samples, infrared spectroscopy (IR) was conducted on all sBM samples (HK and HK-GO 0.15-2.5% w/w GO) to assess their chemical structure. IR spectra of all the samples performed similar features and had almost the same band displacement. Figure 4.17 shows as an example, IR spectrum of the pristine HK and HK-0.50e for samples synthesized sBM method along with HK and HK-0.25e samples obtained using MSM to compare the results from both methods of synthesis.

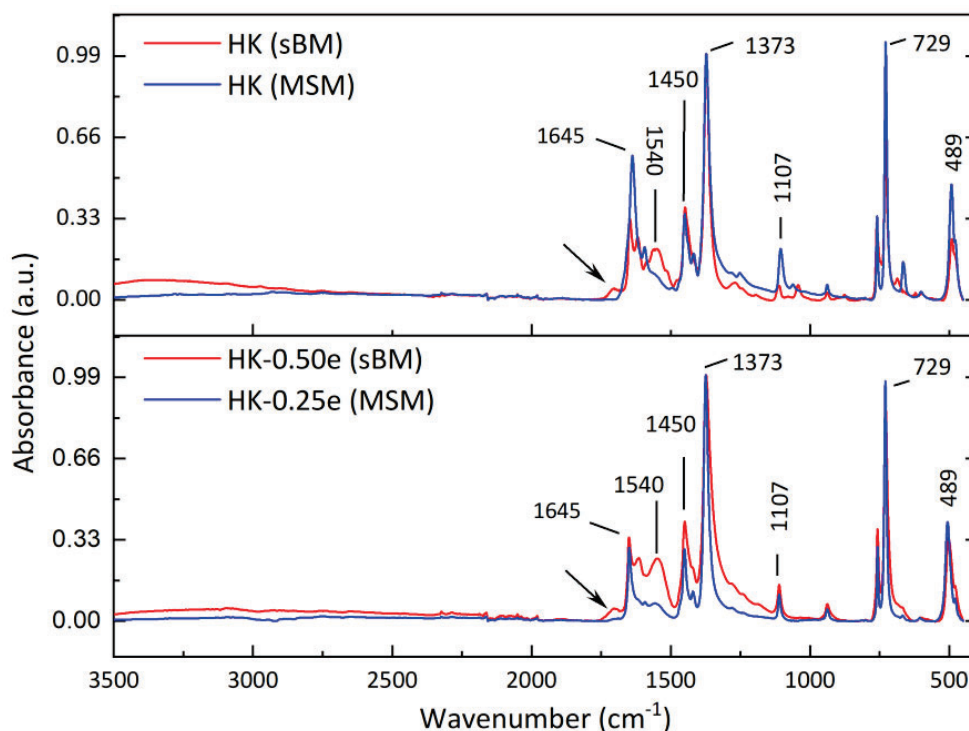


Figure 4.17. Infrared spectra of HK, HK-0.25 synthesized using MSM and sBM.

The results indicate almost the same bands observed on MSM samples, confirming that the introduction of GO did not alter the corresponding bands attributed to the MOF and verifying the successful formation of the material. Moreover, the characteristic bands corresponding to GO functional groups don't appear in the spectra, probably due to the small quantities used in the synthesis of the samples.

IR spectra of all the samples show a small band which appeared at approximately  $1700\text{ cm}^{-1}$  (indicated as a black arrow in the spectrum), indicating the presence of C=O vibrational bands, probably related to ligand traces. Subsequently, additional washing was carried out in the procedure to minimize the presence of ligand in the product. The samples were invariable in the spectra after several washing steps using 1:1 EtOH:H<sub>2</sub>O followed by filtrations. On the other hand, the band at  $1540\text{ cm}^{-1}$ , which corresponds to C=C vibration of the benzenic ring, presents higher intensity in sBM than in MSM samples.

The results of the samples obtained by both methods expose similar characteristics, indicating a chemical resemblance in the vibration carboxylic bands and the vibrations from BTC ligands within the MOF structure, previously described in *Chapter III, Section 3.2.2*. The similarity of the IR spectra suggests that sBM and MSM methods are equally valid for obtaining HK-GO samples, implying consistent and reproducible results regarding the structural characteristics of the material.

#### **4.2.5 Thermogravimetry analysis**

Thermogravimetric tests were conducted to explore the thermal behavior and to compare the thermal stability of the samples obtained by both methods (sBM and MSM).

All tests using thermogravimetric analysis on samples obtained using sBM method were conducted in air atmosphere at a flow rate of  $50 \text{ mL min}^{-1}$  and performed from  $25^\circ\text{C}$  up to  $1000^\circ\text{C}$ , using a heating ramp of  $10^\circ\text{C/min}$ .

Only the results for HK and HK-0.50e samples obtained via the sBM method are presented (Figure 4.18), as thermogravimetric analyses were conducted on all HK-GO samples, revealing similar thermal behavior.

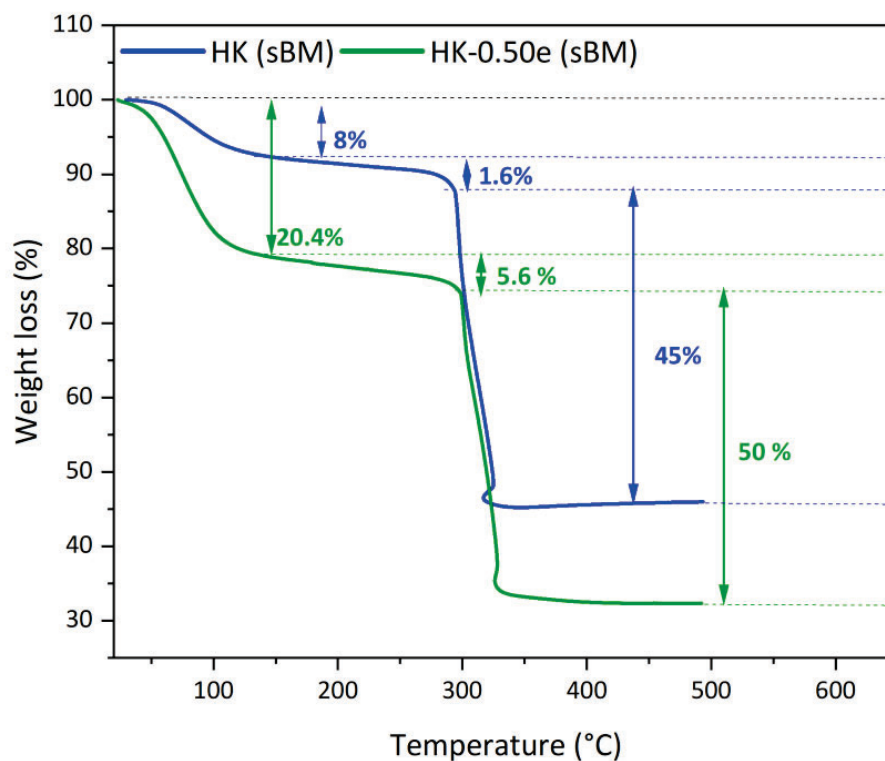


Figure 4.18. TGA curves of HK and HK-0.25 (sBM) samples.

The results from thermogravimetry displayed the same thermal degradation observed on MSM samples divided into three steps:

1. **Solvent removal**
2. **Degradation of the functional groups**
3. **Thermal decomposition of the carbon skeleton**

When comparing the HK and HK-0.50e (sBM) samples, it was noted that both exposed almost identical thermal stability profiles. Initially, the evaporation of solvents such as water and ethanol occurred around 100 °C, with approximately 8% for HK and 20.4% for the HK-0.50e, which strictly differs depending on the initial dryness level of the sample. The variation in this aspect can be attributed to differences in the initial activation conditions of the sample and the relative humidity in the air prior to each measurement. Subsequently, a gradual weight loss was observed until reaching approximately 300 °C, attributed to the degradation of

functional groups on the material's surface, accounting for around 1.6% for HK and 5.6% for HK-0.50e. Finally, both samples exhibited the decomposition of their carbon-based skeletons, marked by a sharp decline starting at 300°C and continuing until 320 °C for both samples, losing approximately 45% for HK and 50% for HK-0.50e of the weight.

In summary, both samples exhibited similar decomposition behaviors, differing only in the percentage of solid residue (CuO). This variance depends on the solvents trapped in the porous structure of the sample and the quantity of GO introduced in the synthesis of the HK-GO sample, resulting in a final solid of approximately 46% for HK and around 32% for HK-0.50e of the total mass analyzed.

Additionally, a comparative analysis of the thermal behavior of HK-GO samples synthesized by both methods (MSM and sBM) revealed slight differences. As an example, the degradation curves of the most adsorbent samples, HK-0.25e (MSM) and HK-0.50e (sBM); are analyzed and the corresponding diagram is shown in Figure 4.19.

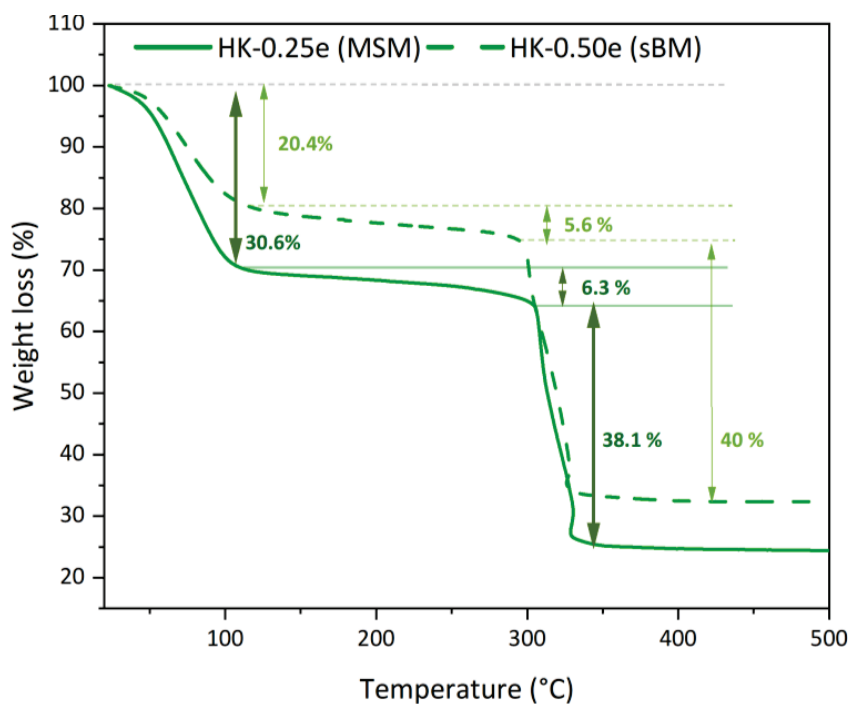


Figure 4.19. TGA curves of HK-0.25 (MSM) and HK-0.25 (sBM) samples.

The initial weight loss, occurring around 100 °C, was attributed to solvent elimination. There was a notable difference in the percentage of extracted solvents, with HK-0.25e (MSM) showing a higher removal (30.6%), likely due to residual DMF trapped in its structure or the water molecules that remained unextracted during the first weight loss. Following this, a second slight weight loss phase occurred up to approximately 300 °C in both cases, due to the functional groups' degradation, where in both samples the weight loss is around 6%. From 300 °C onwards, the carbon skeleton of the samples decomposes, and the weight loss for HK-0.25e (MSM) is slightly lower than for HK-0.50e (sBM), at around 38%.

The final weight loss indicated different percentages of remaining CuO solid, consistent with the initial difference of weight loss attributed to the solvent content in the samples. This indicates that having a lower percentage of water initially trapped in the structure leads to a higher final solid product weight after thermal decomposition. Notably, the final solid percentages in both samples differed by only approximately 7.6%, closely matching the initial weight difference attributed to solvent removal (which is around 10.2%). Therefore, based on these thermal decomposition curves, it is interpreted that both samples, despite being synthesized using different procedures, exhibit very similar thermal stability.

#### **4.2.6 Scanning electron microscopy**

To further investigate the morphology and textural properties of the synthesized materials, Scanning Electron Microscopy (SEM) analysis was performed, following the same steps as in MSM sample characterization. Given the similarities observed in the XRD patterns, SEM analysis was carried out to examine whether the incorporation of GO induces noticeable morphological changes. Representative images of selected sBM and MSM samples are presented and compared in the following section to evaluate potential differences in particle size and surface textures.

SEM images of the sBM samples reveal agglomerates of smaller crystals, in the range of nanometers (Figure 4.20 (a)- (d)). This observation aligns with the findings from the XRD spectroscopy analysis, in *Section 4.2.3*, where it was suspected the obtention of smaller crystals because of the detection of broad peaks in the diffractogram. On the other hand, no differences between sBM samples without GO (Figure 4.20 (a-b)) and with GO (Figure 4.20 (c-d)) are detected.

On the other hand, the images of MSM samples (Figure 4.20 (e-f)) exhibit higher particle size, with appreciable defects in the surface of the crystals, the extent of which appear to correlate with the incorporated GO, as determined in the results presented in *Chapter III, Section 3.2.4*.

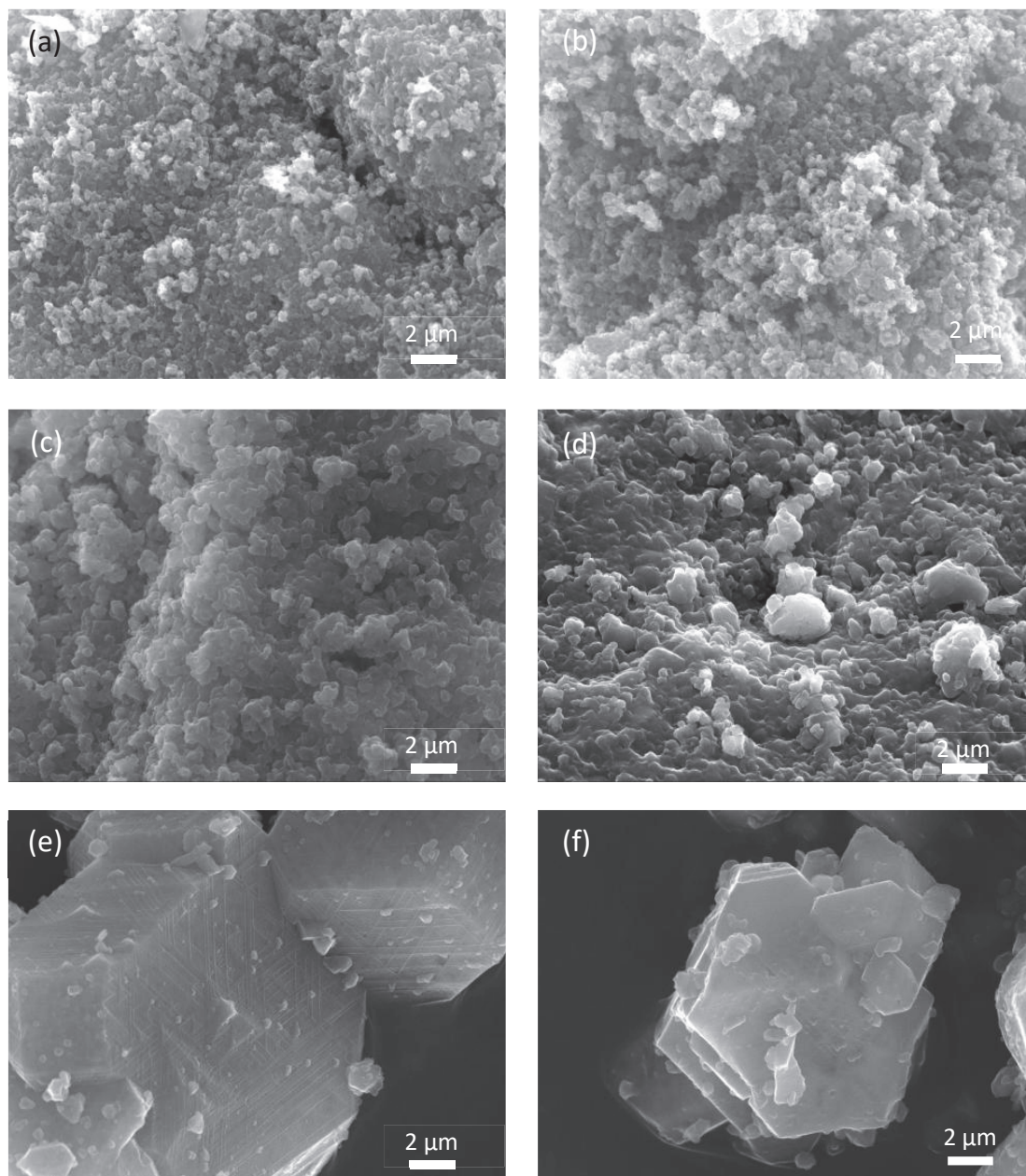


Figure 4.20. SEM images of (a-b) HK (sBM), (c-d) HK-0.50e (sBM), (e) HK-0.50e (MSM) and (f) HK-0.25e (MSM).

### 4.3 Statistical analysis (small ball milling)

Considering CO<sub>2</sub> adsorption performance, *Section 4.2.2* presents the results as individual scattered samples. This approach was selected to reflect the practical incorporation of GO, which may differ from theoretical values. The results presented certain challenges in reproducibility due to yield and environmental factors, along with the inherent characteristics of each individual sample.

To further investigate these observations, statistical analysis was performed, specifically based on the MSM and sBM results, focusing on analyzing the trends and variances to provide a quantitative understanding of the scattering. A comprehensive and extensive explanation of these statistical analyses, including the calculation ranges, detailed methods for Pearson's correlation coefficient, coefficient of variation, and ANOVA tests, along with the corresponding tables and graphs, is provided in the *Appendix*. A summary of the key findings is presented below.

#### **MSM and sBM**

The MSM and sBM synthetic methods produced sets of samples that behave similarly. The HK-GO materials obtained from both MSM and sBM are a material that is significantly influenced by the percentage of GO added during synthesis. CO<sub>2</sub> adsorption results are directly related to the quantity of experimental GO content acquired in the final composite. The data reveals a specific range in which maximum CO<sub>2</sub> adsorption values are achieved. The Pearson coefficient in both methods reinforces the correlation between CO<sub>2</sub> adsorption performance and experimental GO content.

For MSM samples, the range of 0.00 to 0.25 indicates a strong positive correlation, afterward the correlation becomes strongly negative until a range of 1.00% of experimental GO. For contents above 1.00% the correlation remains neutral.

Contrastingly, sBM samples indicate the same tendency regarding the correlation of CO<sub>2</sub> adsorption and experimental GO but the shift occurs up to 0.61% of experimental GO.

Moreover, the coefficient of variance indicates that both methods are reproducible, considering CO<sub>2</sub> adsorption performance, while the synthesis of samples is not as reproducible regarding the quantity of experimental GO content, with sBM exhibiting greater variability of results.

Based on ANOVA statistics, the CO<sub>2</sub> adsorption performance of the samples obtained from both methods is significantly influenced by the content of experimental GO, since p-values are lower than the established reference threshold of 0.05.

On the other hand, the statistics of sBM samples indicate an F value higher than that of the MSM samples (10.69 versus 8.79). This aspect suggests that the samples of sBM provide a higher differentiation across the range of experimental GO. However, this does not necessarily imply more precise results, since CO<sub>2</sub> adsorption results indicate higher variance coefficients.

Hence, the Pearson coefficient, variance coefficient, and ANOVA determined a more robust relationship between CO<sub>2</sub> adsorption performance and experimental GO content in the MSM method, despite the slightly lower differentiation compared to sBM sample results.

#### **4.4 Materials characterization and performance for samples obtained via bBM**

The following section provides the corresponding analysis of the results from samples synthesized using the big ball milling method (bBM). As in the case of sBM samples, the first point of this section was to determine experimental GO utilizing Reverse Quantification (RQ). Once the results of the quantification are presented, the CO<sub>2</sub> performance of all the samples are shown.

Additionally, subsequently to RQ and gas sorption properties, the results of the characterization measurements performed on bBM samples are exposed for the same purpose as in the case of sBM and MSM samples: validating the formation of HKUST-1 and analyzing the effects of GO on HK-GO samples. The characterization techniques utilized the same equipment as in sBM samples.

#### 4.4.1 Reverse quantification

Proceeding as the same as when analyzing the results of MSM and sBM sample performances, a quantification of the experimental GO was realized to bBM samples.

The results from RQ show, in general, similar outcomes to those previously observed in sBM samples (Figure 4.21). Additionally, the results also slightly deviate from the ideal behavior. The experimental content of GO is higher than theoretical GO content employed in the synthesis for samples below 0.50% w/w of theoretical GO. And above 0.50% w/w of theoretical GO, the results exhibit that samples contain a lower content of experimental GO than theoretical GO. The following figure illustrates the relationship between experimental and theoretical GO across different batches of samples.

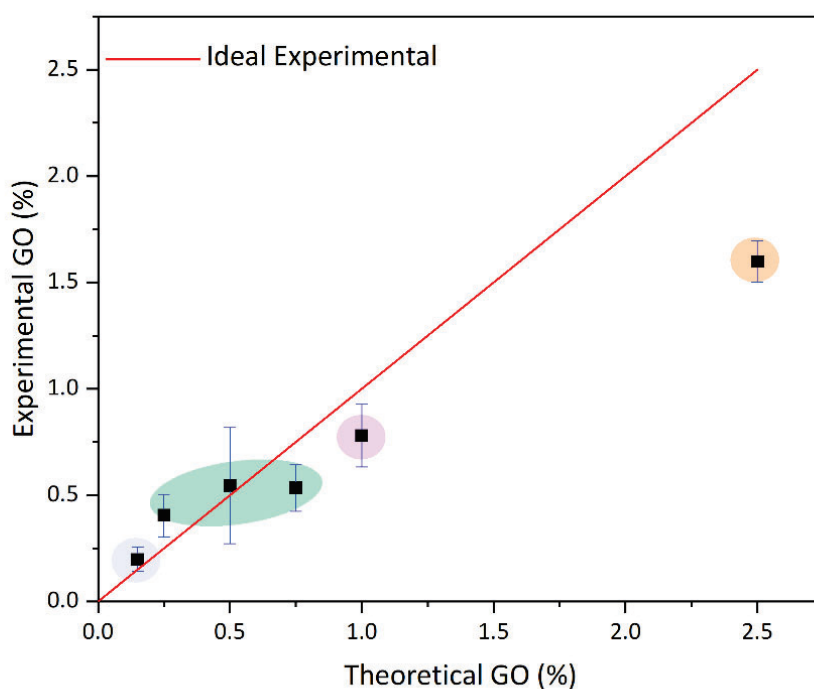


Figure 4.21. Experimental %GO vs. theoretical %GO of the synthesized samples (bBM). Red line represents the ideal value of 100% incorporation of GO in synthesis and shaded areas indicate group of samples with similar experimental GO values.

Moreover, like for sBM samples, in this case four different groups of samples were detected considering experimental GO determined using RQ: there's a group of samples around 0.20% w/w GO, another group of samples around 0.50% w/w GO, a group of around 0.75% w/w GO and another group of around 1.5% w/w GO (indicated each group using a different color).

Likewise, to the sBM samples, the grinding process combined with the challenging dispersive behavior of GO at low concentrations, probably produced that the reagents didn't completely react producing less formation of HK and related with the obtained yield. In the case of bBM samples, in general, all the yields were around 70%.

Considering the previous analysis of the samples, which determined the experimental GO content, the nomenclature of the samples will henceforth be HK-Xe in the following sections, following the same approach as in this chapter with the sBM samples. Where HK refers to the MOF HKUST-1, while X represents the experimental GO content of the sample, emphasizing that it is experimental by using the letter 'e'.

#### **4.4.2 Gas sorption measurements properties and surface properties**

Following the research focus of this study, the next section presents the CO<sub>2</sub> performance results obtained from bBM samples. First, it discusses the CO<sub>2</sub> isotherms of the synthesized samples, followed by an analysis of the relationship between experimental GO and the CO<sub>2</sub> adsorption performance of all samples.

##### **CO<sub>2</sub> adsorption isotherms**

CO<sub>2</sub> adsorption isotherms were performed at 298 K using BET equipment to evaluate the CO<sub>2</sub> capacity adsorption of the synthesized samples up to 1000 mmHg and at 25°C, using the same conditions of measurement as the HK-GO (sBM) and (MSM) samples, presented in *Section 4.2.2* of this chapter and in *Section 3.2.6 of Chapter III*.

In this case, Figure 4.22 exhibits the CO<sub>2</sub> isotherms of some samples selected as an example along with the CO<sub>2</sub> adsorption isotherm of GO powder. As can be seen, in this case, all the samples also exhibit higher CO<sub>2</sub> adsorption performance than GO. Moreover, samples which retain more CO<sub>2</sub> molecules are those represented in green, which contain 0.30 and 0.25% w/w experimental GO. Samples which contain more than this range of experimental GO exhibit a decrease in the adsorbent properties, as can be seen in those samples exceeding this range. On the other hand, pristine HK also exhibits a CO<sub>2</sub> adsorption performance close to those with increased performance compared to the rest of the samples, which indicates that, in this case, the enhancement of CO<sub>2</sub> adsorption performance is not as pronounced as for the samples synthesized using sBM and MSM.

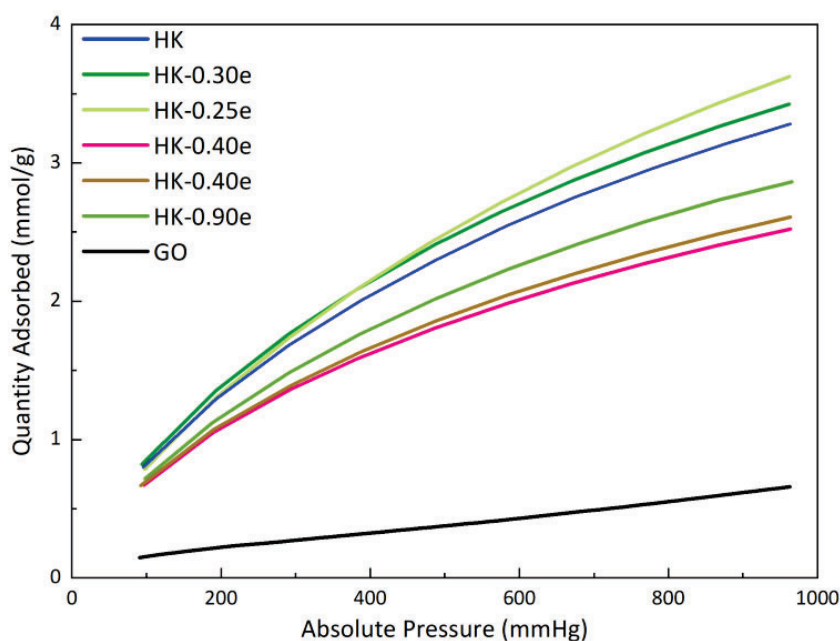


Figure 4.22. CO<sub>2</sub> adsorption isotherms of samples synthesized using bBM, performed at 298 K and up to around 1000 mmHg.

### **Challenges and Limitations during Adsorption Measurements**

During the initial experiments of adsorption, it is detected that the samples obtained via bBM secreted a significant release of water throughout the activation step, evidenced because of the condensation of water noted inside the tubes used for BET measurements. Despite prolonging the time of desiccation or applying some cycles of nitrogen stream or vacuum, the material was continuously extracting water, which in all cases was a difficult task to extract from the analysis tubes. The process was carried out several times, but the results of BET specific surface area and CO<sub>2</sub>/N<sub>2</sub> adsorption isotherms couldn't be completed in these conditions due to software errors and the collapse of the BET equipment. Consequently, the preparation process of HK-GO (bBM) samples was slightly modified before the activation step and prior each adsorption measurement. It was suspected that the new as-synthesized samples were highly agglomerated compared with the previous ones, making the extraction of water from their pores and the activation of the sample an exceedingly challenging task. Thus, the time of sonication in EtOH:H<sub>2</sub>O before the activation step was extended to 30 minutes, and the samples were ground again after filtration, prior to the activation step. Following these adjustments, the activation step proceeded as before: the material was heated at 170 °C overnight while a nitrogen gas stream was introduced. Afterwards, it was noted that isotherm measurements became feasible.

### **Specific surface area and pore size distribution**

Evaluating specific surface area and pore size distribution was also considered in the case of bBM samples, like in *Section 4.2.1* of this chapter. However, in this case the pore size measurements were only performed on HK and HK-0.30e samples, as a representative example. The equipment utilized in this case was 3P Micro from Nane.

Based on the results, the specific surface area for HK is 462 m<sup>2</sup>/g, while for HK-0.30e, it is 486 m<sup>2</sup>/g. These results indicate a relatively low specific surface area compared to samples synthesized using other methods.

On the other hand, the total pore volume is around  $0.30 \text{ cm}^3/\text{g}$ , with a pore size diameter of approximately 3 nm for both samples. It appears that the presence of GO in these particular samples does not significantly affect the pore size or total porosity, as both samples exhibit similar characteristics. However, considering the results from other samples and the high level of agglomeration observed in the bBM samples, it is difficult to definitively conclude that GO does not influence porosity in all cases. This suggests that trends observed in other concentrations of GO may not be present here. Consequently, additional experiments on pore size distribution would be necessary to draw more definitive conclusions.

These results may be attributed to the high level of agglomeration found in bBM samples, or possibly due to incomplete activation of the samples during the experiments. Therefore, further experiments would be required to establish a more robust trend, but this was not possible due to time constraints.

#### **CO<sub>2</sub> adsorption performance**

The CO<sub>2</sub> adsorption performance of different batches of bBM samples were analyzed and related with their experimental GO resulting from the RQ (Figure 4.23). Despite showing great variability of results, the CO<sub>2</sub> adsorptive behavior remains consistent with the behavior observed in the samples obtained through MSM and sBM procedures, indicating, in this case, a trend in which samples ranged between 0.25-0.30% w/w of experimental GO are the most adsorbent samples. On the other hand, it is also noted that while the concentration of GO is increasing, the maximum capacity of CO<sub>2</sub> adsorption decreases.

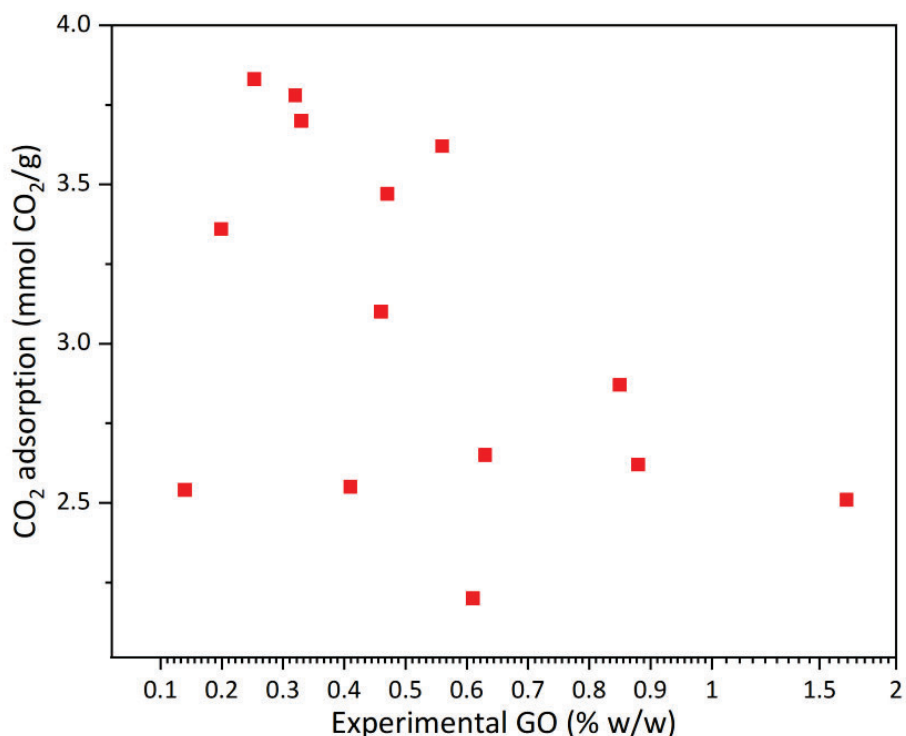


Figure 4.23. CO<sub>2</sub> adsorption values at 1000 mmHg vs. experimental %GO of HK-GO (bBM) samples.

Based on the results, a high variability concerning the experimental GO content quantified and the CO<sub>2</sub> adsorbent properties are detected, especially in the range of 0.40-0.85% w/w GO. This area of results shows a decrease in and increase in the adsorption capacity without a defined pattern. In the case of bBm samples, probably, the distributed GO in HK structure varies in function of other intrinsic parameters, such as the particle size or the purity phase of samples. Even though all the inconveniences and difficulties found during the fabrication of the samples using bigger quantities (such as the high hygroscopic character and the high level of agglomeration found in the samples), the results indicate a similar trend compared with the results obtained from the small scales, where the CO<sub>2</sub> adsorption capacity is presented with a maximum peak of performance in a specific range of experimental GO (0.25-0.30% w/w GO), reaching values of optimized CO<sub>2</sub> adsorption of  $3.77 \pm 0.07$  mmol CO<sub>2</sub>/g.

On the other hand, sBM samples indicate higher CO<sub>2</sub> adsorption values than bBM samples.

#### 4.4.3 Particle size measurements

Like performed in the other cases with sBM and MSM samples, particle size measurements were carried out to analyze the sizes of the synthesized samples obtained via bBM method. As an example, Figure 4.24 presents the particle size of HK-0.30e (bBM) sample, along with HK-0.50e (sBM) and HK-0.25e (MSM).

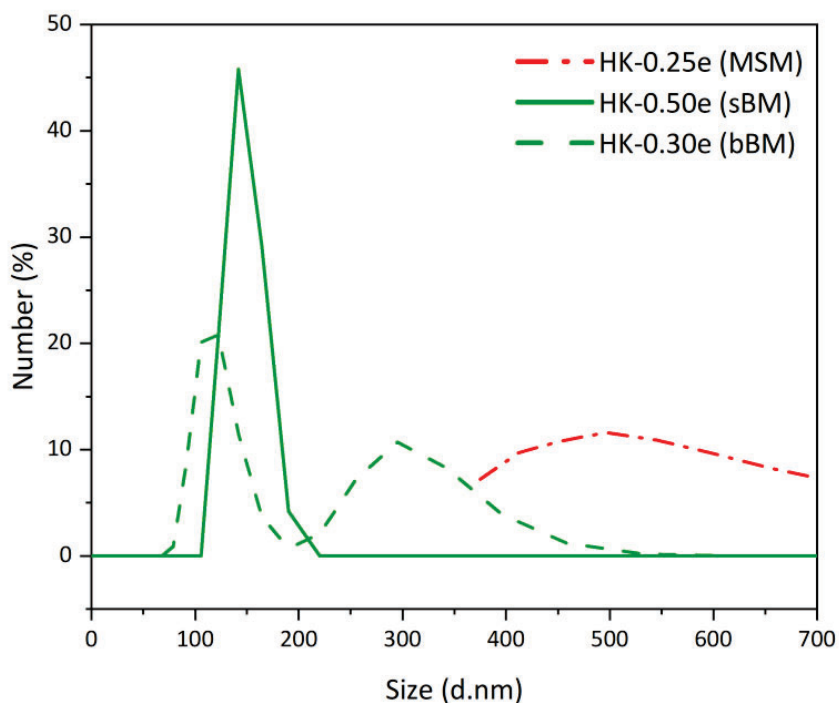


Figure 4.24. Particle size distribution by number for the most adsorbent samples synthesized using MSM, sBM and bBM.

Concerning the results, it is observed that although the samples continue to reveal a nanometric size, the size shows a bimodal distribution, which is not observed in the particle size of sBM and MSM samples. There is a group of particles which tend to be around 200 nm and there is another group of around 500 nm. This trend is consistent across all the samples synthesized using bBM, although the result presents only the size distribution of HK-0.30e as an example.

The bimodal profile of the particle size distribution can be attributed to several factors. Firstly, the use of fewer revolutions in the grinding procedure likely influences the formation of the HK crystal, resulting in nanometric particles with varying sizes and less homogeneity across the sample. Secondly, as described in the following section, during the activation step it is detected that bBM samples exhibit a higher level of agglomeration compared to sBM and MSM samples, which potentially influences the performance of measurements.

Comparing the particle size of the samples obtained using all the methods studied in this work, a tendency is noticeable. Samples with higher particle size are synthesized using MSM, with a particle size  $d_{50}$  between 586-600 nm. Following this, samples obtained by bBM achieve fewer particle sizes than MSM but are slightly larger than sBM in most cases. The results indicate a particle size  $d_{50}$  ranging between 121 and 321 nm, presenting a bimodal distribution with a group of particles reaching values up to 400- 500 nm. On the other hand, sBM samples achieve the smallest particle size, with a particle size  $d_{50}$  ranging between 139 and 255 nm.

#### **Effect of particle size in the CO<sub>2</sub> adsorption performance**

Producing material with two distinct particle sizes could lead to varying CO<sub>2</sub> adsorption results. As previously discussed in *Section 4.4.2*, the adsorption performance and experimental GO (Figure 4.23) exhibit significant variability. Given the nature of the bBM samples, the particle size distribution aligns with the fluctuations observed in their CO<sub>2</sub> adsorption performance, suggesting a direct correlation between particle size and adsorption behavior.

#### **4.4.4 X-ray diffraction and infrared spectroscopy**

As described in the previous procedures, XRD was conducted to verify the correct formation of all HK-GO (bBM) samples, synthesized in the range of 0.15-2.5% w/w GO. As an example, the most adsorbent samples of MSM, sBM and bBM methods are represented in Figure 4.25.

In this instance, the XRD diffractograms of bBM samples shows a broadening of the peaks, as in the case of sBM samples. Moreover, small additional peaks are detected suggesting that trimesic acid and copper acetate probably didn't completely react, as well as the initial peaks at  $\sim 5.6^\circ$  related to the activation level of the samples (analyzed in *Section 4.2.3* of this chapter).

Comparing the diffractograms of the most adsorbent samples, the MSM diffractogram of sample HK-0.25e exhibits narrower peaks than those of sBM and bBM samples. This suggests that the MSM samples have larger crystal sizes compared to those obtained via sBM and bBM, whose diffractograms display broader peaks. Additionally, in all cases, the diffractograms of the samples closely resemble the simulated pattern of HKUST-1, confirming the successful formation of MOFs through all three synthesis methods.

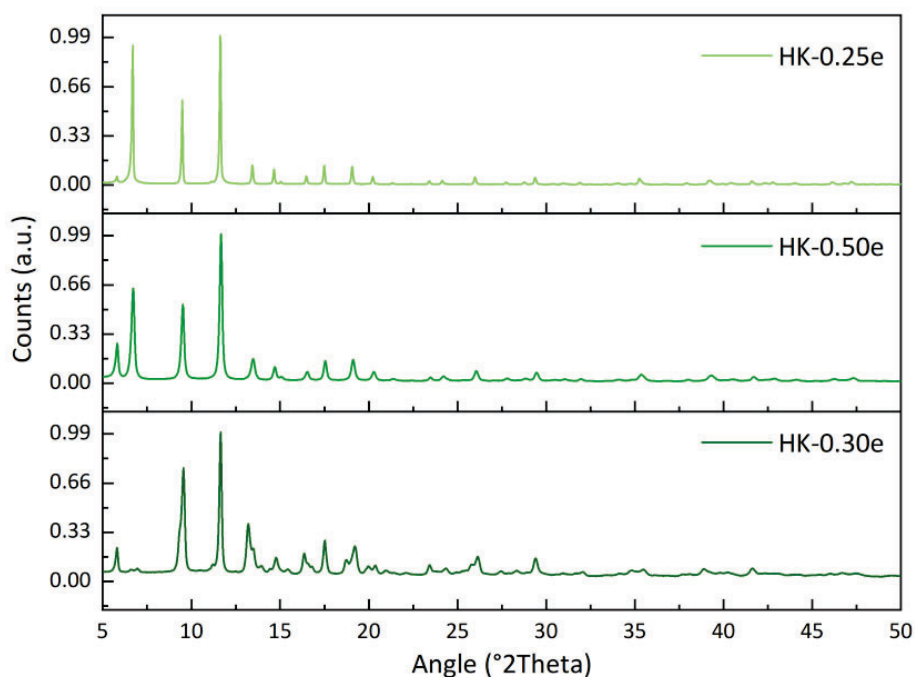


Figure 4.25. XRD diffractograms of the most adsorbent samples synthesized using MSM, sBM and bBM, respectively.

On the other hand, IR spectroscopy measurements were performed for all the synthesized samples obtained using bBM. As a result, the spectra are practically

identical as the small-scale samples and confirm the presence of trimesic acid with the aparison of the band at  $1700\text{ cm}^{-1}$  (Figure 4.26).

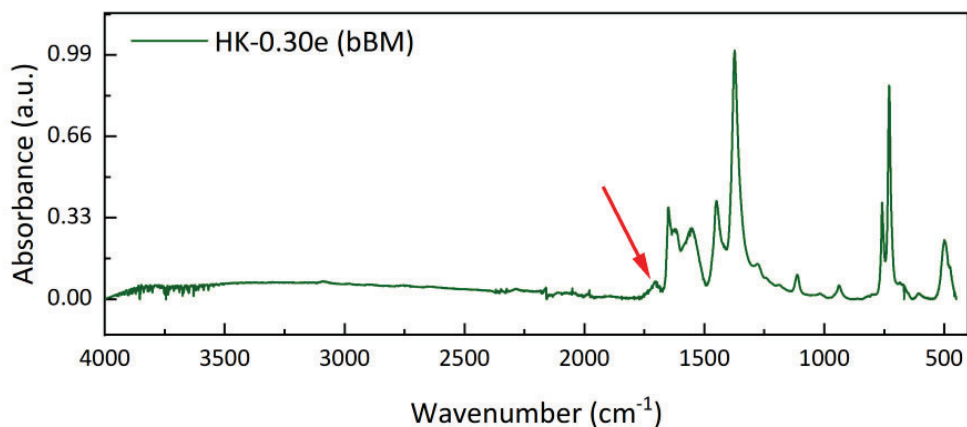
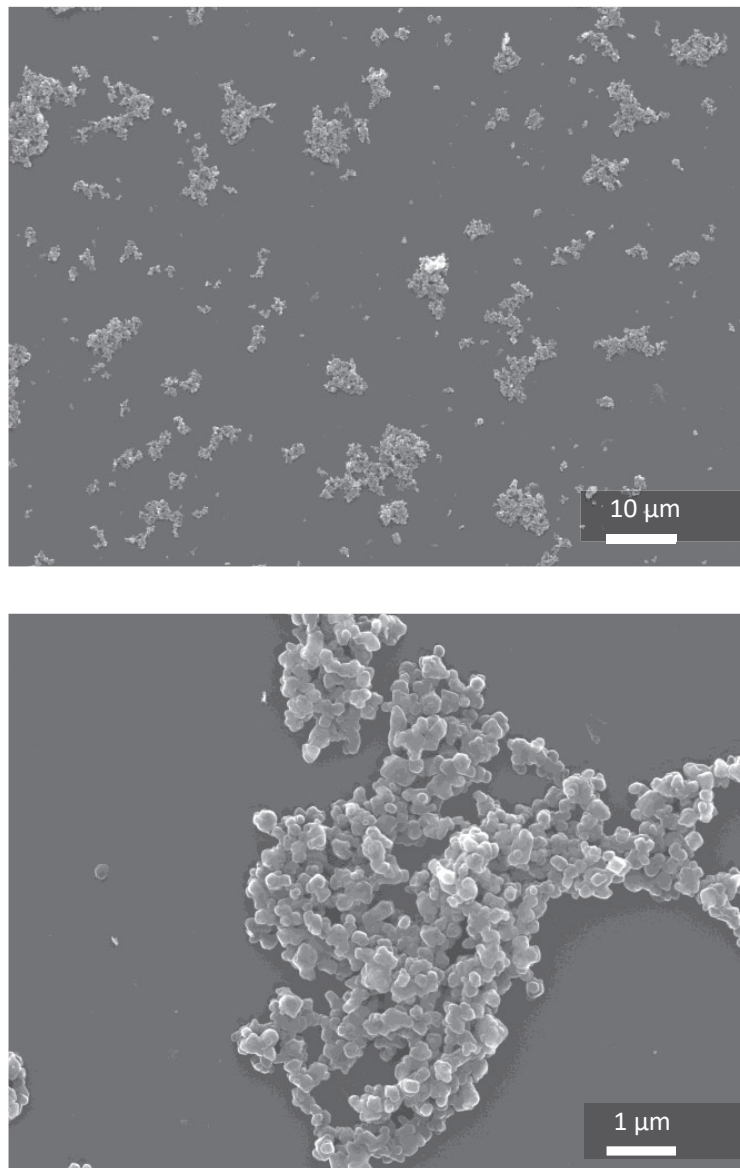


Figure 4.26. IR spectrum of the most adsorbent sample synthesized using bBM.

#### 4.4.5 Scanning electron microscopy

Following the procedure established in the previous sections, bBM samples were examined using SEM microscopy. In this case, a few milligrams of sample were sonicated for 10 minutes in ethanol. Immediately after deagglomerating the sample, a drop was placed onto the step where the samples are usually set before being coated with graphene before analysis. For these samples, the preparation of the bBM samples for SEM analysis was modified to obtain images of the nanoparticles in a slightly more deagglomerated state, compared to the previous SEM analysis of HK-GO samples.

The Figure 4.27 (a) and (b) display that the nanoparticle agglomerates have separated into more dispersed particles compared to the previous sBM samples observed in SEM images (*Section 4.2.5* of this chapter). In addition to presenting a morphology very similar to the HK-GO (sBM) samples, no difference was observed with the images of the samples containing GO.



*Figure 4.27. SEM images of HK (bBM), top and down.*

## 4.5 Statistical analysis (big ball milling)

Since the bBM methodology provided samples with higher dispersion and variability of CO<sub>2</sub> performance and experimental GO, a more precise analysis using statistics is presented below.

Following the same statistical approach used for the MSM and sBM methods, Pearson coefficients and variance coefficients for samples of bBM method are analyzed to detect if there is a correlation between CO<sub>2</sub> adsorption values and the experimental GO content in the samples. Below, the results of this analysis are summarized, along with a comparison of MSM, sBM and bBM results regarding CO<sub>2</sub> adsorption performance and GO content.

The detailed explanation of the statistical calculations, as in *Section 4.3*, is presented in the Appendix of the *Chapter VIII*.

### **bBM, sBM and MSM**

On the one hand, the coefficient of variance showed to be less than 10%. The good consistency between experimental GO and CO<sub>2</sub> adsorption values is determined by low standard deviations and good reproducibility of the results. However, this statistical parameter does not evaluate differences between groups (ranges of GO).

On the other hand, the Pearson correlation coefficients denoted that although there are no close-to-0 values, the results obtained by dividing the measurements into two ranges are moderately positive (1<sup>st</sup> range) and weakly negative (2<sup>nd</sup> range). These results suggest at first glance that although the relation between both parameters is intuitive, there is not a strong correlation between them.

Finally, the ANOVA test contrasted the tendencies, where statistics indicate that results obtained between groups (ranges of experimental GO) are not significantly different, as the p-values are greater than the commonly accepted threshold of 0.05.

When considering all the data analyzed in this section, along with the statistics presented in *Section 4.3* regarding MSM and sBM methods, there are some differences between the results obtained using each method. Specifically, compared to sBM, the statistical data suggest that sBM samples show a stronger correlation between GO content and CO<sub>2</sub> adsorption than bBM samples, while the MSM method shows an even stronger correlation than sBM.

Therefore, the ANOVA results highlight a notable difference for the bBM method, where all parameters follow a distinct trend compared to the other two methods.

*Table 4.2. ANOVA test results of MSM, sBM and bBM methods.*

<i>Method</i>	<i>Origin of variation</i>	<i>Sum of squares</i>	<i>Degrees of freedom</i>	<i>Mean squares</i>	<i>F</i>	<i>P-value</i>	<i>Critical value F</i>
<b>MSM</b>	Between groups	15.32	6	2.55	8.79	5.79x10 <sup>-04</sup>	2.91
	Into the groups	3.77	13	0.29			
	Total	19.09	19				
<b>sBM</b>	Between groups	10.98	6	1.83	10.69	2.32x10 <sup>-05</sup>	2.59
	Into the groups	3.42	20	0.17			
	Total	14.41	26				
<b>bBM</b>	Between groups	1.66	5	0.33	1.37	0.31	3.33
	Into the groups	2.41	10	0.24			
	Total	4.07	15				

Firstly, the sum of squares between groups for bBM is lower than the sum of squares within the groups, which is the opposite observed for MSM or sBM. Additionally, bBM samples indicate a similar mean square within and between groups, suggesting similar results in both groups. Finally, the p-value for bBM is higher than 0.05, while for the other methods the p-values are lower.

Among the three methodologies, the highest calculated F value corresponds to sBM samples, indicating that this method shows more clearly a higher differentiation

between the ranges of experimental GO. This is followed by a lower calculated F value for MSM (but still high and indicate the same trend). In contrast, bBM method doesn't show important differences between groups, indicating the lowest calculated F value. Based on these results, the bBM method yielded samples that do not show a significant correlation between CO<sub>2</sub> adsorption performance and experimental GO content.

Consequently, experimental results and statistical analyses determine that ball milling using bigger quantities is not sufficient to maintain the material's performance. In this case, the results indicate that there are some parameters that, unfortunately, weren't controlled. As a result, some property correlations are lost during the scale-up, and despite obtaining intuitive results, there is insufficient evidence to conclude that bBM can be used to reliably produce optimized HK-GO materials within a specific GO range.

Although a clear range for sample optimization by introducing GO was not identified when using bigger quantities in bBM, it is assumed that improvement and optimization of the experimental procedure are still required. The energy implied in the synthesis through the working RPM, reaction time, and probably the addition of a dispersant agent may be reasonable modifications to continue the research using bBM in future studies and facilitate scaling up the product to a pilot scale.

Based on these findings, it was decided to continue the study using the small BM method (sBM), incorporating reduced graphene oxide (rGO) to further explore the potential for introducing new properties to the HK-GO materials (*See Chapter V*).

## 4.6 Comparative evaluation of the synthetic methods: MSM, sBM and bBM

Considering all the aspects mentioned during *Chapter III* and *IV* regarding the results from the HK-GO samples synthesized using bBM, sBM and MSM, the following section presents a detailed discussion of the findings obtained from the three methods of synthesis.

Regarding the synthesis utilized in each methodology, MSM requires the use of harmful and ecotoxic solvents such as dimethylformamide (DMF), whereas sBM and bBM eliminate the need for such solvents, aligning with green synthesis standards. The grinding mechanized process positions BM as a simpler process than MSM for potentially obtaining large quantities of sample, since MSM method is focused on laboratory procedures using small amounts. However, achieving reproducibility poses challenges regarding sBM and bBM methods of synthesis, with special emphasis when using bBM method. On the other hand, when considering reaction yields in the synthesis process, MSM achieves the highest yield, reaching approximately 90%. In contrast, samples obtained through the sBM and bBM methods exhibit lower yields, with sBM ranging between 70-80% and bBM ranging around 70%.

The initial characterization of the samples, including XRD and IR results, provided information about the crystalline structure and chemical composition of the synthesized samples. In the case of MSM samples, XRD spectra presented narrower peaks, indicating a high level of crystallinity and probably bigger crystal sizes than sBM and bBM. In contrast, the samples obtained via bBM presented additional peaks in XRD spectra, indicating the formation of a material with possible traces of the unreacted starting materials utilized in the synthesis (copper acetate and trimesic acid). This is consistent with the IR spectra, where a characteristic band from the benzene vibration of the free ligand in the synthesis is observed ( $1700\text{ cm}^{-1}$ ). On the other hand, while the sBM samples presented broader XRD peaks as well and similar

IR spectra in all cases, their crystallinity more closely resembled that of the pristine HKUST-1, without additional peaks.

Moreover, in line with the obtained broad peaks on XRD spectra, SEM images revealed that samples obtained using MSM presented higher particle size and formed octahedral crystals, with surface defects observable in those containing GO. In contrast, the samples of sBM and bBM methods exhibited agglomerates of nanoparticles with similar morphologies in all cases. However, the particle size distribution indicated that sBM and bBM led to different particle sizes. The sBM samples exhibited particle sizes of around 180 nm up to 400 nm, while the bBM samples displayed a bimodal distribution, with sizes of around 100-200 nm and 200-500 nm. This characteristic is likely due to several factors, including the higher energy used in sBM synthesis at 600 RPM, which leads to more frequent collisions between reagents during grinding, resulting in slightly smaller particle sizes. Otherwise, particle size results for MSM samples were consistent with SEM images, exhibiting a mean of particle size of around 600 nm.

Considering the results from CO<sub>2</sub> adsorption isotherms, MSM and sBM samples presented similar performance regarding the most adsorbent samples. For MSM, the sample which presents the highest CO<sub>2</sub> adsorption performance is HK-0.25e and reaches  $5.33 \pm 0.16$  mmol of CO<sub>2</sub>/g, while for samples obtained via sBM, the most adsorbent sample is HK-0.50e and reaches  $4.93 \pm 0.28$  mmol CO<sub>2</sub>/g. On the other hand, the most adsorbent bBM sample, HK-0.30e, showed a CO<sub>2</sub> performance of  $3.77 \pm 0.7$  mmol CO<sub>2</sub>/g. Although samples from each method performed different CO<sub>2</sub> performances, the trends in CO<sub>2</sub> adsorption were consistent when analyzing the results: in all the methods the findings suggest that specific ranges of experimental GO produce an increase in CO<sub>2</sub> adsorption. In the case of samples synthesized using MSM method, samples with 0.25% w/w experimental GO exhibited higher CO<sub>2</sub> adsorption. However, the most adsorbent sBM samples were

those with experimental GO contents in the range of 0.48-0.55% w/w, while the bBM samples were in the range of 0.25-0.30% w/w.

Among the three methodologies, sBM samples showed the highest F value, indicating the greatest differentiation between experimental GO ranges. MSM had a slightly lower but still significant F value, showing a similar trend. In contrast, bBM exhibited the lowest F value, suggesting minimal differences between groups. Thus, experimental and statistical analyses confirm that the bBM method did not show significant differences between groups when correlating CO<sub>2</sub> adsorption with experimental GO content. This suggests that the bBM procedure needs optimization.

Concerning the stability of the sample, although the three methods produce the same powdered product, the nanometric size of the sBM and bBM samples makes their manipulation particularly challenging. This is due to the observed higher degree of agglomeration and increased hygroscopicity of the powder.

In summary, MSM and sBM differ in methodology, both produce similar results, and they are equally suitable for producing HK-GO materials with enhanced CO<sub>2</sub> adsorption properties. This allows flexibility in the choice of the most convenient technique.

In this regard, if the objective of production is obtaining large amounts of HK-GO materials, bBM may be the most efficient option due to its simpler synthesis process for obtaining bigger amounts of material. However, for small-scale production, initial experiments, or studies that analyze the effect of introducing new compounds in the structure, the most suitable procedure may be MSM which ensures greater precision in yield.

Despite bBM samples exhibit lower adsorption performance than sBM samples, the manufacture of HK-GO materials on a large scale remains a highly adaptable option. By adjusting the synthesis and optimizing the procedure used, the study could yield more substantial results than those currently observed in this research with samples

obtained via bBM. Therefore, it is determined that scaling-up the production of HK-GO samples is feasible if the final application of the HK-GO material aligns with the CO<sub>2</sub> capture efficiency of bBM samples.

In the following page, there is a summary table with some of the characteristics and parameters discussed in this section (Table 4.3).

Table 4.3. Comparative analysis between MSM and sBM procedures.

Aspect	Mixed Solvent Method (MSM)	Small Ball Milling (sBM)	Big Ball Milling
<b>CO<sub>2</sub> capture efficacy</b> (mmol CO <sub>2</sub> /g)	max. uptake: 5.33 ± 0.16	max. uptake: 4.93 ± 0.28	max. uptake: 3.77 ± 0.7
<b>Synthesis procedure</b>	Requires harmful and ecotoxic solvents (DMF)	Eliminates the use of ecotoxic solvents (DMF).	Eliminates the use of ecotoxic solvents (DMF)
<b>Experimental procedure</b>	Reflux columns equipped with a magnetic stirrer and temperature controller.	Planetary Micro Mill PULVERISETTE 7 600 RPM, 4 cycles (5min), 2 min-pause between cycles, same process using reverse mode	PM 100 planetary ball mill from RETSCH 250 RPM, 1 cycle (30 min), 10 min-pause between cycles, same process using reverse mode
<b>Complexity</b>	Utilization of DMF as a solvent, and the need of increased temperatures for the reaction.	Small jars employed.	Security closure for the jars and equipment instability at higher RPM.
<b>Crystalline structure</b>	Smaller width of peaks and high level of crystallinity	Slight broader peaks	Slight broader peaks and additional peaks of unreacted reagents from the synthesis.
<b>Morphology</b>	Some defects are detected on the surface of HK-GO samples. The crystal morphology is like octahedral.	Smaller crystal size indicating agglomerates of nanoparticles	Smaller crystal size indicating agglomerates of nanoparticles
<b>Exp. %GO most ads. samples</b>	0.25%	0.48 -0.55%	0.25-0.30%
<b>Particle size (d<sub>50</sub>)</b>	Monomodal profile ≈ 0.586-600 μm	Monomodal profile ≈ 0.139-0.255 μm	Bimodal profile: ≈ 0.121-0.300 μm

<b>Aspect</b>	<b>Mixed Solvent Method (MSM)</b>	<b>Small Ball Milling (sBM)</b>	<b>Big Ball Milling (bBM)</b>
<b>Yield</b>	≈ 90 %	≈ 70-80%	≈ 70%
<b>Statistical approach</b>	Correlation between GO and CO <sub>2</sub> adsorption, with variability and significant sample differences.	Correlation between GO and CO <sub>2</sub> adsorption, with variability and significant sample differences.	There is no significant correlation between GO and CO <sub>2</sub> adsorption, with variability and limited sample differences.
<b>Mass</b>	0.5 g	0.8-1.3 g	10-13 g
<b>Applicability</b>	Small scale production for initial tests on HK-GO samples.	Small scale production for initial tests on HK-GO samples with potential for scaling-up.	The method requires optimization; however, it could potentially enable the large-scale synthesis of HK-GO materials



## 4.7 Conclusions

The optimization of HKUST-1/GO synthesis materials has been accomplished using mechano-chemical synthesis, a method more aligned with the green chemistry standards approach which avoids the use of dimethylformamide (DMF) solvents and takes place at room temperature.

The optimized synthesis method, which utilizes liquid-assisted grinding method via ball milling; has been explored using two approaches: a small (sBM) and medium-scale (bBM) production of HKUST-1/GO hybrid materials.

For sBM samples, Reverse Quantification (RQ) reveals some key aspects related to the synthesis yield. The results indicate that samples synthesized using smaller amounts of GO, specifically between 0.15 and 0.50% w/w GO; exhibit higher experimental contents of GO than the actual theoretical added during the synthesis. Particularly that range of samples also presents lower yields in synthesis compared to those synthesized with higher GO contents. This suggests that the MOF growth within the GO layers, particularly at these lower GO concentrations, hinders crystal growth and results in incomplete reactions. In contrast, samples synthesized with higher GO contents demonstrate more favorable yields.

Samples obtained via small ball milling (sBM) achieve CO<sub>2</sub> adsorption up to  $4.93 \pm 0.28$  mmol CO<sub>2</sub>/g at 0.48-0.55% w/w of experimental GO, comparable to MSM results. In contrast, the CO<sub>2</sub> performance for samples obtained via big ball milling (bBM) reaches  $3.77 \pm 0.07$  mmol CO<sub>2</sub>/g at 0.25-0.30% w/w of experimental GO.

In both sBM and MSM samples, a correlation between GO content and adsorbed CO<sub>2</sub> is found since ANOVA tests and tendencies indicate that CO<sub>2</sub> adsorption performance is influenced by experimental GO content, as probability values are below 0.05. In contrast, for bBM samples, the statistics indicate that there's no correlation between CO<sub>2</sub> adsorption performance and experimental GO, suggesting that optimization is needed.

On the other hand, particle size analyses show that samples obtained via sBM present nanometric sizes (around 200 nm), which were significantly smaller than those samples obtained via MSM method (around 600 nm). X-ray diffraction further corroborates these findings, as slight differences in the width of the peaks align to the particle size results and *Debye-Scherrer* equation provides an approximate result consistent with the experimental measurements.

For the samples obtained via bBM, RQ results also reveal that using lower contents than 0.50% w/w GO, the reaction led to higher experimental content of GO than theoretical content, consistent with the observed yields and with the results of sBM. Moreover, the synthesis yield of bBM samples ( $\approx 70\%$ ) is lower than yields of sBM ( $\approx 70-80$ ) and MSM samples ( $\approx 90\%$ ).

Additionally, the results of particle size indicate that bBM samples display a bimodal distribution, which correlates with their lower CO<sub>2</sub> adsorption performance and the yields observed during synthesis.

Measuring CO<sub>2</sub> adsorption isotherms along with the rest of the characterization techniques proves to be challenging due to the high hygroscopic and agglomerated character of BM samples. However, the results suggest that this method offers a promising alternative for synthesizing materials with enhanced CO<sub>2</sub> capture properties. Overall, mechano-chemical synthesis using ball milling proves effective, potentially scalable, and environmentally friendly.

In summary, a comparative analysis of the results from MSM and BM experimental methods concludes that ball milling presents a simpler and faster approach, avoiding the use of harmful solvents and holding considerable potential for industrial scalability. Nevertheless, the choice of the appropriate method will depend on considerations such as the desired CO<sub>2</sub> capture efficacy or sustainability. Specifically improving the reproducibility by optimizing the parameters of synthesis when using

big ball milling is needed to adjust the method and scale up the production of HKUST-1/GO materials.



---

## Chapter V: Synthesis of HKUST-1/Graphenic Materials via Ball Milling

---

### *Summary of the chapter*

*In the previous chapter, mechano-chemical synthesis using BM was studied to develop HK-GO samples, and the results, similar to those obtained with the MSM method, revealed that the addition of GO within specific ranges enhances CO<sub>2</sub> adsorption properties.*

*In this chapter, the impact on the adsorbent properties is also evaluated, but this time for samples containing reduced graphene oxide (rGO) instead of graphene oxide (GO), as well as for samples that contain a mixture of both oxides.*

*rGO is the graphene oxide molecule with a reduction in functional groups on its surface. This selection is based on the similarity between rGO and GO structures, with rGO exhibiting fewer oxygenated functional groups on its surface. Given rGO's electrical and thermal conductivity, there is a projected path for potential CO<sub>2</sub> cyclability processes wherein samples could undergo adsorption and desorption through the application of electrical current, increasing the temperature and facilitating repeated CO<sub>2</sub> capture cycles.*

*The synthesis of HKUST-1/rGO materials is focused on samples with 0.25%, 0.50% and 0.75% of theoretical GO, since in this range, HK-GO samples exhibit the maximum adsorption performance. In this case, the adsorption results indicate lower CO<sub>2</sub> adsorption performance than for the samples obtained using only GO. However, the highest CO<sub>2</sub> adsorption values are found in those samples with 0.80% of experimental GO, reaching 5.1 mmol CO<sub>2</sub>/g.*

*On the other hand, a modified approach which involves combining rGO and GO mixtures is carried out. For this purpose, the synthesis of HKUST-1 combined with rGO and GO is carried out using the same specified range of oxide proportions, 0.25%, 0.50%, and 0.75% of graphenic material (GM). Consequently, the characteristics and CO<sub>2</sub> adsorption properties of HK-GM samples are exposed.*

*In this case, a wide range of CO<sub>2</sub> adsorption results are obtained. In general, the results indicate that these samples exhibit higher adsorption values compared to those containing only rGO. Notably, the adsorption values ranged from 3.25 to 6.00 mmol CO<sub>2</sub>/g, being the sample that contain 0.60% of experimental graphenic material (in a proportion of 1:3 rGO/GO) the most adsorbent sample.*

*The results of the following chapter demonstrate that, under certain conditions, the adsorption performance of HK-GM samples approaches or even matches that of HK-GO most adsorbent samples, demonstrating an enhancement of the adsorption properties as a result of introducing to the synthesis of HK materials rGO/GO mixtures.*

## 5.1 Mechano-chemical synthesis with graphenic materials

The following chapter describes the results of HKUST-1 samples combined with graphenic materials: reduced graphene oxide (rGO) and graphene oxide (GO). In this case, the incorporation of rGO aims to enhance the final material introducing improved electrical and thermal properties characteristic of this component.

rGO, in contrast to GO, is a molecule formed by graphene nanosheets with less proportion of hydroxy, epoxy and carboxylate groups than GO (Figure 5.1). Although the rGO molecule exhibits a one-atom-thick graphene structure by reducing the oxygenous groups, compared to pristine graphene it still contains defects. Generally, it is prepared via chemical reduction of GO, and the properties of this material usually depend on the reduction process utilized during the synthesis. In addition, rGO presents higher electrical and thermal conductivity than GO. This property is the result of the moderate defect density of states at the graphene basal plane, which tends to facilitate fast electron transfer.<sup>157</sup>

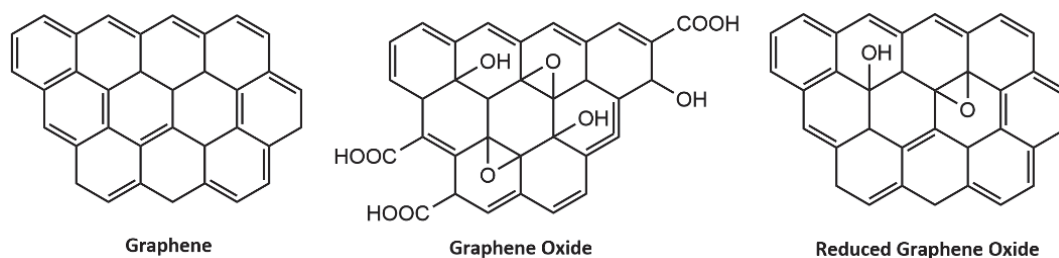


Figure 5.1. Structure of graphene and its derivatives: graphene oxide and reduced graphene oxide.

Considering the characteristics and properties of rGO, HKUST-1 materials are synthesized by combining rGO and GO instead of using only GO. This modification in the synthesis is explored to enhance the thermal and electrical properties of the HKUST-1-based materials studied in this research, to enable CO<sub>2</sub> desorption via thermal conductivity as a potential future application.

In this chapter, the samples are prepared using only rGO and mixtures of rGO and GO. Thus, the nomenclature used is referred as follows: HK-XrGO, where HK refers to the synthesized MOF, HKUST-1; X refers to the total mass percentage of rGO; and rGO

indicates that the samples are synthesized using only rGO. For the samples prepared using mixtures of graphenic material (rGO and GO), the nomenclature used is the following: HK-XGM (i:n), where HK refers to the synthesized MOF, HKUST-1; X represents the total mass percentage of the mixtures of graphenic material (rGO and GO); and n and i denote the proportion of rGO and GO, respectively. This chapter compares the results of HK-rGO and HK-GM samples with HK-GO samples obtained via sBM, presented in *Chapter IV*; and the nomenclature of HK-GO (sBM) samples is adapted to HK-XGO to facilitate the reading of the results.

In this regard, the synthesis of HK-rGO and HK-GM materials followed a similar procedure described in the previous chapter (See *Chapter IV, Section 4.1*), using the small ball milling (sBM) method. However, in this instance, instead of incorporating GO powder dispersed in EtOH, rGO or mixtures of GM (rGO and GO) were utilized. The range for these combinations was, in a first instance, 0.25-0.75% w/w of total GM, since the results obtained from the previous analyzed HK-GO samples showed the optimization of CO<sub>2</sub> capture in this range of theoretical %GO. Additionally, a set of samples with 1% and 2.5% w/w of GM were also synthesized (following the same nomenclature and procedure). However, these samples were only prepared to collect more experimental data related to RQ experiments, which are exposed in Section 5.2.1 of this chapter.

The synthesis process involved adding the reactants into the grinding container (0.59 g of Cu(CH<sub>3</sub>COOH)<sub>2</sub>·H<sub>2</sub>O and 0.41 g of H<sub>3</sub>BTC) along with 7.5 mL of the dispersed graphenic material in ethanol. The parameters for the milling cycles remained consistent: 4 cycles at 600 RPM in one direction, with a 2-minute pause between each cycle, followed by 4 additional cycles at 600 RPM in the opposite direction, with corresponding 2-minute pauses between each cycle.

Initial experiments were conducted utilizing only rGO. Next, focusing on understanding the synergy established between the graphenic materials and

HKUST-1, HK-GM samples are synthesized using proportions of 3:1, 1:1 and 1:3 of graphenic material (rGO and GO).

Once the product was obtained, the corresponding washing, activation and grinding steps were followed, just like proceeding in the same way as in HK-GO samples (*See Chapter IV, Section 4.1*).

As a result, in the case of those samples synthesized using only rGO (HK-rGO) the yield obtained for all the samples was around 60-75%. In contrast, samples synthesized using the combinations of GM presented variable yields, which are related to the specific combinations utilized in the synthesis. Those with 3:1 proportion of GM resulted in lower yields (around 70%), 1:1 of GM presented variable yields (around 70-80%) and, in general; those samples with 1:3 proportions of GM resulted in higher yields (around 80%).

## 5.2 Materials characterization and performance

As proceeded in Chapter IV, the first aspect described in this section is the results of Reverse Quantification (RQ), which indicates the experimental proportions of graphenic materials in all the samples. As mentioned above, additional combinations of samples with 1% and 2.5% of GM were analyzed along with 0.25, 0.50 and 0.75% w/w to compare the results with those samples synthesized using only GO.

Additionally, after the description of the results from RQ, the evaluation of the CO<sub>2</sub> adsorption performance of all the samples is presented correlating the experimental GO and the maximum adsorption values. Then, the subsequent sections provide the results of all the characterization techniques utilized for validating HK-rGO and HK-GM samples, which in all cases utilized the same equipment as in the case of HK-GO synthesized using sBM and MSM.

### 5.2.1 Reverse quantification

The same *modus operandi* established in the previous chapters was followed in this section. To better assess the influence of adding rGO, rather than limiting the analysis to a narrow range of studied samples, additional batches containing 1% and 2.5% w/w of graphenic material were prepared and quantified along with the other 0.25, 0.50 and 0.75% w/w GM samples, as previously mentioned. Consequently, RQ was carried out and, although not being able to determine the amount of rGO and GO separately, the total content of GM was quantified.

Considering the samples synthesized using only rGO (HK-rGO), the results indicate that the experimental rGO of all the samples is higher than the theoretical rGO employed in the synthesis (Figure 5.2 (a)). This trend is particularly evident in samples containing 0.25% and 0.50% w/w rGO. In contrast, for samples with 0.75%, 1%, and 2.5% w/w rGO, although the experimental content remains higher than the theoretical rGO content, some samples display the opposite behavior, leading to increased deviations. This suggests that the formation of the MOF is likely less facilitated at lower rGO contents (0.25% and 0.50% w/w) compared to higher contents (0.75%-2.5% w/w), although increasing the rGO content does not necessarily ensure this trend since is not maintained in all cases of higher rGO contents.

Directly related to the obtained yield, the results suggest that samples obtained using rGO instead of GO provide a final product with lower yields in all the samples (specifically, between 60 and 75% of yield), which influence directly in the quantity of rGO weighed at the last step of RQ. This particularity was also observed in specific samples of sBM synthesized with GO, specifically those in the range of 0.15-0.50% w/w GO (Figure 5.2 (b)). In this case, the yield also presented lower performance compared to the rest of the quantified samples, indicating a direct relationship between the complete formation of the HK and the quantity of theoretical GO utilized during the mechano-chemical synthesis.

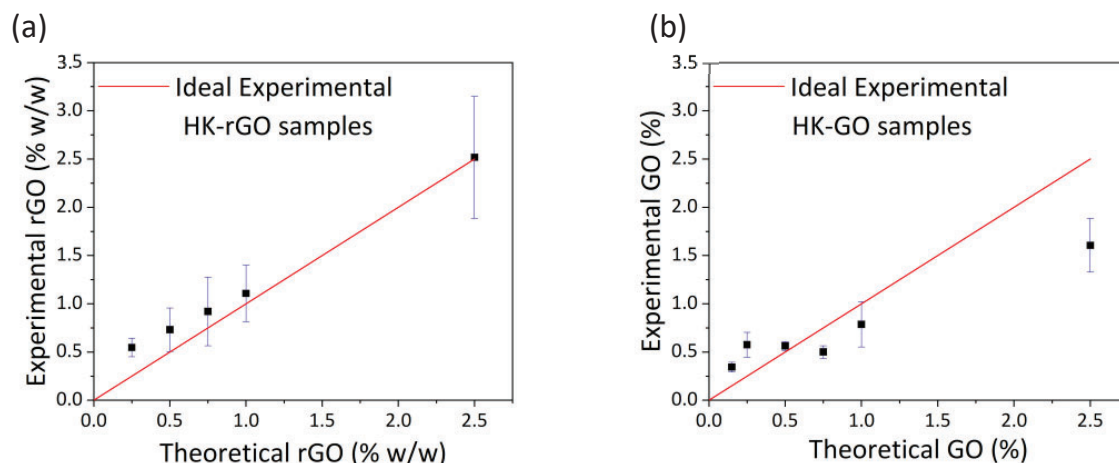


Figure 5.2. (a) Experimental %rGO vs. theoretical %rGO of HK-rGO (sBM) samples. (b) Experimental %GO vs. theoretical %GO of HK-GO (sBM) samples. Red line represents the ideal value of 100% incorporation of GO or rGO in synthesis.

As explained in Section 4.2.1 of Chapter IV, one of the benefits of combining HKUST-1 and GO molecules in the synthesis is the fact that MOF crystals grow in the potential nucleation points of GO, which are carboxylate, epoxy and hydroxyl groups.<sup>158</sup> rGO is a reduced graphene oxide molecule, which implies a reduced content of oxidative functional groups (particularly those who act like seed points). Obtaining lower yields in the synthesized samples using rGO can be related to the loss of nucleation points in the surface of the molecule. Consequently, rGO incorporation, instead of synergistically improving and facilitating the formation of HKUST-1 crystals, hinders and collapses, creating the opposite effect. As a result, increasing the rGO content, in this case for HK-rGO synthesis, does not necessarily lead to higher yields compared to those samples using smaller contents or rGO.

Once analyzed samples that were only synthesized using rGO, RQ of HK-GM samples was performed. Here, a strong particularity is observed: in general, as more rGO content has the combination of GM, higher experimental content of GM has the samples. As can be seen in the Figure 5.3 (a), blue triangle symbols which correspond to the samples with higher rGO contents (3:1 GM) present the highest values, indicating higher experimental amounts of GM compared to those samples with less

rGO and more GO contents (1:1 and 1:3 GM), which are red circles and black squares symbols, easier of distinguish in the Figure 5.3 (b) with a magnified scale.

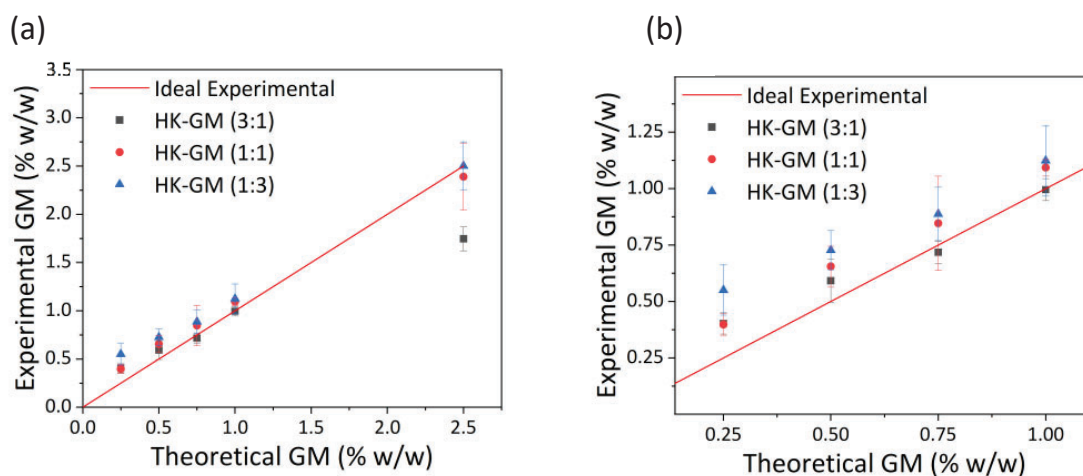


Figure 5.3. (a) Experimental %GM vs. theoretical %GM of HK-GM samples (sBM). (b) Expanded section of experimental %GM vs. theoretical %GM of HK-GM samples (sBM). Red line represents the ideal value of 100% incorporation of GM in synthesis

Based on all the results above, the synthesis using rGO produces samples with lower yields, which consequently is reflected in the results obtained by RQ (where experimental GM exceeds the amount of theoretical GM). Consequently, when rGO and GO are combined during the synthesis of HK, as much rGO content is added, lower yields of HK are obtained and higher is experimental GM is quantified.

## 5.2.2 Gas sorption measurements

Like in the case of HK-GO samples synthesized using sBM and MSM methods, CO<sub>2</sub> isotherms of HK-rGO and HK-GM samples were carried out using the same conditions, at 25 °C and up to 1000 mmHg. As a result, the highest CO<sub>2</sub> adsorption value from the isotherms for each sample, along with the experimental GM content of HK-rGO and HK-GM samples, is presented in the Figure 5.4.

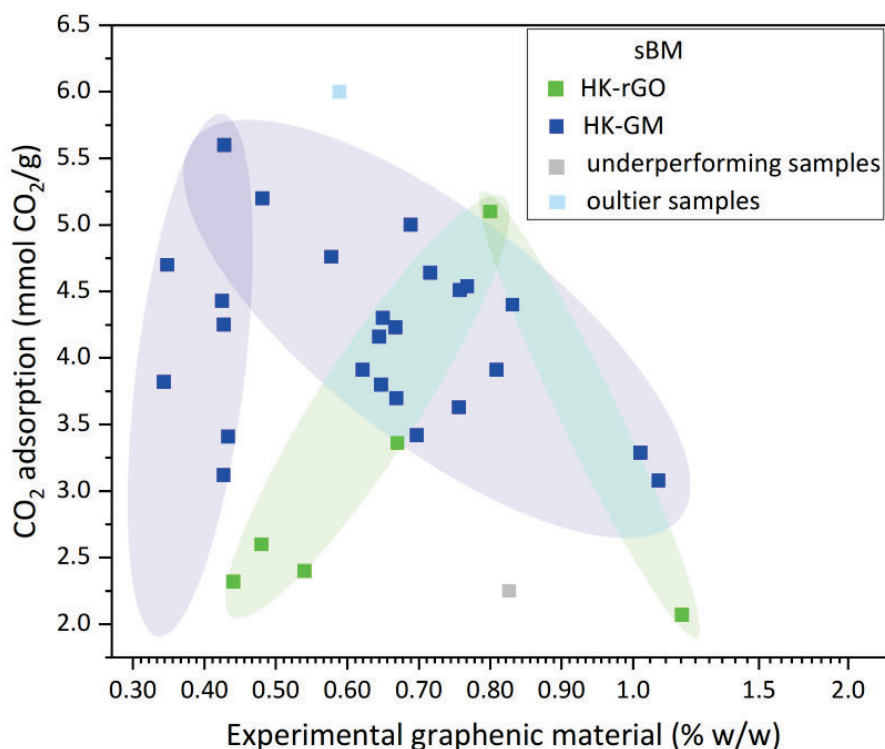


Figure 5.4. CO<sub>2</sub> adsorption values at 1000 mmHg vs. experimental graphenic material of HK-rGO and HK-GM (sBM) samples. Shaded areas highlight the proposed trends of the results.

The results suggest that, although there's noticeable variability in the scattering, the adsorption of CO<sub>2</sub> increases and decreases following a similar pattern observed on HK-GO samples (indicated by a shadow pattern in the Figure 5.4).

On the one hand, the overall adsorption values of HK-rGO samples are lower compared to HK-GM samples. Moreover, the trend of the maximum adsorbent samples is based on a sample which deviates from the rest, positioned around 0.80% w/w of experimental rGO, reaching an adsorption value of 5.1 mmol CO<sub>2</sub>/g. In this case, the tendency of maximum adsorption related to the experimental rGO is shifted to higher experimental contents, which indicates that rGO molecules enhances the adsorbent properties of HKUST-1 materials when the combination contains more quantity of rGO. However, when the content is higher than 0.80% w/w rGO, the adsorption performance decreases, as in the case of the sample with 1.30% w/w rGO.

On the other hand, HK-GM samples exhibit a different trend, exhibiting a peak of maximum CO<sub>2</sub> adsorption detected in the range of 0.45-0.55% w/w GM, reaching a maximum CO<sub>2</sub> uptake of 5.6 mmol CO<sub>2</sub>/g. However, the most absorbent HK-GM sample is the indicated in lighter blue, which reaches 6 mmol CO<sub>2</sub>/g and presents an experimental GM content of 0.60% w/w GM, with a proportion 1:3 of theoretical GM (rGO/GO). This sample is marked as a outlier sample, however the reason for this shifting in the adsorbent properties is directly related to the particle size, which in this case is slightly lower than for the rest of the samples. Moreover, CO<sub>2</sub> adsorption performance tends to decrease when the content of GM increases, as can be observed in the results of these samples located between 0.60 and 1% w/w of experimental GM.

Figure 5.5 shows the results of RQ from all the samples obtained via sBM: HK-GO, HK-rGO and HK-GM samples. As observed, HK-GM samples reveal a common maximum point around 0.45-0.55% of experimental GM (excluding outlier's samples). This indicates that using the same synthesis procedure (in this case, sBM), the samples are produced with consistent CO<sub>2</sub> adsorption properties, even when some contain rGO. In this case, the maximum total uptake of CO<sub>2</sub> adsorption performance reaches  $5.18 \pm 0.60$  mmol CO<sub>2</sub>/g, which is very close to those improved values obtained in most adsorbent samples using the MSM method.

However, HK-rGO samples exhibit a different trend from HK-GO and HK-GM. The highest CO<sub>2</sub> adsorption at 0.80% suggests that, due to the lower defect density in rGO, its synergy with HKUST-1 differs and requires a higher amount than GO.

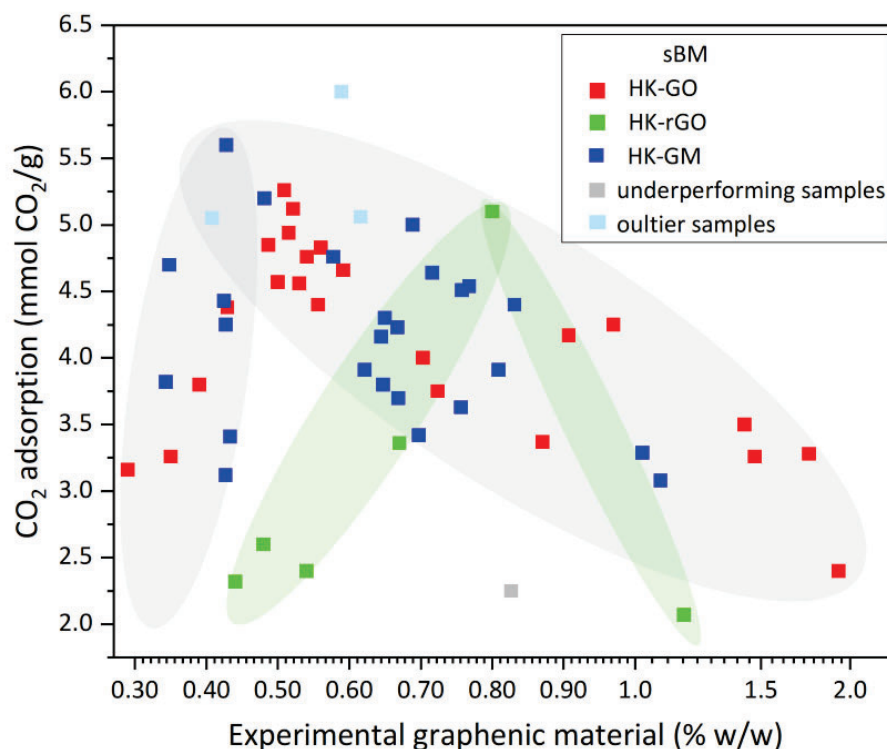


Figure 5.5 CO<sub>2</sub> adsorption values at 1000 mmHg vs. experimental graphenic material of HK-GO, HK-rGO and HK-GM (sBM) samples. Shaded areas highlight the proposed trends of the results.

The variability observed in scattering (with the most extreme samples indicated as a lighter blue symbols and unperformed samples those with the lowest experimental yields, indicated as a grey symbol) can be attributed to factors such as the rGO-to-GO ratio, particle size, or the degree of agglomeration during measurements.

Like in *Chapter IV*, the following sections expose the results of the characterization techniques used to verify the proper formation of HK-rGO and HK-GM samples, obtained via sBM method. Although most techniques involved measurements of all the samples, the results are focused on those with the highest CO<sub>2</sub> adsorption performance, and the nomenclature includes the letter 'e' because emphasizes that the content of GM is the experimental content determined in RQ experiments.

### 5.2.3 Particle size measurements

Particle size measurements were performed to determine if the synthesis using rGO instead GO and using the combination of both influenced the size of the nanoparticles obtained. Hence, an accurate measurement of the particle size was performed, following the same experimental procedure described in *Chapter IV, Section 4.2.2*. In this case, the particle size of all the samples was measured. Since the results are similar for all cases, this section presents the results of one sample from each synthesis as a representative example, selected as the most CO<sub>2</sub> adsorbent sample of each group.

As indicated in the results depicted in Figure 5.6, HK-rGO exhibit greater dispersion in particle size as they have a broader distribution, comprehended between 230 and 530 nm. On the other hand, the particle size of HK-GM samples is also slightly higher than HK-GO samples, but not as polydisperse as the previous ones containing only rGO, indicating smaller particle sizes with a maximum percentage of particles around 220 nm of size.

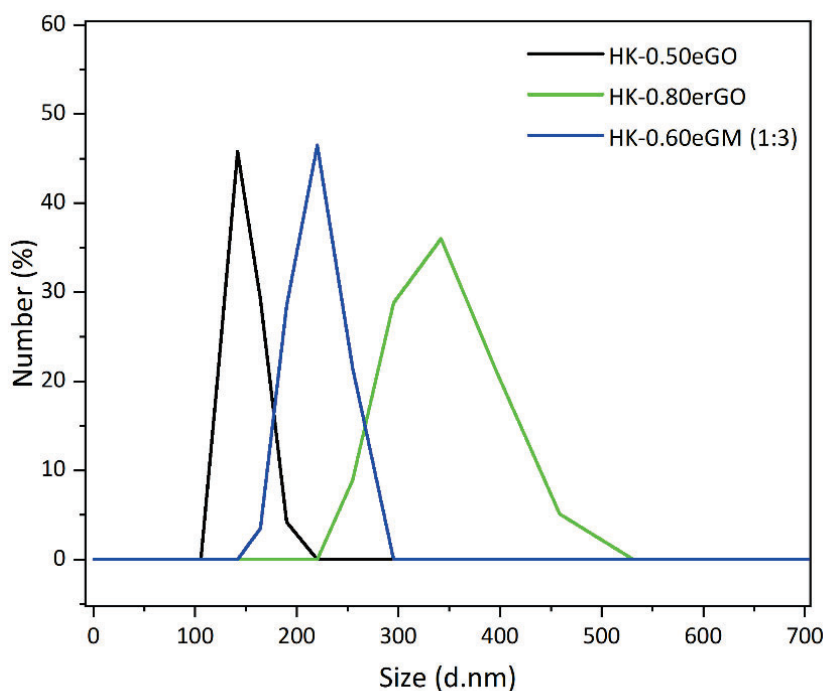


Figure 5.6 .Particle size distribution by number of HK-GO, HK-rGO and HK-GM of samples synthesized using sBM.

The data show that the incorporation of rGO may interact with the nucleation of the HK crystals when sBM method is carried out, and subsequently with the particle size as well. Therefore, when the proportion of rGO decreases and GO proportion increases, the particle size obtained from the samples is slightly reduced. And, subsequently, when the only oxide introduced in the synthesis is GO, the achieved particle size is the smaller one obtained when comparing with HK-rGO and HK-GM samples. However, in general, all the samples present a nanometric particle size (around 150-300 nm), which can be correlated with the increased CO<sub>2</sub> adsorption performance. Particle size directly influences the specific surface area of the sample; the smaller the particle size, the greater the total surface area exposed to the adsorbed molecules. Additionally, the smaller the particle, the easier the diffusion of gases through the material, which also enhances the CO<sub>2</sub> adsorption performance of the sample.

Comparing these results of particle size with the results obtained from HK-GO samples obtained via MSM, it is possible to detect a trend (Figure 5.7). First, MSM synthesis provides the highest particles of HK-GO materials synthesized, ranging between 400 nm and 1µm of size and with the percentile  $d_{50}$  located at 594 nm. Secondly, sBM samples indicate smaller particle sizes but are distributed in different groups according to the incorporated oxide. On the first hand, HK-GO (sBM) samples showed the smallest particle size, with a maximum percentage number of particles distributed around 140 nm. Followed by this group, the second smallest particle size material is the group that contains mixtures of rGO and GO, HK-GM samples, which achieve a maximum percentage number of particles with a size of around 220 nm. Next to this group, HK-rGO samples showed higher particle size and more variability in the distribution of dimensions, suggesting a maximum percentage of particles around 343 nm of size. Finally, the results indicate that BM method using higher quantities of reagents (bBM) produces particles with a bimodal particle size, with smaller particle sizes of around 150 nm and higher sizes located around 300 nm.

Considering all the results, there's a direct relationship between particle size and CO<sub>2</sub> adsorption performance of the samples. In general, all the sBM most CO<sub>2</sub> adsorbent samples present similar particle size. In contrast, the most adsorbent bBM sample achieves an enhancement of the CO<sub>2</sub> adsorption considerably low, which may be related to the bimodal distribution observed in the results. This suggests that the bBM samples are more polydisperse than in the cases of sBM and MSM samples and, as a result, they present more variability and lower CO<sub>2</sub> adsorption performance.

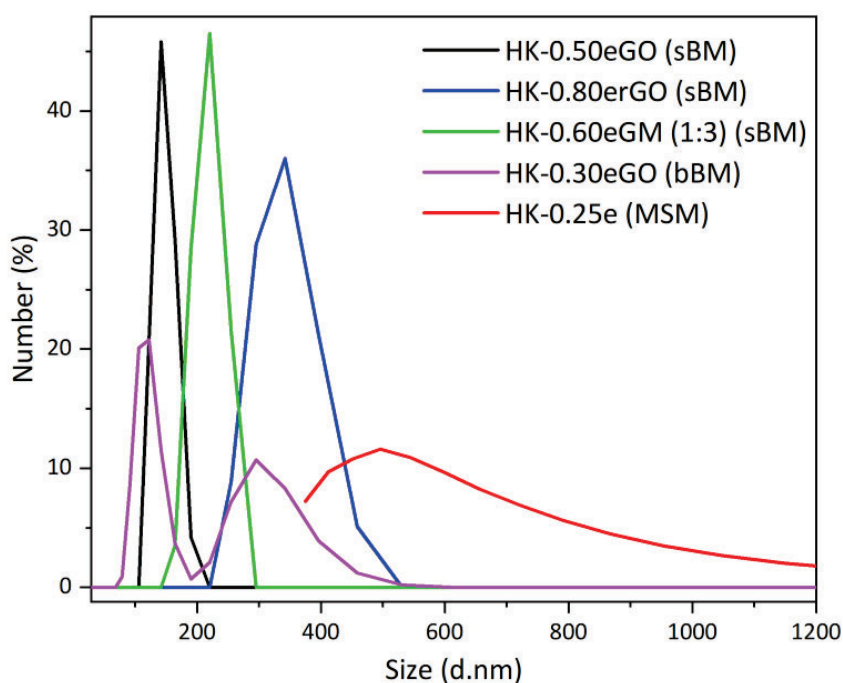


Figure 5.7. Particle size distribution by number for HK-GO, HK-rGO and HK-GM samples synthesized using MSM, sBM and bBM methods.

#### 5.2.4 X-ray diffraction and infrared spectroscopy

All samples were analyzed using X Ray Diffraction to examine and assess the crystalline structure of the HK samples and determine whether it was altered by the incorporation of rGO and GM combinations. Hence, the diffractogram of HK-rGO (0-0.75% w/w rGO) and HK-GM sBM samples (0-0.75% w/w GM) were analyzed and compared to the pristine HKUST-1 XRD simulated pattern with HK-GO diffractograms. However, since the crystalline phase of all the samples was almost the same, only the

diffractograms of the HK-0.0.80erGO and HK-0.60eGM (1:3) samples are shown in Figure 5.8, along with the diffractogram of the HK-0.50eGO.

As a result, samples that contain rGO instead of GO, as well as the samples which contain the mixture of GM, show a very similar crystalline structure compared to the pristine HKUST-1 and to the spectra of HK-GO (sBM) samples. Most of the diffractograms remain practically identical, despite slight variations in the intensity of certain peaks, attributed to the presence of water, as in the cases of  $5.8^\circ$  or  $6.7^\circ$  discussed in *Chapter IV, Section 4.2.3*.

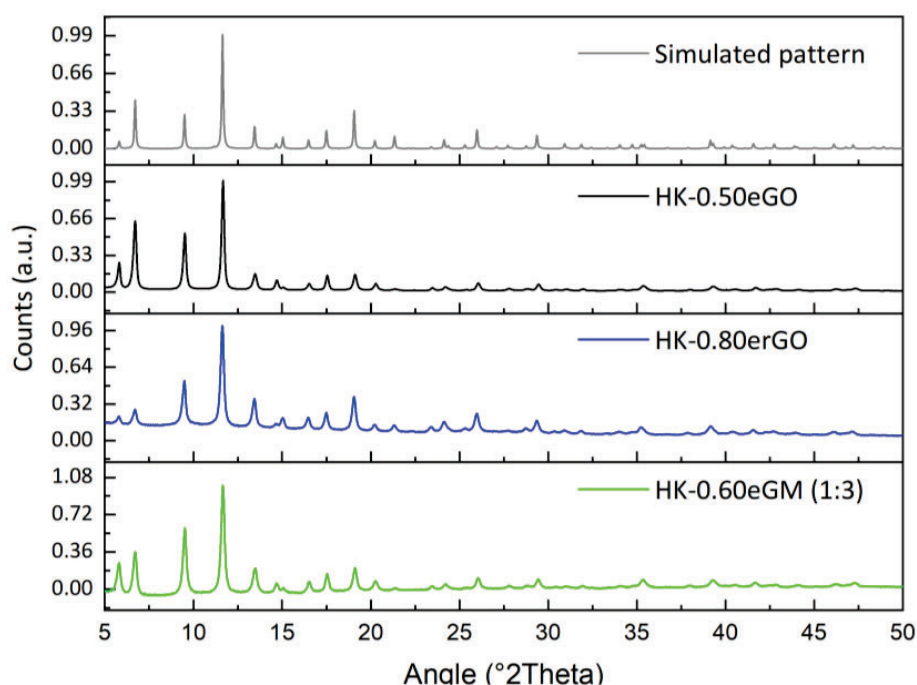


Figure 5.8. (top) Simulated pattern of HKUST-1 and XRD diffractograms of HK-GO, HK-rGO and HK-GM samples synthesized using sBM, respectively.

### **Infrared Spectroscopy measurements**

The structures were validated using IR to identify the functional groups, confirm the chemical composition, and detect any modifications in the structures. As all the samples presented a similar IR spectrum, Figure 5.9 exhibit the result of HK-0.80erGO and HK-0.60eGM (1:3) as representative examples, along with HK-50eGO to compare

the results using only GO in the synthesis. Moreover, the bottom part of the figure also shows the IR spectra of GO and rGO.

Concerning the results, the same main bands previously observed in IR spectra of HK-GO (sBM) samples are also observed, corresponding to the carboxylate group ligand at  $1647\text{ cm}^{-1}$ , C-C band attributed to the benzene ring of the ligand at  $489$  and  $940\text{ cm}^{-1}$  and the -OH vibration band at around  $3200\text{ cm}^{-1}$ , which indicates the activation level of the sample during the moment of the measurement. Small indications of traces of ligand used in the syntheses are suspected because the band was detected at  $1710\text{ cm}^{-1}$ .

On the other hand, when analyzing rGO infrared spectra and comparing it with the spectra of GO, some differences arise. First, the broad -OH band detected around  $3200\text{ cm}^{-1}$  is not observed in rGO spectra, indicating that the rGO powder sample contains fewer oxidized functional groups due to its reduced character. Moreover, a band located around  $1200\text{ cm}^{-1}$  in GO, indicating the presence of C-O-C epoxy groups is displaced in the case of rGO to lower values, specifically  $1157\text{ cm}^{-1}$ . In the case of  $1554\text{ cm}^{-1}$  band, rGO increases its intensity due to the prevalence of C=C vibration groups rather than -COOH vibration groups. Also, another particularity is the presence of C-H vibration groups  $2975$  and  $2880\text{ cm}^{-1}$ , indicating more proportion of these bonding in the structure, since oxidation causes the formation of double bonds and reduces, in consequence, the presence of C-H vibration bands.<sup>137</sup>

No additional peaks related to GO or rGO are observed on the HK-rGO and HK-GM spectra analyzed, probably due to the low concentrations employed during the fabrication of the materials.

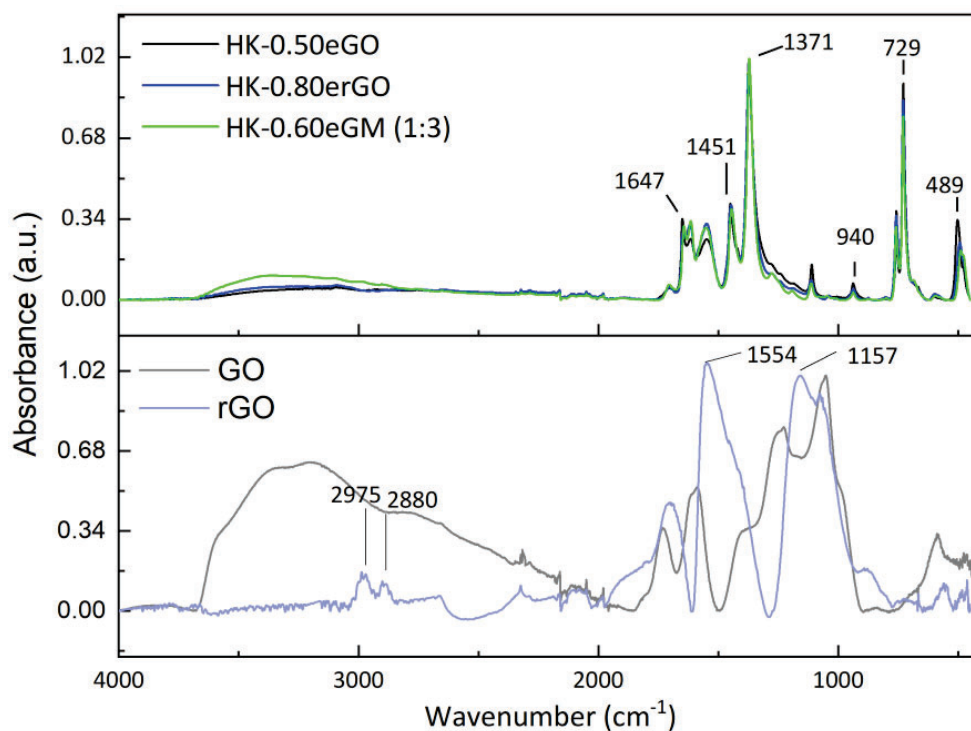


Figure 5.9. Infrared spectra of HK-GO, HK-rGO and HK-GM samples and GO and rGO powder, respectively.

### 5.2.5 Thermogravimetric analysis

As proceeded in the previous chapters, the thermogravimetric analysis of the samples is performed to validate the correct structure and to study the thermal stability. Although the measurements were carried out for all the HK-rGO and HK-GM samples, Figure 5.10 exposes the results of the most adsorbent samples as a representative example.

As demonstrated by the results, the thermal behavior of the samples is like the previous one observed on HK-GO samples obtained through MSM and BM, which indicates:

1. **Solvent removal**
2. **Degradation of the functional groups**
3. **Decomposition of the carbon skeleton**

The first degradation step shows the extraction of the solvents trapped in the pores of the structure, until 100 °C approximately, followed by a slightly degradation of superficial functional groups of the material, until around 290-300°C and the final complete decomposition of the MOF and GO structure provided by the skeleton of C, H and O atoms, which ended at around 330°C, providing CuO as a final solid (Figure 5.10 (a)).

As a specific particularity of these samples, it's noted that although thermal stability is practically identical to HK-GO samples, the final step of degradation occurs a little earlier than in the samples that only contain GO, starting the degradation in this case at approximately ~ 290°C for HK-0.80erGO and 288°C for HK-0.60eGM sample instead of ~ 300°C (Figure 5.10 (b)). This could be attributed to the lack of functional groups in the surface of samples which contain rGO, since GO has more atoms to degrade than rGO in terms of the quantity of functional groups provided to the structure. Moreover, the final quantity of solid remaining is again variable according to the initial conditions of trapped solvents in the pores of structure and the experimental proportion of atoms which act as the main structure of the sample.

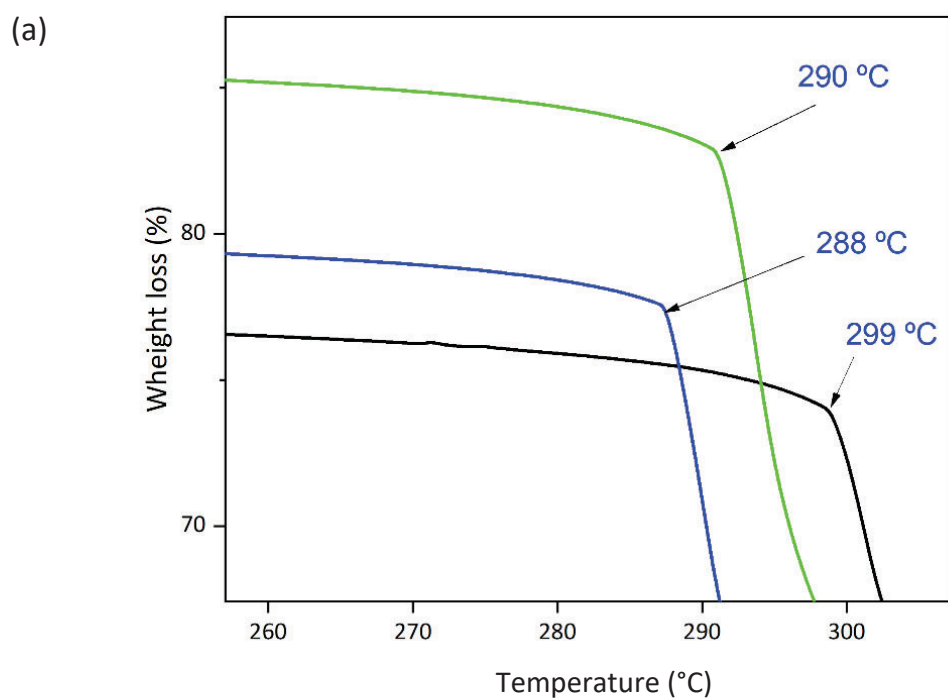
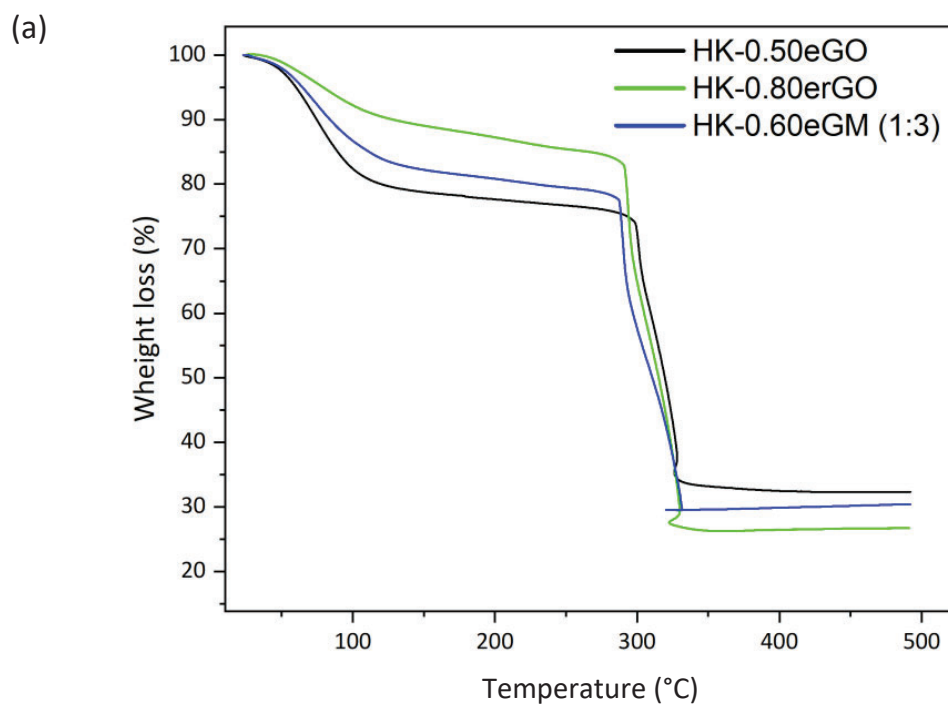


Figure 5.10. (a) TGA diagram of HK-GO, HK-rGO and HK-GM of samples synthesized using sBM and (b) expanded area of the diagram.

### 5.2.6 Scanning electron microscopy

The samples were analyzed using SEM images for corroborating morphology and the possible defects obtained through the samples. In this instance, the preparation of the samples followed the same methodology described for sBM samples in *Chapter IV, Section 4.2.5*.

Since all the samples exhibited a similar morphology, Figure 5.11 (a), (b) and (c) display the SEM images of HK-0.80erGO, HK-0.60eGM (1:3) and HK-0.50eGO as a representative example, respectively.

In this case, the images provide similar results to those observed in the previous chapter, characterized by spherical, agglomerated nanoparticles. The content of rGO and GO is undetectable for HK-rGO and HK-GM samples, as was also observed in HK-GO samples. Moreover, the particle size appears to be in the nanometric range. The morphological features of all the samples seem to be similar.

In conclusion, the results indicate that the incorporation of rGO or mixtures of rGO/GO to the samples doesn't produce any relevant change concerning the morphology of the samples compared to HK-GO synthesized using sBM.

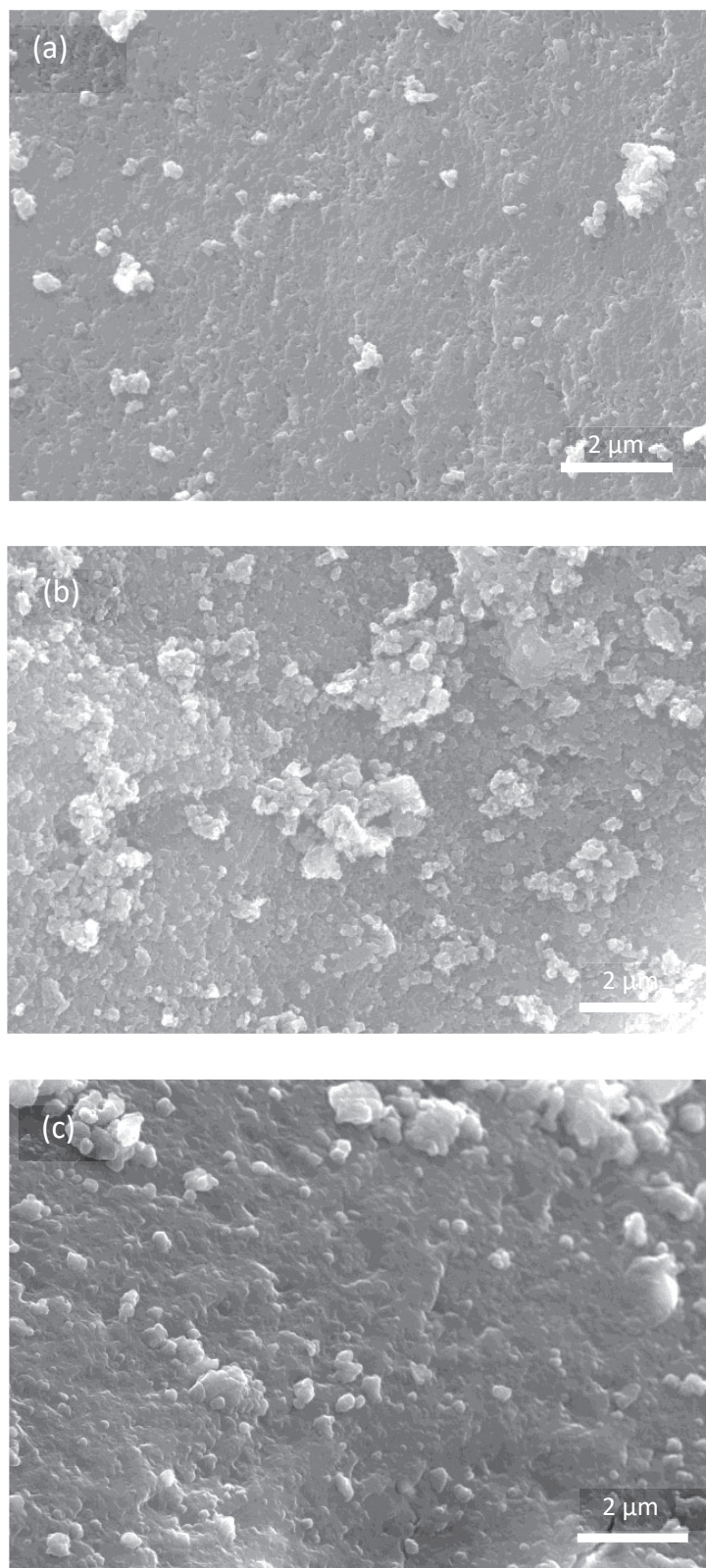


Figure 5.11. SEM images of (a) HK-0.80erGO (b) HK-0.60eGM and (c) HK-0.50eGO.

### 5.3 Comparative evaluation of the synthetic methods for HKUST-1/Graphenic materials

The effect of introducing rGO instead of GO alters two characteristics of the obtained materials: the yield of the chemical reaction and the CO<sub>2</sub> adsorption performance. The HK-rGO samples indicate that sBM synthesis performs lower yields compared to HK-GO samples, which is directly related to the experimental rGO content determined in RQ. Adsorption results of HK-rGO samples are less reproducible, probably due to the low yields as well and other external factors (humidity, agglomeration degree, experimental errors, etc.). Moreover, if the 0.25-0.75 % range of GO is placed by a combination of rGO and GO when using sBM synthesis, it is possible to obtain better results of adsorption compared to those observed with samples containing only GO or rGO. The behavior described is clearer to understand if the most adsorbent samples of each procedure are represented in the same plot (excluding parameters like reproducibility and variability). Figure 5.12 shows the results of the most CO<sub>2</sub> adsorbent samples of each synthesis using sBM.

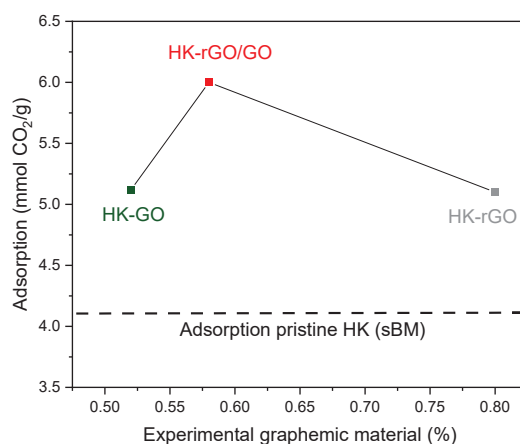


Figure 5.12. Results of the most CO<sub>2</sub> adsorbent sample of each sBM synthesis.

GO and rGO samples achieved an improvement of 46% with 0.50% and 0.80% of experimental graphemic material compared to pristine HK (sBM), and 67% compared to pristine HK (MSM), respectively. Whereas rGO/GO samples achieved an improvement of 46% with the sample containing 0.58% of experimental graphemic

material compared to pristine HK (sBM) and 102% compared to pristine HK (MSM). These findings are reasonable since decreasing the oxidized functional groups when using rGO, suggests that a higher rGO content may be needed to compensate for the loss of carboxylates and epoxy groups. In contrast, samples synthesized using only GO show better adsorption results with less content due to enough supply of functional groups on the surface. On the other hand, the optimal mixture of rGO/GO appears in the middle of optimal oxide contents of GO and rGO, assuming that a balance between both molecules is established in that range.

Although obtaining reproducibility using sBM was a complex task, tendencies indicate that HK-GO materials obtained through ball milling techniques can capture higher CO<sub>2</sub> quantities than HK samples. Moreover, the combination of rGO and GO provides the material conductive electrical properties, making these materials more appealing for application in emerging technologies.

In summary, considering all the samples analyzed from each chapter of this study, it is determined that MSM and BM synthesis procedures can produce HK-GO materials with improved CO<sub>2</sub> adsorption properties compared with pristine HK. Therefore, the previous chapters demonstrate the synergy established between MOF HKUST-1 and GO when synthesized using two different methods: MSM and BM. The results indicate that the optimal range for this purpose is 0.25% w/w of experimental GO for MSM samples and 0.48-0.55% w/w of experimental GO for sBM samples, leading to an enhancement of 80% in adsorption for MSM samples and 67% for sBM samples compared to pristine HK (MSM).

Additionally, the scalability of these materials was slightly analyzed when the samples were obtained using more quantities of reactants and higher jar pots, using bBM, as described in *Section 4.1 of Chapter IV*. The results showed similar trends to MSM samples in the optimal range of combined experimental GO, which falls within 0.25-0.30%. These values led to a 23.5% increase in CO<sub>2</sub> adsorption compared to the pristine HK samples obtained through bBM and to a 26% increase compared to

pristine HK (MSM). Regarding all the methods and combinations analyzed during this study, Figure 5.13 indicates the maximum values of CO<sub>2</sub> capture obtained of the most adsorbent sample from each method considering experimental GO. As can be seen, although bBM method can be performed for obtaining HK-GO samples with increased adsorption properties, the results suggest that this method obtains the lowest increment of enhancement for CO<sub>2</sub> adsorption. Moreover, the experimental GO of the most adsorbent bBM samples is similar in MSM samples (0.25-0.33% for bBM and 0.25% for MSM). Since bBM samples share similarities in particle size with HK-GO (MSM) samples (comparable particle size to MSM samples, since the bimodal profile includes particle sizes of around 600 nm) the lower CO<sub>2</sub> adsorption performance may be attributed to the material's polydisperse nature, even though the most adsorbent samples present similar experimental GO on the most adsorbent samples. This characteristic in particle size could also explain the differences observed between the results of sBM and bBM samples.

On the other hand, during this chapter, the synthesis of HK materials has been performed using rGO and rGO/GO mixtures instead of only GO by means of sBM synthesis. Regarding the analysis of samples containing only GO and the batches synthesized using rGO, the observations suggest that yields play a crucial role in the production of these materials. Yields affect the incorporated graphene material, which seems to be lower when rGO is incorporated, and the CO<sub>2</sub> adsorption performance is directly related to the experimental amount of GO. Consequently, samples synthesized using only HK-rGO presented, in general, the lowest CO<sub>2</sub> adsorption values compared to the rest of the samples, with a mean of maximum adsorbent performance around 3 mmol CO<sub>2</sub>/g.

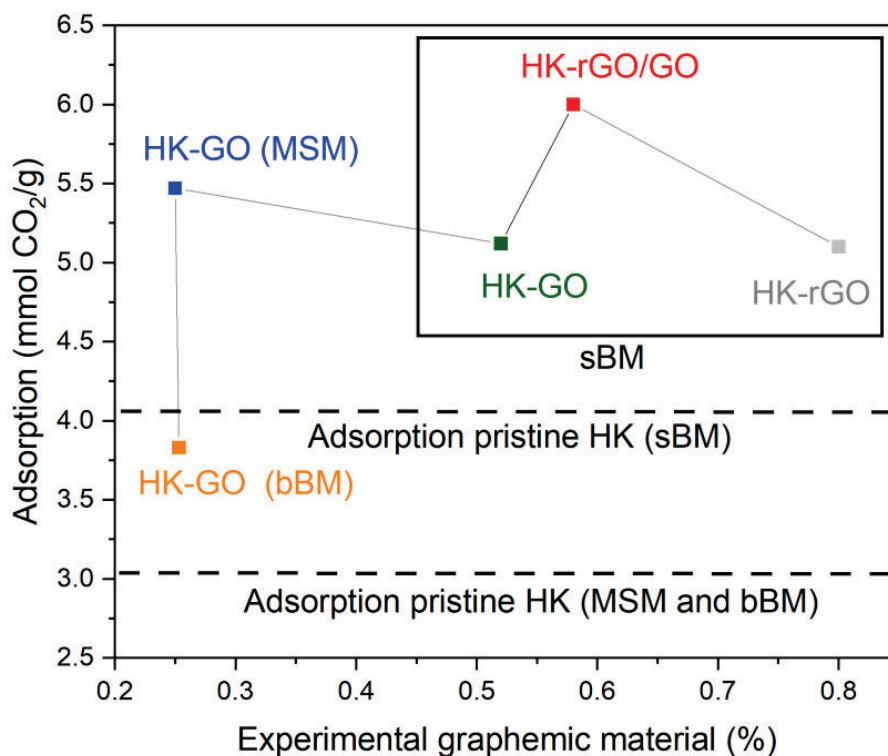


Figure 5.13. Results of the most CO<sub>2</sub> adsorbent sample of all the procedures used in the obtention of HK materials combined with GO, rGO or rGO/GO.

Given all the results collected, Table 5.1 summarizes the main aspects described during this study concerning the synthesis, the structural determination and the adsorption properties related to GO and rGO contents added.

Table 5.1. Characteristics and obtained data from samples synthesized using MSM, sBM and bBM.

Aspect	Mixed Solvent Method (MSM)	Ball Milling (sBM)		Ball Milling (bBM)
<b>HK-X material</b> (X=GO, rGO or rGO/GO)	HK-GO	HK-rGO	HK-rGO/GO	HK-GO
<b>CO<sub>2</sub> adsorption (mmol CO<sub>2</sub>/g)</b>	5.33 ± 0.16	5.10	5.18 ± 0.6	3.77 ± 0.7
<b>Experimental % GO</b> (most ads. samples)	0.25	0.80	0.42-0.57	0.25-0.33
<b>Reproducibility</b>	Good	Low	Medium	Low
<b>Solvents</b>	DMF and EtOH	EtOH	EtOH	EtOH
<b>Experimental conditions</b>	24 h, 85 °C and magnetic stirring	600 RPM, 4 cycles of 5 min with 2-min pause between cycle, 4 cycles of 5 min with 2-min pause (reverse mode)		
<b>Particle size (nm)</b> (Mean of most ads. samples)	Monomodal profile: ≈ 400	Monomodal profile ≈ 0.140 μm	Monomodal profile ≈ 0.340 μm	Bimodal profile: ≈ 0.121-0.300 μm
<b>Morphology</b>	Octahedral crystals. Defects detected when GO is added to the synthesis.	Agglomerated nanoparticles		

Aspect	Mixed Solvent Method (MSM)	Ball Milling (sBM)	Ball Milling (bBM)
<b>Complexity</b>	Needs: reflux column, laboratory fume hood, extraction system	Limited amount obtained and high hygroscopic character of the sample	High hygroscopicity. Need to use a security closure for the jars.
<b>Yield</b>	≈ 90 %	≈ 80-70 %	≈ 70 %
<b>Mass (g)</b>	0.5	0.8-1.3	10-13
<b>Statistics</b>	Correlation between GO and CO <sub>2</sub> adsorption, with variability and significant sample differences.	Correlation between GO and CO <sub>2</sub> adsorption, with variability and significant sample differences	Correlation between GO and CO <sub>2</sub> adsorption, with reproducibility and limited sample differences.
<b>Applicability</b>	Suitable for obtaining small scale samples to optimize material efficiency	Suitable for obtaining small scale samples to optimize material efficiency	Suitable for large-scale synthesis. Optimization of the procedure is crucial.

## 5.4 Conclusions

The obtention of HKUST-1 materials combined with rGO has been effectively achieved utilizing the small ball milling (sBM) method of synthesis. The characterization techniques indicate the correct formation of the MOF, without any alteration in the crystalline structure.

For those samples synthesized using only reduced graphene oxide (rGO), the CO<sub>2</sub> adsorption isotherms exhibit in general lower performance compared with those samples synthesized using only graphene oxide (GO), except for samples which contained 0.80% of experimental rGO, which presents an adsorption performance of 5.1 mmol CO<sub>2</sub>/g. This range of rGO is higher than the optimal ranges determined for HKUST-1/GO samples, suggesting that as rGO presents a different structure than GO, in this case, the content needed to increase the CO<sub>2</sub> adsorption properties is higher.

On the other hand, the analysis of the yield in the synthesis reveals that samples synthesized with rGO exhibited lower yields compared to HKUST-1/GO samples in all the ranges of GO content. Moreover, this is also reflected in Reverse Quantification (RQ) results, which present higher experimental rGO contents than the theoretical rGO used in the synthesis. This may be attributed to the intrinsic characteristics of rGO, since it presents fewer defects than GO molecules that act as a nucleation point on the surface of the molecule.

rGO incorporation during the synthesis of HKUST-1, instead of synergistically improving and facilitating the formation of the MOF crystals, hinders and collapses creating the opposite effect. For this reason, the yield of HKUST-1/rGO samples does not present an improvement for higher contents of theoretical rGO, unlike the samples synthesized using GO.

Samples synthesized using combinations of graphenic materials (GM), specifically mixtures of rGO and GO, exhibit different results compared to the HKUST-1/rGO

samples. Regarding the synthesis yield, the data indicates that increasing the rGO content in the GM mixture led to a decrease in yield, consistent with the trend observed for the HKUST-1/rGO samples. The CO<sub>2</sub> adsorption performance results in a maximum CO<sub>2</sub> adsorption performance of 6.00 mmol CO<sub>2</sub>/g at 0.60% of experimental GM (1:3 rGO/GO weight ratio).

In summary, the combination of rGO and GO into HKUST-1 presents the best performance of CO<sub>2</sub> capture, offering a potential cycling by electrical heating.

---

## Chapter VI: The influence of H<sub>2</sub>O molecules on HK-GO materials

---

### *Summary of the chapter*

*As indicated in the initial chapters of this study, when samples are dried (activated), there is a color change in the sample, from light blue to dark blue. This variation was studied using XRD, where the results indicated changes in the crystalline structure (Chapter IV, Section 4.2.3). This experiment confirmed that the presence of water molecules interacts with HKUST-1 material.*

*As in the majority of gas capture processes water molecules play an important role. In the following chapter, the interaction between H<sub>2</sub>O molecules and HKUST-1/GO samples is analyzed using several techniques and considering different conditions of relative humidity combined with CO<sub>2</sub>.*

*Firstly, the color change of HK and HK-GO samples is analyzed using colorimetric sensors. The results of these measurements provide information about samples colorimetric response when HKUST-1/GO interact with a specific percentage of relative humidity (RH) and with CO<sub>2</sub> molecules, allowing the monitorization in-situ and continuously the state of the materials under operational conditions. Moreover, a relationship between color change and CO<sub>2</sub> adsorption isotherms is established, enabling the quantification of CO<sub>2</sub> capture using colorimetry of HK-GO materials.*

*Furthermore, the interaction of the samples with H<sub>2</sub>O and CO<sub>2</sub> samples is also analyzed through Infrared Spectroscopy and solid-state <sup>13</sup>C NMR measurements. On the one hand, IR experiments are divided into three experiments, where the sample is exposed to different RH and CO<sub>2</sub> concentrations using independent streams of CO<sub>2</sub> (15%), RH (50%), and simultaneous streams of both gases.*

Through these experiments, the results indicate that both  $\text{CO}_2$  and  $\text{H}_2\text{O}$  molecules interfere with the sample producing changes in the carboxylate bond vibrations of HKUST-1/GO samples, specifically around the carboxylate ligand surrounding. These results confirm that carboxylate functional groups are potential adsorption sites for  $\text{H}_2\text{O}$  molecules. However, when the conditions imply simultaneous  $\text{CO}_2$  and  $\text{H}_2\text{O}$  adsorption, the results suggest that  $\text{CO}_2$  act as a carrier gas displacing the adsorbed  $\text{H}_2\text{O}$ . Through the results obtained using IR it is suggested that  $\text{CO}_2$  molecules are not adsorbed into carboxylate bonds. It is also determined that the incorporation of GO increases the number of favorable adsorption sites for  $\text{CO}_2$ , such as aromatic carbon, and partially block  $\text{H}_2\text{O}$  adsorption near copper nuclei, reducing the sample degradation.

On the other hand,  $^{13}\text{C}$  NMR experiments confirmed that  $\text{H}_2\text{O}$  molecules are adsorbed in carboxylate bonds, as well as into other specific regions such as the aromatic ring of the sample. In this case, it is observed that  $\text{CO}_2$  molecules are particularly adsorbed into aromatic functional, confirming the competence between both molecules.

Additional insights involving the co-adsorption of  $\text{CO}_2$  and  $\text{H}_2\text{O}$  are presented as a result of the measurements performed using Dynamic Vapor Sorption (DVS) and volumetric Breakthrough analysis (BTA) measurements. The objective of this part is to evaluate the competitive adsorption of both molecules in the samples and assess the  $\text{CO}_2$  adsorption capacity under post-combustion conditions. These experiments exhibit that the presence of GO enhances the  $\text{CO}_2$  and  $\text{H}_2\text{O}$  uptake, along with improved regeneration capabilities. Moreover, although  $\text{CO}_2$  presents faster kinetics than  $\text{H}_2\text{O}$  adsorption, the results suggest that HK-GO materials can be effective for  $\text{CO}_2$  uptake, but preferably only under dry conditions. However, under humid conditions,  $\text{CO}_2$  capture becomes negligible due to competition with  $\text{H}_2\text{O}$  molecules.

## 6.1 The influence of H<sub>2</sub>O in the color of HKUST-1

As extensively reported in the literature,<sup>159</sup> the color of HKUST-1 (HK) changes when it is in contact with the air, and this behavior was observed in the initial phases of the study. The intensity and degree of the color of the samples seemed to be variable depending on the laboratory conditions (relative humidity and temperature). When the samples were synthesized, just before the oven step for the activation process; the color was light turquoise. In contrast, once the samples were activated, their dry state of them showed a dark blue color, suggesting that the extraction of solvents produced this modification in the material. When the samples were removed from the oven and remained for a few minutes in contact with air at room temperature, their color changed again to light turquoise.

To analyze the color change of the samples, an experiment was performed. Letting the sample rest at laboratory conditions, the color of the materials was monitored, and the results suggested that probably the relative humidity of the ambient air was responsible for this change of color (Figure 6.1).

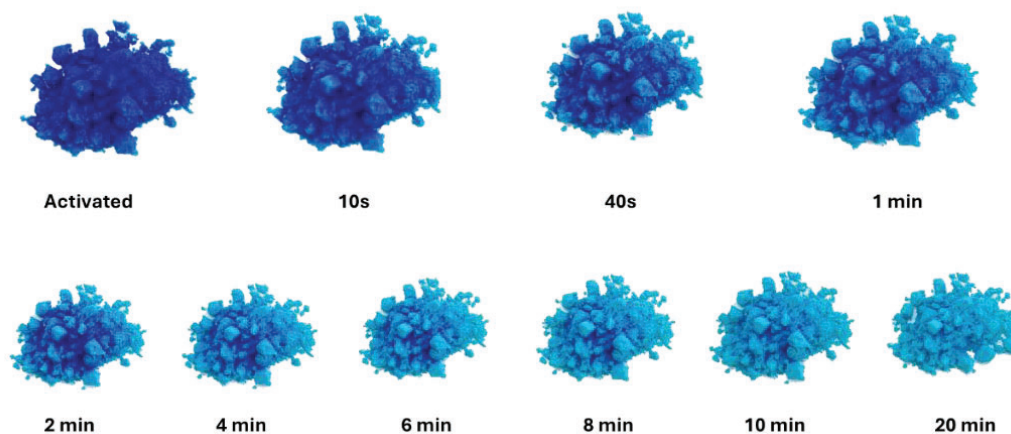


Figure 6.1. Color monitorization of HK sample under laboratory conditions over time.

Upon further investigation of this change in the sample color, literature describes that the cause is the H<sub>2</sub>O adsorption in the surface of the HKUST-1. The coordination of H<sub>2</sub>O with the copper atoms produces a structure with a lighter blue color due to

the interaction of  $\text{Cu}^{2+}$  centers and  $\text{H}_2\text{O}$ . However, these molecules are easily removed when temperature and vacuum are applied during the activation step. As the sample dries, the loss of coordinated water alters the  $\text{Cu}^{2+}$  electronic environment, leading to a darker blue color. In consequence, the dehydration of the sample makes the copper coordination sites accessible to other molecules (such as  $\text{CO}_2$  for example).<sup>159</sup>

Considering the previous behavior of the samples when water is adsorbed, a concept which facilitates the incorporation of the adsorbed molecules is the metal open sites (OMS). As described in Chapter I of this thesis, OMS are the obtained not fully coordinated metal ions produced when vacant Lewis's acid sites on the metal ions or cluster nodes are created, which can also be named as coordinatively unsaturated sites (CUS) or open coordination sites (OCS). A distinct feature of OMS is that their presence on the MOFs can give  $\pi$ -interactions with olefins and feature a high, exothermic adsorption enthalpy of  $\text{CO}_2$  which is advantageous for its gas sorption, and separation.<sup>160</sup> However, these potential  $\text{CO}_2$  adsorption sites can be occupied by solvent molecules like  $\text{H}_2\text{O}$ , alcohols, acetonitrile, or DMF used during synthesis or from atmospheric air with varying relative humidity (RH). The most common strategy to increase OMS in MOF structures involves solvent exchange followed by thermal treatment or activation steps.<sup>161</sup>

In the case of HKUST-1, the framework consists of dicopper paddlewheel secondary building units (SBUs) linked by trigonal  $\text{H}_3\text{BTC}$  ligands. During the activation step, the extraction of coordinated  $\text{H}_2\text{O}$  molecules from the Cu centers induces a change in the coordination number of  $\text{Cu}^{2+}$  cations from five (square-pyramidal geometry) to four (square-planar geometry). The Jahn Teller effect of  $d^9$ -ion explain the displacement of solvent molecules in HKUST-1 at the surroundings of  $\text{Cu}^{2+}$ , leading to weakly-bound axial ligands with long M-L bonds and a preference for a square-planar geometry (Figure 6.2).<sup>162</sup>

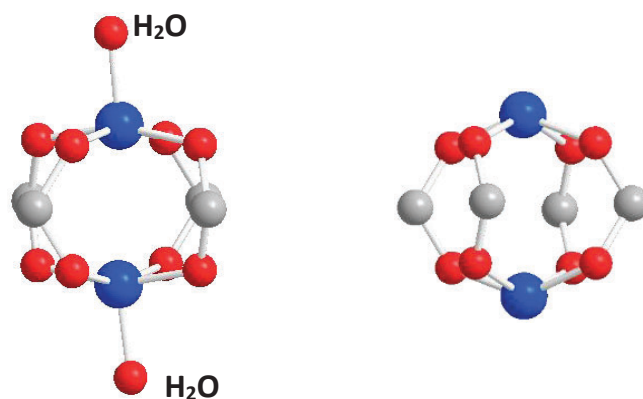


Figure 6.2. Molecular representation of the coordination sites of H<sub>2</sub>O molecules into the HKUST-1 structure. Blue: copper, red: oxygen and white: hydrogens. Adapted from ref.<sup>162</sup>

Considering other aspects of the synthesized samples related to color, it was observed that synthesizing HK-GO materials resulted in darker samples than the pristine HK. Higher percentages of graphene oxide (GO) led to darker samples under normal conditions. This correlation aligns with the light-absorbing nature of GO molecules, where even small quantities incorporated during synthesis noticeably affected the darkness of the samples (Figure 6.3).

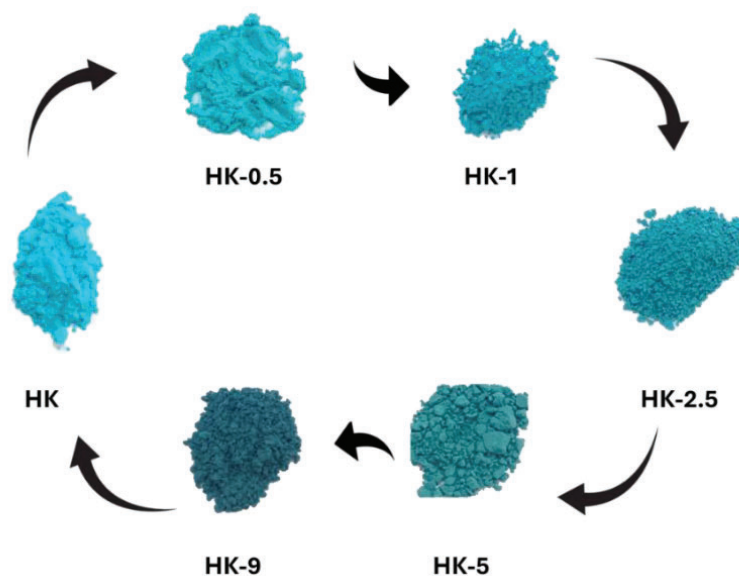


Figure 6.3. HK-GO samples with different theoretical GO content (at room temperature and 1 atm).

In this context, the following sections include experiments focused on assessing the influence of water molecules in the CO<sub>2</sub> adsorption performance of HK and HK-GO samples. To analyze this, some experiments are performed, including colorimetry of the samples, where the influence of H<sub>2</sub>O and CO<sub>2</sub> adsorption is investigated through the changes in the color; infrared spectroscopy (IR) and <sup>13</sup>C solid-state experiments (<sup>13</sup>C NMR), where the competition for the potential adsorption sites between both molecules is analyzed; and dynamic vapor sorption (DVS) along with breakthrough analysis (BTA) experiments, where the simultaneous sorption capacity, cyclability and kinetics of H<sub>2</sub>O and CO<sub>2</sub> adsorption processes are analyzed.

## 6.2 Colorimetry

The objective of these measurements is to determine the relationship between the change of color and the adsorption of H<sub>2</sub>O and CO<sub>2</sub> molecules under saturation conditions at varying concentrations, in order to monitor the state of the material.

To achieve this, the preparation of the samples before the colorimetric measurements followed the next steps. The samples were deposited onto 1 cm<sup>2</sup> white polypropylene sheets (Sappi Magno Matt 300 g/m<sup>2</sup>). For MSM samples, the material was applied directly onto the adhesive side of the sheet, created using double-sided tape, while for sBM samples, the material was deposited using an airbrush (Airbrush ABPST01, Timbertech, 0.3 mm nozzle). The airbrushing technique was unsuitable for MSM, as the material did not adhere properly. In both cases, the samples contained 1 mg of dried powder. The back of each polypropylene sheet was also covered with double-sided tape and placed in a custom-made holder to align the sample with the readout device (Figure 6.4 (a)).

Color variation was transduced into a digital signal using a commercial MAX30105 module (Sparkfun Electronics), which integrates three LEDs emitting in the green (537 ± 35 nm), red (660 ± 20 nm), and infrared (880 ± 30 nm) spectral regions, along with a photodiode (640-980 nm, >30% quantum efficiency). The module was controlled by an ESP8266 microcontroller through the gas chamber walls. The sample, placed in front of the sensor illuminated by LEDs (Figure 6.4 (b)), and the photodiode detected the reflected and transmitted light (Figure 6.4 (c)). During the color change, some of the previously reflected light was absorbed, causing variations in the signal. The magnitude of this change depended on the wavelength used, as the material does not absorb equally across the entire spectrum. However, signal variations for a given light source were exclusively related to the color transition induced by gas interaction.

Gas control inside the chamber, Figure 6.4 (c), was achieved using mass flow controllers (Bronckhorst) connected to pre-mixed gas bottles. Synthetic Air (SA, 20% O<sub>2</sub>, 80% N<sub>2</sub>) and pure CO<sub>2</sub> were introduced, while different humidity levels were generated using a gas bubbler system. CO<sub>2</sub> concentrations were adjusted by diluting pure CO<sub>2</sub> in SA. Experiments were conducted at room temperature, with samples activated by flowing SA for 3.3 hours at a constant gas flow rate of 200 ml/min. The increment of signal ( $\Delta\text{Signal}$ ) was calculated by obtaining the difference between the signal value at half of the gas inlet time and the pre-inlet signal value.

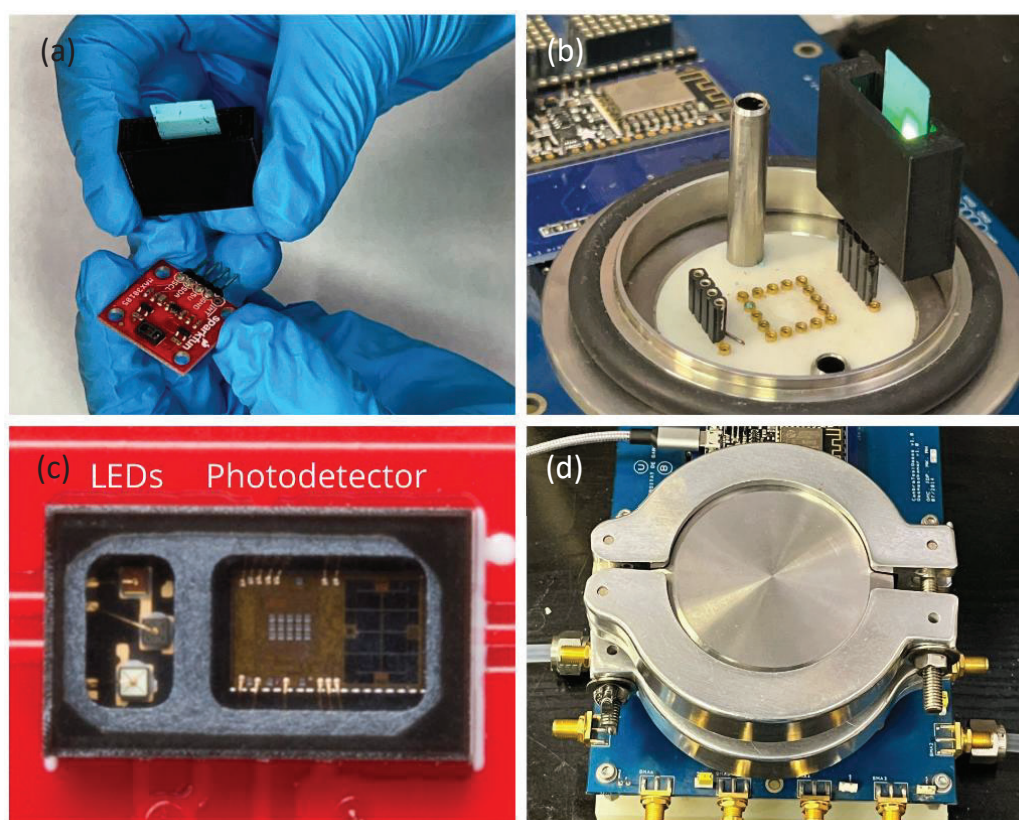


Figure 6.4. (a) Sample positioned in front of the MAX30105 module, (b) Readout module operating inside the gas chamber, (c) Close-up view of the MAX30105 showing the LED and photodiode, (d) Sealed gas chamber to maintain controlled light conditions and gas environment.

---

Considering this, the following sections are divided into three parts. Firstly, the color change of HK samples is investigated when they are exposed to streams of relative humidity (RH%) and CO<sub>2</sub>. Next, the color change of HK-GO samples is analyzed in order to evaluate the effect of GO on the color changes by monitoring the signal while exposing the samples at varying concentrations of CO<sub>2</sub>. And finally, the color change of the samples is studied through an experiment where a simultaneous stream of H<sub>2</sub>O and CO<sub>2</sub> is applied to the sample, to evaluate the influence of water in the color change of the sample during CO<sub>2</sub> adsorption process. The experiments were performed on samples obtained by MSM and sBM and as the behavior was similar, the results presented correspond to samples obtained via sBM.

Additionally, all the experiments were performed using red and green LED. However, the following sections expose the results of color change using the green LED since the signal obtained was significantly more pronounced than using red LED.

### **6.2.1 Color change of HKUST-1**

To study the color transition during humidity interaction, the HK sample was activated and then sequentially exposed to increasing relative humidity levels from 25% to 30%, by activating the sample and introducing intervals of 60 min of synthetic air (SA) for activating the sample after the stabilization of the color in each step. The introduction of RH was performed once the sample remained with a constant dark blue color after introducing SA for activation of the sample. The response obtained was immediate, with a color stabilization of around 20 minutes in each step. Additionally, when the sample was activated again passing through SA without RH, the color turned dark blue showing a reversible behavior.

In Figure 6.5 are represented the results of HK obtained via sBM as an example, since the color behavior of HK synthesized using MSM is identical. In this representation, the signal corresponds to the variation of the reflected and the transmitted light detected by photodetector when the green LED illuminates the sample. The signal obtained (measured in counts) is modulated by the humidity inside the gas chamber.

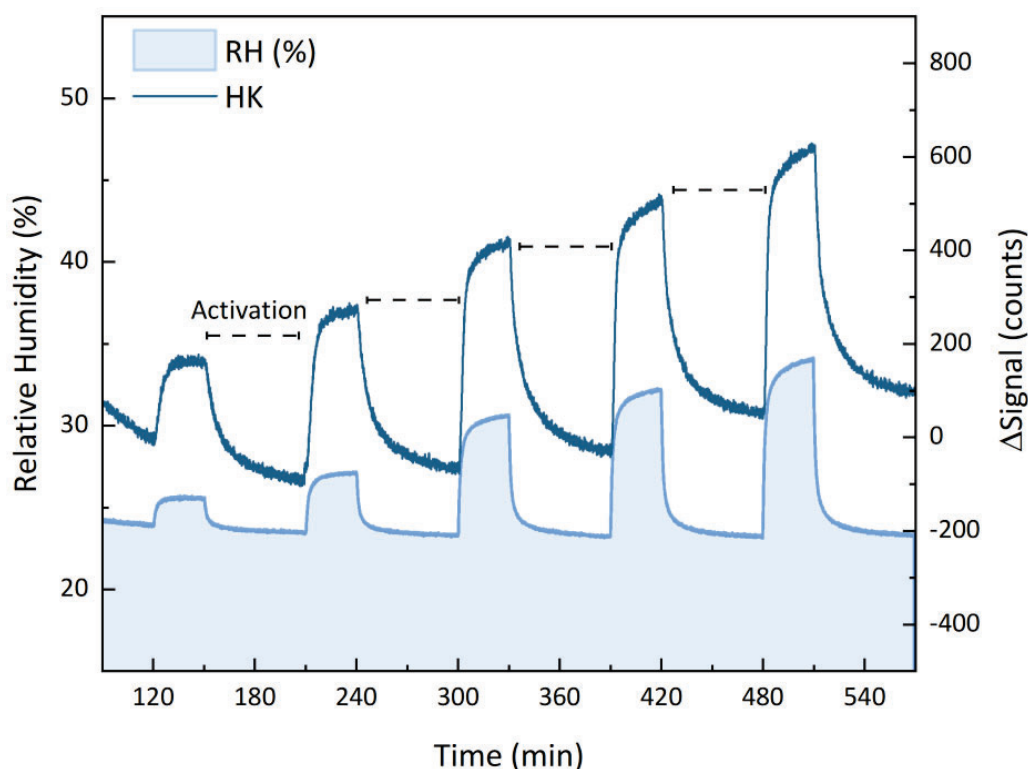


Figure 6.5. Photodiode signal when the color of HK is changing according to varying RH%. Activation time of 60 min with SA between the steps of RH exposure.

During activation steps the signal response decreases according to the release of water molecules inside the chamber. Once the signal stabilizes, the introduction of %RH produces changes in the color of the sample, and it is detected with an increase of the signal response. The photodiode signal changed immediately, stabilizing within approximately 20 minutes at each step. Additionally, when the sample was reactivated by exposure to dry SA, the signal returned to its initial state, demonstrating reversible behavior. So, this confirms that in this case the change of the color in HK materials is subjected to the interaction with H<sub>2</sub>O molecules.

Given that HKUST-1 exhibits color changes in response to the adsorption of water molecules, additional experiments were conducted to investigate if the samples also change the color when they adsorb CO<sub>2</sub> molecules. These experiments were

considered since monitoring changes in the color attributed to the CO<sub>2</sub> adsorption allows for the evaluation of the material's potential for sensing applications.

Hence, the color change was monitored by introducing 10-minute steps with different CO<sub>2</sub> concentrations up to 100%, allowing 20-minute intervals with SA for the sample to return to its initial activated color before the next step. The results demonstrate a gradual color change in the sample corresponding to the amount of gas introduced, as depicted in the Figure 6.6. The drift of the signal baseline is caused by a non-complete activation of the sample.

As a result, HK samples exhibit signal increments corresponding to increased CO<sub>2</sub> concentrations, suggesting a linear correlation and showing a color shift that linearly correlates with the increased introduction of CO<sub>2</sub> gas into the chamber.

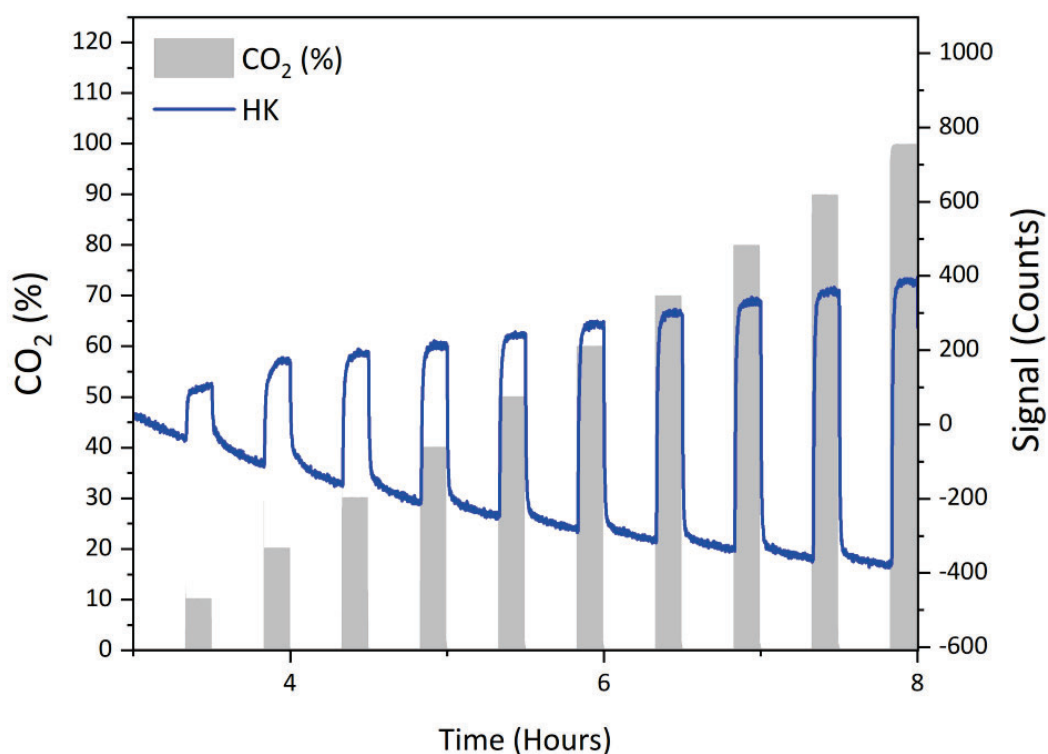


Figure 6.6. Signal response of HK when a stream of varying concentrations of CO<sub>2</sub> is introduced into the chamber (using green LED).

Hence, the results confirm that HK samples exhibit a clear and progressive color change in response to increasing CO<sub>2</sub> concentrations, with a signal intensity that correlates linearly with the amount of gas introduced. These findings indicate a way to monitor in-situ and continuously the state of the materials under operational conditions, both adsorption and desorption processes. In the next two sections, apart from confirming the same effect in HK-GO, additionally, the potential of HK-GO materials for sensing CO<sub>2</sub> molecules is evaluated by the monitorization of color change.

### 6.2.2 Color change of HKUST-1/GO

The same experiment performed on HK samples using CO<sub>2</sub> gas concentrations was carried out on HK-GO samples to determine whether the GO content, which is responsible for the darker appearance of the samples, produced any changes in the color detection. Figure 6.7 displays the results of HK-GO (sBM) considering the color changes when samples are exposed to CO<sub>2</sub> gas streams. The results are plotted according to the signal increment ( $\Delta$ Signal) against the concentration of CO<sub>2</sub> and the lineal correlation is confirmed in all the samples.

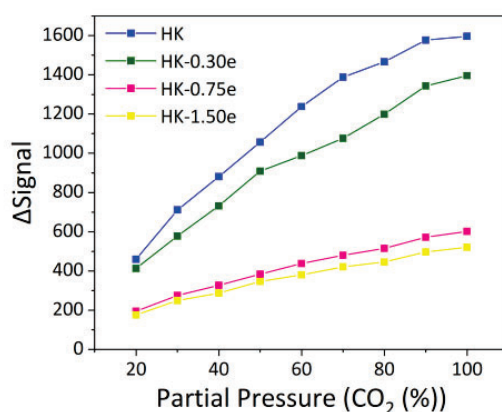


Figure 6.7.  $\Delta$ Signal of HK-GO samples obtained via sBM when a stream of varying concentrations of CO<sub>2</sub> is introduced into the chamber (using green LED).

The results indicate that green LEDs differ in how GO modulates the  $\Delta$ Signal. HK-GO samples exhibit lower  $\Delta$ Signal with increasing amounts of GO in the green LED, which

is directly related to the darkening of the sample as the amount of GO increases. This causes a shift to a higher wavelength at which HK-GO absorbs light, making it unfeasible to detect the color change with the same intensity as in the sample without GO, since the green illumination only covers the  $537 \pm 35$  nm region. However, the results exhibit that even with darkening samples (like those which contain GO), the signal produced when CO<sub>2</sub> is adsorbed by HK-GO samples is still detectable in all the range of GO content utilized in this research. This confirms the feasibility of monitoring in-situ and continuously the state of HK-GO materials under operational conditions, both the adsorption and desorption process, as well as HK materials.

Upon comparing the signals obtained from the color change in the most adsorbent sample with the CO<sub>2</sub> adsorption isotherms (HK-0.50e obtained via sBM), a correlation is observed (Figure 6.8 (a)). An observation is the remarkable similarity between the  $\Delta$ Signal and the adsorption behavior obtained from CO<sub>2</sub> adsorption isotherms, both exhibiting a linear relationship along with the partial pressure of CO<sub>2</sub> (Figure 6.8 (b)).

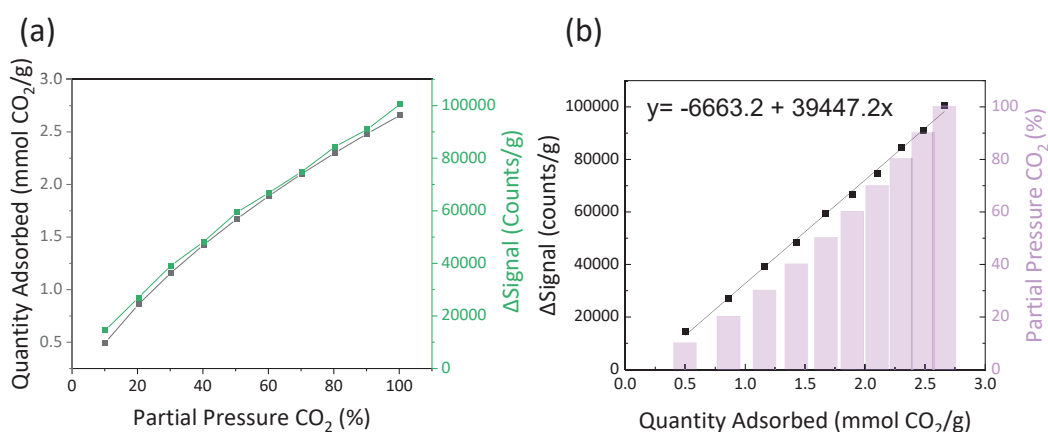


Figure 6.8. (a) CO<sub>2</sub> and color signal response isotherms tested at 298 K and (b) CO<sub>2</sub> adsorption and color signal response relationship. The sample tested is HK-0.50e obtained via sBM.

This relationship enables the quantification of CO<sub>2</sub> adsorption amounts for various samples from different batches of HK samples through colorimetry, according to the equation  $y = -6663.2 + 39447.2x$ .

### 6.2.3 Simultaneous CO<sub>2</sub> and H<sub>2</sub>O signal response

In order to address whether the determination of CO<sub>2</sub> saturation in HK-GO sample is feasible using colorimetry in environments where H<sub>2</sub>O is present, another experiment considering simultaneous H<sub>2</sub>O and CO<sub>2</sub> adsorption is performed. In this case, the results shown in Figure 6.9 were obtained using synthesized samples. The interaction of H<sub>2</sub>O and CO<sub>2</sub> and its effect on the color signal was explored in the pristine HK and the most adsorbent sample.

The experiment is divided into two sequences, where 25% and 50% of CO<sub>2</sub> concentration steps were conducted in dry conditions (left side of the graph) and, in the second experiment, the same steps of CO<sub>2</sub> were carried out under humid conditions by simultaneously introducing 25% of RH into the chamber (right side of the graph).

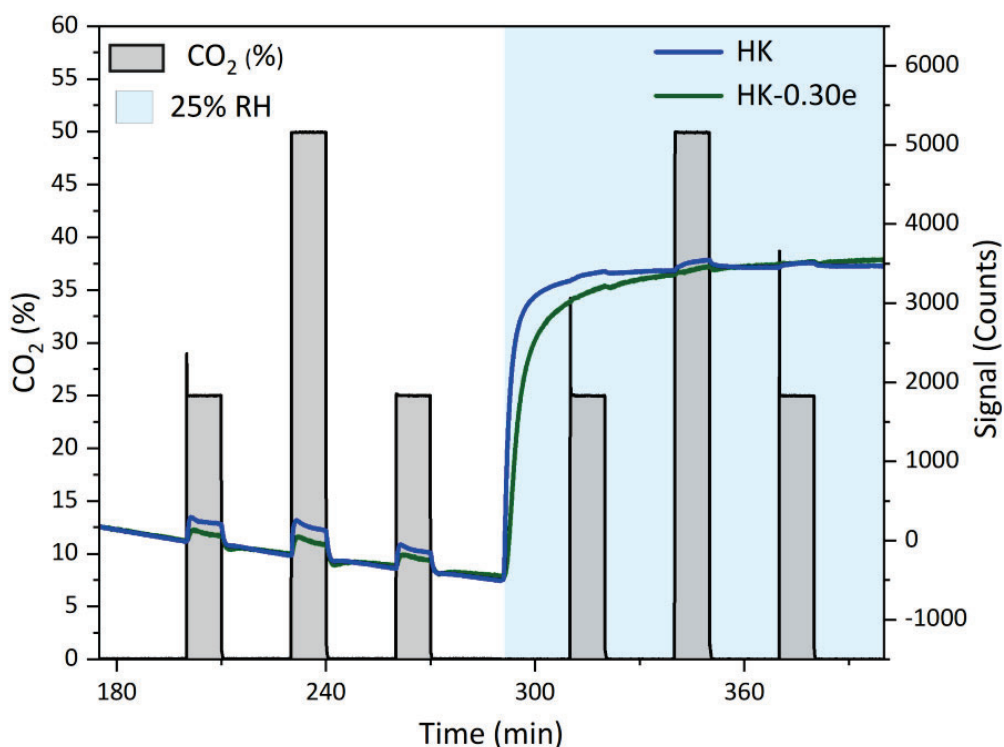


Figure 6.9. Signal response of samples HK and HK-0.30e when are exposed to 25 and 50% of CO<sub>2</sub> in dry conditions and along with 25% of RH (using green LED).

Based on the results illustrated in the Figure 6.9, there is a signal response to the change of color when CO<sub>2</sub> is introduced, where the signal displays slightly higher in the 50% CO<sub>2</sub> step. These results align with the prior observations when HK and HK-GO samples were exposed to different percentages of CO<sub>2</sub> and the signal obtained presented a linear behavior related to the quantity of CO<sub>2</sub> gas introduced to the chamber (Figure 6.6 and Figure 6.7).

When 25% of RH is introduced inside the chamber along with the CO<sub>2</sub>, the signal is completely altered because the introduction of H<sub>2</sub>O molecules changes drastically the color of the sample and, as a result, there is a huge increment of the signal. Once the signal stabilizes, the stream of CO<sub>2</sub> is introduced again using 25% and 50% of CO<sub>2</sub>. In this case, the signal attributed to the color change is low.

Therefore, although this method allowed for determining responses based on the adsorption of CO<sub>2</sub> and H<sub>2</sub>O molecules while the sample color changes, the simultaneous adsorption of both molecules doesn't lead to significant results regarding adsorption, selectivity, or competitive adsorption between H<sub>2</sub>O and CO<sub>2</sub> molecules.

### 6.3 Infrared spectroscopy: Influence of H<sub>2</sub>O and CO<sub>2</sub> adsorption

The main objective of analyzing the HK-GO samples using IR technique is to determine and study the vibrational transition of the material when adsorbing H<sub>2</sub>O and CO<sub>2</sub>. The vibration changes due to the adsorption can provide insight into where the adsorbed CO<sub>2</sub> and H<sub>2</sub>O molecules are positioned within the chemical structure. Although water molecules are also absorbed into other regions of the sample, the first experiments of this section are focused on the carboxylate bands since these regions present more significant changes in IR spectra when samples are in contact with H<sub>2</sub>O and CO<sub>2</sub> (Figure 6.10). This makes sense with the literature since CO<sub>2</sub> and H<sub>2</sub>O are acidic molecules with strong affinity for basic environments, such as the carboxylate groups derived from the ligand H<sub>3</sub>BTC of HKUST-1 or the surface of GO.

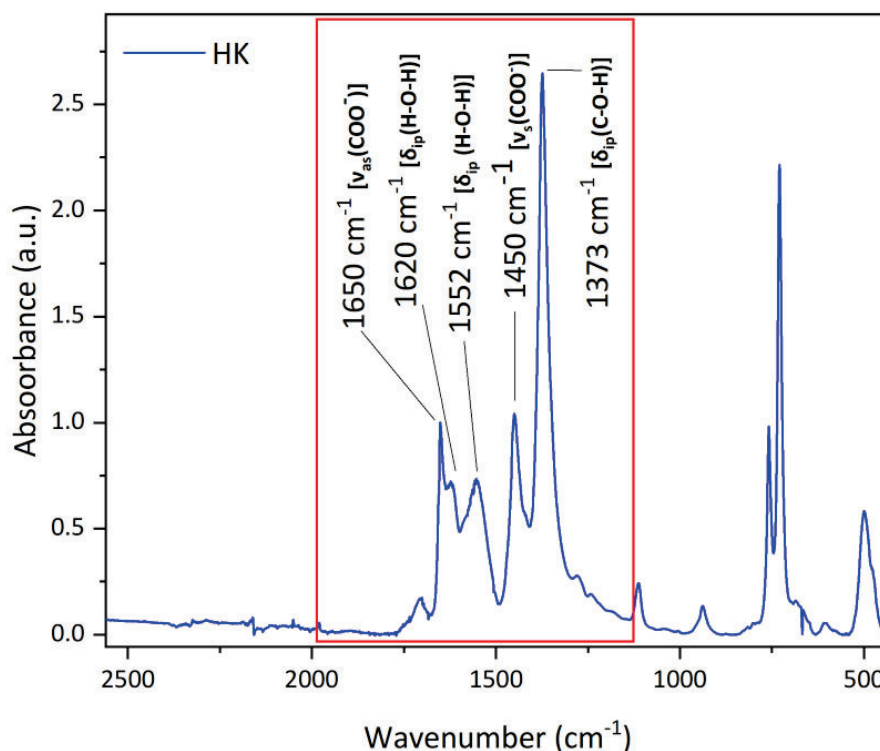


Figure 6.10. Infrared spectrum of HK. The red square highlights the area where carboxylate bands of the sample appear.

In IR spectroscopy, vibrations can be attributed to either bending or stretching, depending on the movement of the atoms. When the movement is directed towards the center, like a spring that compresses and extends, it is a stretching vibration. There are two types of stretching: symmetric stretching, where the atoms move in the same direction ( $\nu_s$ ), and asymmetric stretching ( $\nu_{as}$ ), where the atoms move in opposite directions. When the movement of the atoms resembles the action of scissors, the vibration is classified as bending. This bending can occur within the same plane ( $\delta_{ip}$ ) or out of plane ( $\delta_{op}$ ) (Figure 6.11).<sup>163</sup>

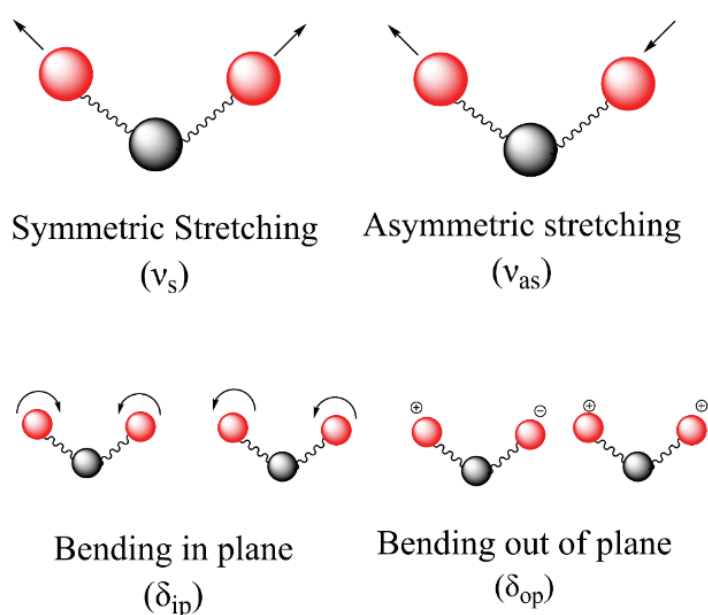


Figure 6.11. Representation of the vibrational bending and stretching movements of the atoms.

Considering all the above, the IR spectrum of HK sample shows the following stretchings and bendings (Figure 6.10). The carboxylate band is divided into two well-differentiated regions: the bands located between 1655-1555  $\text{cm}^{-1}$ , which corresponds to the asymmetric  $\text{-COO}^-$  stretching,  $\nu_{as}(\text{COO}^-)$  at 1651  $\text{cm}^{-1}$ , and the bands between 1450-1373  $\text{cm}^{-1}$ , which corresponds to the symmetric  $\text{-COO-}$  stretching,  $\nu_s(\text{COO}^-)$  at 1450  $\text{cm}^{-1}$ . Additionally, the bendings vibration attributed to H-O-H vibration ( $\delta_{ip}$ ) appears at 1615  $\text{cm}^{-1}$ , while the  $\text{-C-O-H}$  bending mode ( $\delta_{ip}$ ) is observed at 1373  $\text{cm}^{-1}$ .<sup>164</sup>

### 6.3.1 Experimental approach to analyze vibrational changes in HK-GO materials under CO<sub>2</sub> and H<sub>2</sub>O adsorption

The following experiments focus on analyzing the effect of CO<sub>2</sub> and H<sub>2</sub>O on the chemical structure of the samples. The initial experiments specifically evaluate the carboxylate vibration region of asymmetric -COO<sup>-</sup> stretching (1650 cm<sup>-1</sup>) and the bendings attributed to H-O-H vibration bands in plane at 1615 cm<sup>-1</sup> since these regions produced significant changes relating to the adsorption of both molecules. However, other observations across the IR spectra are provided, such as the -OH vibrational changes, at around 3200 cm<sup>-1</sup>; and the copper nuclei vibrations at around 490 cm<sup>-1</sup>. Significant changes are only observed in those specific bands, as the aromatic region exhibits high stability due to the strong benzene ring bonds, resulting in less energetic vibration changes. Thus, as it is not possible to confirm whether H<sub>2</sub>O and CO<sub>2</sub> molecules interact with aromatic functional groups, additional characterization techniques are needed. For this reason, *Section 6.4* of this chapter utilizes <sup>13</sup>C Nuclear Magnetic Resonance experiments, and this section only focuses on carboxylate, hydroxyl and copper-nuclei vibration bands.

In this regard, the following outcomes (experiments 1, 2 and 3) provide the results of experiments performed using a continuous exposure of relative humidity (RH) or/and CO<sub>2</sub> in different orders. Then, additional experiments using pure streams of RH or CO<sub>2</sub> are presented (experiments A and B). All these experiments are conducted on HK and HK-0.30e samples to compare the pristine MOF with the most adsorbent sample, both obtained through bBM method of synthesis.

#### **IR experiments under continuous relative humidity (RH) or/and CO<sub>2</sub> exposure**

HK and HK-0.30e were exposed to similar conditions to the industrial environment of a post-combustion system, which typically contains approximately 15% CO<sub>2</sub> and 50% relative humidity (RH), using SA as carrier gas. Hence, the tests conducted on the first experiment were the following:

- 1) Spectra of samples exposed to CO<sub>2</sub> at a concentration of 15%.

- 2) Spectra of samples exposed to simultaneously 15% of CO<sub>2</sub> and a 50% of RH.
- 3) Spectra of the sample when the RH is removed while maintaining a continuous flow of 15% CO<sub>2</sub> after steps 1 and 2.

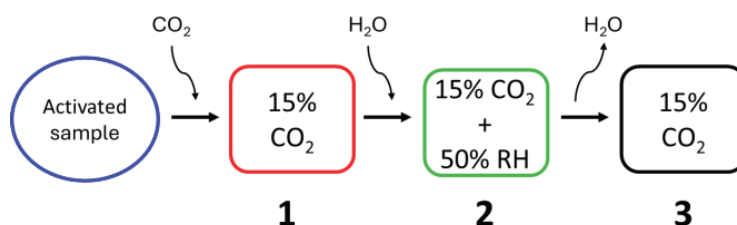


Figure 6.12. Scheme of the steps performed on HK and HK-0.30e in the first experiment.

Following the procedure described above, infrared spectra were measured just after each step for HK and HK-0.30e samples. The results of both samples are presented in Figure 6.13 (a) and (b), indicating in each graph an expanded region of the spectrum where the carboxylate band appears, between 1600-1650 cm<sup>-1</sup>, and the bending attributed to H-O-H vibration bands at 1615 cm<sup>-1</sup>.

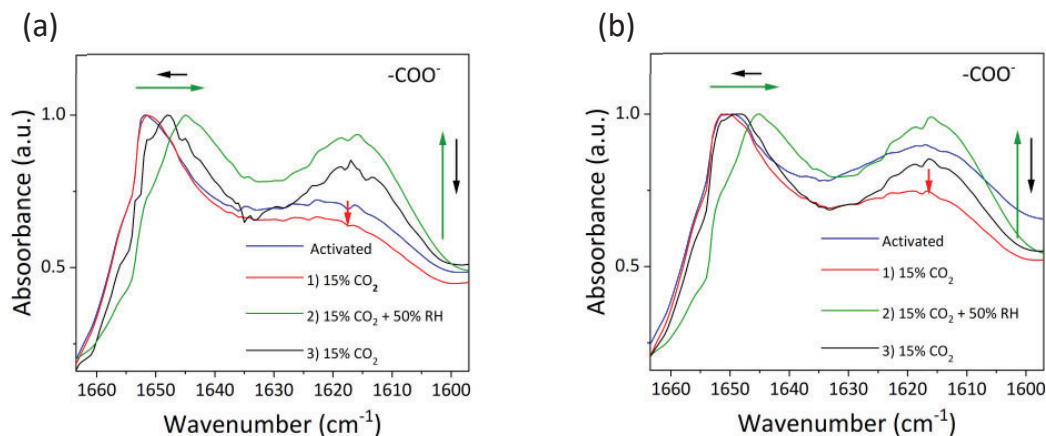


Figure 6.13. Infrared spectra measurements of (a) HK and (b) HK-0.30e performed after each step of experiment 1.

Despite not observing any apparent change in the band corresponding to  $\nu_{as}$  -COO<sup>-</sup> when step 1 was performed, the band ascribed to the  $\delta_{(ip)} \text{H-O-H}$  at 1615 cm<sup>-1</sup> decreased slightly in intensity, indicating a reduction in this vibrational movement. However, when introducing relative humidity in step 2, the intensity of this band increased significantly, even surpassing the initial value in the active state. Additionally, the

band corresponding to  $\nu_{as} \text{-COO}^-$  shifted to the right of the spectrum, up to  $7 \text{ cm}^{-1}$ . This suggests that the introduction of  $\text{H}_2\text{O}$  to the system drastically modified both the bending and stretching movements of the carboxylate groups. Otherwise, when the introduction of water to the system was stopped and only a stream of 15% of  $\text{CO}_2$  was passed through again, the band corresponding to stretching began to return to its initial position (step 3). Simultaneously, the bending band decreased in intensity. These results suggest that water is likely adsorbed around the carboxylate groups of the sample and when a  $\text{CO}_2$  stream is applied,  $\text{CO}_2$  replaces the molecules of adsorbed water, and the carboxylate bands return to the initial position. This reversible behavior of the vibration band in step 3 suggests that probably  $\text{CO}_2$  is acting like a 'carrier gas' displacing the adsorbed  $\text{H}_2\text{O}$  molecules.

At this point, the same methodology was carried out again but modifying the saturation gas steps. In this second experiment, the tests conducted followed the next steps (indicated as well in the Figure 6.14):

- 1) Spectra of samples exposed to 50% RH.
- 2) Spectra of samples exposed simultaneously to 15% of  $\text{CO}_2$  along with 50% RH.
- 3) Spectra of the sample when the 15% of  $\text{CO}_2$  is removed while maintaining a continuous flow of 50% of RH after steps 1 and 2.

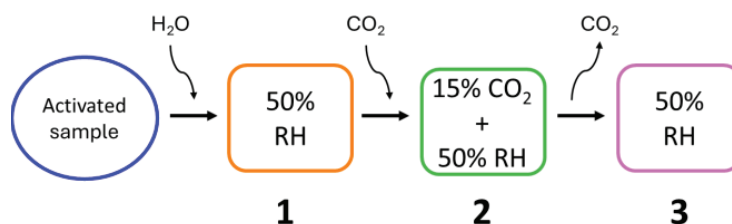


Figure 6.14. Scheme of the steps performed on HK and HK-0.30e in experiment 2.

Following the procedure described above, infrared spectra was measured just after each step for HK and HK-0.30e samples. The results of both samples are presented in Figure 6.15 (a) and (b), indicated in each graph an expanded region of the spectrum

where the carboxylate band appears between  $1600\text{-}1650\text{ cm}^{-1}$ , and the bending attributed to H-O-H vibration bands at  $1615\text{ cm}^{-1}$ .

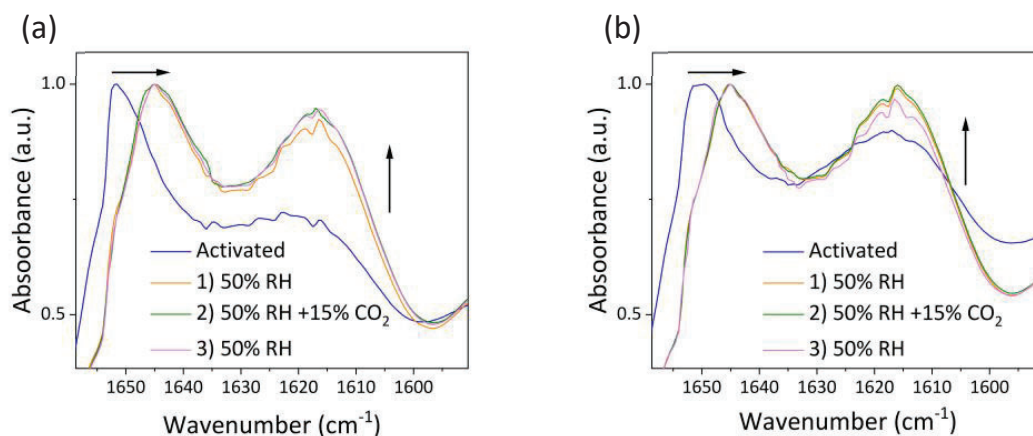


Figure 6.15. Infrared spectra measurements of (a) HK and (b) HK- 0.30e performed after each step in experiment 2.

As observed in the collected spectra, the band corresponding to stretching moved to the right and the intensity of the band corresponding to bending increased (step 1), replicating the behavior previously observed in experiment 1 when H<sub>2</sub>O was introduced together with CO<sub>2</sub>. In contrast to the first experiment, steps 2 and 3 didn't provide any substantial change in the samples, since the spectra remained constant.

Additionally, a third experiment was performed. In this case, the measurements taken followed the steps of experiment 2 but with a modification in the last step. Instead of removing CO<sub>2</sub> stream and maintaining RH%, RH% was removed and the stream of CO<sub>2</sub> was maintained. The steps are described below and schematically represented in Figure 6.16.

- 1) Spectra samples exposed to 50% RH.
- 2) Spectra of samples simultaneously exposed to 15% of CO<sub>2</sub> along with 50% RH.
- 3) Spectra of the sample when the RH is removed while maintaining a continuous flow of 15% CO<sub>2</sub> after steps 1 and 2.

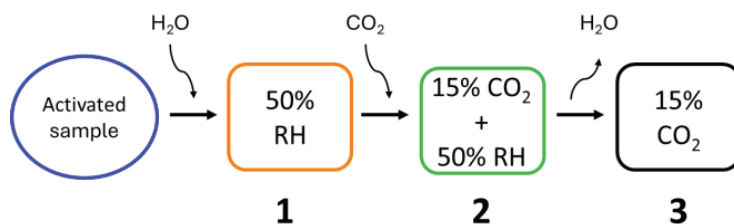


Figure 6.16. Scheme of the steps performed on HK and HK-0.25 in the third experiment.

Following the procedure described above, infrared spectra was measured just after each step for HK and HK-0.30e samples. The results of both samples are presented in Figure 6.15 (a) and (b), indicating in each graph an expanded region of the spectrum where the carboxylate band appears between  $1600\text{--}1650\text{ cm}^{-1}$ , along with the bending attributed to H-O-H vibration bands at  $1615\text{ cm}^{-1}$ .

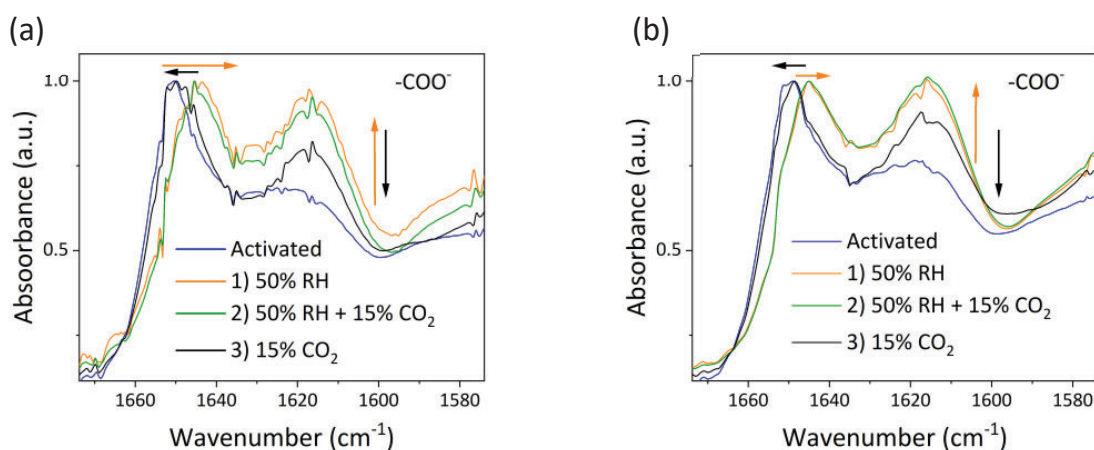


Figure 6.17. Infrared spectra measurements of (a) HK and (b) HK-0.30e performed after each step in experiment 3.

The results indicate that when step 2 is carried out, the intensity of the bending decreases (Figure 6.17 (a) and (b)). Moreover, the shifting of the stretching observed in step 1 and 2 is reversible when 15% of  $\text{CO}_2$  remained alone saturating the sample during step 3. This behavior indicates that  $\text{CO}_2$  is replacing the molecules of  $\text{H}_2\text{O}$  adsorbed in the carboxylate positions of the sample.

These findings imply that  $\text{H}_2\text{O}$  and  $\text{CO}_2$  interact with each other during the adsorption process. Moreover, experiments 1,2 and 3 indicate that  $\text{H}_2\text{O}$  molecules are potentially

adsorbed in the asymmetric carboxylate bonds, while  $\text{CO}_2$  molecules are not adsorbed but interact with  $\text{H}_2\text{O}$  displacing them.

On the other hand, other regions of the spectra also present significant changes attributed to the introduction of  $\text{CO}_2$  and RH% stream, as in the case of -OH band vibrations detected around  $3200\text{ cm}^{-1}$ . The band associated with -OH vibrations is increased when %RH is introduced to the sample. When %RH and 15% of  $\text{CO}_2$  streams remained at the same moment, this band decreased. Once relative humidity is no longer introduced and only the  $\text{CO}_2$  flow persists, the band practically disappears, suggesting the desorption of  $\text{H}_2\text{O}$  molecules directly induced by  $\text{CO}_2$ . Figure 6.18 exhibits the spectra obtained in the third experiment, where the band of -OH bonds is indicated by a red circle. These changes of vibration intensity in -OH bonds are observed in 1,2 and 3 experiments. However, only experiment 3 is represented below as an example.

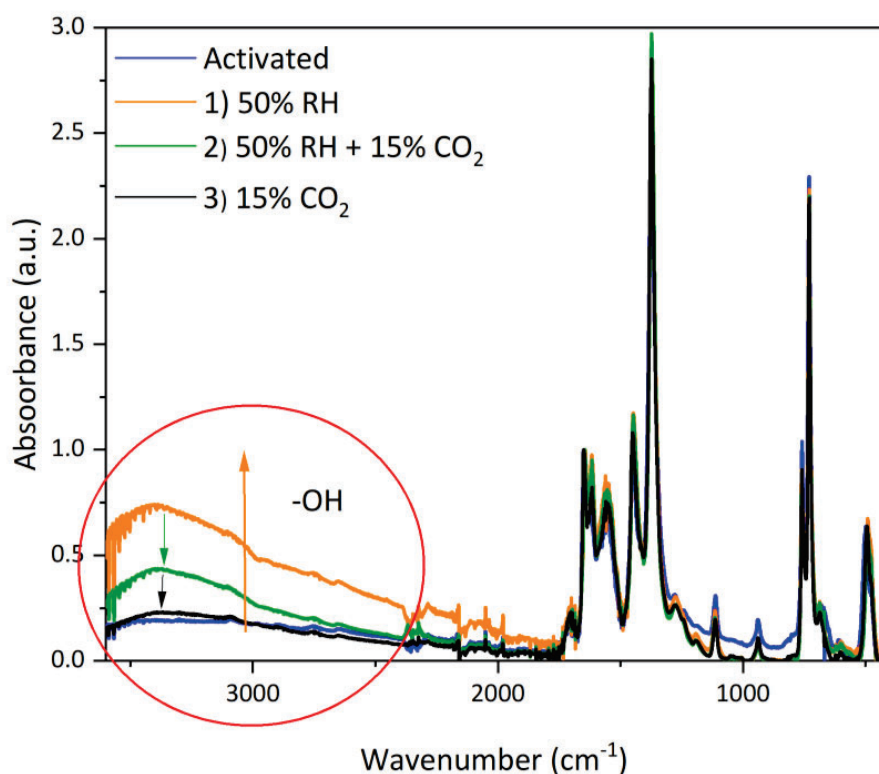


Figure 6.18. Infrared spectra of HK-0.30e after each step of experiment 3. The red circle highlights the region corresponding to the hydroxyl bands.

Overall, experiments 1,2 and 3 confirm that there's a shift of the asymmetric stretching of carboxylate bands at  $1650\text{ cm}^{-1}$  in all cases when  $\text{H}_2\text{O}$  molecules are interacting with the samples. Moreover, this interaction with water is also detected in the  $-\text{OH}$  bonds at  $3200\text{ cm}^{-1}$ . When 15% of  $\text{CO}_2$  is introduced, some changes are detected in cases where an earlier step of RH is produced. In those cases, the behavior observed corresponds to a reversible displacement of the carboxylate band, suggesting that when the sample contain adsorbed  $\text{H}_2\text{O}$  molecules, the exposure to  $\text{CO}_2$  produces a displacement of  $\text{H}_2\text{O}$ . These results indicate that probably  $\text{CO}_2$  molecules are not being adsorbed in the carboxylate band, thereby acting as a carrier gas instead of replacing the molecules of adsorbed water. This suspicion arises because the observed spectral shifts are reversible with  $\text{CO}_2$  exposure and the spectra under  $\text{CO}_2$  exposures remain identical to those of activated samples.

To further investigate this and evaluate if  $\text{CO}_2$  is competing with  $\text{H}_2\text{O}$  for the potential adsorption of carboxylate sites or acting as a 'carrier gas', additional IR experiments were performed. In this regard, the following section shows the results of exposing the samples to several concentrations of pure RH% (experiment A) and pure  $\text{CO}_2$  (experiment B).

#### **IR experiments under pure relative humidity (RH) or $\text{CO}_2$ exposure**

$\text{CO}_2$  or RH streams were carried out to the samples to determine whether  $\text{CO}_2$  molecules are competing for the same carboxylate adsorption sites as  $\text{H}_2\text{O}$  molecules.

On the one hand, experiment A was performed using several concentrations of RH (5-80%). As in the case of the previous experiments of this section, infrared spectra were measured just after exposure of RH% for HK and HK-0.30e samples. In this case, the intention of experiment A was to confirm the adsorption sites of  $\text{H}_2\text{O}$  and detect differences between the most adsorbent sample and the pristine HK.

Figure 6.19 expose the results of both samples indicating an expanded region of the carboxylate band (asymmetric stretching) at  $1650\text{ cm}^{-1}$ .

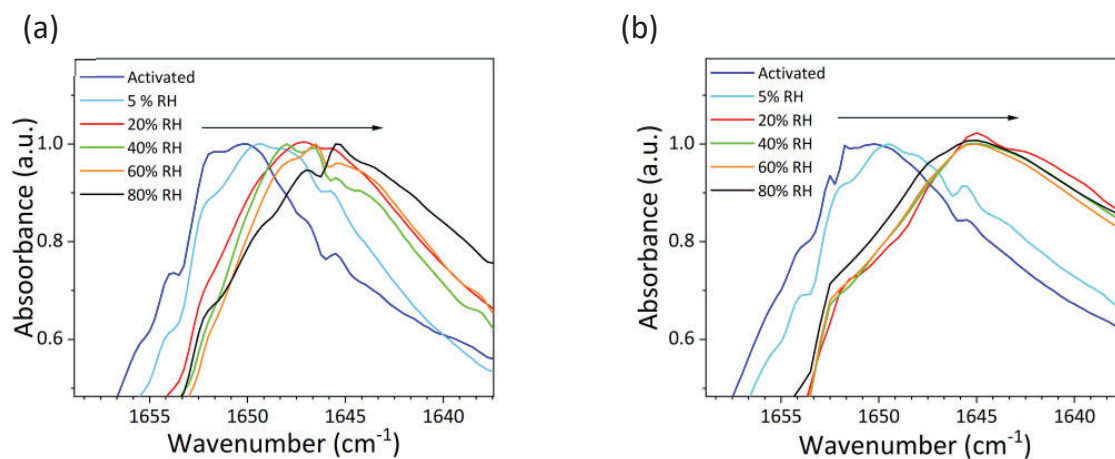


Figure 6.19. Expanded region of the carboxylate band in the infrared spectra of experiment A for (a) HK and (b) HK-0.30e.

As a result, a shift to the right of the spectrum is observed as the concentration of RH increases, reaching the equilibrium at  $7\text{ cm}^{-1}$  of displacement. Both samples, HK and HK-0.30e, indicate identical behavior concerning the adsorption of  $\text{H}_2\text{O}$  in the carboxylate band. These results align with experiments 1,2 and 3 and confirm that the asymmetric stretching in the carboxylate band of the samples is one of the potential adsorption sites for  $\text{H}_2\text{O}$  molecules.

Moreover, additional significant shifting in IR spectra of experiment A was also detected, but in this case, in the band associated with the copper nuclei bonds (Cu-O), at  $490\text{ cm}^{-1}$ . Figure 6.20 exhibits an expanded region of the copper-nuclei band in the spectra of both samples.

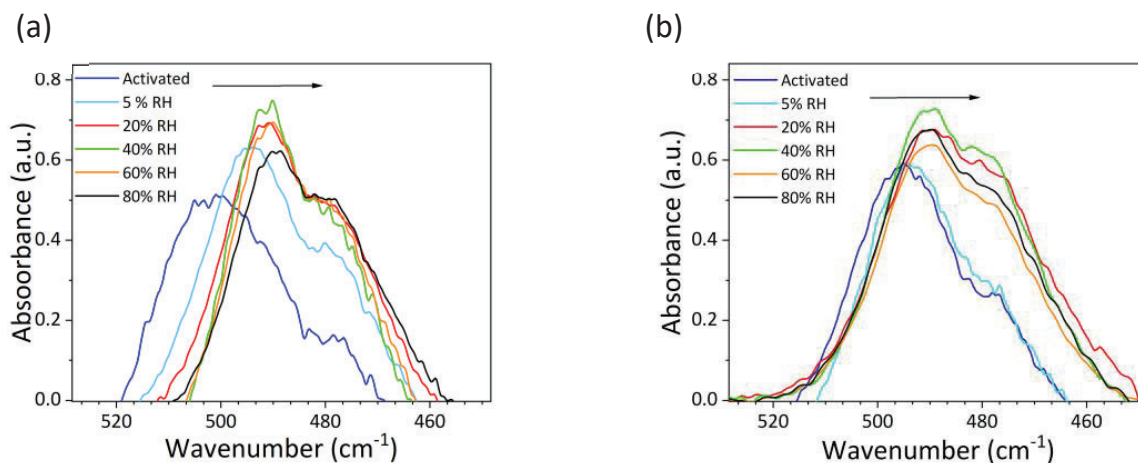


Figure 6.20. Expanded region of the copper-nuclei band in the infrared spectra of experiment A for (a) HK and (b) HK-0.30e.

In this case, the samples behave slightly differently. Pristine HK shows a shift of up to  $10\text{ cm}^{-1}$  to the right, while HK-0.30e exposes a lower shift, of up to  $5\text{ cm}^{-1}$ . Moreover, the Cu-O band in the activated state of the samples doesn't exhibit the same position, which could be related to the content of GO in sample HK-0.30e ( $500\text{ cm}^{-1}$  for pristine HK and  $495\text{ cm}^{-1}$  for HK-0.30e). These results suggest that, as HK-0.30e contains 0.30% of experimental GO in the structure, probably GO molecules are blocking partially the adsorption sites of  $\text{H}_2\text{O}$  molecules and the vibrational changes resulting from the adsorption are lower. This suggests that HKUST-1 with GO; HK-0.30e sample, offers improved stability against water molecules, which is relevant considering that prolonged interaction with  $\text{H}_2\text{O}$  can lead to sample degradation (confirmed by DVS measurements presented in *Section 6.5.1*).

On the other hand, experiment B was performed following a similar procedure as experiment A, but instead of exposing the samples to RH%, several streams of  $\text{CO}_2$  concentrations (40-100%) were applied. This experiment was carried out to determine whether adsorption of  $\text{CO}_2$  molecules is produced in carboxylate bands, like  $\text{H}_2\text{O}$  molecules. The results are presented in Figure 6.21, illustrating an expanded region of the carboxylate band (asymmetric stretching), like in the case of experiment A.

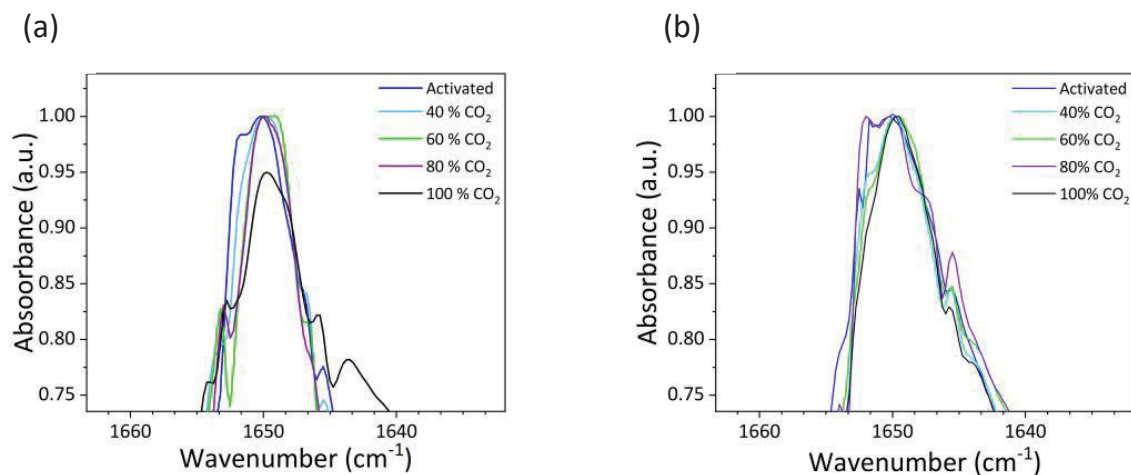


Figure 6.21. Expanded region of the carboxylate band in the infrared spectra of experiment B for (a) HK and (b) HK-0.30e.

In this case, all the spectra performed using varying streams of CO<sub>2</sub> indicate identical positions of the carboxylate band in both samples (HK and HK-0.30e), with slight variations possibly attributed to the resolution of the equipment. Given that the carboxylate band remains without any apparent shifting, it is suspected that CO<sub>2</sub> molecules are not adsorbed in carboxylate bands.

Additionally, Figure 6.22 shows the expanded region associated with the Cu-O band in all the experiments performed using infrared spectroscopy of experiment B.

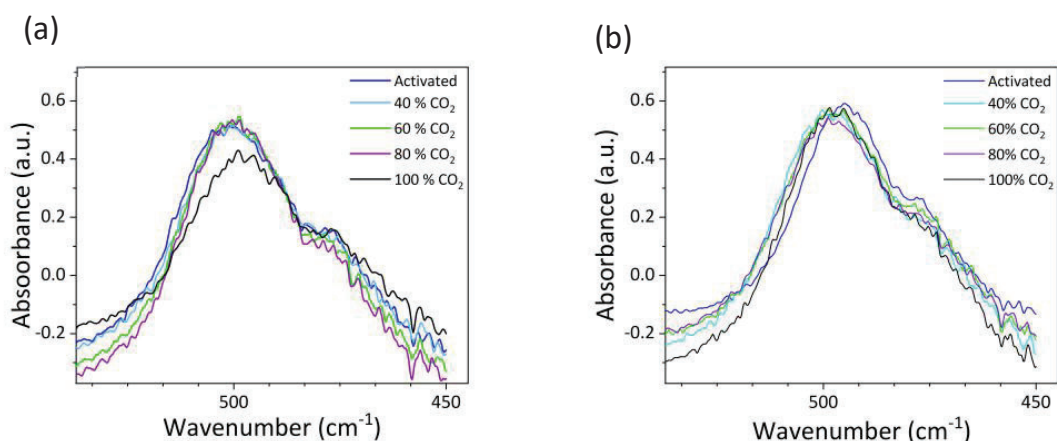


Figure 6.22. Expanded region of the copper-nuclei band in the infrared spectra of experiment B (a) HK and (b) HK-0.30e.

The copper nuclei band remained at the same position after all the exposure of CO<sub>2</sub> to the samples, without any apparent shifting in both samples, unlike experiment A. These results suggest that adsorbed CO<sub>2</sub> molecules do not interact with the Cu-O bonds of HK and HK-0.30e samples, in contrast to H<sub>2</sub>O adsorbed molecules, where such interaction is observed.

In summary, the results obtained in experiments A and B aligned with the results of experiments 1,2 and 3, since the exposure of several RH% to the samples produced some vibrational change, whereas the carboxylate band in spectra of both samples remained unchangeable when the samples were exposed to some CO<sub>2</sub> concentrations. These results suggest that CO<sub>2</sub> molecules are not adsorbed in carboxylate functional groups, whereas the H<sub>2</sub>O molecules produce some vibrational changes in this band, indicating a clear interaction with the material. Moreover, considering the copper-nuclei bands, the observed shift in experiment A not only confirms that H<sub>2</sub>O coordinates around the copper center, as previously reported in the literature, but also reveals that the sample containing GO exhibits fewer vibrational changes. This suggests that HKUST-1 with GO; HK-0.30e sample, offers improved stability against water molecules, which can lead to the sample degradation (confirmed by DVS measurements presented in *Section 6.5.1*). Otherwise, the results of experiment B indicate that CO<sub>2</sub> does not interact with the copper-nuclei atoms in both HKUST-1 with and without GO.

The potential adsorption sites for both molecules, CO<sub>2</sub> and H<sub>2</sub>O, is a key finding and complementary experiments are performed to understand the influence of GO to HKUST-1 in front of H<sub>2</sub>O and CO<sub>2</sub> adsorption. In this context, the next section provides the results of <sup>13</sup>C NMR experiments.

## 6.4 Mapping adsorption of $\text{H}_2\text{O}$ and $\text{CO}_2$ via solid-state $^{13}\text{C}$ NMR

Solid-state  $^{13}\text{C}$  Nuclear Magnetic Resonance ( $^{13}\text{C}$  NMR) was utilized for exploring relevant information about the potential active sites for the adsorption of  $\text{CO}_2$  and  $\text{H}_2\text{O}$  molecules.

The experiments in this section provide some insights related to the contribution of adsorbed molecules to the samples, despite the presence of copper-nuclei, which exhibits a high paramagnetic behavior. This paramagnetism typically causes chemical shifts and shift anisotropies due to the paramagnetic interaction, broadening the spectrum beyond excitation and detection limits. Additionally, paramagnetic relaxation enhancement significantly shortens the lifetimes of excited signals, producing a challenging task to interpret and evaluate the results.<sup>165</sup> In this case, the experiments were also performed in pristine HK and the most  $\text{CO}_2$  adsorbent sample, HK-0.30e, both obtained via bBM method of synthesis.

### *$^{13}\text{C}$ NMR experiments designed to analyze $\text{H}_2\text{O}$ and $\text{CO}_2$ adsorption*

For  $^{13}\text{C}$  NMR experiments, the analysis was performed using one pulse technique, at a spinning speed of 13 kHz. The measurements were carried out using a 4 m double resonance CPMAS probe and the spectra were recorded with 4.5- $\mu\text{s}$   $90^\circ$  pulse, a 0.15-s relaxation delay (D1), and 410,000 scans. Additionally, the experiments were recorded at room temperature and the equipment was equipped with a 4.0 mm double-resonance DVT probe at a spinning rate of 13 kHz. The magnetic field was 14.1 T, corresponding to a  $^{13}\text{C}$  resonance frequency of 150.89 MHz. The  $^{13}\text{C}$  chemical shifts were referred to as adamantane.

The experiments performed were the following: (1) activated HK, activated HK-0.30e and activated GO powder using the same conditions, (2) HK, HK-0.30e and GO samples exposed to 50% RH, (3) HK and HK-0.30e exposed to  $\text{CO}_2$  pure gas.

The results of  $^{13}\text{C}$  NMR spectra in experiment (1) with activated samples are presented in the following figures (Figure 6.23 (a) and (b)).

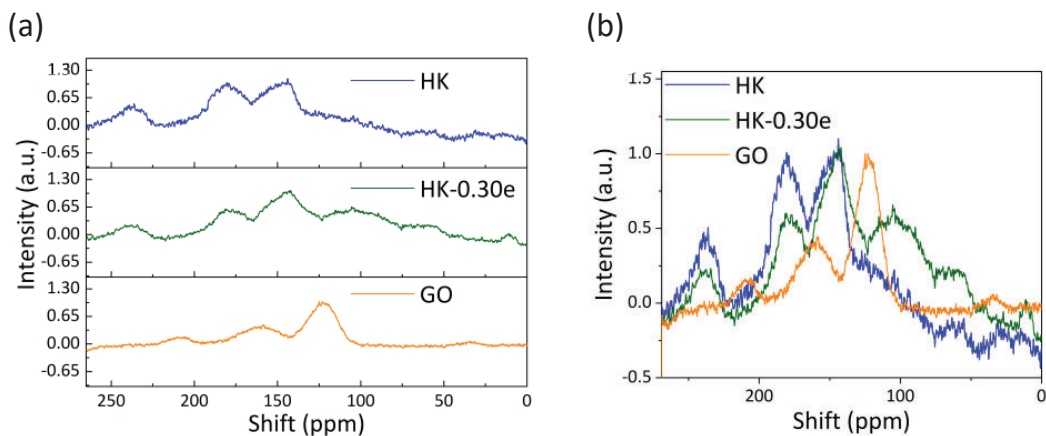


Figure 6.23. (a)  $^{13}\text{C}$  NMR of activated HK, HK-0.30e and GO samples and (b) overlapped spectra.

The NMR spectra show that the chemical environment of HK-0.30e was modified due to the incorporation of GO, since some broad signals are detected on 10, 57, 70 and 100 ppm, which is the region characteristic of  $\text{Csp}^3$  peak signals (Figure 6.23 (a)).<sup>166</sup> Specifically, these peaks don't appear in the NMR spectra of HK samples, suggesting that GO molecules are accommodated into the HK matrix structure and are interacting with the resonance of HK surroundings, creating some defects or interactions between both components and introducing  $\text{CH}_2\text{-OH}$  and  $-\text{CH}_2\text{O-}$  surrounding resonance from GO in the HKUST-1.

Peaks at 140-150 ppm and at 170-180 ppm, which appear in HK and HK-0.30e samples, are ascribed to aromatic carbon atoms. In this case, there are notable differences between the intensity of both peaks, since HK sample presents similar intensity in both while HK-0.30e exhibit less contribution in the 170-180 ppm peak (ascribed to tertiary carbon atoms) compared to the 140-150 ppm peak (ascribed to the secondary carbon atoms). This is attributed to the structural differences between both samples since the presence of GO provides disrupted benzene rings and some defects to the HK structure. Going further, GO powder NMR spectrum presents similar peaks at 130 and 160 ppm, also indicating the presence of the carbon atoms

arising from the aromatic ring with different contributions, similar to the HK-0.30e sample. Remarkably, the paramagnetic nature of the HK and HK-GO samples produces a shift to the left of the whole spectrum compared to the GO powder spectrum.

The overlapping spectra in Figure 6.23 (b) shows in more detail the differences between HK, HK-0.30e and GO. Additionally, the peak located at 235 approximately (for HK and HK-0.30e samples) and at 200 ppm (GO powder) is attributed to the quaternary carbon from the contribution of carbonyl bonds.<sup>167</sup> Remarkably, the paramagnetic nature of the HK and HK-GO samples produces a shift to the left of the whole spectrum compared to the GO powder spectrum.

On the other hand, if the peaks between both samples are analyzed in detail, the HK-0.30e sample performed broader resonance signals in comparison with the HK sample, which suggests that probably GO molecules produce this effect and, along with the paramagnetic nature of copper, the resolution is lower, and peaks are broader.

On the other hand, experiments (2) with RH showed some differences in comparison with experiments (1) with activated samples. The NMR spectra are displayed below in Figure 6.24.

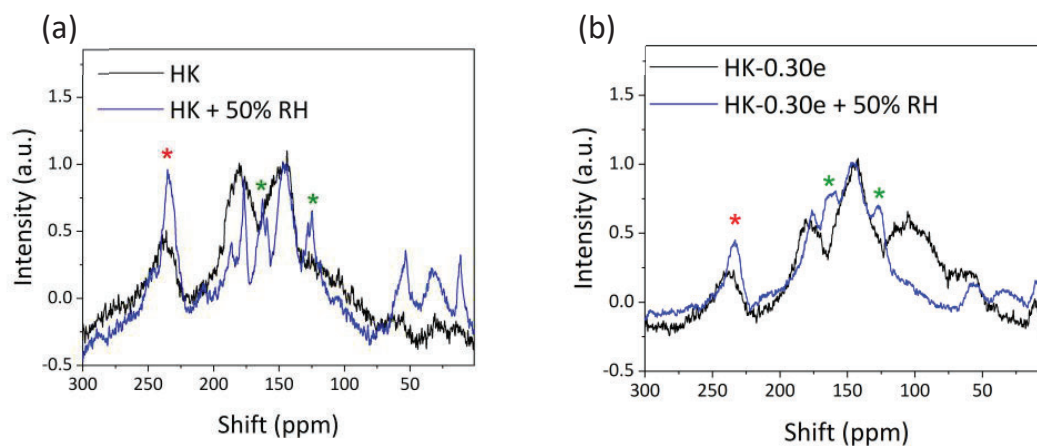


Figure 6.24.  $^{13}\text{C}$  NMR spectrum of overlapped activated sample and sample exposed to %RH (a) HK and (b) HK-0.30e.

As a result, in both the HK and HK-0.30e samples, the peak attributed to carbonyl carbon from carboxylate functional groups increases their relative intensity up to double. This increment of intensity indicates that there are perturbations in the chemical environment of these bonds (Figure 6.24 (a) and (b), marked by a red asterisk). This effect may be attributed to the *Overhauser Nuclear Effect (NOE)*, in which protons from H<sub>2</sub>O molecules influence the carbonyl atoms in the samples. Here, spin-spin coupling occurs through space rather than via a directly established bond, increasing the intensity of the 235 ppm signal as a result.<sup>168</sup>

On the other hand, if the intensity of the carbonyl peak is compared to the main peaks associated with aromatic carbon bonds (140-150 and 170-180 ppm), the spectra reveals that their relative intensity is higher in HK + 50 %RH than in the case of HK-0.30e + 50 %RH sample. This is produced since the presence of GO induces more contribution of aromatic carbons than carbonyl carbons in the HK-0.30e sample. Consequently, the contribution of aromatic carbons in front of carbonyl carbons is higher during H<sub>2</sub>O adsorption and this is reflected in the intensity of the spectrum.

Moreover, new peak signals appeared in the corresponding resonances range of aromatic carbons, 124 and 161 ppm (marked by a green asterisk in Figure 6.24 (a) and (b)). These signals arising from hydrated samples indicate that H<sub>2</sub>O molecules, even though interacting with most of the chemical structure on HK and HK-0.30e samples, potentially change the chemical environment from the surrounding aromatic carbon bonds. This interaction produces changes in the symmetry of the resonances, and, in consequence, the ascribed peaks arise.

In the case of the hydrated HK-0.30e sample, peaks initially observed ascribed to the aromatic carbon bonds associated with GO at 100 ppm disappeared and new peaks arose at 52, 30 and 11 ppm. This may suggest that water sorption could interact with the surrounding GO molecules, changing the contribution of resonance from GO and

increasing the effect of  $\text{Csp}^3$  bonds, which probably appears due to the formation of carboxylic acid or impurities, specially arising when water interacts with the sample.

NMR  $^{13}\text{C}$  spectrum of GO saturated with 50% RH is examined and some changes are detected between the activated GO sample and hydrated GO sample (Figure 6.25). A decrease in relative intensity is observed in the peaks attributed to the aromatic and carbonyl bonds, at 158 and 210 ppm respectively (marked by a red asterisk); in addition to detecting a displacement of the peak at 119 ppm to 125 ppm (marked by a yellow asterisk). These findings determine that  $\text{H}_2\text{O}$  molecules also interact with GO molecules since the contribution of carbon bonds changes when GO is hydrated.

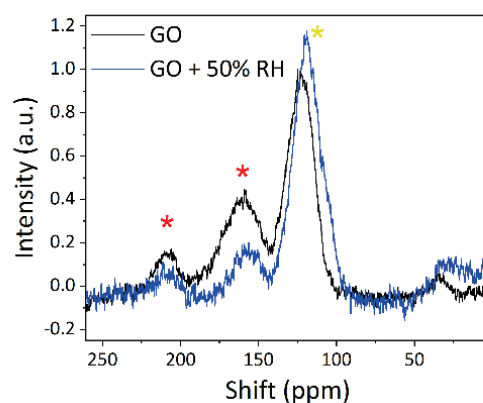


Figure 6.25.  $^{13}\text{C}$  NMR from sample GO (activated) and GO (saturated using 50% of RH) from the experiment (2).

Figure 6.26 (a) and (b) show the measurements performed following experiment (3) with  $\text{CO}_2$ , where the pristine HK and the most adsorbent sample, HK-0.30e were exposed to a stream of  $\text{CO}_2$  just before the performance of the NMR spectrum.

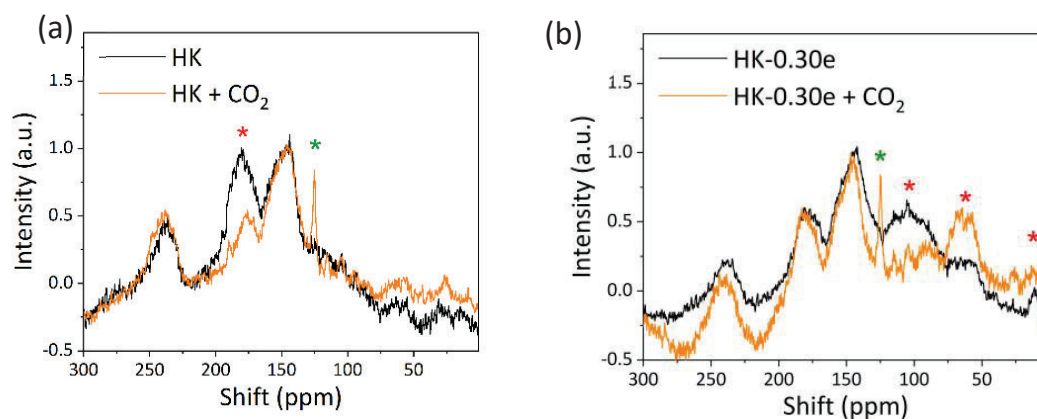


Figure 6.26.  $^{13}\text{C}$  NMR spectrum of overlapped activated sample and sample exposed to  $\text{CO}_2$  of (a) HK and (b) HK-0.30e.

The spectrum of the sample HK reflects a decrease in intensity in the peak located at 170 ppm (indicated by a red asterisk), which may indicate perturbations in the aromatic carbon bonds of HK, probably because  $\text{CO}_2$  molecules are being adsorbed in these locations. Moreover, a new peak appears at 124 ppm in the spectrum of both samples, corroborating the presence of adsorbed  $\text{CO}_2$ , since this specific peak is attributed to the carbon of  $\text{CO}_2$  molecule.<sup>169</sup>

On the other hand, the HK-0.30e NMR spectrum presents some differences compared to the pristine HK spectrum. In this case, there is an increase in intensity in the peaks located at 55-65 and 11 ppm and a decrease of peaks at around 100 ppm (marked by a red asterisk), ascribed to GO carbon contributions of aromatic carbons and  $\text{C-sp}^3$  resonances. These differences in the spectra indicate that most probably  $\text{CO}_2$  molecules are interacting with the GO molecules of the HK-0.30e sample and, in consequence, the signals detected in 50-100 ppm changes due to the perturbation that arises from the adsorption of  $\text{CO}_2$ .

In contrast to the spectrum of samples exposed to %RH, where the carbonyl carbon peaks attributed to carboxylate indicate an increase of intensity due to the NOE effect, in this case, this peak remain consistent without any change but it is not possible to determine whether  $\text{CO}_2$  is adsorbed in carboxylate functional groups since the NOE effect can't be applied to  $\text{CO}_2$  molecules (which don't contain hydrogen

atoms). However, it is suggested that  $\text{CO}_2$  is not adsorbed in carboxylate functional groups since IR measurements of the previous section, *Section 6.3*, corroborate that when samples are exposed to  $\text{CO}_2$ , carboxylate bands remain unchanged and maintain their original position without any shifting, indicating that  $\text{CO}_2$  molecules don't interact with this part of the molecule.

Regarding the observations presented above, GO plays a determinant role in the  $\text{CO}_2$  adsorption process when using HK-GO materials. Thus, experiment (3) is performed in GO powder and Figure 6.27 presents the results.

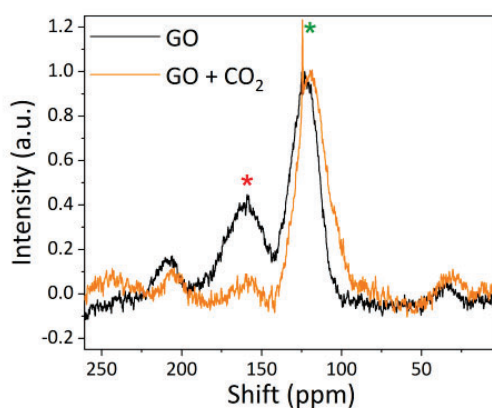


Figure 6.27.  $^{13}\text{C}$  NMR from sample GO (activated) and GO (exposed to  $\text{CO}_2$ ).

Based on the results, similar resonances are observed compared to HK and HK-0.30e. The band at 124 ppm appears in the  $^{13}\text{C}$  NMR spectra of the  $\text{CO}_2$  saturated sample (indicated by a green asterisk), which indicates the presence of adsorbed  $\text{CO}_2$  molecules. Moreover, there's a decrease in intensity of the peak at 160 ppm (marked in red), ascribed to the aromatic carbon bonds, also detected in HK spectrum, which further suggests that adsorption of  $\text{CO}_2$  is carried out near these functional groups.

Hence, comparing the spectra of HK and HK-0.30e when samples are saturated with  $\text{H}_2\text{O}$  and  $\text{CO}_2$ , it is possible to establish a relationship between potential adsorption sites from both samples. The results suggest that  $\text{H}_2\text{O}$  and  $\text{CO}_2$  may compete for the same strong potential adsorption sites, specifically those situated at  $\text{C-sp}^2$  atom

surroundings, which in this case are attributed to aromatic rings. This is consistent with the fact that both samples (once exposed to CO<sub>2</sub>) present spectra with noted changes associated with the aromatic carbon contributions.

On the other hand, HK-0.30e behaves differently from HK sample during the adsorption of CO<sub>2</sub>, since the intensity of Csp<sup>3</sup> atoms resonance, particularly at 55-65 ppm, increases when adsorption is performed. Thus, GO interferes with the adsorption of CO<sub>2</sub> and <sup>13</sup>C NMR reflects this behavior.

To summarize the results of this section, Figure 6.28 (a) and (b) show the <sup>13</sup>C NMR spectra of activated samples and CO<sub>2</sub> and H<sub>2</sub>O saturated samples.

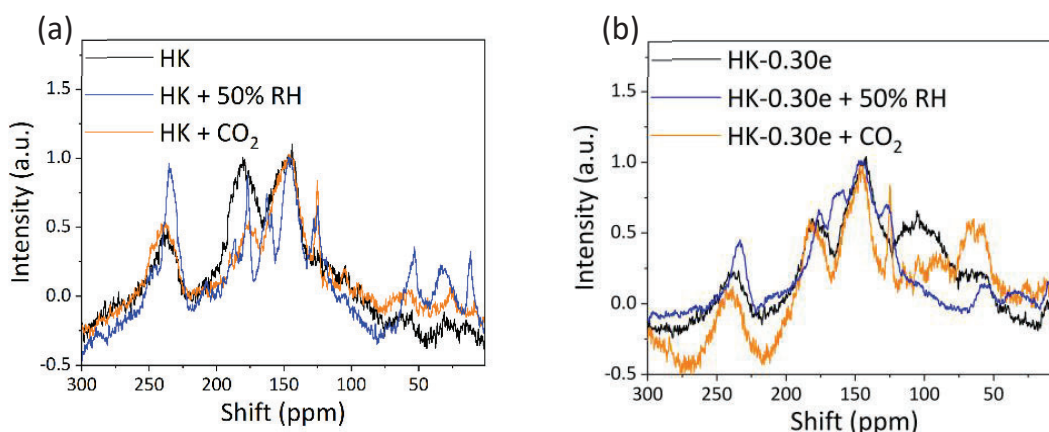


Figure 6.28. (a) <sup>13</sup>C NMR spectrum of overlapped HK activated sample, HK saturated with H<sub>2</sub>O and HK saturated with CO<sub>2</sub> and (b) <sup>13</sup>C NMR spectrum of overlapped HK-0.25 activated sample, HK-0.25 saturated with H<sub>2</sub>O and HK-0.25 saturated with CO<sub>2</sub>.

In summary, <sup>13</sup>C NMR experiments provided some insights into the potential adsorption sites for both CO<sub>2</sub> and H<sub>2</sub>O. The differences in the symmetry of the molecules when contain adsorbed gases produce additional signals in the spectrum, providing key information about where the adsorbed molecule is located. In this context, the results confirm that H<sub>2</sub>O molecules are adsorbed in carboxylate functional groups since changes in carbonyl signal are detected. These results align with IR experiments presented in the previous section of this chapter.

---

Furthermore, apart from corroborating carboxylate bonds as potential adsorption sites for  $\text{H}_2\text{O}$  molecules, NMR experiments also indicate that aromatic carbon functional groups are also potential adsorption sites for  $\text{H}_2\text{O}$  molecules. Similarly, the most probable regions where  $\text{CO}_2$  is adsorbed in HK and HK-GO samples are also the aromatic carbon functional groups. These findings align with the literature since  $\pi$ -interactions attract  $\text{CO}_2$  molecules. For this reason, the most adsorbent sample, which in this case is HK-0.30e, presents additional changes in the  $^{13}\text{C}$  NMR spectra corresponding to the aromatic carbons when the sample contains  $\text{CO}_2$  adsorbed molecules. In this regard, as the carbonyl signal in the spectrum does not suffer any change when the sample contains adsorbed  $\text{CO}_2$  molecules, it is suggested that  $\text{CO}_2$  molecules are not adsorbed in carboxylate functional groups. Although not being possible to corroborate this using NMR since  $\text{CO}_2$  molecules don't produce the NOE effect, IR experiments confirmed this hypothesis since the vibration of carboxylate groups is not perturbed once  $\text{CO}_2$  molecules are adsorbed. As a result, through IR and NMR experiments it is confirmed that  $\text{CO}_2$  and  $\text{H}_2\text{O}$  molecules are mainly adsorbed in the aromatic functional groups, the  $\pi$ -interactions. Whereas  $\text{H}_2\text{O}$  molecules present higher affinity with the HK samples and it is also adsorbed in carboxylate functional groups, mainly by hydrogen bonding.

To finalize this part of the study, additional measurements were performed using other techniques. The adsorption, cyclability and kinetics of  $\text{H}_2\text{O}$  and  $\text{CO}_2$  are evaluated, and the following section provides the results of Dynamic Vapor Sorption (DVS) experiments and Breakthrough analysis (BTA), which focus on analyzing the adsorption behavior of the samples in simultaneous co-adsorption systems with  $\text{CO}_2$  and  $\text{H}_2\text{O}$ .

## 6.5 Co-adsorption of CO<sub>2</sub> and H<sub>2</sub>O

Gravimetry using dynamic gravimetric vapor sorption (DVS) and breakthrough analysis (BTA) was employed to determine the co-adsorption of H<sub>2</sub>O and CO<sub>2</sub> in HK-GO materials.

The DVS system is specifically designed for performing detailed analysis of gravimetric measurements saturating the sample with H<sub>2</sub>O or other gases (such as CO<sub>2</sub>), even two different gases in the system. This technique, offers high precision and control, allowing for meticulous measurement of water vapor uptake by porous materials under a wide range of humidity conditions and allows the ability of performing the measurement with two different gases introduced in the system at the same time. This capability enables the study of adsorption and desorption isotherms with exceptional accuracy. This level of detail is impossible to achieve with traditional methods, making the DVS system an indispensable instrument for this research.

On the other hand, Breakthrough Analysis (BTA) equipment is specifically designed for studying sorption and desorption kinetics and employed to calculate the maximum quantity of adsorbed gas. The equipment can analyse the rate at which gases are captured and released by the material, providing crucial information to optimize process time in industrial applications. It also determines the preference of the adsorbent material for certain gases over others, which is essential in the separation of gas mixtures.

The measurements using DVS and BTA were conducted through a collaborative study with **Surface Measurement Systems Ltd.**, and the results are described in the following sections. As in the case of IR and NMR experiments, DVS and BTA experiments were carried out using the same samples: pristine HK and the most CO<sub>2</sub> adsorbent sample, HK-0.30e, both synthesized using bBM.

### 6.5.1 Dynamic vapor sorption

Experiments were performed using the DVS Carbon and DVS Adventure equipment, both from Surface Measurements Systems. For performing the experiments, a mass of around 10 mg of sample was loaded in the gravimetric pan and loaded in the device, activating the sample in situ with a local sample heater. In this context, the activation of the samples was performed at 170 °C with a heating ramping rate of 5 °C per minute while under 300 sccm N<sub>2</sub> flow for 180 minutes. After cooling, all sorption stages were performed under isothermal conditions at 25 °C. The total flow rate was fixed at 300 sccm. Each sorption step equilibrated until the sample's mass had reached a rate of mass change of 0.002 %/min or within 360 minutes.

In the following experiments, dry air was utilized as a carrier gas. Two approaches were proposed:

- Atmospheric conditions: 400 ppm CO<sub>2</sub> and 50% of RH.
- Post-combustion conditions: 15% of CO<sub>2</sub> and 50% of RH.

#### Atmospheric conditions

The experiments conducted were performed to simulate the concentration of CO<sub>2</sub> and H<sub>2</sub>O currently in the atmosphere. As humidity is variable depending on the geographic area, it was decided to select 50% of RH.

The measurements followed the next experiments, considering single and multi-component conditions:

- 1) Exposure of the sample to 50% of RH. (Experiment 1)
- 2) Exposure of the sample to 400 ppm CO<sub>2</sub>. (Experiment 2)
- 3) Exposure of the sample to 50% RH and 400 ppm CO<sub>2</sub>. (Experiment 3)

Before each experiment, the samples were activated using 0% of RH with nitrogen gas as carrier gas and increasing the temperature up to 170°C for 170 min.

The results of gravimetric measurements using 1), 2) and 3) conditions on HK and HK-0.30e samples are shown in Figure 6.29.

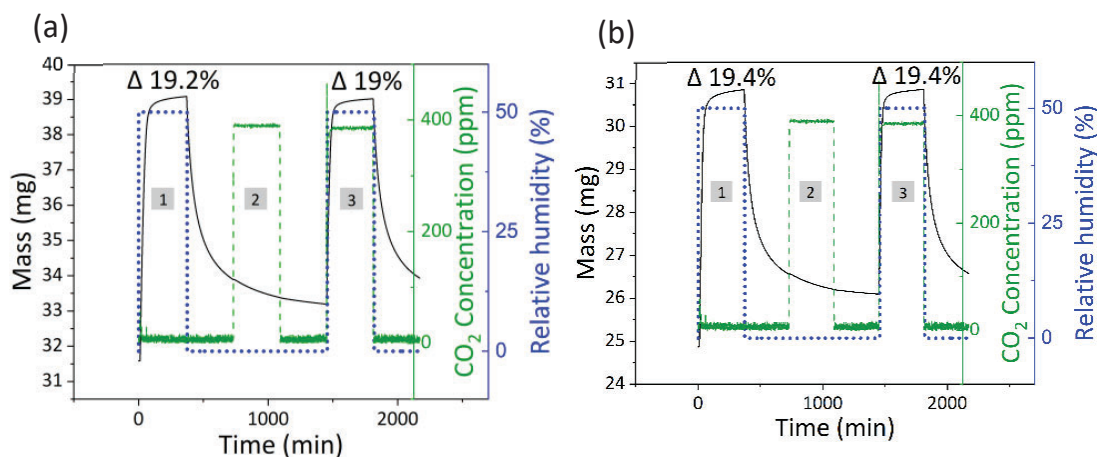


Figure 6.29. DVS gravimetries of experiments 1,2,3 performed on (a) HK and (b) HK-0.30e samples.

Thus, when H<sub>2</sub>O is introduced, a weight increase of 19% for HK and 19.4% for HK-0.30e is detected in experiment 1. In contrast, in the second experiment, when the 400 ppm of CO<sub>2</sub> is introduced, the sample's weight decrease constantly and the results show no stabilization of the weight loss (partially activated). Therefore, although CO<sub>2</sub> is introduced, the effect is a continued loss of adsorbed H<sub>2</sub>O molecules without any evidence of whether the CO<sub>2</sub> is retained or not.

Additionally, when the sample is saturated with both gases during experiment 3 (50% RH and 400 ppm of CO<sub>2</sub>) the results are almost identical to experiment 1, with both samples showing a weight increase of around 19% again. However, HK-0.30e (Figure 6.29 (a)) exhibited a marginally higher relative uptake compared to sample HK (Figure 6.29 (b)) concerning water sorption and co-sorption.

Subsequently, another measurement was performed on HK-0.30e to assess the CO<sub>2</sub> capture with an activated sample under dry conditions. In this case, only experiment 2 was conducted separately, and the results are shown in Figure 6.30.

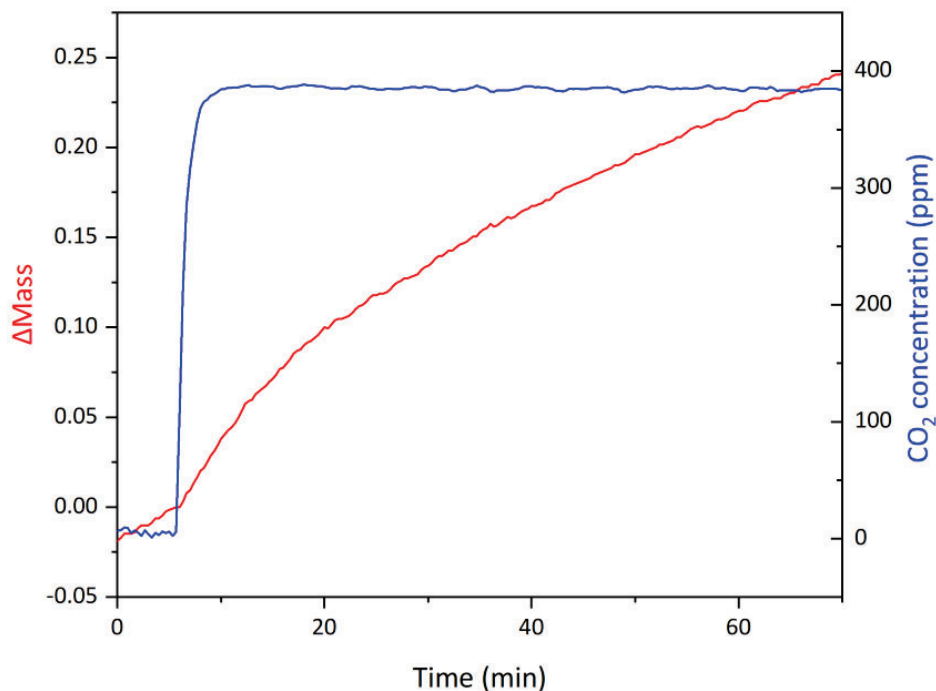


Figure 6.30. DVS gravimetry was performed on HK-0.30e (experiment 2).

This experiment lasted for 70 minutes as this is the length of time it took for the sample to reach the mass equilibrium value. Regarding the results, the uptake from atmospheric quantities of CO<sub>2</sub> is 0.25% of the sample's 'dry mass' in dry conditions, which corresponds to 0.732 mmol CO<sub>2</sub>/g.

In real conditions, RH is always present in the atmosphere. Therefore, using this material in such conditions would require an additional drying system and the development of a complex engineering structure for the device. Scaling up production while maintaining the adsorption rate is a complex task; likely, the adsorption efficiency would decrease with shaping and scaling.

Hence, based on these initial results, it is determined that more effective conditions for using HK-GO materials would be in post-combustion conditions where CO<sub>2</sub> concentrations are higher (around 15%).

### Post-combustion conditions

The following experiments are based on gravimetric measurements using post-combustion conditions into the pristine HK and HK-0.30e.

The experimental procedure is the same utilized when performing IR measurements, as described before in *Section 6.3* of this chapter. The experiments were carried out using CO<sub>2</sub> concentrations comparable to those typically found in a post-combustion system. All the samples were activated before each experiment at 170°C under a stream of nitrogen flow for 180 minutes. Hence, the experiments followed the steps described in Table 6.1.

*Table 6.1. Experimental conditions utilized in each stage of DVS measurements using a post-combustion approach.*

Experiment	Flow composition* (Step)
I	(1) 15% CO <sub>2</sub>
II	(1) 50% RH.
III	(1) 15% CO <sub>2</sub>
	(2) 15% of CO <sub>2</sub> + 50% RH
	(3) 15% of CO <sub>2</sub>
IV	(1) 50% of RH
	(2) 50% RH + 15% CO <sub>2</sub>
	(3) 50% RH.

\* Dry air is utilized as a carrier gas in all the steps

The results of all the experiments are represented in Figure 6.31. The curves of weight increase are different because mass stabilization for each sample takes different times.

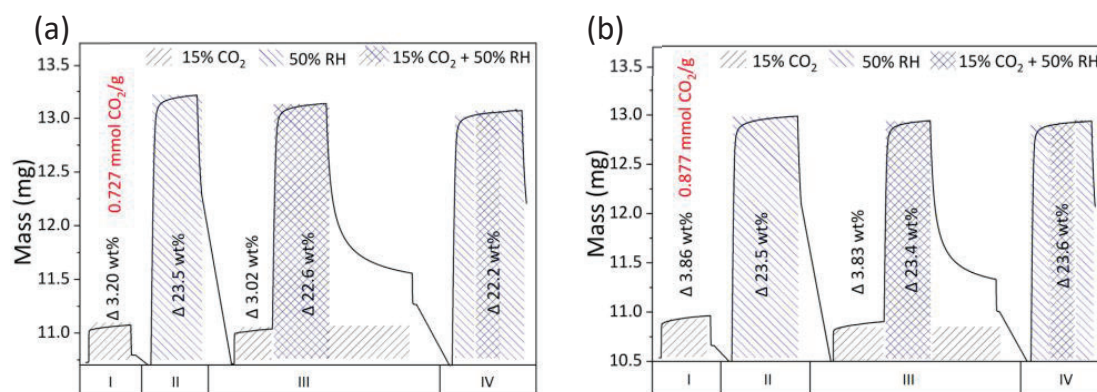


Figure 6.31. DVS gravimetric measurements of experiments 1, 2, 3 and 4 performed on (a) HK and (b) HK-0.30e.

Thus, both samples, HK and HK-0.30e, increased in weight according to the adsorption of the introduced gas at each step (Figure 6.31 (a) and (b)). Specifically, in experiment I, when the sample was exposed to 15% CO<sub>2</sub>, the weight mass increased, indicating adsorption of up to 0.727 mmol CO<sub>2</sub>/g for HK and 0.877 mmol CO<sub>2</sub>/g for HK-0.30e. This indicates that under these conditions, HK-0.30e achieved a 20.6% higher capacity of CO<sub>2</sub> adsorption than the pristine HK.

Contrastingly, the results for experiment II suggest that both samples exhibit a highly water-adsorbent behavior, increasing their mass by about 23-24% of the initial weight. Nevertheless, during experiment III, the samples were first exposed to 15% CO<sub>2</sub> (step 1), followed by exposing the samples to a mixture of 15% CO<sub>2</sub> along with 50% RH (step 2). The weight increase in the second step is lower for the HK sample and the same sorption capacity is noted for HK-0.30e, which indicates the same increase in weight. Moreover, when the introduction of RH is removed and only the CO<sub>2</sub> is maintained (step 3), the sample's weight decreases continuously without stabilizing. This is also observed in both samples, indicating probably that the CO<sub>2</sub> stream acted like purge gas, extracting water from the pores under those conditions. This hypothesis matches the results obtained from IR experiments, where the experiments suggested that CO<sub>2</sub> molecules acted as a carrier gas displacing the adsorbed H<sub>2</sub>O molecules. Due to the complexity of achieving stabilization, it was not

possible to attribute the final weight obtained exclusively to CO<sub>2</sub> adsorption, as H<sub>2</sub>O and CO<sub>2</sub> were likely co-existing within the sample.

In experiment IV, the results for HK and HK-0.30e indicate that the weight remains stable across the three steps, suggesting that once H<sub>2</sub>O is adsorbed in both samples, the introduction of CO<sub>2</sub> along with H<sub>2</sub>O doesn't affect the increased weight of step 1.

Although interesting results were obtained through all the analyzed experiments, the gravimetric profile of both samples was almost the same suggesting similar adsorption for CO<sub>2</sub> and H<sub>2</sub>O.

### **Co-sorption cycling study**

The same steps conducted in stage III were performed again, but the process was repeated over multiple cycles to assess the cyclability capacity of the material. Figure 6.32 represents, as an example, the experiment performed for HK-0.30e sample since HK presents a similar behavior. The sequential cycles consisted of activating the samples for 100 minutes at 170°C in situ. Then, the sample is exposed to 15% CO<sub>2</sub> until equilibration, subsequently, 50% RH along with CO<sub>2</sub> is maintained and, in the last step, the RH is removed and only CO<sub>2</sub> passes through the sample. This stage is repeated over 3 cycles.

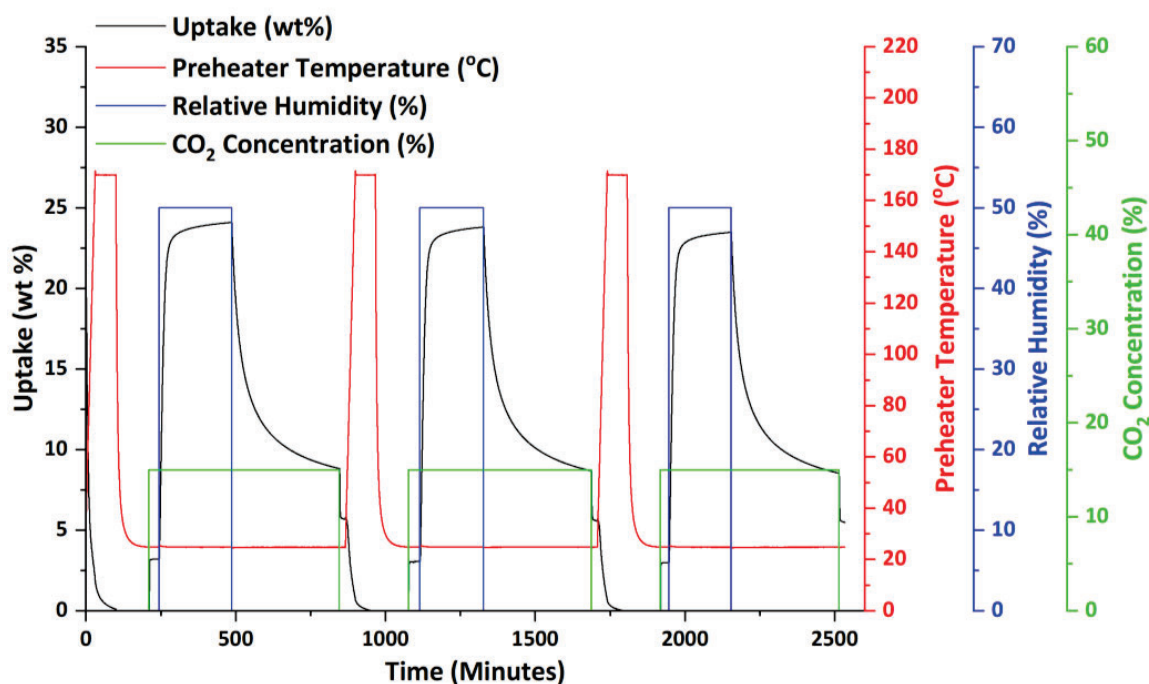


Figure 6.32. Experimental procedure and sequence for the multi-component cycling DVS gravimetric experiments performed in stage 3 (HK-0.30e).

As a result, the uptake performance of the HK-0.30e is similar in all the cycles, suggesting that the material is potentially regenerable. Looking at the sorption kinetics, the initial uptake of CO<sub>2</sub> is fast, with over 90% of total uptake in the first minute. In contrast, water sorption is much slower (211 minutes).

In the case of pristine HK, although the behavior is like HK-0.30e, the uptake performance is slightly lower over the cycles. To assess in more detail the cyclability and regenerability of both samples, the total equilibrium mass uptake at 15% CO<sub>2</sub> (step 1), and 15% CO<sub>2</sub> + 50% RH (step 2) is depicted in Figure 6.33 (a) and (b).

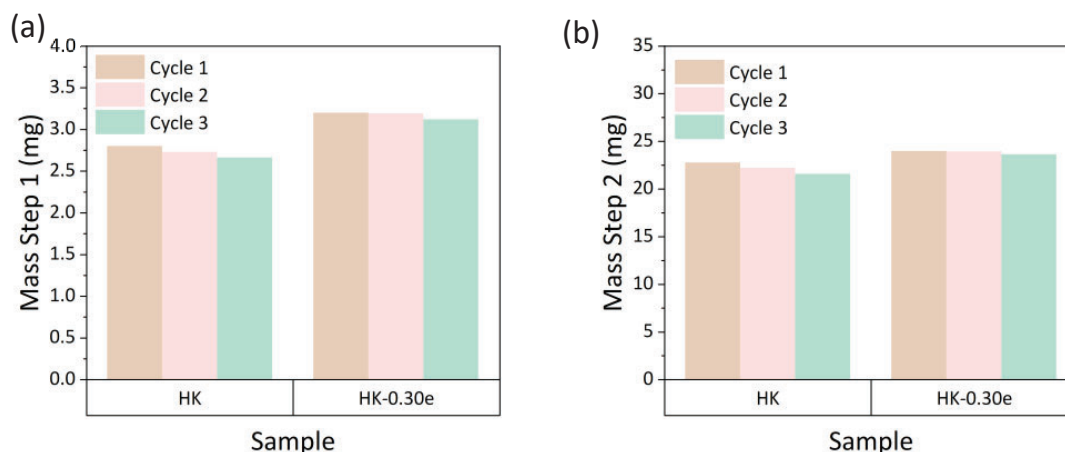


Figure 6.33. (a) Total uptake (wt%) of 15% CO<sub>2</sub> for HK and HK-0.30e and (b) Total uptake (wt%) of 15% CO<sub>2</sub> + 50% relative humidity for HK and HK-0.30e.

By the third cycle, HK shows a CO<sub>2</sub> capture capacity reduced by up to 5% when performing step 1 and by up to 5.3% for step 2. In comparison, HK-0.30e demonstrated more stability in gas capture, with only a reduction of 2.5% and 1.5% in step 1 and 2, respectively. This indicates that HK sorption capacity decreases to a greater extent after each cycle while HK-0.30e saw its sorption capacity reduced to a smaller extent, which may give an indication of less degradation after each sorption and reactivation cycle. This may be closely related to the fact that the introduction of GO to HK could have an impact on the material's efficiency of reactivation by enhancing its thermal properties, therefore allowing it to active and reactivate more effectively upon multiple sorption cycles. Moreover, these results are consistent with IR experiments, where experiments A suggested that the presence of GO in HK-0.30e sample hinders the coordination of H<sub>2</sub>O molecules to the copper-nuclei of the MOF, which could lead to long-term degradation and reduce the regeneration capacity of the sample.

### **Pure water sorption study**

Once analyzed the co-adsorption performance of HK and HK-0.30e, the total water uptake was evaluated in detail using water sorption isotherms at 25°C, introducing 0-95% RH steps and using dry air as carrier gas. Figure 6.34 shows the results of the gravimetric curves and the hysteresis loop derived from water sorption uptakes.

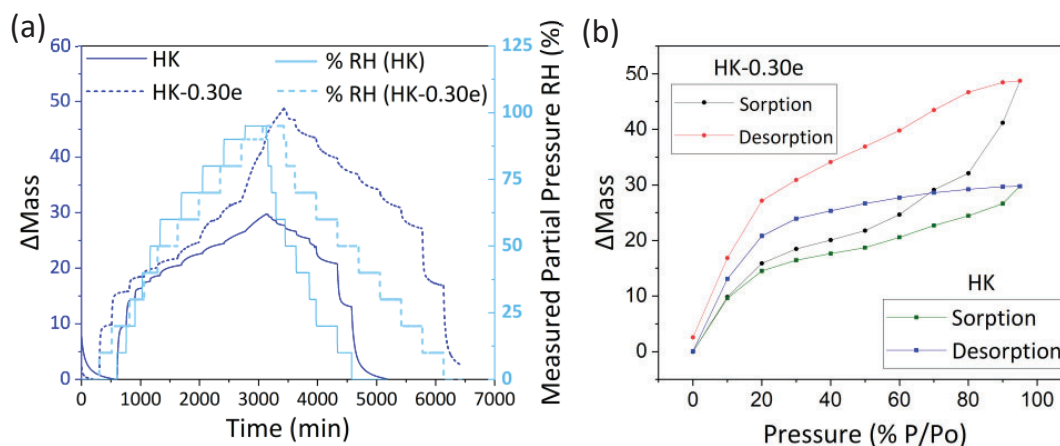


Figure 6.34. (a) DVS gravimetric of pure-water measurements and (b) Hysteresis loop of water adsorption of HK and HK-0.30e.

As can be seen in the graphical data, a huge difference between both samples regarding water adsorption is observed (Figure 6.34(a)). HK and HK-0.30e display similar uptakes at low relative humidity but begin to deviate at RH above 50%. Near saturation, HK-30e shows a significantly higher sorption capacity of 49% w/w compared to 29% w/w for HK. The RH steps are different for each sample since mass stabilization when the samples reach equilibrium in water uptake, varies for each case. Moreover, the final step of water desorption for HK-0.30e does not reach a zero-weight increment, which likely indicates that water molecules are more strongly adsorbed in the sample compared to HK.

Considering this, the kinetics for water adsorption in both samples are almost the same, since at around 3000 minutes both samples reach the equilibrium of total water uptake. Otherwise, when observing the desorption profile, HK-0.30e takes approximately 1600 minutes longer than HK. This is consistent with the fact that HK-0.30e adsorbs a greater amount of water, leading to a longer desorption time. Specifically, the water uptake rate for HK-0.30e is 0.015%/min, with a corresponding desorption rate of 0.008%/min. In contrast, for HK, the water uptake is around 0.007%/min, while the desorption rate is 0.011%/min. Considering this data, it is suggested that the adsorption kinetics of water are higher for HK-0.30e sample than for HK, whereas the desorption kinetics is higher for HK than for HK-0.30e sample.

On the other hand, the hysteresis loop of both samples indicates some differences as depicted in Figure 6.34 (b), where the y axis is the percentage of change in mass with respect to the reference mass and x axis represents the relative pressure. The different trajectories of sorption and desorption indicate that the interaction of water with the material once adsorbed is strong since the desorption process implies higher energy than the adsorption process. Additionally, adsorption and desorption kinetics also play a role in this process, since as indicated before, through hysteresis curves is also possible to determine an approximation of water uptake kinetics. The adsorption curve for HK-0.30e shows a higher increase in weight as the relative pressure of water increases, compared to HK. Contrastingly, for desorption of the adsorbed water, HK exhibits a greater weight loss RH considering the partial pressures of RH, indicating higher kinetics of desorption for HK.

As the main difference between both samples is the content of GO, a third measurement of the water sorption capacity was performed using only pure GO powder utilized in the synthesis of the samples. The results are shown in the following figures (Figure 6.35 (a) and (b)).

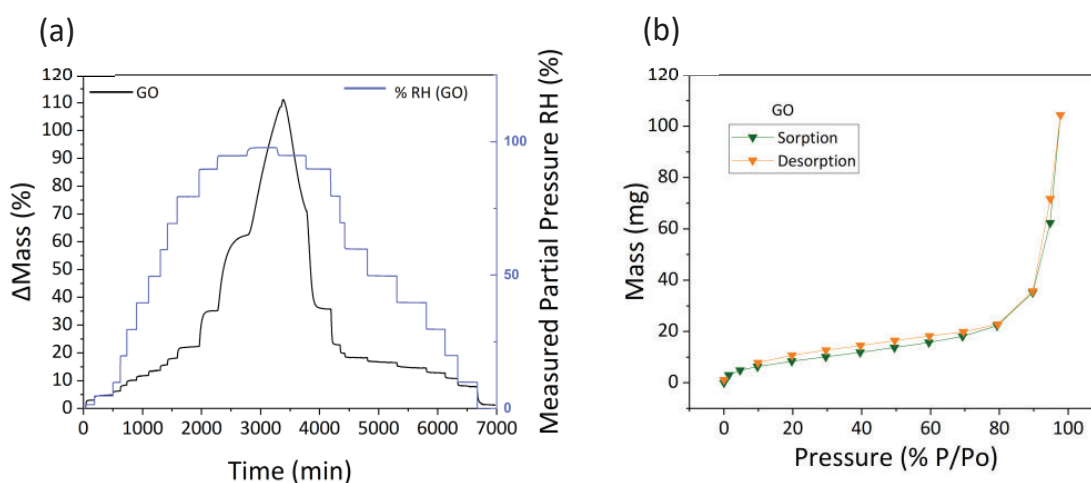


Figure 6.35. (a) DVS gravimetric of pure-water measurements and (b) Hysteresis loop of water adsorption of GO.

The results show a high capacity of water adsorption in the case of GO (up to an increase of around 50% at 50% RH and 110% at 100% RH) (Figure 6.35 (a)). The

hysteresis loop exhibits similar sorption and desorption trajectories, which indicates that the energy required for adsorbing and desorbing H<sub>2</sub>O molecules is nearly the same (Figure 6.35 (b)). Unlike hysteresis loops of HK and HK-0.30e samples, GO presents similar adsorption-desorption energy for H<sub>2</sub>O. This is probably because H<sub>2</sub>O molecules interact with GO mainly by hydrogen bonds and  $\pi$ -interactions with GO, since it is formed by graphene-sheet layers with some defects. However, the interaction of H<sub>2</sub>O with HK and HK-0.30e implies higher energy during the adsorption of the molecules since carboxylate functional groups of the samples facilitate hydrogen-bonding with H<sub>2</sub>O molecules, along with the  $\pi$ -interactions of the benzenic ring of the ligand and the contribution of GO in the case of HK-GO samples. As a result, both HK and HK-GO require more energy to desorb water molecules than GO, and in turn, the hysteresis curve of HK-GO indicates a higher desorption energy required, which aligns with the higher uptake of H<sub>2</sub>O.

These results suggest that the incorporation of GO also promotes the increase of water uptake, apart from enhanced CO<sub>2</sub> adsorption performance as previously seen in the results of *Chapters III* and *IV*. In this regard, the introduction of GO in the sample may help prevent the degradation of HKUST-1 compared to samples without GO, since water molecules can interact and coordinate more effectively with the additional coordination sites that GO promotes. As a result, the coordination of water molecules is more stable in the presence of GO. Otherwise, the samples, without GO, present lower stable coordination sites and could lead to the formation of copper hydroxides, which would cause faster degradation of the material.

Overall, gravimetric results using DVS suggest that the incorporation of GO enhances significantly the CO<sub>2</sub> and H<sub>2</sub>O uptakes, together with the regeneration of the sample over multiple cycles. This is consistent with the results of IR experiments, where there is a suspicion that the presence of GO introduces to the sample more additional sites of H<sub>2</sub>O coordination, along with blocking partially the copper-nuclei sites, producing as a result a better stabilization of the sample in humid conditions.

### 6.5.2 Breakthrough analysis

Given that sample HK-0.30e showed a higher total uptake among the two samples in both single and multicomponent conditions (i.e., single-gas sorption measurements and simultaneous H<sub>2</sub>O/CO<sub>2</sub> uptake measurements, respectively), dynamic column breakthrough studies were undertaken to evaluate the kinetics and selectivity of CO<sub>2</sub> under both dry and humid conditions.

For the performance of these experiments, the preparation of the sample consisted of mixing homogeneously 80-90 mg of powdered sample with 900 mg of 0.4 mm diameter glass beads (loaded in a silanized glass column of 4mm ID) to prevent pressure buildup during the experiments. Moreover, the samples were activated at 170 °C under a 30 sccm flow of N<sub>2</sub> for 3 hours, then cooled under the same flow to 25 °C before introducing a feed gas mixture.

On the other hand, the feed gas mixture was made of 15% CO<sub>2</sub> in N<sub>2</sub> or 15% CO<sub>2</sub> and 50% Relative Humidity (RH) in N<sub>2</sub> at a flow rate of 30 sccm and the outlet RH and CO<sub>2</sub> concentrations were continuously monitored using the integrated sensors of the instrument. Once the outlet concentration equilibrated with the inlet feed concentration, the feed gas concentration was switched back to dry N<sub>2</sub> and the temperature of the adsorbent bed was raised to 170 °C to regenerate the adsorbent. Breakthrough and regeneration capacities were calculated from the adsorption and regeneration concentration profiles of individual components after applying corrections for dead space, generation delay, and sensor response delay. Blank experiments, conducted under identical conditions but without the adsorbent in the column, were used to account for these corrections.

Thus, given that sample HK-0.30e showed a higher total uptake among the two samples in both single and multicomponent conditions, the adsorption kinetics were studied through breakthrough analysis using this sample.

Experiments were performed under dry conditions (15% CO<sub>2</sub>) and humid conditions (15% CO<sub>2</sub> + 50% RH) and the results are depicted in Figure 6.36 and Figure 6.38.

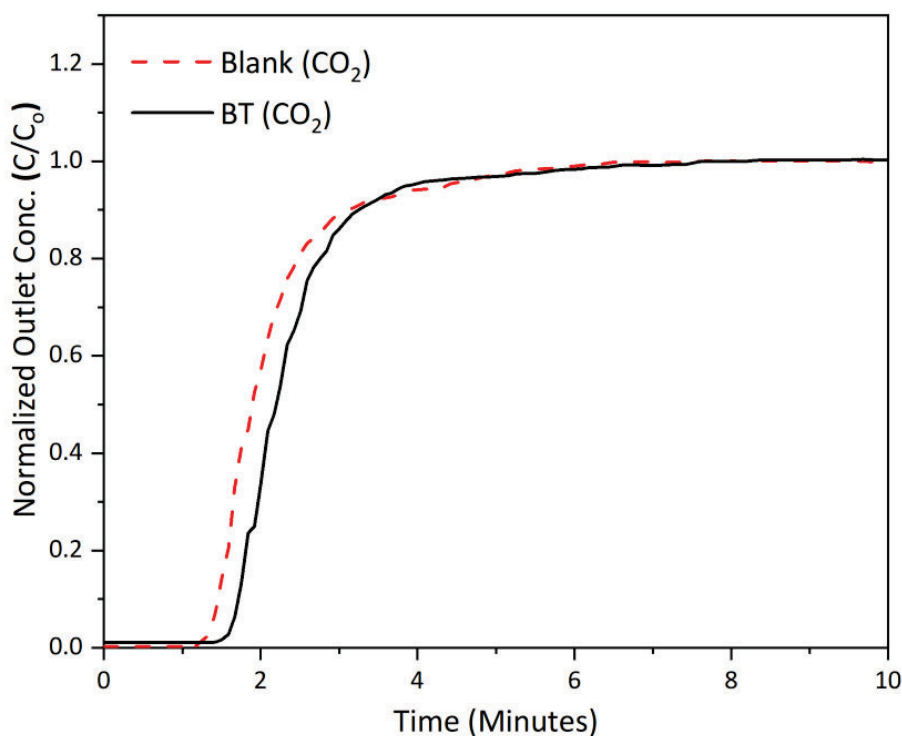


Figure 6.36. Breakthrough analysis under dry conditions (15% CO<sub>2</sub>) of HK-0.30e sample.

Hence, HK-0.30e was exposed to CO<sub>2</sub> under dry conditions and the initial insights show fast uptake kinetics, reaching the equilibrium of complete saturation only within 10 minutes. The total CO<sub>2</sub> uptake is calculated by integrating the areas between the blank curve and the BTA measured curve when CO<sub>2</sub> is introduced into the system. Consequently, HK-0.30e achieves a CO<sub>2</sub> adsorption of 0.636 mmol CO<sub>2</sub>/g (2.83% w/w of the capacity adsorption, like the gravimetric results obtained using DVS).

Capacity uptake was again corroborated by the desorption profile shown in Figure 6.37, which confirms the complete desorption of the CO<sub>2</sub> molecules during regeneration stage (extraction of the adsorbed molecules by applying temperature).

Specifically focusing on the regeneration of the sample, apart from achieving complete desorption, the bulk of adsorbed molecules were extracted below the temperature of 80°C (See Regeneration curve, indicated in black, which completely stabilizes at around 17 minutes reaching 80°C, indicated in red with a blue arrow).

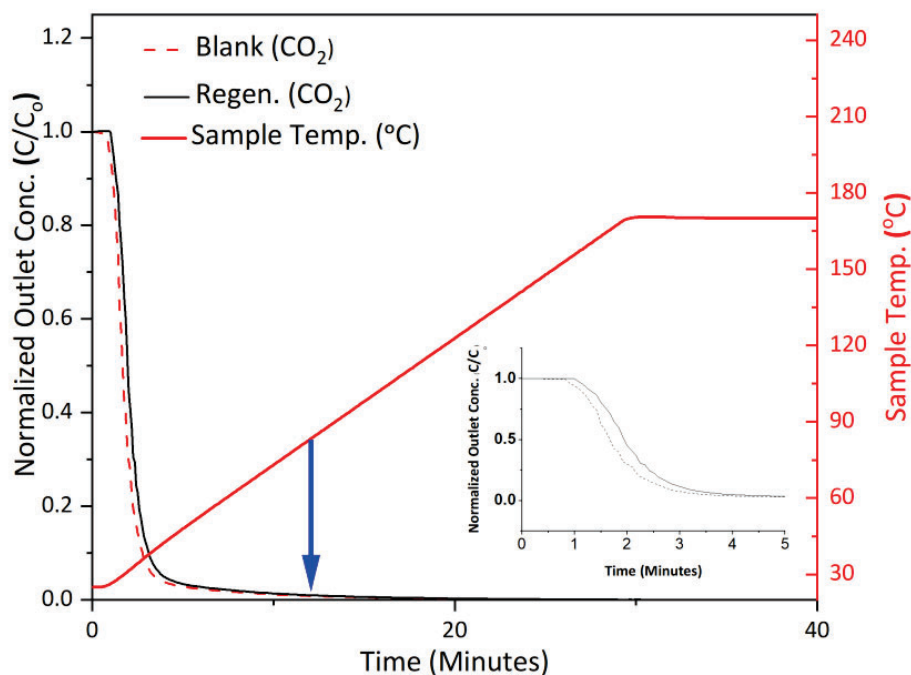


Figure 6.37. Desorption curves after  $\text{CO}_2$  adsorption under dry conditions of HK-0.30e using breakthrough analysis and the monitored temperature during the experiment. Blue arrow indicates the time and temperature of the complete  $\text{CO}_2$  desorption.

On the other hand, experiments under humid conditions are shown in Figure 6.38. By using streams of 50% RH and 15%  $\text{CO}_2$ , breakthrough curves demonstrate that  $\text{CO}_2$  kinetics of adsorption are faster than  $\text{H}_2\text{O}$ . Hence, the data suggests that  $\text{H}_2\text{O}$  continues to adsorb over  $\text{CO}_2$ -saturated bed, which may be attributed to the displacement of adsorbed  $\text{CO}_2$  molecules by  $\text{H}_2\text{O}$ , as previously suspected in IR and DVS results. Consequently, although a specific concentration (15%) of  $\text{CO}_2$  is introduced in the breakthrough inlet, once  $\text{CO}_2$  adsorption reaches the equilibrium, the stream of 50% RH produces a desorption of the  $\text{CO}_2$  forced by  $\text{H}_2\text{O}$  molecules. This results in a slight increase in  $\text{CO}_2$  concentration at the outlet, exceeding 15% of

CO<sub>2</sub>. This is further confirmed when the uptake capacity is calculated for both components from the obtained curves (Figure 6.38), by integrating the area of the blank curves by the area of the kinetic sorption performance.

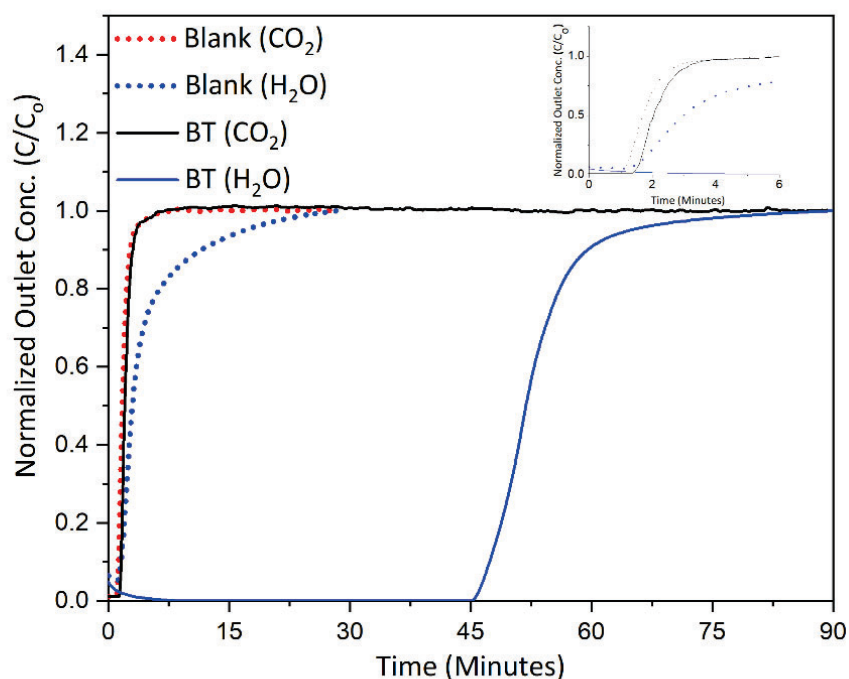


Figure 6.38. Breakthrough under humid conditions (15 % CO<sub>2</sub> and 50 % RH) of HK-0.30e.

HK-0.30e breakthrough curve exhibits a negligible net CO<sub>2</sub> uptake, indicating that there's a competitive interaction between H<sub>2</sub>O and CO<sub>2</sub> molecules for the adsorption sites. Consequently, water molecules may replace the adsorbed CO<sub>2</sub>, effectively 'winning' this competition. Despite not achieving a high CO<sub>2</sub> adsorption capacity, the sample adsorbs a significant amount of water, reaching a 23.37% increase in its initial weight.

Regarding these results, it is determined that although HK-0.30e samples present higher affinity for H<sub>2</sub>O molecules, CO<sub>2</sub> adsorption presents faster kinetics of adsorption than H<sub>2</sub>O, which takes 15-17 minutes in front of 75 minutes, respectively. Moreover, complete desorption of CO<sub>2</sub> molecules is feasible below 80 °C of

temperature, which indicates that although these materials are not as efficient at operating in humid conditions, adsorption-desorption cycles of  $\text{CO}_2$  molecules before reaching a complete  $\text{H}_2\text{O}$  saturation in the sample are feasible. This is consistent with the fact that  $\text{H}_2\text{O}$  molecules imply higher energy during adsorption-desorption processes than  $\text{CO}_2$  molecules since  $\text{H}_2\text{O}$  denotes hydrogen bonds and  $\pi$ -interactions during the adsorption process. In contrast,  $\text{CO}_2$  molecules only interact with the sample through weaker bonds considering only the contribution of  $\pi$ -interactions.

Consequently, these observations suggest that although water and  $\text{CO}_2$  compete for adsorption sites on HK-GO, a significant  $\text{CO}_2$  adsorption capacity can still be achieved under humid conditions if the adsorbent is regenerated immediately after the initial  $\text{CO}_2$  breakthrough, rather than allowing complete saturation with  $\text{H}_2\text{O}$ .

To understand this behavior, regeneration experiments were performed, and the results are depicted in Figure 6.39.

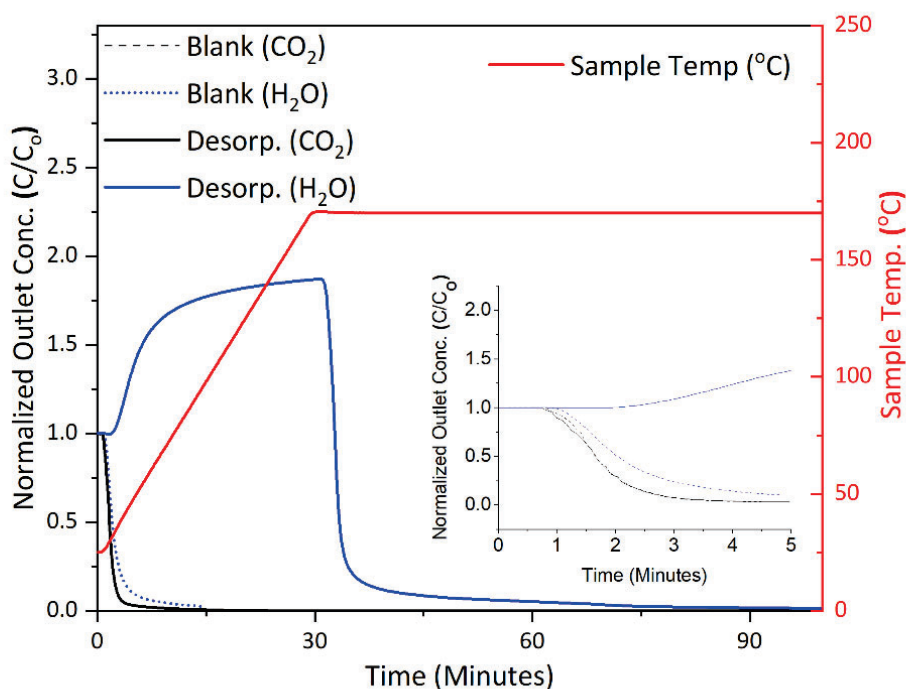


Figure 6.39. Desorption curves of HK-0.30e after  $\text{CO}_2$  adsorption under humid conditions. Insets are the magnified regions of the same data up to 5 mins.

---

As a result, these experiments corroborate the behavior described above, since CO<sub>2</sub> desorption curves are almost the same as the blank experiment, closely overlapping both curves, demonstrating that this material performs no net CO<sub>2</sub> adsorption under humid conditions (Figure 6.39). Otherwise, water is desorbed in high proportion. The desorption kinetics of H<sub>2</sub>O breakthrough curves indicate that even when the adsorbent is heated to 160°C, the material continues desorbing molecules which suggests strong interactions between HK-0.30e and H<sub>2</sub>O, previously suspected in the hysteresis curves of DVS measurements (*Section 6.5.1*, Figure 6.34(b)).

Ultimately, breakthrough analysis confirms that HK-0.30e exhibits efficient CO<sub>2</sub> adsorption uptake under dry conditions, showing fast CO<sub>2</sub> capture kinetics and a complete regeneration behavior under 80°C. However, this material presents a high affinity for H<sub>2</sub>O molecules and, consequently, under humid conditions the CO<sub>2</sub> capture capacity is negligible. These results reinforce evidence that H<sub>2</sub>O and CO<sub>2</sub> compete for the same potential adsorption sites, which in this case may be the aromatic carbon functional groups, as supported by NMR experiments of *Section 6.4* in this chapter. Additionally, the findings suggest that early regeneration after CO<sub>2</sub> adsorption in 15-17 minutes, may enhance the performance under humid conditions since thus complete adsorption of H<sub>2</sub>O implies slower adsorption kinetics and takes around 75 minutes.

## 6.6 Conclusions

This chapter highlights and corroborates, using various techniques, the critical role played by water molecules in CO<sub>2</sub> capture processes using HKUST-1/GO materials.

Firstly, the colorimetric analysis demonstrates a strong interaction between MOF and water molecules. This analysis not only revealed color changes induced by H<sub>2</sub>O but also indicated that CO<sub>2</sub> adsorption causes similar modifications. As a result, the colorimetric measurements expose that both HKUST-1 and HKUST-1/GO samples undergo chromatic changes associated with the amount adsorbed CO<sub>2</sub>, establishing a strong correlation between the adsorption isotherms and the observed color response. These findings indicate a way to monitor in-situ and continuously the state of HKUST-1/GO under operational conditions, both adsorption and desorption process, as well as exhibiting a potential alternative for quantifying CO<sub>2</sub> adsorption by monitoring the color change.

Infrared experiments indicate that H<sub>2</sub>O interacts with the samples influencing the vibration of the asymmetric carboxylate stretching band (both for the pristine and the enhanced HKUST-1/GO sample). In contrast, the carboxylate band in the spectra of both samples remained unchangeable when the samples were exposed to some CO<sub>2</sub> concentrations. These results suggest that carboxylate bands are one of the potential adsorption sites for H<sub>2</sub>O, whereas CO<sub>2</sub> molecules are not adsorbed in those positions of the samples.

Additionally, HK-0.30e presents lower vibrational changes in the copper-nuclei bands when H<sub>2</sub>O is adsorbed, which indicates that the presence of GO may be blocking partially H<sub>2</sub>O molecules and the vibrational changes resulting from the adsorption are lower. This suggests that an enhanced HKUST-1/GO sample offers improved stability against water molecules, which is relevant considering that prolonged interaction with H<sub>2</sub>O can lead to sample degradation.

---

$^{13}\text{C}$  NMR experiments have evidenced the competition between  $\text{H}_2\text{O}$  and  $\text{CO}_2$  for the potential adsorption sites in these materials, indicating as a result that both  $\text{H}_2\text{O}$  and  $\text{CO}_2$  molecules are adsorbed in the aromatic functional groups. This is the result of the  $\pi$ -interactions generated by the aromatic ring of the sample, which suggest that HKUST-1/GO samples perform enhanced  $\text{CO}_2$  adsorption due to the additional  $\pi$ -interactions introduced into the sample derived from the presence of GO. Moreover, the results also confirm that  $\text{H}_2\text{O}$  molecules are adsorbed by hydrogen bonds in carboxylate functional groups since changes in carbonyl peaks are detected, aligning with IR experiments. Hence, the incorporation of GO increases the number of favorable adsorption sites for both  $\text{CO}_2$  and  $\text{H}_2\text{O}$ , such as aromatic carbon and carboxylate groups, which not only enhance water adsorption but also reduce the likelihood of sample degradation.

DVS experiments performed under post-combustion conditions confirm a higher adsorption capacity and less reduction in the adsorption performance over multiple cycles for most adsorbent samples. Moreover, the enhanced HKUST-1/GO material exhibited higher  $\text{H}_2\text{O}$  uptake than the pristine HKUST-1. These results suggest that the incorporation of GO also promotes the increase of water uptake, apart from enhanced  $\text{CO}_2$  adsorption performance as previously seen in the results of *Chapters III and IV*.

The introduction of GO in HKUST-1 prevents the degradation of HKUST-1 compared to samples without GO. This is consistent with the results of IR experiments, where GO is partially blocking the copper-nuclei sites, producing a better stabilization of the sample in humid conditions.

Additionally, breakthrough analysis demonstrates the ability of water to replace  $\text{CO}_2$  adsorbed molecules when the adsorption is produced using humid conditions. Consequently, this material presents a high affinity for  $\text{H}_2\text{O}$  molecules, and, under humid conditions, the  $\text{CO}_2$  capture capacity is negligible. However, the temperature implied in the desorption process for  $\text{H}_2\text{O}$  molecules is higher than for  $\text{CO}_2$

desorption, up to 160 °C in front of 80°C respectively. Consequently, the findings suggest that early regeneration after CO<sub>2</sub> adsorption in 15-17 minutes may enhance the performance under humid conditions since thus complete adsorption of H<sub>2</sub>O implies slower adsorption kinetics and takes around 75 minutes. These results open the way to future experiments with the potential to capture CO<sub>2</sub> molecules under humid conditions, currently being a complex task considering all the implications that water presents during CO<sub>2</sub> adsorption processes.

---

## **Chapter VII: Conclusions**

---



The materials synthesized and characterized during the development of this thesis contribute to the development of more efficient and sustainable materials for gas CO<sub>2</sub> capture.

HKUST-1 and HKUST-1/GO materials were synthesized via the mixed-solvent method (MSM), confirming the preservation of MOF structure and achieving significant improvements in CO<sub>2</sub> adsorption. The most adsorbent samples synthesized, with 0.25% w/w experimental GO ( $5.33 \pm 0.16$  mmol CO<sub>2</sub>/g), have an 80% increase in CO<sub>2</sub>, demonstrating both high performance and selective adsorption at elevated pressures.

Graphene oxide (GO) was successfully quantified using Reverse Quantification (RQ) process presented in this research and utilized along all the samples synthesized using different methods. In this case, RQ for the MSM method reveals that samples with lower amounts of GO are closer to ideal performance. This behavior is attributed to the fact that small amounts of GO disperse and adhere more easily to the final structure of the HKUST-1 compared to the addition of larger amounts of GO, which agglomerate and tend to separate from the HKUST-1.

SEM images provide information about the effect of GO produced on the size and geometry of the MOF particles. GO promotes and increases the nucleation points for the formation of HK crystals as well as the creation of different structural and morphological defects. Moreover, particle size measurements indicate that MSM samples exhibit around 600 nm.

Mechano-chemical synthesis via ball milling was explored as a method more respectful of the green chemistry standards. Both small and medium-scale ball milling (sBM and bBM, respectively) were utilized to synthesize HKUST-1 and HKUST-1/GO materials.

On the one hand, the sBM approach led materials with nanometric particle sizes ( $\sim 200$  nm) and high adsorption (up to  $4.93 \pm 0.28$  mmol/g at 0.48-0.55% w/w of experimental GO), reaching similar values to those obtained using MSM synthesis.

On the other hand, bBM samples show lower yields and a bimodal particle size distribution of sizes between 200 and 300 nm, which contributed to lower performance on the CO<sub>2</sub> adsorption properties of the samples ( $3.77 \pm 0.07$  mmol CO<sub>2</sub>/g at 0.25-0.30% w/w of experimental GO). Despite the challenges of synthesis, ball milling proves to be a promising and scalable route for MOF production.

Reverse Quantification (RQ) reveals some key aspects related to the synthesis yield for sBM and bBM samples. The results indicate that samples synthesized using smaller amounts of GO, specifically between 0.15 and 0.50% w/w GO; exhibited higher experimental contents of GO than the theoretical one added during the synthesis. Particularly, that range of samples also presents lower yields in synthesis compared to those synthesized with higher GO contents. This suggests that the MOF growth within the GO layers, particularly at these lower GO concentrations, may hinder crystal growth and result in incomplete reactions. In contrast, samples synthesized with higher GO contents demonstrated more favorable yields.

The incorporation of rGO in HKUST-1, HKUST-1/rGO, achieves comparable CO<sub>2</sub> adsorption to sBM samples with an experimental content of 0.80% rGO (5.1 mmol/g).

rGO has few defects and hinders nucleation, resulting in lower synthesis yields and poorer integration. Combining HKUST-1 with graphenic materials in a 1:3 ratio (rGO/GO mixtures, respectively) improves the CO<sub>2</sub> adsorption performance (up to 6.00 mmol/g), suggesting a synergistic effect when both materials are mixed and incorporated in the synthesis of HKUST-1/GM materials.

Chromatic changes in the samples during CO<sub>2</sub> and H<sub>2</sub>O exposure reveal strong interactions between the HKUST-1 (with and without GO) and CO<sub>2</sub> and H<sub>2</sub>O, closely relating the adsorption of both gases to the color change. The change is from darker blue for activated samples to blue turquoise for gas adsorbed samples.

The colorimetric measurements expose that the synthesized samples undergo chromatic changes associated with the amount of adsorbed CO<sub>2</sub>, establishing a strong correlation between the adsorption isotherms and the observed color response. These findings indicate a way to monitor in-situ and continuously the state of HKUST-1/GO under operational conditions, both adsorption and desorption process, as well as exhibiting a potential alternative for quantifying CO<sub>2</sub> adsorption by monitoring the color change.

Infrared experiments indicate that H<sub>2</sub>O interacts with the samples influencing the vibration of the asymmetric carboxylate stretching band (both for the pristine and the optimal HKUST-1/GO sample). In contrast, the carboxylate band in the spectra of both samples remained unchangeable when the samples are exposed to some CO<sub>2</sub> concentrations. These results suggest that carboxylate bands are one of the potential adsorption sites for H<sub>2</sub>O, whereas CO<sub>2</sub> molecules are not adsorbed in those positions of the samples.

Additionally, the optimal HKUST-1/GO presents lower vibrational changes in the copper-nuclei bands when H<sub>2</sub>O is adsorbed, which indicates that the presence of GO is partially blocking H<sub>2</sub>O molecules and the vibrational changes resulting from the adsorption are lower. This suggests that HKUST-1/GO sample offers improved stability against water molecules, which is relevant considering that prolonged interaction with H<sub>2</sub>O can lead to sample degradation.

<sup>13</sup>C NMR experiments evidence the competition between H<sub>2</sub>O and CO<sub>2</sub> for the potential adsorption sites in these materials, indicating that both H<sub>2</sub>O and CO<sub>2</sub> molecules are adsorbed in the aromatic functional groups. This is the result of the  $\pi$ -

interactions generated by the aromatic ring of the sample, which suggest that HKUST-1/GO samples perform enhanced CO<sub>2</sub> adsorption due to the additional  $\pi$ -interactions introduced into the sample derived from the presence of GO.

The results also confirm that H<sub>2</sub>O molecules are adsorbed by hydrogen bonds in carboxylate functional groups since changes in carbonyl peaks are detected, aligning with IR experiments. Hence, the incorporation of GO increases the number of favorable adsorption sites for both CO<sub>2</sub> and H<sub>2</sub>O, such as aromatic carbon and carboxylate groups, which not only enhance water adsorption but also reduce the likelihood of sample degradation.

DVS experiments performed under post-combustion conditions confirm a higher adsorption capacity and less reduction in the adsorption performance over multiple cycles for the most adsorbent sample.

The optimal HKUST-1/GO sample exhibits a higher H<sub>2</sub>O uptake than the pristine HKUST-1. These results suggest that the incorporation of GO also promotes the increase of water uptake, apart from increasing CO<sub>2</sub> adsorption performance.

The introduction of GO in HKUST-1 prevents the degradation of HKUST-1 compared to samples without GO. This is consistent with the results of IR experiments, where GO is partially blocking the copper-nuclei sites, producing a better stabilization of the sample in humid conditions.

Additionally, breakthrough analysis demonstrates the ability of water to replace CO<sub>2</sub> adsorbed molecules when the adsorption is produced using humid conditions. Consequently, this material presents a high affinity for H<sub>2</sub>O molecules and, under humid conditions, the CO<sub>2</sub> capture capacity is negligible. However, the temperature in the desorption process for H<sub>2</sub>O molecules is higher than for CO<sub>2</sub> desorption, up to 160 °C in front of 80°C respectively. Consequently, the findings suggest that early regeneration after CO<sub>2</sub> adsorption in 15-17 minutes may enhance the performance under humid conditions since thus complete adsorption of H<sub>2</sub>O implies slower

adsorption kinetics and takes around 75 minutes. These results open the way to future experiments with the potential to capture CO<sub>2</sub> molecules under humid conditions, currently being a complex task considering all the implications that water presents during CO<sub>2</sub> adsorption processes.

In conclusion, this thesis demonstrates that the integration of graphene-based materials into HKUST-1 and the use of mechano-chemical synthesis offer a path toward efficient, scalable, and environmentally friendly CO<sub>2</sub> adsorbents. Each strategy presented in the thesis provides insights into optimizing material properties for future industrial applications.



---

## References

---



1. Park, S. W., Kim, J. S. & Kug, J. S. The intensification of Arctic warming as a result of CO<sub>2</sub> physiological forcing. *Nat Commun* **11**, 1–7 (2020).
2. Lang, A. & Mikolajewicz, U. Rising extreme sea levels in the German Bight under enhanced CO<sub>2</sub> levels: a regionalized large ensemble approach for the North Sea. *Clim Dyn* **55**, 1829–1842 (2020).
3. Sadatshojaie, A. & Rahimpour, M. R. CO<sub>2</sub> emission and air pollution (volatile organic compounds, etc.)-related problems causing climate change. in *Current Trends and Future Developments on (Bio-) Membranes: Membranes in Environmental Applications* 1–30 (Elsevier, 2020). doi:10.1016/B978-0-12-816778-6.00001-1.
4. Melzner, F., Mark, F. C., Seibel, B. A. & Tomanek, L. Ocean Acidification and Coastal Marine Invertebrates: Tracking CO<sub>2</sub> Effects from Seawater to the Cell. *Ann Rev Mar Sci* **12**, 499–523 (2020).
5. Burrell, A. L., Evans, J. P. & Kauwe, M. G. De. Anthropogenic climate change has driven over 5 million km<sup>2</sup> of drylands towards desertification. *Nat Commun* **11**, 1–11 (2020).
6. Rayer, Q., Pflaederer, P. & Haustein, K. Global Warming and Extreme Weather Investment Risks. in *Ecological, Societal, and Technological Risks and the Financial Sector* 39–68 (Springer, 2020).
7. Pierrehumbert, R. T. High levels of atmospheric carbon dioxide necessary for the termination of global glaciation. *Nature* **429**, 646–649 (2004).
8. Friedlingstein P *et al.* Global Carbon Budget. *Earth Syst Sci Data* **15**, 5310–5369 (2023).
9. Denman, K. L. *et al.* Couplings Between Changes in the Climate System and Biogeochemistry Coordinating. in *Climate Change 2007: The Physical Science Basis* 499–588 (Cambridge University Press, 2007).
10. Friedlingstein, P. *et al.* Global Carbon Budget 2022. *Earth Syst Sci Data* **14**, 4811–4900 (2022).
11. Maroto-Valer, M. M. Carbon dioxide capture, transport and industrial applications. in *Developments and innovation in carbon dioxide capture and storage technology* 426 (Elsevier, 2010).

12. Atalla, T., Blazquez, J., Hunt, L. C. & Manzano, B. Prices versus policy: An analysis of the drivers of the primary fossil fuel mix. *Energy Policy* **106**, 536–546 (2017).
13. Kåberger, T. Progress of renewable electricity replacing fossil fuels. *Global Energy Interconnection* **1**, 48–52 (2018).
14. Friedlingstein, P. *et al.* Global Carbon Budget 2024. *Earth Syst Sci Data* **17**, 965–1039 (2025).
15. Reuters. Renewables provided a record 32% of global electricity in 2024. (2025).
16. International Energy Agency. *World Energy Outlook 2024*. [www.iea.org/terms](http://www.iea.org/terms).
17. Rana, R. L., Lombardi, M., Giungato, P. & Tricase, C. Trends in Scientific Literature on Energy Return Ratio of Renewable Energy Sources for Supporting Policymakers. *Adm Sci* **10**, 21 (2020).
18. Freire, A. L. *et al.* Geopolymers produced with fly ash and rice husk ash applied to CO<sub>2</sub> capture. *J Clean Prod* **273**, 122917 (2020).
19. Sanz-Pérez, E. S. *et al.* Effectiveness of amino-functionalized sorbents for CO<sub>2</sub> capture in the presence of Hg. *Fuel* **267**, 117250 (2020).
20. Ooi, Z. L., Tan, P. Y., Tan, L. S. & Yeap, S. P. Amine-based solvent for CO<sub>2</sub> absorption and its impact on carbon steel corrosion: A perspective review. *Chin J Chem Eng* **28**, 1357–1367 (2020).
21. Udara, S. P. R. A. *et al.* Simulation of carbon dioxide capture for industrial applications. *Energy Reports* **6**, 659–663 (2020).
22. Ochedi, F. O., Yu, J., Yu, H., Liu, Y. & Hussain, A. *Carbon Dioxide Capture Using Liquid Absorption Methods: A Review*. *Environmental Chemistry Letters* (Springer Science and Business Media Deutschland GmbH, 2020).
23. Strojny, M., Gładysz, P., Hanak, D. P. & Nowak, W. Comparative analysis of CO<sub>2</sub> capture technologies using amine absorption and calcium looping integrated with natural gas combined cycle power plant. *Energy* **284**, 128599 (2023).
24. Meng, F. *et al.* Novel low energy mixed amine biphasic solvent for carbon dioxide capture in biogas upgrading. *Sep Purif Technol* **326**, 124724 (2023).

- 
25. Umeda, Y. & Yamashita, H. Analysis of the Characteristics of Decompression Capture of CO<sub>2</sub> in Flue Gas by Cryogenic Heat. *Journal of Chemical Engineering of Japan* **56**, 1–23 (2023).
  26. Raksajati, A., Ho, M. & Wiley, D. Solvent Development for Post-Combustion CO<sub>2</sub> Capture: Recent Development and Opportunities. *MATEC Web of Conferences* **156**, 1–8 (2018).
  27. Folger, P. Carbon capture and sequestration (CCS). *Geologic Carbon Dioxide Storage* **325**, 17–52 (2012).
  28. Xiao, M. *et al.* Role of mono- and diamines as kinetic promoters in mixed aqueous amine solution for CO<sub>2</sub> capture. *Chem Eng Sci* **229**, 116009 (2021).
  29. Yu, C. H., Huang, C. H. & Tan, C. S. A review of CO<sub>2</sub> capture by absorption and adsorption. *Aerosol Air Qual Res* **12**, 745–769 (2012).
  30. Krishnamurthy, S., Lind, A., Bouzga, A., Pierchala, J. & Blom, R. Post combustion carbon capture with supported amine sorbents: From adsorbent characterization to process simulation and optimization. *Chemical Engineering Journal* **406**, 127121 (2021).
  31. Prats-Salvado, E., Monnerie, N. & Sattler, C. A techno-economic and environmental evaluation of the integration of direct air capture with hydrogen derivatives production. *Int J Hydrogen Energy* (2020) doi:10.1016/j.ijhydene.2024.10.026.
  32. Wang, Y. *et al.* Comprehensive 3E analysis and multi-objective optimization of a novel process for CO<sub>2</sub> capture and separation process from syngas. *J Clean Prod* **274**, 122871 (2020).
  33. Xin, K., Hashish, M., Roghair, I. & van Sint Annaland, M. Process Simulation and Economic Analysis of Pre-combustion CO<sub>2</sub> Capture With Deep Eutectic Solvents. *Front Energy Res* **8**, 573267 (2020).
  34. Einloft, S. & Bernard, F. L. *Encapsulated Liquid Sorbents for CO<sub>2</sub> Capture*. *Advances in Carbon Capture* (Elsevier Inc., 2020). doi:10.1016/b978-0-12-819657-1.00006-2.
  35. Hafeez, S. *et al.* CO<sub>2</sub> capture using membrane contactors: a systematic literature review. *Front Chem Sci Eng* (2020) doi:10.1007/s11705-020-1992-z.

36. Okeke, I. J. & Thomas, A. A. Advanced petroleum coke oxy-combustion power generation with carbon capture and sequestration: Part II—Environmental assessment and cost of CO<sub>2</sub> avoided. *Can J Chem Eng* **99**, 0–2 (2021).
37. Sanz-Pérez, E. S., Murdock, C. R., Didas, S. A. & Jones, C. W. Direct Capture of CO<sub>2</sub> from Ambient Air. *Chem Rev* **116**, 11840–11876 (2016).
38. Pardakhti, M. *et al.* Trends in Solid Adsorbent Materials Development for CO<sub>2</sub> Capture. *ACS Appl Mater Interfaces* **11**, 34533–34559 (2019).
39. Nogalska, A., Zukowska, A. & Garcia-Valls, R. Atmospheric CO<sub>2</sub> capture for the artificial photosynthetic system. *Science of the Total Environment* **621**, 186–192 (2018).
40. Atkins, P. *Student's Solutions Manual to Accompany Atkins' Physical Chemistry*. (Oxford University Press, 2002).
41. Ruesch, T. & Wurzbacher, J. A. Direct air capture device. 1–11 (2017).
42. Beaumont, M. L. & Thirkettle, A. C. Method and device for the reversible adsorption of carbon dioxide. 1–8 (2017).
43. Klaus S. Lackner, D. F. N. Removal of carbon dioxide from air. 1–18 (2012).
44. Héder, M. From NASA to EU: the evolution of the TRL scale in Public Sector Innovation. *Innov J* **22**, 3.
45. Shang, S. *et al.* Facile synthesis of CuBTC and its graphene oxide composites as efficient adsorbents for CO<sub>2</sub> capture. *Chemical Engineering Journal* **393**, (2020).
46. Pokhrel, J. *et al.* Cu- and Zr-based metal organic frameworks and their composites with graphene oxide for capture of acid gases at ambient temperature. *J Solid State Chem* **266**, 233–243 (2018).
47. Liu, N., Cheng, J., Hou, W., Yang, X. & Zhou, J. Unsaturated Zn–N<sub>2</sub>–O active sites derived from hydroxyl in graphene oxide and zinc atoms in core shell ZIF-8@ZIF-67 nanocomposites enhanced CO<sub>2</sub> adsorption capacity. *Microporous and Mesoporous Materials* **312**, 110730 (2021).
48. He, Y. *et al.* One-step fabrication of PEI-modified GO particles for CO<sub>2</sub> capture. *Appl Phys A Mater Sci Process* **125**, 437 (2019).
49. Rouquerol, F., Rouquerol, J. & Sing, K. S. W. *Adsorption by Powders and Porous Solids: Principles, Methodology and Applications*. (Academic Press, 1999).

- 
50. Bernard, P., Stelmachowski, P., Broś, P., Makowski, W. & Kotarba, A. Demonstration of the Influence of Specific Surface Area on Reaction Rate in Heterogeneous Catalysis. *J Chem Educ* **98**, 935–940 (2021).
  51. Zhang, Y., Zhang, Y., Wang, X., Yu, J. & Ding, B. Ultrahigh Metal-Organic Framework Loading and Flexible Nanofibrous Membranes for Efficient CO<sub>2</sub> Capture with Long-Term, Ultrastable Recyclability. *ACS Appl Mater Interfaces* **10**, 34802–34810 (2018).
  52. Taheri, A., Babakhani, E. G. & Towfighi Darian, J. A MIL-101(Cr) and Graphene Oxide Composite for Methane-Rich Stream Treatment. *Energy and Fuels* **31**, 8792–8802 (2017).
  53. Szczeńniak, B. & Choma, J. Graphene-containing microporous composites for selective CO<sub>2</sub> adsorption. *Microporous and Mesoporous Materials* **292**, 109761 (2020).
  54. Lu, W. *et al.* Building multiple adsorption sites in porous polymer networks for carbon capture applications. *Energy Environ Sci* **6**, 3559–3564 (2013).
  55. Henry, W. III. Experiments on the Quantity of Gases adsorbed by Water, at different Temperatures, and under different Pressures. *Royal Society* **93**, 29–43 (1802).
  56. Wang, M., Wang, J., Qiao, W., Ling, L. & Long, D. Scalable preparation of nitrogen-enriched carbon microspheres for efficient CO<sub>2</sub> capture. *RSC Adv* **4**, 61456–61464 (2014).
  57. Lee, D. W., Didriksen, T., Olsbye, U., Blom, R. & Grande, C. A. Shaping of metal-organic framework UiO-66 using alginates: Effect of operation variables. *Sep Purif Technol* **235**, (2020).
  58. Arul, C. *et al.* Temperature modulated Cu-MOF based gas sensor with dual selectivity to acetone and NO<sub>2</sub> at low operating temperatures. *Sens Actuators B Chem* **329**, 129053 (2021).
  59. Huang, T. C. *et al.* Fabrication of pebax-1657-based mixed-matrix membranes incorporating N-doped few-layer graphene for carbon dioxide capture enhancement. *J Memb Sci* **602**, 117946 (2020).
  60. Li, X., Yang, X., Xue, H., Pang, H. & Xu, Q. Metal-organic frameworks as a platform for clean energy applications. *EnergyChem* **2**, 100027 (2020).

- 
61. Kinoshita, Y., Matsubara, I., Higuciu, T. & Saito, Y. *The Crystal Structure of Bis(Adiponitrilo)Copper(I) Nitrate*. (1959).
  62. Tranchemontagne, D. J., Hunt, J. R. & Yaghi, O. M. Room temperature synthesis of metal-organic frameworks: MOF-5, MOF-74, MOF-177, MOF-199, and IRMOF-0. *Tetrahedron* **64**, 8553–8557 (2008).
  63. Raptopoulou, C. P. Metal-Organic Frameworks: Synthetic Methods and Potential Applications. *Materials* **14**, 310 (2021).
  64. Mason, J. A. *et al.* Application of a High-Throughput Analyzer in Evaluating Solid Adsorbents for Post-Combustion Carbon Capture via Multicomponent Adsorption of CO<sub>2</sub>, N<sub>2</sub>, and H<sub>2</sub>O. *J Am Chem Soc* **137**, 4787–4803 (2015).
  65. Roy, S., Darabdhara, J. & Ahmaruzzaman, M. Recent advances of Copper- BTC metal-organic frameworks for efficient degradation of organic dye-polluted wastewater: Synthesis, mechanistic insights and future outlook. *Journal of Hazardous Materials Letters* **5**, 100094 (2024).
  66. ChemTube3D. UiO-66 Metal Organic Framework. <https://www.chemtube3d.com/mof-uio66/>.
  67. Wahiduzzaman, M., Lenzen, D., Maurin, G., Stock, N. & Wharmby, M. T. Rietveld Refinement of MIL-160 and Its Structural Flexibility Upon H<sub>2</sub>O and N<sub>2</sub> Adsorption. *Eur J Inorg Chem* **2018**, 3626–3632 (2018).
  68. Chae HK. Design and synthesis of an exceptionally stable and highly porous metal organic framework. *Letters to nature* **402**, 276–279 (1999).
  69. Yaghi, O. M. *et al.* Reticular synthesis and the design of new materials. *Nature* **423**, 705–714 (2003).
  70. Cavka, J. H. *et al.* A new zirconium inorganic building brick forming metal organic frameworks with exceptional stability. *J Am Chem Soc* **130**, 13850–13851 (2008).
  71. Ediati, R. *et al.* One-pot solvothermal synthesis and characterization of UiO-66/HKUST-1 composites. *IOP Conf Ser Mater Sci Eng* **578**, (2019).
  72. Lee, Y. R., Kim, J. & Ahn, W. S. Synthesis of metal-organic frameworks: A mini review. *Korean Journal of Chemical Engineering* **30**, 1667–1680 (2013).
  73. Ahmed, I. & Jhung, S. H. Applications of metal-organic frameworks in adsorption/separation processes via hydrogen bonding interactions. *Chemical Engineering Journal* **310**, 197–215 (2017).

- 
74. Jiang, B. X., Wang, H., Zhang, Y. T. & Li, S. B. Microwave-assisted synthesis of Zr-based metal-organic frameworks and metal-organic cages. *Polyhedron* **243**, 116569 (2023).
  75. Jhung, S. H. *et al.* Microwave synthesis of chromium terephthalate MIL-101 and its benzene sorption ability. *Advanced Materials* **19**, 121–124 (2007).
  76. Horcajada, P. *et al.* Porous metal-organic-framework nanoscale carriers as a potential platform for drug delivery and imaging. *Nat Mater* **9**, 172–178 (2010).
  77. Seo, Y. K. *et al.* Microwave synthesis of hybrid inorganic-organic materials including porous Cu<sub>3</sub>(BTC)<sub>2</sub> from Cu(II)-trimesate mixture. *Microporous and Mesoporous Materials* **119**, 331–337 (2009).
  78. Horcajada, P. *et al.* Metal-Organic Frameworks as Efficient Materials for Drug Delivery. *Angewandte Chemie* **118**, 6120–6124 (2006).
  79. Choi, J. S., Son, W. J., Kim, J. & Ahn, W. S. Metal-organic framework MOF-5 prepared by microwave heating: Factors to be considered. *Microporous and Mesoporous Materials* **116**, 727–731 (2008).
  80. Cathy Einhorn, Jaques Einhorn, J.-L. L. Sonochemistry- The use of ultrasonic waves in synthetic organic chemistry. *Synthesis (Stuttg)* **787–813**, (1989).
  81. Gedanken, A. Using sonochemistry for the fabrication of nanomaterials. *Ultrason Sonochem* **11**, 47–55 (2004).
  82. Qiu, L. G. *et al.* Facile synthesis of nanocrystals of a microporous metal-organic framework by an ultrasonic method and selective sensing of organoamines. *Chemical Communications* 3642–3644 (2008) doi:10.1039/b804126a.
  83. Son, W. J., Kim, J., Kim, J. & Ahn, W. S. Sonochemical synthesis of MOF-5. *Chemical Communications* 6336–6338 (2008) doi:10.1039/b814740j.
  84. Li, Z. Q. *et al.* Ultrasonic synthesis of the microporous metal-organic framework Cu<sub>3</sub>(BTC)<sub>2</sub> at ambient temperature and pressure: An efficient and environmentally friendly method. *Mater Lett* **63**, 78–80 (2009).
  85. Yang, D. A., Cho, H. Y., Kim, J., Yang, S. T. & Ahn, W. S. CO<sub>2</sub> capture and conversion using Mg-MOF-74 prepared by a sonochemical method. *Energy Environ Sci* **5**, 6465–6473 (2012).

- 
86. Cho, H. Y., Kim, J., Kim, S. N. & Ahn, W. S. High yield 1-L scale synthesis of ZIF-8 via a sonochemical route. *Microporous and Mesoporous Materials* **169**, 180–184 (2013).
  87. Yi, J., Lee, G. & Park, S. S. Solvent-Induced Structural Rearrangement in Ultrasound-Assisted Synthesis of Metal–Organic Frameworks. *Small Methods* (2024) doi:10.1002/smt.202400363.
  88. Ghoorchian, A., Afkhami, A., Madrakian, T. & Ahmadi, M. Electrochemical synthesis of MOFs. in *Metal-Organic Frameworks for Biomedical Applications* 177–195 (Elsevier Inc., 2020). doi:10.1016/B978-0-12-816984-1.00011-1.
  89. Mueller, I. U. *et al.* Method for electrochemical production of a crystalline porous metal organic skeleton material. vol. 2 (2011).
  90. Martinez Joaristi, A., Juan-Alcañiz, J., Serra-Crespo, P., Kapteijn, F. & Gascon, J. Electrochemical synthesis of some archetypical Zn 2+, Cu 2+, and Al 3+ metal organic frameworks. *Cryst Growth Des* **12**, 3489–3498 (2012).
  91. Wei, J. Z. *et al.* Rapid and large-scale synthesis of irdmof-3 by electrochemistry method with enhanced fluorescence detection performance for tnp. *Inorg Chem* **57**, 3818–3824 (2018).
  92. Osadchii, D. Y. *et al.* Isolated Fe sites in metal organic frameworks catalyze the direct conversion of methane to methanol. *ACS Catal* **8**, 5542–5548 (2018).
  93. Yang, H. M. *et al.* In situ electrochemical synthesis of MOF-5 and its application in improving photocatalytic activity of BiOBr. *Transactions of Nonferrous Metals Society of China (English Edition)* **25**, 3987–3994 (2015).
  94. Pichon, A., Lazuen-Garay, A. & James, S. L. Solvent-free synthesis of a microporous metal-organic framework. *CrystEngComm* **8**, 211–214 (2006).
  95. Afshariazar, F. & Morsali, A. The unique opportunities of mechanosynthesis in green and scalable fabrication of metal-organic frameworks. *J Mater Chem A Mater* **10**, 15332–15369 (2022).
  96. Taheri, M., Enge, T. G. & Tsuzuki, T. Water stability of cobalt doped ZIF-8: a quantitative study using optical analyses. *Mater Today Chem* **16**, 100231 (2020).
  97. Friiç, T. & Fábíán, L. Mechanochemical conversion of a metal oxide into coordination polymers and porous frameworks using liquid-assisted grinding (LAG). *CrystEngComm* **11**, 743–745 (2009).

- 
98. Prochowicz, D. *et al.* A mechanochemical strategy for IRMOF assembly based on pre-designed oxo-zinc precursors. *Chemical Communications* **51**, 4032–4035 (2015).
99. Chen, D., Zhao, J., Zhang, P. & Dai, S. Mechanochemical synthesis of metal–organic frameworks. *Polyhedron* **162**, 59–64 (2019).
100. Fu, X. P., Wang, Y. L. & Liu, Q. Y. Metal-organic frameworks for C<sub>2</sub>H<sub>2</sub>/CO<sub>2</sub> separation. *Dalton Transactions* **49**, 16598–16607 (2020).
101. Vrtovec, N. *et al.* Structural and CO<sub>2</sub> Capture Properties of Ethylenediamine-Modified HKUST-1 Metal-Organic Framework. *Cryst Growth Des* **20**, 5455–5465 (2020).
102. Cui, P., Zhang, X., Kang, Y., Zhao, Y. & Sun, W. Cobalt-Based Metal – Organic Frameworks for Adsorption of CO<sub>2</sub> and C<sub>2</sub> Hydrocarbons: Effect of Auxiliary Ligands with Different Functional Groups. (2020) doi:10.1021/acs.inorgchem.0c03461.
103. Silva, M. P. *et al.* MIL-160(Al) MOF’s potential in adsorptive water harvesting. *Adsorption* (2021) doi:10.1007/s10450-020-00286-5.
104. Gaikwad, S., Kim, S. J. & Han, S. Novel metal–organic framework of UTSA-16 (Zn) synthesized by a microwave method: Outstanding performance for CO<sub>2</sub> capture with improved stability to acid gases. *Journal of Industrial and Engineering Chemistry* **87**, 250–263 (2020).
105. Roh, D. K., Jae, H., Mun, H., Jo, J. H. & Chi, W. S. Precise tuning of morphology and pore size of amine-functionalized MIL metal–organic frameworks using a directing agent. *Mater Sci Eng B Solid State Mater Adv Technol* **263**, (2021).
106. Bahamon, D., Anlu, W., Builes, S., Khaleel, M. & Vega, L. F. Effect of Amine Functionalization of MOF Adsorbents for Enhanced CO<sub>2</sub> Capture and Separation: A Molecular Simulation Study. *Front Chem* **8**, (2021).
107. Zhao, Y., Ge, H., Miao, Y., Chen, J. & Cai, W. CO<sub>2</sub> capture ability of Cu-based metal-organic frameworks synergized with amino acid-functionalized layered materials. *Catal Today* **356**, 604–612 (2020).
108. Saha, D. & Kienbaum, M. J. Role of oxygen, nitrogen and sulfur functionalities on the surface of nanoporous carbons in CO<sub>2</sub> adsorption: A critical review. *Microporous and Mesoporous Materials* **287**, 29–55 (2019).

109. Huang, H. *et al.* Enhancing CO<sub>2</sub> adsorption and separation ability of Zr(IV)-based metal-organic frameworks through ligand functionalization under the guidance of the quantitative structure-property relationship model. *Chemical Engineering Journal* **289**, 247–253 (2016).
110. Iqbal, N., Wang, X., Yu, J. & Ding, B. Robust and Flexible Carbon Nanofibers Doped with Amine Functionalized Carbon Nanotubes for Efficient CO<sub>2</sub> Capture. *Adv Sustain Syst* **1**, (2017).
111. Kueh, B. *et al.* Asphaltene-Derived Activated Carbon and Carbon Nanotube Membranes for CO<sub>2</sub> Separation. *Energy and Fuels* **32**, 11718–11730 (2018).
112. He, G. *et al.* High-permeance polymer-functionalized single-layer graphene membranes that surpass the postcombustion carbon capture target. *Energy Environ Sci* **12**, 3305–3312 (2019).
113. Zhao, Y., Cai, W., Chen, J., Miao, Y. & Bu, Y. A highly efficient composite catalyst constructed from NH<sub>2</sub>-MIL-125(Ti) and reduced graphene oxide for CO<sub>2</sub> photoreduction. *Front Chem* **7**, 789 (2019).
114. Zhao, H., Bahamon, D., Khaleel, M. & Vega, L. Insights into the performance of hybrid graphene oxide/Mofs for CO<sub>2</sub> capture at process conditions by molecular simulations. *Chemical Engineering Journal* **449**, 137884 (2022).
115. He, G. *et al.* Synergistic CO<sub>2</sub>-Sieving from Polymer with Intrinsic Microporosity Masking Nanoporous Single-Layer Graphene. *Adv Funct Mater* **30**, 1–10 (2020).
116. Zhao, Y., Ding, H. & Zhong, Q. Synthesis and characterization of MOF-aminated graphite oxide composites for CO<sub>2</sub> capture. *Appl Surf Sci* **284**, 138–144 (2013).
117. Zhou, X., Huang, W., Liu, J., Wang, H. & Li, Z. Quenched breathing effect, enhanced CO<sub>2</sub> uptake and improved CO<sub>2</sub>/CH<sub>4</sub> selectivity of MIL-53(Cr)/graphene oxide composites. *Chem Eng Sci* **167**, 98–104 (2017).
118. Taheri, A., Babakhani, E. G. & Towfighi Darian, J. A MIL-101(Cr) and Graphene Oxide Composite for Methane-Rich Stream Treatment. *Energy and Fuels* **31**, 8792–8802 (2017).
119. Ullah, S. *et al.* Influence of post-synthetic graphene oxide (GO) functionalization on the selective CO<sub>2</sub>/CH<sub>4</sub> adsorption behavior of MOF-200 at different temperatures; an experimental and adsorption isotherms study. *Microporous and Mesoporous Materials* **296**, (2020).

- 
120. Pourebrahimi, S., Kazemeini, M., Ganji Babakhani, E. & Taheri, A. Removal of the CO<sub>2</sub> from flue gas utilizing hybrid composite adsorbent MIL-53(Al)/GNP metal-organic framework. *Microporous and Mesoporous Materials* **218**, 144–152 (2015).
  121. Alfe, M., Policicchio, A., Lisi, L. & Gargiulo, V. Solid sorbents for CO<sub>2</sub> and CH<sub>4</sub> adsorption: The effect of metal organic framework hybridization with graphene-like layers on the gas sorption capacities at high pressure. *Renewable and Sustainable Energy Reviews* **141**, 110816 (2021).
  122. Xu, F. *et al.* Ultrafast room temperature synthesis of GrO@HKUST-1 composites with high CO<sub>2</sub> adsorption capacity and CO<sub>2</sub>/N<sub>2</sub> adsorption selectivity. *Chemical Engineering Journal* **303**, 231–237 (2016).
  123. Xiang, Z. *et al.* Metal-organic frameworks with incorporated carbon nanotubes: Improving carbon dioxide and methane storage capacities by lithium doping. *Angewandte Chemie - International Edition* **50**, 491–494 (2011).
  124. Ata-ur-Rehman *et al.* Synthesis of highly stable MOF-5@MWCNTs nanocomposite with improved hydrophobic properties. *Arabian Journal of Chemistry* **11**, 26–33 (2018).
  125. Cortés-Suárez, J. *et al.* Synthesis and Characterization of an SWCNT@HKUST-1 Composite: Enhancing the CO<sub>2</sub> Adsorption Properties of HKUST-1. *ACS Omega* **4**, 5275–5282 (2019).
  126. Anafcheh, M. & Zahedi, M. Sustainable conversion of carbon dioxide to formic acid with Rh-decorated phosphorous-doped fullerenes: a theoretical study. *Struct Chem* **32**, 97–106 (2021).
  127. Xu, G. *et al.* Molecular simulations on CO<sub>2</sub> adsorption and adsorptive separation in fullerene impregnated MOF-177, MOF-180 and MOF-200. *Comput Mater Sci* **168**, 58–64 (2019).
  128. Zhao, Y., Seredych, M., Jagiello, J., Zhong, Q. & Bandosz, T. J. Insight into the mechanism of CO<sub>2</sub> adsorption on Cu-BTC and its composites with graphite oxide or aminated graphite oxide. *Chemical Engineering Journal* **239**, 399–407 (2014).
  129. Policicchio, A., Zhao, Y., Zhong, Q., Agostino, R. G. & Bandosz, T. J. Cu-BTC/aminated graphite oxide composites as high-efficiency CO<sub>2</sub> capture media. *ACS Appl Mater Interfaces* **6**, 101–108 (2014).

- 
130. Gargiulo, V., Policicchio, A., Lisi, L. & Alfe, M. CO<sub>2</sub> Capture and Gas Storage Capacities Enhancement of HKUST-1 by Hybridization with Functionalized Graphene-like Materials. *Energy and Fuels* **37**, 5291–5302 (2023).
  131. Zhao, Y., Cai, W., Chen, J., Miao, Y. & Bu, Y. A Highly Efficient Composite Catalyst Constructed From NH<sub>2</sub>-MIL-125(Ti) and Reduced Graphene Oxide for CO<sub>2</sub> Photoreduction. *Front Chem* **7**, (2019).
  132. Chui, S. S. Y., Lo, S. M. F., Charmant, J. P. H., Orpen, A. G. & Williams, I. D. A chemically functionalizable nanoporous material [Cu<sub>3</sub>(TMA)<sub>2</sub>(H<sub>2</sub>O)<sub>3</sub>](n). *Science (1979)* **283**, 1148–1150 (1999).
  133. You, Y. W., Xue, C., Tian, Z. F., Liu, S. X. & Ren, X. M. Three orders of magnitude enhancement of proton conductivity of porous coordination polymers by incorporating ion-pairs into a framework. *Dalton Transactions* **45**, 7893–7899 (2016).
  134. Rowsell, J. L. C. & Yaghi, O. M. Effects of functionalization, catenation, and variation of the metal oxide and organic linking units on the low-pressure hydrogen adsorption properties of metal-organic frameworks. *J Am Chem Soc* **128**, 1304–1315 (2006).
  135. Bhunia, M. K., Hughes, J. T., Fettinger, J. C. & Navrotsky, A. Thermochemistry of paddle wheel MOFs: Cu-HKUST-1 and Zn-HKUST-1. *Langmuir* **29**, 8140–8145 (2013).
  136. Yakovenko, A. A., Reibenspies, J. H., Bhuvanesh, N. & Zhou, H. C. Generation and applications of structure envelopes for porous metal-organic frameworks. *J Appl Crystallogr* **46**, 346–353 (2013).
  137. Hinrichs, K. *et al.* Infrared and Raman spectroscopic analysis of functionalized graphene. *Applied Research* **2**, (2023).
  138. Schlesinger, W. H. & Bernhardt, E. S. The Atmosphere. in *Biogeochemistry* 51–97 (Elsevier, 2020). doi:10.1016/B978-0-12-814608-8.00003-7.
  139. Langmuir, I. THE CONSTITUTION AND FUNDAMENTAL PROPERTIES OF SOLIDS AND LIQUIDS. PART I. SOLIDS. in vol. 1148 2267–2269 (1916).
  140. Lingling Liu, Xu-Biao Luo, Lin Ding, S.-L. L. 4 - Application of Nanotechnology in the Removal of Heavy Metal From Wate. in *Nanomaterials for the Removal of Pollutants and Resource Reutilization* 89–91 (1918).
  141. Cao, Y. *et al.* UiO-66-NH<sub>2</sub>/GO composite: Synthesis, characterization and CO<sub>2</sub> adsorption performance. *Materials* **11**, 1–16 (2018).

- 
142. Szczeńniak, B., Phuriragpitikhon, J., Choma, J. & Jaroniec, M. Mechanochemical synthesis of three-component graphene oxide/ordered mesoporous carbon/metal-organic framework composites. *J Colloid Interface Sci* **577**, 163–172 (2020).
  143. Huang, K. & Xu, Y. Enhancing the catalytic behaviour of HKUST-1 by graphene oxide for phenol oxidation. *Environmental Technology (United Kingdom)* **42**, 694–704 (2021).
  144. Braga, D. *et al.* Supramolecular complexation of alkali cations through mechanochemical reactions between crystalline solids. *Chemistry - A European Journal* **10**, 3261–3269 (2004).
  145. Yamamoto, K., Borjas García, S. E. & Muramatsu, A. Zeolite synthesis using mechanochemical reaction. *Microporous and Mesoporous Materials* **101**, 90–96 (2007).
  146. García-Pacheco, G., Cabñas-Moreno, J. G., Yee-Madeira, H. & Cruz-Gandarilla, F. Co<sub>3</sub>O<sub>4</sub> nanoparticles produced by mechanochemical reactions. *Nanotechnology* **17**, 2528–2535 (2006).
  147. Xing, F. *et al.* Multifunctional metal–organic frameworks for wound healing and skin regeneration. *Mater Des* **233**, 112252 (2023).
  148. Kang, H. J., Choi, Y. H., Joo, I. W. & Lee, J. E. Mechanochemical Synthesis of CD-MOFs and Application as a Cosmetic Ingredient. *Bull Korean Chem Soc* (2021) doi:10.1002/bkcs.12253.
  149. Prochowicz, D. *et al.* A mechanochemical strategy for IRMOF assembly based on pre-designed oxo-zinc precursors. *Chemical Communications* **51**, 4032–4035 (2015).
  150. Friiç, T. & Fábíán, L. Mechanochemical conversion of a metal oxide into coordination polymers and porous frameworks using liquid-assisted grinding (LAG). *CrystEngComm* **11**, 743–745 (2009).
  151. Piras, C. C., Fernández-Prieto, S. & De Borggraeve, W. M. Ball milling: A green technology for the preparation and functionalisation of nanocellulose derivatives. *Nanoscale Adv* **1**, 937–947 (2019).
  152. Retsch. *An Expert Guide to Neutral-to-Analysis Size Reduction and Homogenization in the Laboratory The Art of Milling 2.* (2017).

153. Steenhaut, T., Grégoire, N., Barozzino-Consiglio, G., Filinchuk, Y. & Hermans, S. Mechanochemical defect engineering of HKUST-1 and impact of the resulting defects on carbon dioxide sorption and catalytic cyclopropanation. *RSC Adv* **10**, 19822–19831 (2020).
154. Ahmed, A. S., Alsultan, M., Sabah, A. A. & Swiegers, G. F. Carbon Dioxide Adsorption by a High-Surface-Area Activated Charcoal. *Journal of Composites Science* **7**, (2023).
155. Sherif El-Eskandarany, M. *Mechanical Alloying. Nanotechnology, Materials Science and Powder Metallurgy*. (2015).
156. Hassanzadeh-Tabrizi, S. A. Precise calculation of crystallite size of nanomaterials: A review. *J Alloys Compd* **968**, 171914 (2023).
157. Liu, Z. *et al.* Graphene-based materials prepared by supercritical fluid technology and its application in energy storage. *Journal of Supercritical Fluids* **188**, (2022).
158. Bhoria, N. *et al.* Functionalization effects on HKUST-1 and HKUST-1/graphene oxide hybrid adsorbents for hydrogen sulfide removal. *J Hazard Mater* **394**, 122565 (2020).
159. Schlichte, K., Kratzke, T. & Kaskel, S. Improved synthesis, thermal stability and catalytic properties of the metal-organic framework compound Cu<sub>3</sub>(BTC)<sub>2</sub>. *Microporous and Mesoporous Materials* **73**, 81–88 (2004).
160. Kökçam-Demir, Ü. *et al.* Coordinatively unsaturated metal sites (open metal sites) in metal-organic frameworks: Design and applications. *Chem Soc Rev* **49**, 2751–2798 (2020).
161. Mondloch, J. E., Karagiari, O., Farha, O. K. & Hupp, J. T. Activation of metal-organic framework materials. *CrystEngComm* **15**, 9258–9264 (2013).
162. Ursueguía, D., Díaz, E. & Ordóñez, S. Metal-Organic Frameworks (MOFs) as methane adsorbents: From storage to diluted coal mining streams concentration. *Science of the Total Environment* **790**, 148211 (2021).
163. Mendes, E. & Duarte, N. Mid-infrared spectroscopy as a valuable tool to tackle food analysis: A literature review on coffee, dairies, honey, olive oil and wine. *Foods* **10**, 1–32 (2021).
164. Gentile, F. S. *et al.* Metal defects in HKUST-1 MOF revealed by vibrational spectroscopy: a combined quantum mechanical and experimental study. *J Mater Chem A Mater* **8**, 10796–10812 (2020).

- 
165. Pell, A. J. & Pintacuda, G. Broadband solid-state MAS NMR of paramagnetic systems. *Prog Nucl Magn Reson Spectrosc* **84–85**, 33–72 (2015).
166. Worsley, M. A. *et al.* Mechanically robust 3D graphene macroassembly with high surface area. *Chemical Communications* **48**, 8428–8430 (2012).
167. Tang, J. *et al.* Solid-state NMR studies of the acidity of functionalized metal–organic framework UiO-66 materials. *Magnetic Resonance in Chemistry* **58**, 1091–1098 (2020).
168. Kuhlmann, K. F., Grant, D. M. & Harris, R. K. Nuclear overhauser effects and  $^{13}\text{C}$  relaxation times in  $^{13}\text{C}$ - $\{^1\text{H}\}$  double resonance spectra. *J Chem Phys* **52**, 3439–3448 (1970).
169. Hoffmann, H. C. *et al.* Solid-state NMR spectroscopy of metal-organic framework compounds (MOFs). *Materials* **5**, 2537–2572 (2012).
170. Schober, P. & Schwarte, L. A. Correlation coefficients: Appropriate use and interpretation. *Anesth Analg* **126**, 1763–1768 (2018).
171. García-Alegría, A. M., Gómez-Álvarez, A., García-Rico, L. & Serna-Félix, M. Validation of an analytical method to quantify serum electrolytes by atomic absorption spectroscopy. *Acta Univ* **25**, 3–12 (2015).
172. Aronhime, S. *et al.* DCE-MRI of the liver: Effect of linear and nonlinear conversions on hepatic perfusion quantification and reproducibility. *Journal of Magnetic Resonance Imaging* **40**, 90–98 (2014).
173. Thompson, M., Ellison, S. L. R. & Wood, R. Resulting from the Symposium on Harmonization of Quality Assurance Systems for Analytical Laboratories. *Pure Appl. Chem* **74**, 4–5 (2002).
174. Thompson, M., Ellison, S. L. R. & Wood, R. The International Harmonized Protocol for the proficiency testing of analytical chemistry laboratories: (IUPAC technical report). *Pure and Applied Chemistry* **78**, 145–196 (2006).
175. Dagnino, J. Análisis de variancia. *Revista Chilena de Anestesia* **43**, 306–331 (2014).



---

# Appendix

---



### **Small ball milling (sBM) and mixed solvent method (MSM) statistical analysis**

Figure A. 1 (a) and (b) show the results represented as individual sample results of experimental GO versus adsorption of CO<sub>2</sub>, analyzed in RQ sections of *Chapters III* and *IV*.

The statistical analysis, in this case, is performed across the entire range of synthesized samples for both methods. As a result, Figure A. 1 (a) presents a broader x-axis scale because the amount of GO used in the synthesis of MSM included a wider range of GO, up to approximately 5% w/w of experimental GO.

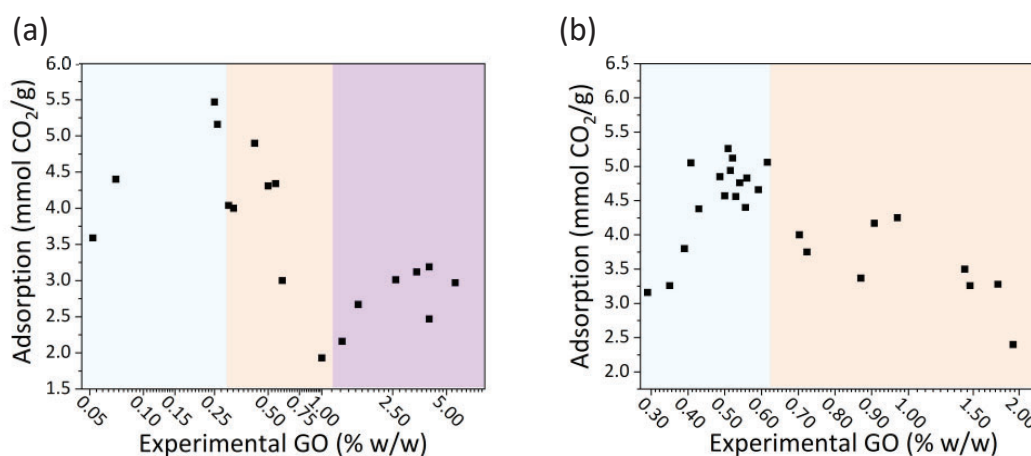


Figure A. 1. (a) CO<sub>2</sub> adsorption results (at 1000 mmHg) vs. experimental GO of MSM samples and (b) CO<sub>2</sub> adsorption results (at 1000 mmHg) vs. experimental GO of sBM samples. The colors indicate the selected ranges for Pearson coefficient calculations.

As the results indicate, there's a maximum adsorption profile in both figures. However, to identify if there's a general correlation between experimental GO and CO<sub>2</sub> adsorption, a more deeply analysis is presented introducing some statistics. To determine the statistical correlation, GO ranges are chosen based on the data distribution observed in the scattered plot of Figure A. 1 (a) and (b), and the selection is determined by identifying maximums and minimums in the CO<sub>2</sub> adsorption tendency. By segmenting the data, as indicated using different colors in the figures, a more detailed analysis of relationships is presented below.

**Coefficient of Pearson**

In this case, experimental GO and CO<sub>2</sub> adsorption can be analyzed using the Pearson Correlation coefficient for each determined range of results. In statistics, this parameter is a correlation coefficient that measures the linear relationship between two sets of data. It is calculated as the ratio of the covariance of the two variables to the product of their standard deviations (Equation A.1).

$$r = \frac{\sum(x_i - \bar{x})(y_i - \bar{y})}{\sqrt{\sum(x_i - \bar{x})^2} \cdot \sqrt{\sum(y_i - \bar{y})^2}} \quad \text{Equation A. 1}$$

Where  $x_i$  and  $y_i$  are the individual values of variables X and Y,  $\bar{x}$  and  $\bar{y}$  are the means of X and Y, respectively;  $\sum x_i$  and  $\sum y_i$  are the sum of all the data. The result of the correlation coefficient always ranges between -1 and 1, where -1 indicates a perfect negative correlation, 1 indicates a perfect positive correlation, and 0 means no linear correlation.<sup>170</sup>

The Pearson correlation coefficient was calculated for specific data ranges within the observed scattering, in order to assess localized linear relationships between the variables. This approach allows a more detailed understanding of correlation trends that may be masked in the overall dataset due to variability and non-linearity. Consequently, for analyzing the correlation between GO and CO<sub>2</sub> performance, as this calculation is for determining linear correlation, it is necessary to establish ranges of experimental GO for determining what is the kind of linear correlation with CO<sub>2</sub> adsorption. Those ranges are selected according to the maximums and minimums of CO<sub>2</sub> performance and Figure A. 1 (a) and (b) show the selection of ranges using different colors.

For the MSM method, the ranges were divided into three groups considering the tendencies of maximum and minimum adsorption of CO<sub>2</sub>: from 0 to 0.25, from 0.25 to 1.00 and from 1.00 to 6.00 % of experimental GO ranges (Table A. 1).

*Table A. 1. Pearson's Coefficient of each group in MSM samples.*

<b>Group</b>	<b>Range of experimental GO (%)</b>	<b>Coefficient of Pearson</b>
<b>1</b>	0.00-0.25	0.95
<b>2</b>	0.25-1.00	-0.81
<b>3</b>	1.00-6.00	0.10

The Pearson coefficient of each range (Table A. 1) follows the observed trend on scattering illustrated in Figure A. 1 (a) and captures the graphic data in a single number ranging between -1 and 1. Group 1 denotes a Pearson coefficient of 0.95, close to 1, which indicates a strong positive correlation. Hence, there's a clear trend suggesting that as GO increases, CO<sub>2</sub> adsorption values tend to increase too. Contrastingly, group 2 shows a strong negative correlation with a value of -0.81, which suggests the contrary effect: as GO increases, CO<sub>2</sub> adsorption of samples tends to decrease. Group 3 (with a value of 0.10), which suggests that in that range (1.00-6.00 % of experimental GO) there's no correlation between GO and CO<sub>2</sub> adsorption performance.

When sBM methodology for obtaining samples is considered, a slightly different scattering is observed in Figure A. 1 (b). The maximum point of adsorption of CO<sub>2</sub> is shifted to a higher % of experimental GO. Given the profile of these results, the ranges for calculating the coefficient of Pearson are divided into two groups: from 0 to 0.61 % of experimental GO and from 0.61 to 2% of experimental GO. Table A. 2 presents the Pearson coefficients of the sBM samples.

*Table A. 2. Pearson's Coefficient of each range group in the sBM samples.*

<b>Group</b>	<b>Range of experimental GO (%)</b>	<b>Coefficient of Pearson</b>
<b>1</b>	0.00-0.61	0.62
<b>2</b>	0.61-2.00	-0.86

As indicated by the coefficient of Pearson, the first range, in this case, is marked by a moderate positive correlation, which indicates that when GO is increased in the samples, CO<sub>2</sub> tends to increase, but at a lower level compared with the range of group 1 of the MSM samples. This result aligns with the graphs presented above due to the increased CO<sub>2</sub> adsorption values obtained in HK samples without GO, which is higher than HK from MSM and this influences the linear correlation. However, samples located in the range of group 2 indicate a strong negative correlation (with a value of -0.86, close to -1), which indicates that in this range there is a tendency where CO<sub>2</sub> adsorption performance decreases as experimental GO increases.

### **Coefficient of variance**

At this point, the results of MSM and sBM samples confirmed a certain correlation and the synergistic effect produced by the incorporation of GO in specific ranges. However, the next parameter for determining the efficiency of each method is analyzing the reproducibility. Evaluating the reproducibility of each method in a simple way and obtaining a conclusion about the tendencies can be carried out using the coefficient of variance (CV%). The coefficient of variance, unlike the Pearson correlation coefficient, facilitates the assessment of reproducibility. It is calculated as the percentage obtained by dividing the standard deviation by the mean of each specific sample (Equation A. 2).<sup>171,172</sup>

$$CV = \frac{\sigma}{\mu} \cdot 100 \quad \text{Equation A. 2}$$

Where  $\sigma$  is the standard deviation of the data set and  $\mu$  is the mean of the data set.

Following the thresholds indicated in Table A. 3, the reproducibility of specific samples can be evaluated.

Table A. 3. Thresholds of the variance coefficient, based on the references. <sup>171-173</sup>

CV (%)	Reproducibility threshold
<10%	High
10% > CV < 20%	Medium
20% > CV > 30%	Medium-Low
>30%	Low

Regarding the most adsorbent samples of each method, the reproducibility of CO<sub>2</sub> adsorption experiments is analyzed. In this case, samples are divided into ranges again, since the results are presented as a scatter plot, and experimental GO varies in each sample. Consequently, the ranges of maximum adsorption performance are segmented as narrowly as possible, enabling the definition of smaller ranges for the experimental GO values, indicated using shaded blue bubbles in Figure A. 2 (a) and (b). These ranges are then used to calculate the mean, standard deviation, and the coefficient of variation as a result.

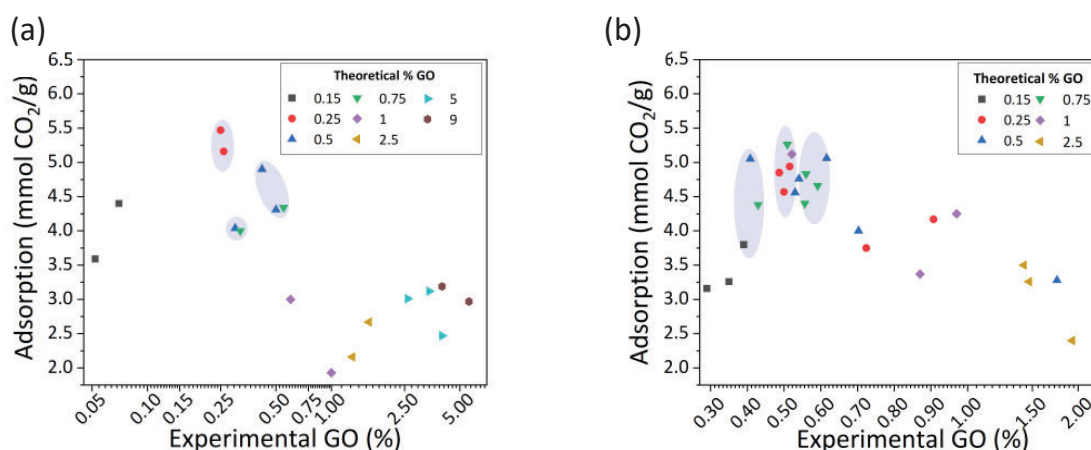


Figure A. 2. Selected samples for CV calculations in (a) MSM results and (b) sBM results. Shaded areas indicate the selected ranges utilized in the coefficient of variance calculations.

Based on the results indicated in Table A. 4, the coefficient variation for MSM samples indicates high reproducibility, as it is located at a value below 10%. On the other hand, although the sBM method also showed good reproducibility (with values

below 10% and in some cases between 10% and 20%), the variance coefficients were higher than those of the MSM method. It is important to note that the MSM method was based on 2-3 duplicate samples, while the sBM method involved 3-6 replicates. Subsequently, although the MSM method exhibited good reproducibility, it could have been more accurate with additional repetitions. Due to time constraints, however, only a limited number of replicates were performed in each method, with the number of repetitions being higher for sBM samples. Considering this, both synthesis methods appear effective in terms of reproducibility when comparing experimental GO with CO<sub>2</sub> adsorption values.

Table A. 4. Calculated coefficient of variance of MSM and sBM samples for CO<sub>2</sub> adsorption in each experimental GO range. \* mmol CO<sub>2</sub>/g

Method	Exp. GO range	Mean*	SD*	CV (%)	Method	Exp. GO range	Mean*	SD*	CV (%)
MSM	0.25-0.30	5.32	0.22	4.1	sBM	0.39-0.49	4.41	0.63	14.2
MSM	0.30-0.32	4.02	0.03	0.7	sBM	0.50-0.54	4.93	0.28	5.8
MSM	0.32-0.55	4.51	0.33	7.4	sBM	0.55-0.61	4.74	0.24	5.1

For evaluating the reproducibility of the synthesis, the variance coefficient of the RQ process was also calculated (Table A. 5). In this regard, the coefficients of variation were calculated for each sample considering the groups of samples synthesized with the same theoretical GO (indicated in the legend of Figure A. 2 (a) and (b)). For example, for the HK-0.25 sample, the CV was calculated by dividing the standard deviation of the experimental GO values from all samples synthesized using 0.25% w/w of theoretical GO by their mean and multiplying by 100.

The findings indicate that, although being an easy and simple method for determining the experimental content of GO introduced to HK samples, the reproducibility of synthesis was not particularly high.

Table A. 5. Calculated coefficient of variance of MSM and sBM samples for RQ experiments.

Method	Sample	Mean (%)	SD (%)	CV (%)	Method	Sample	Mean (%)	SD (%)	CV (%)
MSM	HK-0.25	0.25	0.10	0.15	sBM	HK-0.25	0.58	0.13	22.50
MSM	HK-0.50	0.41	0.10	24.8	sBM	HK-0.50	0.56	0.05	8.3
MSM	HK-0.75	0.45	0.12	27.1	sBM	HK-0.75	0.57	0.24	13.18

Considering the calculations, in general, the reproducibility of RQ is medium for MSM. For sBM samples, the results indicate more variability. This highlights the importance of considering other external parameters that affect sample synthesis, such as the temperature in MSM or the milling revolutions used in sBM. These factors can introduce experimental deviations and lead to deviations in test results (such as observed in CO<sub>2</sub> adsorption).

#### **ANOVA on Mixed Solvent Method (MSM)**

The previous analysis provides two different descriptive statistics:

- Relationship between CO<sub>2</sub> adsorption and experimental GO
- Reproducibility of the CO<sub>2</sub> adsorption performance (through the evaluation of CO<sub>2</sub> maximum adsorption performance at 1000 mmHg)
- Reproducibility of the method of synthesis (through the evaluation of RQ experimental results)

Although the reproducibility of the RQ experimental procedure was complex (Table A. 5), CO<sub>2</sub> adsorption values revealed good reproducibility for those samples that present similar ranges of experimental GO (Table A. 4). Consequently, an ANOVA analysis is carried out to determine if the differences in CO<sub>2</sub> adsorption are statistically significant based on the actual experimental GO content in all the samples.<sup>174</sup> Firstly, an ANOVA test is performed for the samples of each method: MSM and sBM. Once both synthetic methods are analyzed in detail, a comparison of the data obtained from both methods is described.

To analyze these parameters, adsorption results are classified based on different ranges of experimental GO obtained, rather than the theoretical GO used. These ranges are selected according to similarities in experimental GO, based on the maximum and minimum values of CO<sub>2</sub> adsorption performance. The order follows the indicated in Table A. 6 and is represented in Figure A. 3.

Table A. 6. Classification of CO<sub>2</sub> adsorption results at 1000 mmHg according to the experimental range of GO% for MSM samples.

Exp. GO range (%)	[0]	[0.05-0.07]	[0.25-0.30]	[0.40-0.50]	[0.50-0.60]	[1-2]	[>2]
Group	R1	R2	R3	R4	R5	R6	R7
CO <sub>2</sub> ads. (mmol CO <sub>2</sub> /g)	2.77	4.40	5.16	4.31	4.34	2.16	3.00
	3.14	3.59	5.47	4.90	3.00	2.67	3.01
			4.04			1.93	3.19
			4.00				2.97
							2.47

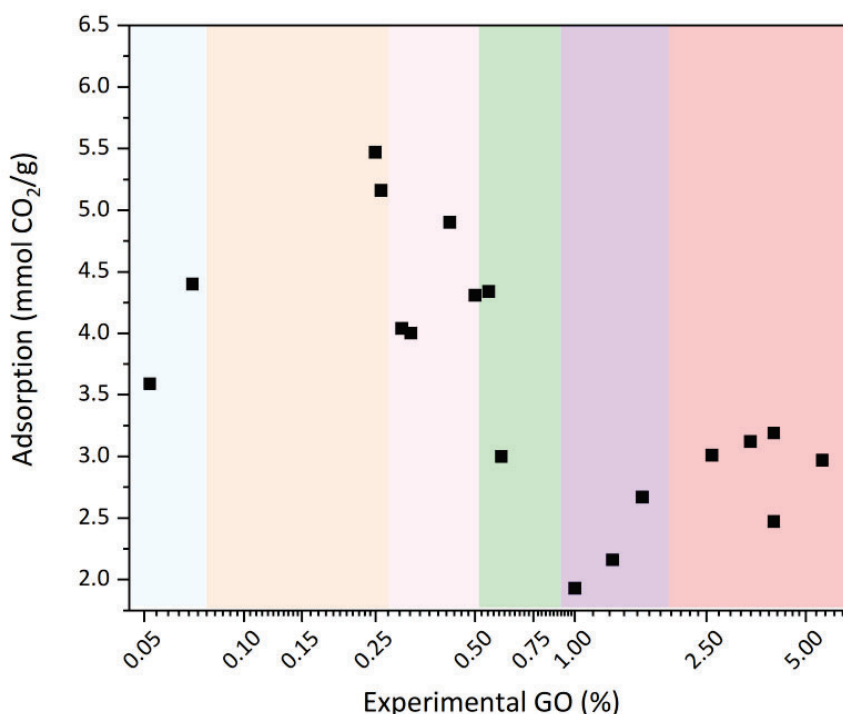


Figure A. 3. Selection of the ranges used for the ANOVA test of MSM sample results of the relationship between CO<sub>2</sub> adsorption performance at 1000 mmHg and experimental GO.

Using these distributions of the data, an analysis of variances using one factor is performed and the results are represented in Table A. 7. The interpretation of this data relies on comparing some parameters obtained from the variance analysis. First, the F value compares the variability between groups versus the variability within the groups. A high F value suggests a significant difference between groups. On the other hand, the p-value indicates the probability of obtaining an F value as extreme as the one calculated if there are no differences between the groups. A p-value of less than 0.05 indicates that there are statistical differences between the groups.

*Table A. 7. ANOVA obtained from the MSM sample results.*

Origin of variation	Sum of squares	Degrees of freedom	Mean squares	F	p-value	Critical value F
Between groups	15.32	6	2.55	8.79	5.79x10 <sup>-04</sup>	2.91
Into the groups	3.77	13	0.29			
<b>Total</b>	19.09	19				

Thus, considering the obtained data, given that the p-value is 5.79x10<sup>-04</sup> (less than 0.05), it is confirmed that statistically, there exist significant differences in the CO<sub>2</sub> adsorption results from the samples of different groups of ranges (e.g. R1, R2, R3...). Moreover, the F value is notably high compared to the F critical value, which suggests that variability between groups is higher than the variability within each group of samples, which reinforces the hypothesis that experimental GO concentrations influence CO<sub>2</sub> adsorption.

In consequence, this analysis reveals that there are significant differences in CO<sub>2</sub> adsorption between different ranges of experimental GO. Therefore, this analysis suggests that rigorous control over the experimental GO is crucial to obtain more consistent results in CO<sub>2</sub> adsorption. Consequently, to improve reproducibility and

efficiency, it is necessary to improve the incorporation and retention of GO in the samples.

### **ANOVA on small Ball Milling Method (sBM)**

For those samples synthesized using sBM, an analysis of variance using one factor was also performed. In this case, the range of experimental GO was divided into different groups regarding experimental GO, as indicated in Table A. 8 and represented in Figure A. 4.

Table A. 8. Classification of CO<sub>2</sub> adsorption results according to the experimental range of GO% for sBM samples.

Exp. GO range (%)	[0]	[0.29-0.39]	[0.40-0.52]	[0.53-0.59]	[0.60-0.89]	[0.90-1]	[>1]
Group	R1	R2	R3	R4	R5	R6	R7
CO <sub>2</sub> adsorption (mmol CO <sub>2</sub> /g)	3.7	3.16	4.38	5.12	4	4.17	3.50
	4.1	3.26	5.05	4.56	3.75	4.25	3.26
		3.8	4.85	4.76	5.06		3.28
			4.57	4.83	3.37		2.4
			4.94	4.40			
			5.26	4.66			

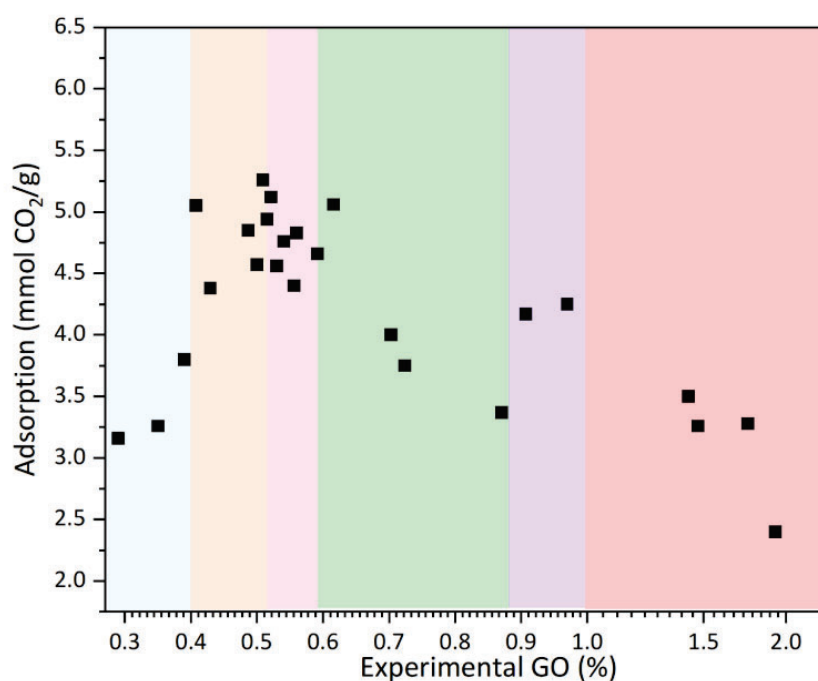


Figure A. 4. Selection of the ranges used for the ANOVA test of the sBM sample results of the relationship between CO<sub>2</sub> adsorption performance at 1000 mmHg and experimental GO.

Grouping the results of CO<sub>2</sub> adsorption in the indicated ranges of experimental GO, the ANOVA test determines the following data in Table A. 9:

Table A. 9. ANOVA results obtained from the sBM sample results.

Origin of variation	Sum of squares	Degrees of freedom	Mean squares	F	p-value	Critical value F
Between groups	10.98	6	1.83	10.69	2.32x10 <sup>-05</sup>	2.59
Into the groups	3.42	20	0.17			
Total	14.41	26				

ANOVA test of sBM provided similar results compared to the MSM ANOVA test, since the p-value was also lower than 0.05 in this case, and the F value was higher than the critical F value. Therefore, statistics indicate that there's a significant difference between samples with different experimental GO and that variability between the

groups of ranges is higher than within their range. As described before, the control of experimental GO content in each sample is crucial for monitoring the CO<sub>2</sub> adsorption properties of these samples.

### **Big ball milling (bBM) and small ball milling statistical analysis**

The results of the bBM are compared with the statistical analysis performed with sBM samples. Figure A. 5 indicates the relationship between CO<sub>2</sub> adsorption performance and the experimental GO of each sample from the sBM and bBM methods.

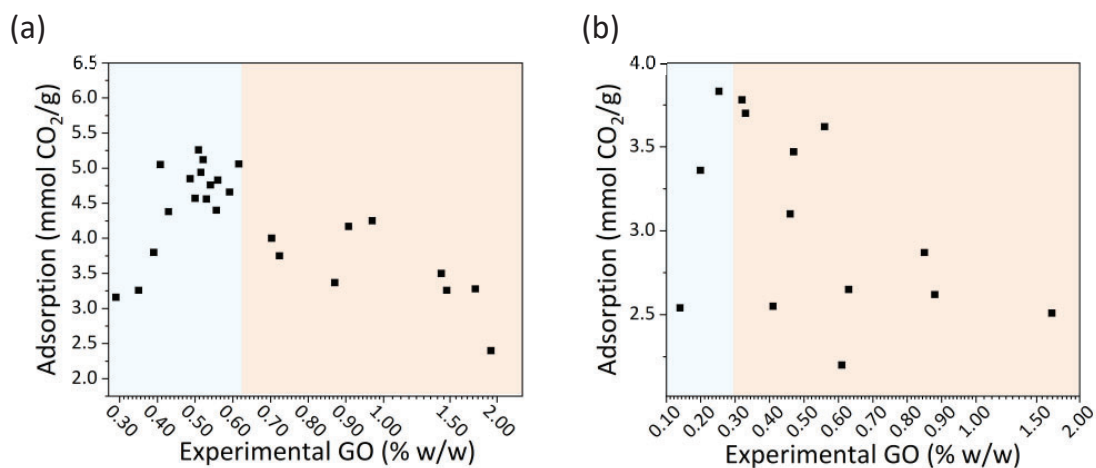


Figure A. 5. (a) CO<sub>2</sub> adsorption results (at 1000 mmHg) versus experimental GO of sBM and (b) CO<sub>2</sub> adsorption results (at 1000 mmHg) versus experimental GO of bBM samples. The colors indicate the selected ranges for Pearson coefficient calculations.

### **Pearson coefficient**

For determining the kind of correlation between experimental GO and CO<sub>2</sub> adsorption values, the experimental GO content ranges were selected based on the data distribution observed in the scatter plot of Figure A. 5 (a) and (b), where the colors indicate the selected ranges based on maximum and minimum of the CO<sub>2</sub> adsorption performance. So, following the same procedure described before, this segmentation allows for a more detailed analysis utilizing Pearson coefficient calculations. The selected ranges are group 1, from 0.00 to 0.30; and group 2, from 0.31 to 1.70.

In this case, the results are depicted in Table A. 10. The qualitative analysis revealed that in group 1, the samples exhibit a moderate positive correlation between experimental GO and CO<sub>2</sub> adsorption, suggesting that while increasing experimental GO in the range of group 1, a parallel increase in CO<sub>2</sub> adsorption is observed. In contrast, group 2 displays a weak negative correlation, indicating that in that range of experimental GO, CO<sub>2</sub> adsorption tends to decrease, though with a weak tendency.

*Table A. 10. Pearson's Coefficient of each group in the bBM samples.*

<b>Group</b>	<b>Range of experimental GO (%)</b>	<b>Coefficient of Pearson</b>
<b>1</b>	0.00-0.30	0.60
<b>2</b>	0.30-1.70	-0.35

Compared to the results of small-scale sBM samples, depicted in Table A. 11, the tendency denoted some similarities. However, group 2 of the sBM samples indicated a higher negative coefficient of Pearson, denoting a stronger correlation. These results indicate that when the samples are scaled up to larger quantities, the correlation between GO and the optimization of CO<sub>2</sub> capture changes.

*Table A. 11. Pearson's Coefficient of each group in the sBM samples.*

<b>Group</b>	<b>Range of experimental GO (%)</b>	<b>Coefficient of Pearson</b>
<b>1</b>	0.00-0.61	0.62
<b>2</b>	0.59-2.00	-0.86

### **Coefficient of variance**

On the other hand, the reproducibility of samples regarding CO<sub>2</sub> adsorption performance and experimental GO are also analyzed through the variance coefficient. In this case, considering the selected ranges (indicated using blue bubbles

in Figure A. 6), variances indicated good reproducible results as in the case of sBM samples. The results are depicted in Table A. 12.

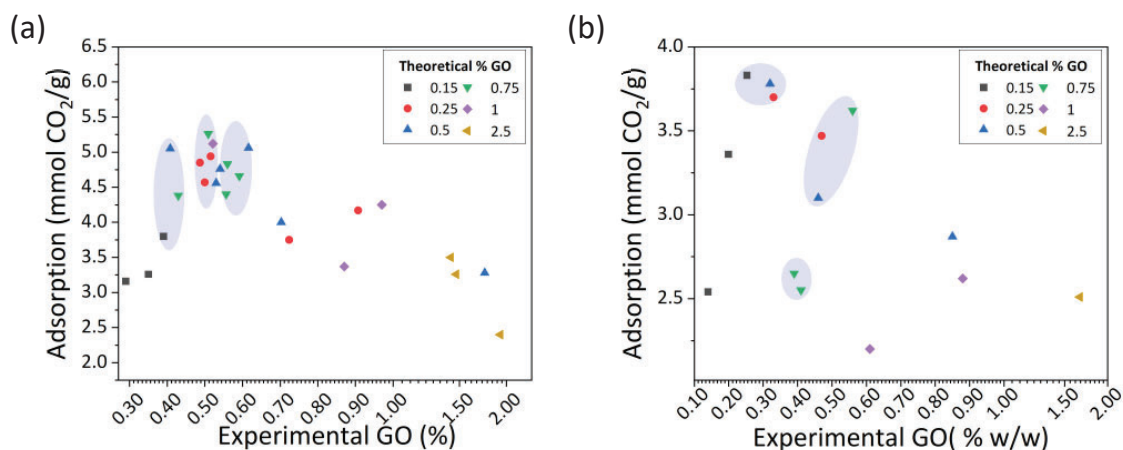


Figure A. 6. Selected samples for CV calculations in (a) sBM results and (b) bBM results. Shaded areas indicate the selected ranges utilized in the coefficient of variance calculations.

Table A. 12. Calculated coefficient of variance (CV) of sBM and bBM samples of experimental GO and CO<sub>2</sub> adsorption performance. \*mmol CO<sub>2</sub>/g

Method	Exp. GO range	Mean*	SD*	CV (%)	Method	Exp. GO range	Mean*	SD*	CV (%)
sBM	0.39-0.49	4.41	0.63	14.2	bBM	0.25-0.30	3.77	0.07	1.7
sBM	0.50-0.54	4.02	0.03	5.8	bBM	0.39-0.41	2.6	0.07	2.7
sBM	0.55-0.61	4.51	0.33	5.1	bBM	0.46-0.56	3.40	0.27	8.0

For both cases, the CV calculations present values under the 10% threshold, even in some cases it slightly deviates, as for the 0.39-0.49 group of samples in sBM. These results, according to the literature<sup>173</sup>, indicate that reproducibility within that range of experimental GO is high.

On the other hand, the reproducibility of the synthesis is also evaluated, proceeding in the same line as for the sBM method. Based on the results of experimental GO related to the theoretical GO, which is indicated in the legend of, CV calculations for bBM samples are presented in Table A. 13. As a result, the values indicate lower reproducibility.

Comparing the results with sBM method, while in the case of the sBM method some variability in reproducibility is observed concerning the experimental RQ, reproducibility is even lower in some cases of bBM samples (like in the HK-0.50 sample).

Table A. 13. Calculated coefficient of variance of sBM and bBM samples for RQ experiments.

Method	Sample	Mean (%)	SD (%)	CV (%)	Method	Sample	Mean (%)	SD (%)	CV (%)
sBM	HK-0.25	0.58	0.13	22.50	bBM	HK-0.25	0.40	0.10	24.8
sBM	HK-0.50	0.56	0.05	8.3	bBM	HK-0.50	0.55	0.27	50
sBM	HK-0.75	0.57	0.24	13.18	bBM	HK-0.75	0.53	0.11	20.4

### **ANOVA on big Ball Milling methods**

Like in Section 4.3 of this chapter, ANOVA test is also performed for asses the correlation between CO<sub>2</sub> performance of the samples obtained via bBM. Table A. 14 presents the values of CO<sub>2</sub> adsorption of each group of samples divided into the ranges depicted in Figure A. 7, indicated using different colors.

Table A. 14. Classification of CO<sub>2</sub> adsorption results at 1000 mmHg according to the experimental range of GO for bBM samples.

Exp. GO range (%)	[0]	[0-0.25]	[0.26-0.33]	[0.34-0.50]	[0.51-0.63]	[0.64-0.88]
Group	R1	R2	R3	R4	R5	R6
CO <sub>2</sub> ads. (mmol CO <sub>2</sub> /g)	3.15	2.54	3.7	2.55	3.62	2.87
	3	3.36	3.78	3.1	2.2	2.62
		3.83		3.47	2.65	2.51

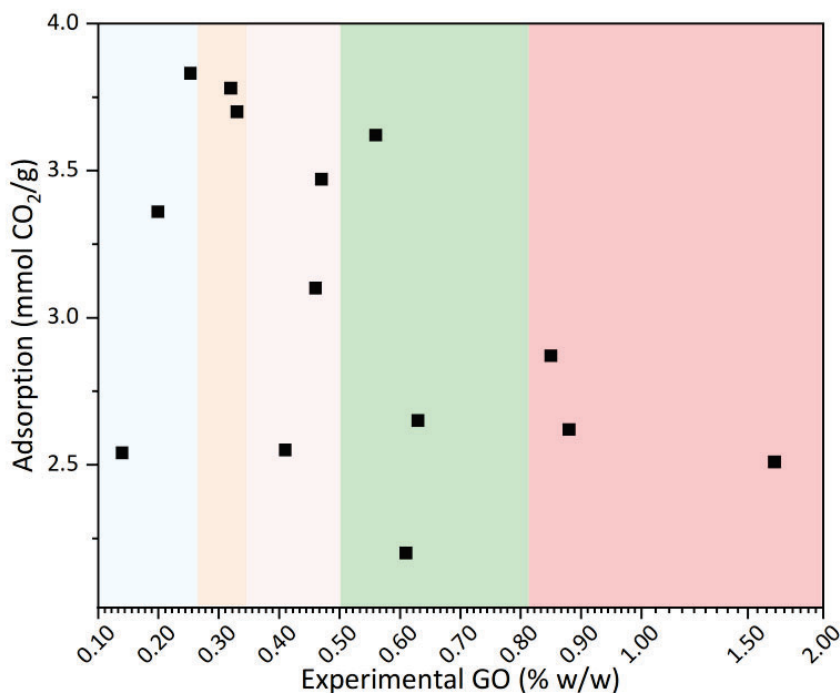


Figure A. 7. Selection of the ranges used for the ANOVA test of the bBM sample results of the relationship between CO<sub>2</sub> adsorption performance at 1000 mmHg and experimental GO.

The results derived from the ANOVA test using bBM data showed that although initial statistical calculations indicated some correlations and good reproducibility relating to CO<sub>2</sub> adsorption and experimental GO, there was not enough evidence using the obtained data to determine that there are differences between ranges. Table A. 15 shows the results calculated from the ANOVA test.

Table A. 15. ANOVA obtained from the bBM sample results.

Origin of variation	Sum of squares	Degrees of freedom	Mean squares	F	p-value	Critical value F
Between groups	1.66	5	0.33	1.37	0.31	3.33
Into the groups	2.41	10	0.24			
Total	4.07	15				

Regarding the statistics, the p-value is higher than the significance threshold of 0.05 established as a reference.<sup>175</sup> Moreover, statistic F compares the variability between groups with the variability within groups. In this case, the sum of squares within groups is greater than the sum of squares between groups, suggesting that the variability inside each group is larger than the differences between group means. This supports the conclusion that the mean values across the different experimental GO content ranges do not differ significantly.

In conclusion, using the data provided by the ANOVA test, the statistics indicate that there's no statistically significant evidence to determine that the CO<sub>2</sub> adsorption measurements differ among the defined experimental GO ranges. Therefore, the different groups of samples can be considered similar when comparing the effect relating to experimental GO and CO<sub>2</sub> adsorption.